Dissertation

submitted to the
Combined Faculty of Natural Sciences and Mathematics
Ruprecht-Karls University Heidelberg, Germany
for the degree of
Doctor of Natural Sciences (Dr. rer. nat.)

Presented by
Stojan Maleschlijski, MSc.
Born in Simitli, Bulgaria
Oral examination: November 21st, 2014

Behavior of barnacle larvae during surface exploration studied by stereoscopy

This dissertation was carried out at the
Department of Applied Physical Chemistry
University of Heidelberg

Referees:
Prof. Dr. Axel Rosenhahn
apl. Prof. Dr. Hans-Robert Volpp

Für Lena Marie

Abstract

Marine biofouling is a global problem with a negative impact on several industrial and maritime branches, causing immense costs. Alongside with the economic consequences of colonization of surfaces, the environmental aspects should not be underestimated. Because of the predominant use of heavy-metal based antifouling coatings in the last decades, the most prominent component of which is tributyltin, TBT, several unacceptable environmental 'side effects' on non-targeted species have emerged. This led to a global ban of the use of TBT-containing coatings in 2008. Since then, the research efforts focus on the development of surfaces which solely rely on physicochemical properties to mitigate the undesired accumulation of biomass. For identification of surface properties which influence and guide settlement, a better understanding of the colonization mechanisms of the target organisms is required.

The purpose of this work was the investigation of the exploratory behaviour of barnacle larvae (cyprids) of *Balanus amphitrite*. This species was selected because it is widely spread in several geographic regions and contributes significantly to biofouling pressure. To enable the extraction of three-dimensional swimming trajectories, a stereoscopic setup was developed. It was utilized to quantify the pre-settlement behaviour of cyprids on surfaces with different wettability, hydration or charge. The analysis of the data allowed the identification of basic reoccurring **patterns** in the motion of cyprids, i.e. spiraling, swimming, sinking, rotating and walking. A detailed evaluation of the distribution of these patterns revealed that swimming was most frequently observed, followed by sinking which seemed to be its counterpart. Furthermore, it could be shown that most surface contacts emerged after sinking, while an active swimming towards the substrate was seldom observed.

In addition, the general distribution of cyprids in the water column demonstrated that there was a clear preference for interfacial regions, and that the main occurrence of cyprids concentrated in three distinct zones above surfaces - the lower, bulk and upper swimming region, denoting the distance of the larvae from the substrate. It was revealed that the settlement preferences of cyprids were reflected in the **motility** parameters of exploration, i.e. linearity of the locomotion, mean velocity, swimming depth and extent of explored area.

Once on a surface, cyprids initiate a **close surface inspection**, involving bipedal walking. The quantification of this mode of movement showed that the step duration and step velocity correlated with the attractiveness of the surface for settlement. Moreover, an analysis of the complete exploration process - from swimming via close surface inspection to **interface interactions**, confirmed literature reports that the

number of surface touchdowns and the amount of organic deposit left behind were guided by the attractiveness of the substrate for biofouling. In addition to this organic deposit, macromolecules and other compounds accumulate on surfaces, immediately after these have been placed in an aquatic environment. The influence of this **'conditioning' film** on the exploratory behaviour was investigated and it was proven to cover the initial chemical end groups of different substrates. This masking process provoked cyprids to explore non-attractive conditioned surfaces in the same manner as attractive ones.

Except on model surfaces, the exploratory behaviour was also investigated on **commercially** available hydrogel-based **coatings** and it was found that the motility of cyprids started to decrease gradually immediately after surface contact and after 4h it completely stopped, which was contributed to mortality of the organisms caused by the paints. Finally, a the stereoscopic setup was modified to allow measurements *in situ*, underwater. The results of the **field experiments** at two test sites are discussed with respect to the applicability of the system for measurements in the natural environment and its capability to reveal colonization dynamics of marine organisms.

Kurzfassung

Die unerwünschte Besiedlung von Oberflächen, marines Biofouling genannt, ist ein alt bekanntes Phänomen, welches große Probleme für eine Vielzahl industrieller und maritimer Bereiche birgt. Neben den entstehenen wirtschaftlichen Zusatzkosten spielen auch Umweltfaktoren eine wichtige Rolle. Die Anwendung von schwermetallhaltigen Komponenten in Beschichtungen in den letzten Jahrzehnten, wie Tributylzinn (engl. *tributyltin*, TBT), hat erhebliche Umweltschäden verursacht. Dies hat dazu geführt, dass 2008 der Einsatz von TBT-haltigen Substanzen in maritimen Beschichtungen gesetzlich verboten wurde. Seitdem hat sich die Forschung auf die Entwicklung von Oberflächen fokussiert, die eine Besiedlung durch physikalisch-chemische Eigenschaften des Substrates vermindern. Um die Reize, die das Biofouling steuern, zu identifizieren, müssen die Kolonisationsmechanismen der besiedelnden Organismen entschlüsselt werden.

Zweck dieser Arbeit war das Explorationsverhalten von Cyprislarven (*Cyprids*) der Seepocke *Balanus amphitrite* zu untersuchen, da diese Spezies in verschiedenen geographischen Regionen weit verbreitet ist und wesentlich zum Biofouling beiträgt. Um die Extraktion von dreidimensionalen Schwimmbahnen zu ermöglichen, wurde ein stereoskopischer Aufbau entwickelt. Das System wurde verwendet, um das Verhalten von *Cyprids* während der Exploration auf Oberflächen mit unterschiedlicher Benetzbarkeit, Hydratation und Ladung zu quantifizieren. Zudem ermöglichte die Analyse der Daten die Identifikation von wiederkehrenden **Grundmustern** in der Bewegung der *Cyprids*. Diese waren *Spiraling*, *Swimming*, *Sinking*, *Rotating* und *Walking*. Eine detaillierte Auswertung der Verteilung dieser Muster ergab, dass *Swimming*, gefolgt von *Sinking*, am häufigsten beobachtet wurde. Darüber hinaus konnte gezeigt werden, dass die meisten Oberflächenkontakte nach *Sinking* erfolgten, und ein aktives Schwimmen in Richtung des Substrats nur sehr selten beobachtet wurde.

Die *Cyprids* schwammen in drei verschiedenen Zonen - untere (*lower*), mittlere (*bulk*) und obere (*upper*) Schwimmzone. Ferner zeigte die Verteilung der Larven in der Wassersäule eine klare Präferenz für die Grenzflächen. Es wurde außerdem beobachtet, dass sich die Besiedlungspräferenzen der *Cyprids* in den **Motilitätsparametern** der Exploration (z.B. Linearität der Bewegung, mittlere Geschwindigkeit, Schwimmtiefe) widerspiegelten.

Einmal auf einer Oberfläche initiieren *Cyprids* die sogenannte **oberflächennahe Inspektion**, eine Art bipedales Gehen. Die Quantifizierung dieser Bewegungsform zeigte, dass die Schrittdauer und Schrittgeschwindigkeit mit der Besiedlungsattraktivität der Oberfläche korrelierten. Darüber hinaus bestätigte eine Analyse des gesamten Explora-

tionsprozesses - von Schwimmen, über oberflächennahe Inspektion bis zu **Interaktion mit der Grenzfläche** Literaturberichte: die Anzahl der Oberflächenkontakte und die Menge der zurückgelassen organischen Masse werden durch die Kolonisationsattraktivität des Substrats bestimmt.

Unmittelbar nachdem Oberflächen in Kontakt mit Wasser kommen, lagern sich darauf Makromoleküle und andere organische Verbindungen an. Der Einfluss dieses **'Konditionierungsfilms'** auf das Erkundungsverhalten der *Cyprids* wurde ebenfalls untersucht. Es konnte nachgewiesen werden, dass die ursprüngliche chemische Endgruppe des Substrates maskiert wurde. Diese Abschirmung hatte zur Folge, dass *Cyprids* konditionierte nicht-attraktive Oberflächen in der gleichen Weise untersuchten wie attraktive.

Außer auf Modelloberflächen wurde das Erkundungsverhalten auch auf **kommerziellen** hydrogel-basierten **Beschichtungen** untersucht. Es wurde festgestellt, dass die Motilität der *Cyprids* nach dem Oberflächenkontakt schrittweise nachlies und nach 4h vollständig stoppte, was auf die Mortalität der Organismen zurückgeführt werden konnte. Schließlich wurde eine Modifikation des Aufbaus vorgenommen, die Messungen *in situ* unter Wasser ermöglicht. Die Ergebnisse der ersten **Feldstudien**, aufgenommen an zwei Standorten (an der Westküste Floridas und der Ostküste Englands), wurden im Hinblick auf die Durchführbarkeit der Messungen analysiert. Desweiteren wurde demonstriert, dass eine Charakterisierung der Kolonisationsdynamik von marinen Organismen in natürlicher Umgebung durch das System möglich war.

Contents

1. Introduction

The textbook definition of *marine biofouling* is the undesired accumulation of biomass on objects submerged underwater [1]. In fact, objects become immediately exposed to a complex biofouling landscape. A combination of macromolecules, bacteria, micro and macro fouling organisms [1] colonizes them and causes a modification of the topographical and a masking of the chemical structure, thus interfering with their initial purpose. These effects have a negative impact on a broad variety of fields ranging from the maritime industry (e.g. shipping and leisure vessels) over the machine industry (e.g. heat exchanger) and research (e.g. oceanographic sensors) to the fishing industry (e.g. aquaculture systems) [1]. For example, for the shipping industry, Schultz et al. [2] showed that a heavy calcareous fouling can cause an increase of the required shaft power by 86% at cruising speed. It is believed that fouling-free ship hulls would lead to a decrease in the current annual fuel consumption of the world fleet (ca. 184 million tonnes) by ca. 4%, yielding an annual saving of 7.36 million tonnes of liquid fuel or ca. 3.2 tonnes of CO_2 emissions [3]. In addition to the environmental considerations, the expenses due to the increased fuel consumption, reduced inter docking periods and higher dry dock costs (renewal of coatings, cleaning, etc.) are enormous.

The negative influence of marine biofouling is not only a problem of modern times and has been recognized and combated for more than 2000 years, when first attempts have been documented for the usage of "seal tar" or lead and wooden sheathing techniques [4]. Later on, copper sheathing was widely spread, which was in turn abandoned with the introduction of iron ships in the 18th and 19th century. In the late 1800s, attempts to deploy an antifouling paint occurred and a very high variance of antifouling paints with different effectiveness has been applied since. In the 1950s a coating containing tributyltin (TBT) was developed expressing a broad spectrum high toxicity [4]. Because these paintings were highly efficient, they dominated the antifouling market for several decades. Due to their wide use, environmental side effects became visible with time - e.g. poisoning of oyster beds or "imposex among dog whelks" [3]. As soon as the effects on the coastal marine life were recognized, the International Maritime Organization reacted by issuing a ban on the application of TBT-based coatings in 2003 [4, 5].

These recent legislative restrictions motivated a new generation of research which aims on developing 'intelligent' TBT-free and biocide-free coatings [1, 6–8]. The new approach does not rely on the application of toxic substances, which are lethal for the fouling organisms, but rather on understanding their life cycles and their exploration and colonization mechanisms. With this knowledge, potential interference stages or

surface cues, which prevent biofoulers from settling, can be identified. This new type of coatings would ideally only inhibit the colonization by the target organisms, without interfering with other species in close proximity. The effect would therefore be highly focused, efficient and environmentally friendly.

The current standard methods for quantification of the settlement behavior of marine organisms, which have been utilized for several decades, are in assay format [9]. They involve the exposure of coated surfaces to the influence of marine biofoulers for a defined period of time and the assessment of the extent of colonization afterwards [10–14]. This allows a direct identification of surface properties which inhibit or enhance settlement. With these methods it was already demonstrated that colonization is not of random nature, but rather involves an active behavioural response to surface characteristics. One disadvantage of the 'post-settlement' approach can be the time period before settlement events occur, which varies from several days to months (especially in the field, [15]). Furthermore, it was recently shown that the surface selectivity of barnacle larvae decreases with age and these eventually also settle on less attractive surfaces [16]. Thus, a direct correlation between the number of organisms settling on a given test surface and the attractiveness of this surface for settlement, even though existent, could be misleading.

Newer methods aim on deriving the settlement preferences of cyprids by applying motion analysis and quantification of the exploratory behavior of the larvae. The 2-D image data, used for this process, is usually collected with various acquisition techniques (e.g. high-speed photography [17], video microscopy [18–25], imaging surface plasmon resonance [26, 27]). Motion analysis on the 2-D data helped to demonstrate that a correlation exists between the way cyprids explore surfaces and the attractiveness of the surface for settlement [28, 29]. One limitation of these methods is that a reliable quantification of the behavior is possible only for motions within the projected plane. Hence, to be able to fully understand the complex three-dimensional exploratory behavior of cyprids and to accurately extract quantitative behavioral parameters, three-dimensional techniques need to be applied. In the case of small organisms such as bacteria or *Ulva* sporelings this has been demonstrated using digital in-line holographic imaging [30–33]. A similar method has been successfully implemented also to reveal predator-prey behavior in dinoflagellates [34]. Holography, however, requires a complicated infrastructure and significant expertise if it is to be applied successfully. One alternative technique is stereoscopy, which allows the 3-D tracking of objects as diverse as people [35, 36], small particles in particle tracking velocimetry [37], dusty plasmas under microgravity [38] or estuarine calanoid copepods [39, 40]. Compared to holography, a major advantage of stereoscopy is that no reconstruction of the recorded data is required.

In the course of this thesis, the exploratory behavior of barnacle cyprids of *Balanus amphitrite* was investigated in three dimensions with a custom-designed stereoscopic system. *B. amphitrite* larvae were selected, as one of the most widely spread biofouling organisms [41], found in different geographical areas and contributing highly to the

colonization of objects submerged underwater. To quantify the exploratory behavior of the cyprids, the setup was utilized to extract three-dimensional locomotion trajectories on surfaces with different chemical properties (charge, wettability and hydration). The trajectories were investigated in order to identify different basic reoccurring **motion patterns** and to quantify their occurrence during locomotion, thus identifying the most and less frequently observed. Furthermore, it was investigated whether the patterns occur under a predefined sequential order and which are the main patterns leading to surface contact. In addition, the **general motility** of cyprids was investigated 'macroscopically', involving an analysis of the distribution of the larvae in the water volume. Parameters describing the motility were correlated with the level of attractiveness for settlement of surfaces with different chemical properties. The topic of **close surface inspection** was covered, by evaluating the motion parameters of cyprids during exploration of surfaces in order to reveal the correlations between these parameters and the attractiveness of the substrates. To obtain a complete description on the exploratory process, in addition to the motility aspect of behavior, also the **interactions** of cyprids with the liquid-solid **interface** were investigated, combining the stereoscopic setup with an imaging surface plasmon resonance device. In addition, the effects of **conditioning films** on the exploratory behavior were analyzed, by quantifying the changes in the exploratory parameters of cyprids on pristine as well as preconditioned surfaces. Furthermore, the aspect of whether exploratory behavior changes on **commercially** available **coatings** when compared to model surfaces was investigated. Finally, a modification of the stereoscopic setup was applied, which allowed to image biofouling organisms *in situ*, in the ocean and it was characterized with respect to its applicability, analyzing the outcome of **field experiments**.

2. Background

In the following sections the state of the art relevant for this work is reviewed. First, a general overview on the different marine biofouling species is given, followed by a description of the life cycle and morphology of the target organism - the barnacle cyprid. The current methods for quantification of exploratory and settlement behavior of cyprids are presented, as well as the surface properties influencing these behaviors. Finally, the mathematical basics of computer stereoscopic vision are discussed.

2.1. Marine biofouling

Marine biofouling is a general term describing the accumulation of organic and inorganic molecules, micro- and macroorganisms on surfaces submerged underwater. The sessile forms of the organisms rather than the larvae usually become visible, because of their impact on surfaces and structures. More than 4000 species have been identified on fouled structures so far, which is just a fraction of the real number, since only organisms capable of adapting to new surfaces do not get washed off and can be assessed quantitatively [4].
The biofouling process is considered to be composed of various organisms exhibiting different sizes and adhering to immersed objects on different time scales. The colonization of a given surface depends on factors like availability of the organisms during the colonization stages and their relative rates of attachment and surface exploration. The specific organisms that occur in the fouling community depend on substratum, geographical location, season, and factors like competition and predation [1].
Figure 2.1 shows an overview of representative organisms of diverse dimensions involved in biofouling. There are four main groups of participants in the colonization of substrates: macromolecules, micro-, soft- and hard-foulers. In the macromolecules group, molecules primarily originating from dissolved organic material are included which form a so called 'conditioning film' [42]. Unicellar microorganisms such as bacteria, diatoms and protozoa are referred to as micro-fouling organisms (often also 'slime'). Macroscopically visible algae and invertebrates such as soft corals, tunicates and anemones are considered macro-foulers. Finally, barnacles, mussels, tube worms and other shelled invertebrates belong to the group of hard macro-fouling organisms [1].

The widely spread linear 'successional' model for colonization of surfaces stating that biofilm formation is followed within a week by macroalgae (seaweeds), followed

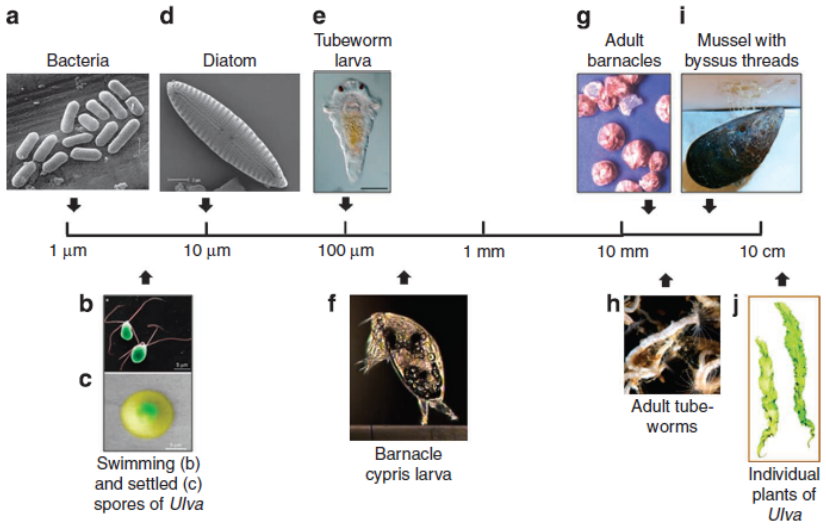

Figure 2.1.: Representative overview of species involved in biofouling. On the left side of the figure the larval stages of the organisms are presented (a-f), whereas on the right the adult forms can be found. The size of the species increases form left to right. Image taken from [1].

in turn, within several weeks by larvae of invertebrates, such as barnacles, proved to be an oversimplification. It could be shown that spores of seaweeds settle on surfaces within minutes and larvae of some barnacle species within a few hours of immersion [15]. For this reason, newer approaches evaluate the colonization of surfaces based on the 'dynamic model' [1, 43, 44].

2.2. Barnacle cyprids

Since the focus of this work lies on the quantification of the exploratory behavior of barnacle cyprids, the next sections discuss the life cycle, morphology and motility of the larvae.

2.2.1. Life cycle of cypris larvae

Barnacle cyprids are one of the main model organisms used in biofouling research as they actively select a substratum for settlement and metamorphosis [41]. Because of their broad distribution in coastal and estuarine regions [12], as well as the fact that they are considered to be a dominant biofouling organism in warm waters worldwide [45], cyprids of *Balanus amphitrite* (also *Amphibalanus amphitrite* [46]) have been extensively examined in field and laboratory research. Due to the fact that they can be successfully reared under laboratory conditions throughout the year without any

specific seasonal dependency and because they settle readily also in static water assays [11], they are widely used in toxicity, settlement and behavioral studies. For that reasons cyprids of the species *Balanus amphitrite* were selected for the experiments in this thesis.

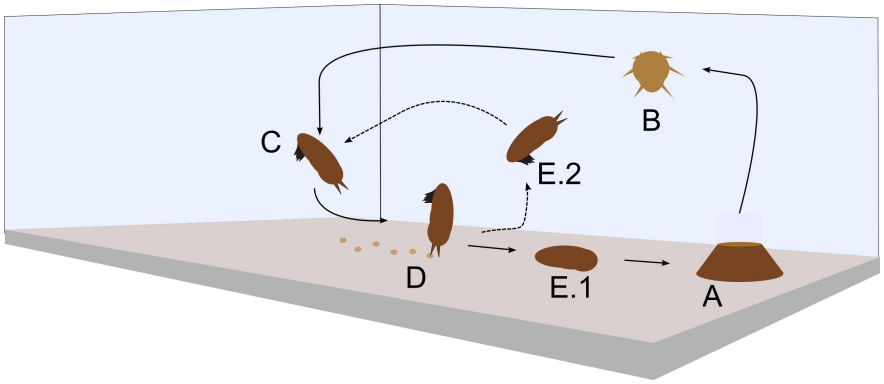

Figure 2.2.: Simplified model of the barnacle lifecycle. (A) The adult barnacle releases (B) nauplii which feed in the water column before they metamorphose into (C) cyprids. Cyprids examine the (D) substratum, referred to as 'exploratory behavior', and either (E.1) settle permanently, denoted as 'settlement behavior', or (E.2) swim up into the water column. Finally, the permanently settled cyprids metamorphose into juvenile barnacles and eventually into (A) adult barnacles. Image inspired by [41].

Figure 2.2 shows a generalized life cycle of barnacles with the different stages in their development including the one at which cyprids appear. Sexually mature barnacles release nauplii, which include six planktonic nauplius stages, last five of which are planktotrophic (Figure 2.2B combines all nauplius stages) [41]. The stages are completed within 5 d for the species *Balanus amphitrite*, when stored at 28.8 °C [47]. After feeding in the water volume for 5 d nauplii metamorphose into cyprids (Figure 2.2C). Cyprids have developed a remarkable and highly discriminatory and complex bio-mechanistic ritual to evaluate surface properties. Depending on the evaluation outcome, settlement can either be delayed or immediately initiated. Interestingly, cyprids have adapted to such an extent, that settlement is possible already after the stage 6 nauplius [41]. After settlement, a metamorphosis occurs and the cyprid develops into a juvenile barnacle. An extensive description of morphological changes in barnacle larvae during the nauplius - cyprid transition is found in Walley et al. [48].

The time span of settlement occurrence differs, depending on the culture conditions, but it is usually within days to weeks, because of the limited amount of energy stored in the lipid cells of the cyprid body [16, 50]. Before settlement, cyprids move through the water column demonstrating less interest in the particular surface. Then, they approach potential settlement sites, which are first explored (e.g. Figure 2.3 shows a cyprid exploring), using a temporary adhesive system [7] and if found attractive for

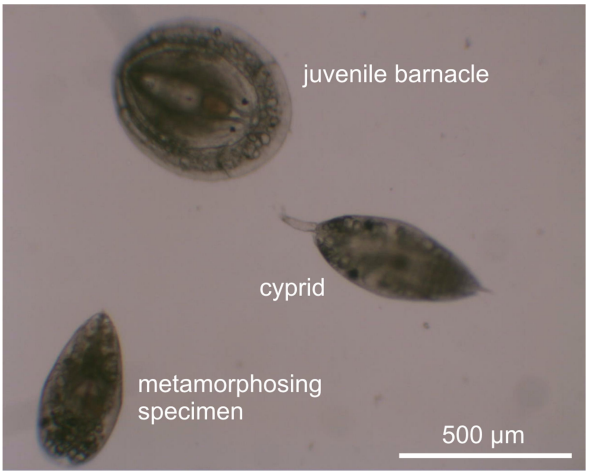

Figure 2.3.: The three main developmental stages of the lifecycle of *Balanus amphitrite* cyprids. In the central part of the figure, a cyprid performing close surface inspection by walking is shown. In the lower left corner a metamorphosing specimen can be found and on the top there is a juvenile barnacle [49].

settlement, cyprids attach permanently secreting a cyprid cement [51]. The attachment normally occurs after a great number of potential spots have been explored and rejected, and an optimal settlement site has been identified. Cyprids may also settle on surfaces with less favorable characteristics after exploring for a long period of time (weeks to months depending on the species) and becoming 'desperate' [16, 52] as a result.

Once the suitable substrate has been identified, a permanent settlement is initiated. The permanently attached cyprids complete metamorphosis (Figure 2.3) into juvenile barnacles within 12 h. After a few months of living the juvenile barnacle (Figure 2.3) closes the cycle and becomes an adult barnacle [41], which then releases nauplii periodically.

2.2.2. Morphological description

In Figure 2.4 the general morphology of cyprids of *Balanus amphitrite* is presented. The typical dimensions of the larvae have been reported to be in the range of 500 µm-600 µm for the length, 200 µm-300 µm for the width and 50 µm-150 µm for the thickness [7, 12, 54, 55]. The carpace of *Balanus amphitrite* is known to possess a relatively smooth outer surface without any pronounced morphological patterns, unlike other thoracian cyprids [55]. The cypris antennules consist of four segments and similar to all other cirrepedes they operate like a mammalian forelimb [57]. The first segment (closest to the cyprid body, 1AS, Figure 2.5a) does not possess any sensory setae and includes two hardened parts (sclerites, [57]) which move at the last elbow-shaped joint

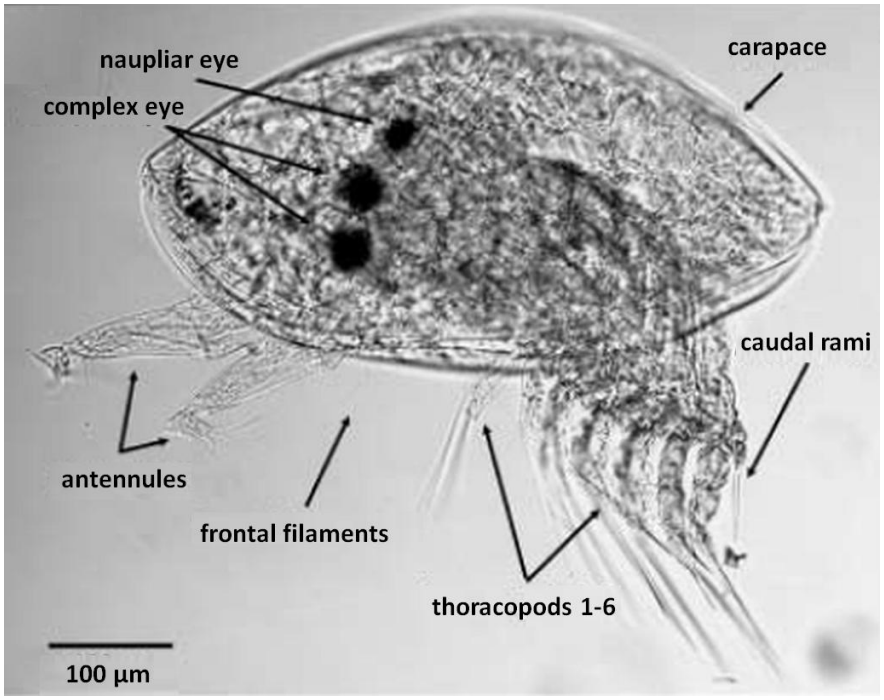

Figure 2.4.: Side view of a barnacle larva of the species *Balanus amphitrite*. The main morphological characteristics of the cyprid including the sensing organs and antennules are shown. The image has been adapted from [53].

of the antennule (Figure 2.5). The following segment (antennular segment 2, 2AS) is longer and has a cone-shaped form [57]. At this position, just before the connection with the third segment, a smooth ventrally located seta arises which is ca. 20 µm long - "the postaxial seta" [57]. In the middle part of the segment a poorly understood cavity has been identified, which seems to accommodate a "setiform projection" [57]. The first two segments play an important role to perform the needed antennular movements during close surface inspection, when the larva walks on the substratum. As reported by Hoeg et al. [57], all cirripede cyprids, including *Balanus amphitrite*, exhibit a modified third antennular segment, consisting of a bell-shaped attachment organ. The attachment disc of this organ is located on the ventral surface. A small cylindrical fourth segment (4AS, Figure 2.5) can be found occurring sideways, at a right angle [57] to the antennule. This fact makes the attachment disc of the third segment already the functional end point of the antennule [57]. The "velum (thin cuticular flaps)" encircles the border of the attachment disc while a dense occurrence of "cuticular villi" covers its surface [57]. Two sensory organs as well as an open-ended axial sensory organ have been identified in the third antennular segment [57] which is also involved in the attachment to a substratum, during walking and the final irreversible settlement. The last fourth segment is, as mentioned above, a small cylinder, possessing a very smooth

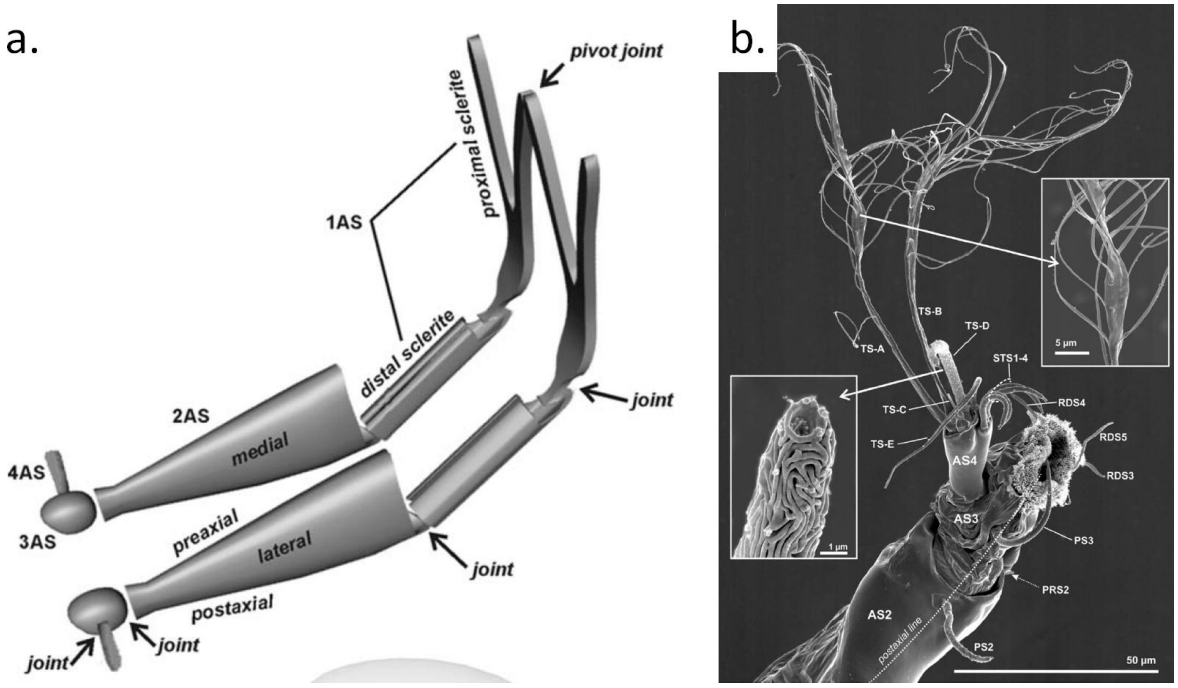

Figure 2.5.: Morphological specifics of the antennules of cyprids. (a) Schematic representation of the antennules. The joints connecting the antennular segments are visualized (AS). The basal pivot joint is not articulating with the body cuticle, but is suspended by muscles only. Image taken from [53]. (b) SEM image of the distal part of a cyprid denoting the different seta and antennular regions (AS). Image taken from [56].

surface. It accommodates most of the setae of the antennules. Four setae have been shown to arise subterminally from a shelf beneath a cluster of five setae located at the most distant part of the antennule [57]. This segment has been proven to be mainly involved in sensory functions [53].

The antennules are used by cyprids for bipedal walking, during close surface inspection and walking on surfaces, and during swimming, whereby there their function is poorly understood. Some hypotheses explain the role of the antennules during swimming with the fact that the chemoreceptors are located in segment 3 and 4 and cyprids extend them in order to sense water-soluble cues. Alternatively, it has been discussed, that these might be used to determine or assist in the direction determination during swimming [53].

As visible from Figure 2.4, cyprids of *Balanus amphitrite* possess six thoracopods, which are used for swimming. The morphological form of the anterior pair has been shown to deviate from the succeeding thoracopods, but all six pairs possess a basal protopod and a "2-segmented rami" [57]. The last thoracic segment, posterior to the thoracopods is called "caudal rami" and consists of a pair of appendages [57]. The rami

are two-segmented and carry several setae. The movements of the caudal appendages during exploration have been suggested to have a surface recognition function based on the mechanical and chemical testing of the substratum [53].
In the carpace, a pair of frontal filaments connect to the compound eyes, whereas the other ends of the filaments protrude from between the carpace valves behind the antennules [55]. The compound eyes play an important role in the selection of a substrate for settlement as reported by Yule et al. and Swain et al. [58, 59].

2.2.3. Motility of cyprids

As it could be revealed in the previous section, cyprids are equipped with an effective motion apparatus. They are highly motile and their swimming includes a range of complex patterns and movements which are employed for locomotion. Already during metamorphosis from nauplius into cyprid, the first set of antennae is modified and can be used as a mixture between a locomotor and a sensory apparatus, thus providing the cyprid with the ability to move along a substratum in a bipedal manner in order to test it and find a suitable site for a permanent settlement [60].

The general motility of cyprids can be divided in five groups: swimming, substratum exploration, wide search, close search, inspection and cementation, as reported by Lagersson et al. [53]. Before cyprids encounter a surface which is a potential candidate for settlement, they exhibit a pelagic phase and swim in the water volume [53]. The thoracopods are utilized as a motor for the locomotion and beat in a burst mode, while the larva extends its retracted antennule to a maximal position [53]. Once it has been fully extended the beating ceases and the antennule is retracted back [53]. During this time, the larva sinks, because no driving force is applied. This sequential order of the movements is repeated continuously.

In the exploratory phase, the larvae approach and walk on the substratum using the antennules. The movements are slower and the cyprids explore the substrate searching for a suitable area to settle permanently, if attractive cues have been detected [53]. Three main behavioural sub patterns can be differentiated during this phase [60]. Initially, the exploration involves a straight line walking of a variable duration, with no changes in the direction [53]. During this walking, the antennules constantly interact with the substratum and counteract the movements of each other (schematic shown in Figure 2.6 and view graph shown in Figure 2.7). As long as this bipedal movement is performed, the thoracopods are not active and are dragged behind the larvae, probably contributing to stability [53]. For the locomotion of the cyprid body, one antennule is attached to the substrate in front of the cyprid and is used to pull the whole body forward [53]. At the same time, the unattached (back) antennule is moved to the front and the cycle is repeated [53]. A fact worth mentioning is, that the larvae are attached with one antennule to the substrate during the whole time, and only for the short duration of the actual body displacement with both of them [53]. The fourth antennule segment is slung constantly across the substrate [53].

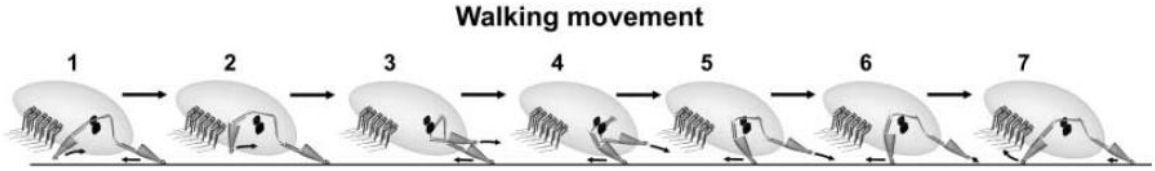

Figure 2.6.: Schematic representation of the walking of barnacle cyprids. Walking involves a bipedal motion, whereby the antennules are extended and retracted continuously. Image sequence 1-7 describes the different stages of a single step. Image taken from [53].

Figure 2.7.: Sequence of microscopic images depicting the walking movement of cyprids. (a) The front antennule (left) is attached to the surface and (b) the cyprid moves its body forward whereby the back antennule comes to the front. In (c) and (d) the leading antennule explores the substrate before it finally (e) attaches. The process is repeated continuously for every step. Image source: [28]

Once favorable surface cues have been detected, the cyprid starts to express a more focused behavior, involving a great number of directional changes. During this testing, the larvae are normally attached with one antennule, while the other explores the substrate employing segments 3 and 4 [53]. Often the thoracopods also contribute to the movement, because they beat fast for a short time immediately after an antennule is attached, which sometimes causes the detachment of the larva. In order to be able to examine a maximal area of the substratum, while one antennule is attached, it is extended and the carpace is elevated vertically (Figure 2.8) [53]. The optimal mechanical properties of antennule segment 2 combined with the properties of the joints allow the larva to rotate completely around an antennulary attachment point [53].
If the 'quality check' is passed, cyprids dedicate to the final phase of exploration. Remaining attached with both antennules to a fixed point on the substratum, they inspect the area, while their body hovers over the attachment point [53] partially touching the substrate with its anterior part. Interestingly, the flicking of segment 4 ceases but the thoracopods continue to beat [53]. The process of inspection is finalized by the secretion of a permanent cement which irreversibly attaches the cyprid to the substrate and a metamorphosis into juvenile barnacle is initiated [53].

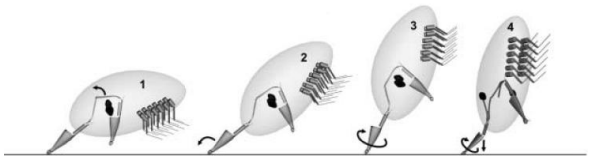

Figure 2.8.: Sketch of the process of surface testing. In the schematic representation of surface testing it can be seen that normally one antennule is attached, while the carpace is elevated vertically. A directional change can originate from this if the cyprid completes a rotation around the attachment point. Image taken from [53].

2.3. Techniques for quantification of cyprid behavior

Many quantification techniques have been developed for the investigation of cyprid behavior, at which the 'post-settlement' method is one of the most widely spread. This approach evaluates the quantity and the spatial distribution of the settled target organisms on surfaces and thus makes conclusions on the cues which invoked this particular behavioral response. Newer strategies apply 2-D video observation as well as other imaging techniques in the analysis of exploratory behavior of cyprids prior to committing to permanent settlement on a surface. Subsequently, behavioral patterns are identified, which indicate the surface preferences of the larvae. This chapter gives a description of the main quantification techniques currently applied in the analysis of barnacle cyprid behavior.

2.3.1. Settlement assays

The barnacle attachment inhibition assays, also known as no choice, static (no flow) assays, e.g. developed by Rittschof et al. [11], are often used to assess and evaluate the attractiveness of a given surface for colonization. In this assay, a certain number of cyprids (ca. 20) is inoculated in a sterile polystyrene dish or multi-well plates containing seawater. The dishes are incubated for 48 h at 28 °C in the dark and the percentage of attached and metamorphosed cyprids is quantified (normally at two time points, after 24 h and 48 h). The assay format is technically simple, rapid, inexpensive and can be repeated in several replicate dishes [61]. Because of its convenience it has been used in numerous studies to test settlement against different physicochemical properties of the substrate and although sometimes considered misleading [23], it is the current standard tool for determining the settlement preferences of cyprids [10–13, 19].

One general disadvantage of post-settlement methods is the low and often variable attachment rate [14]. For this reason, several improvements of the original protocol have been reported in order to optimize the outcome of assays: using a higher larval density [10], using different amounts of liquid in the assay [62], changing the geometry

[62], introducing different environmental conditions [63] or including additional algal supply [52]. Recent publications have demonstrated that procedures eliminating the air-water interface are highly successful in increasing the settlement rates [14, 64].

An additional drawback of the post-settlement approach is that it does not provide information on the complex behavioral process occurring prior to settlement. The knowledge on this behavior could be used to indirectly conclude on the selection strategies of cyprids [65].

2.3.2. 2-D motion analysis

Motion analysis has proven to be an effective tool to study the behavior of different target organisms. Also in the field of marine biofouling research efforts focus on quantifying the swimming movements of barnacle cyprids based on the evaluation of two-dimensional swimming trajectories. Generally, the main fields of application of the method are field experiments, investigation of gregariousness effects, quantification of close surface inspection and pre-settlement behavioral analysis.

To understand and quantify the settlement behavior of barnacle cyprids under field conditions, 2-D camera systems are applied. Matsumura et al. [25] proposed a setup which was feasible for application in underwater experiments and could detect differences in the settlement of cyprids as a response to surface treatment with settlement inducing protein complexes. In addition, Prendergast et al. [23] have reported of a system capable of filming cyprids of the species *S. balanoides* in the field and detecting settlement changes in response to textural and chemical settlement cues. The authors introduced "gross and net distance traveled", which mainly described the total respectively actual displacement of the cyprid body after a defined observation period. Furthermore, the ratio between these patterns has been used as well as acceleration and tortuosity, the latter expressing the turn in degrees per millimeter traveled [66]. The work of DiBacco et al. [24] focused on using a down-welling flume to investigate the mechanisms for maintaining of the swimming depth of cyprids.

Two-dimensional motion analysis has been reported to be applicable in studies of gregariousness effects [21, 67]. Here, evaluation of the motility has revealed the colonization dynamics of cyprids. The authors used measurable trajectory parameters to show that individual cyprids of *B. amphitrite* tend to swim similarly to cyprids in a group [21].

A quantification of close surface inspection has been reported by Chaw et al. [28] recently. A two-dimensional motion analysis system, which can provide quantitative information on the close surface inspection of barnacle cyprids, was introduced. Moreover, it detected differences in two step parameters of cyprids exploring surfaces with different chemical termination and attractiveness for settlement - i.e. step length and step duration. Also Pradhan et al. [20] utilized two-dimensional motion quantification for the analysis of swimming features and parameters including the body orientation of cyprids.

One major field of application of the 2-D approach is the analysis of pre-settlement behavior. Research objective here is mainly to understand and quantitatively describe the complex motion patterns occurring during exploration and to reveal potential correlation between surface properties and the exploratory behavior. Recently, Aldred et. al [17] could reveal that zwitterionic surfaces influence the swimming behavior of cyprids. Moreover, it was shown that on coatings resistant to fouling, a different pre-settlement behavior can be present than on coatings attractive to fouling. Similar approach was followed by Marechal et al. [19] who used the commercially available EthoVision^{TM} system [68] to quantify the swimming of barnacle cyprids of *Balanus amphitrite* (Figure 2.9). Several parameters have been introduced by the authors for description of locomotion, e.g. "movement", "turn angle', "distance moved", "meander". The capability of the system to automatically analyze trajectories, thus to accelerate research, was a big step towards understanding the behavior of barnacle cyprids. Marechal et al. were able to extract swimming velocity profiles which ex-

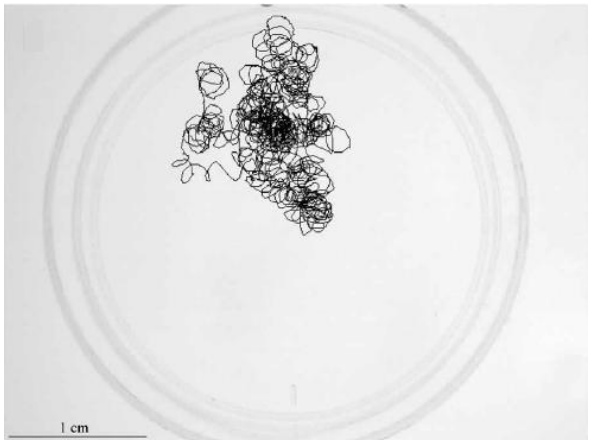

Figure 2.9.: Exemplary 2-D trajectory. The trajectory was obtained with the 2-D tracking system Ethovision^{TM}. It shows a cyprid performing a series of rotational movements in the upper half of a petri dish. Image taken from [19].

hibited a periodic pattern - high velocities were followed by values of zero velocity. A more thorough analysis of the processes during the zero-velocity phases was not possible with the obtained data. In addition, the analysis algorithm used a filter function, which aimed to discard virtual movements of the cyprids. A virtual movement was defined by the authors as a body movement (e.g. rocking from side to side without traversing the substratum) during which the cyprid did not exhibit any locomotion. Because of the filtering, the algorithm eliminated cyprids moving only in z direction, since they possessed a velocity vector with components in x and y direction close to zero. This discarded valuable data from cyprids engaged in close search behavior or particularly inspection. The incapability to automatically distinguish between close and wide search and between searching and swimming [19] was the main limitation of

the method. Working with three-dimensional data would add the missing component and bring more details in understanding the way cyprids move: e.g. passive floating, passive sinking, active swimming, exploring, etc.

Generally, the 2-D motion analysis approaches lack the information on the third dimension, which is of great importance since cyprids swim in a three-dimensional manner and only extraction and evaluation of locomotion in all available dimensions would allow a correct quantification of exploratory behavior.

2.3.3. Microscopic approaches

Methods quantifying the interactions of cyprids with surfaces at microscopic scale have proven to be useful in deriving the specifics of exploratory behavior. In Aldred et al. [17] high-speed photography was used to indirectly investigate the behavior of cyprids during wide search, inspection and detachment, analyzing the process of temporary adhesion. It could be revealed that during wide search, the attachment disc of the third antennular segment rarely exhibited a full contact with the substratum, thus providing a weak attachment [17]. On the contrary, during inspection, in order to ensure a stable attachment, the disc was brought into full contact by spreading it out completely. Furthermore, the detachment mechanisms were investigated and it was found out that during inspection, the process was realized by a decrease in the bond strength and by pulling the antennule until ruptures occurred.

Additionally, new methods, as recently reported by Andersson et al. [27], allow the quantification of interaction of cyprids with the surface using imaging surface plasmon resonance microscopy (iSPR microscopy). This is an imaging optical transducer technique which measures the thickness or refractive index of thin adsorbed dielectric layers [69]. The authors utilized the new method and were able to quantify micro-scale bioadhesion events *in situ* in real time (Figure 2.10). They investigated the occurrences of touchdown events and the amount of deposited organic material remaining after the interaction of the cyprids with the interfaces. Combining conventional SPR with imaging SPR the group could quantify the number touchdowns of cyprids as well as the amount of the temporary adhesive material left behind on surfaces, which are commonly used in biofouling research. The results showed, that relating the footprint deposition to the total number of touchdowns and correlating it to the adsorption of proteins to the same surface significant differences occurred [27] and indicated that cyprids rather than other models should be used in quantification of cyprids adhesion to surfaces.

In Section 5.4 of this thesis a new hybrid system is presented, which combines the iSPR of Andersson et al. with the stereoscopy setup. The technical details on the setup and first results are presented, which demonstrate the potential of the new system. The combination allows to utilize the advantages of both techniques and to be able to quantify cyprid swimming behavior and to correlate it with specific interactions at the interface. Such unique information can be very useful to understand, e.g. how surface

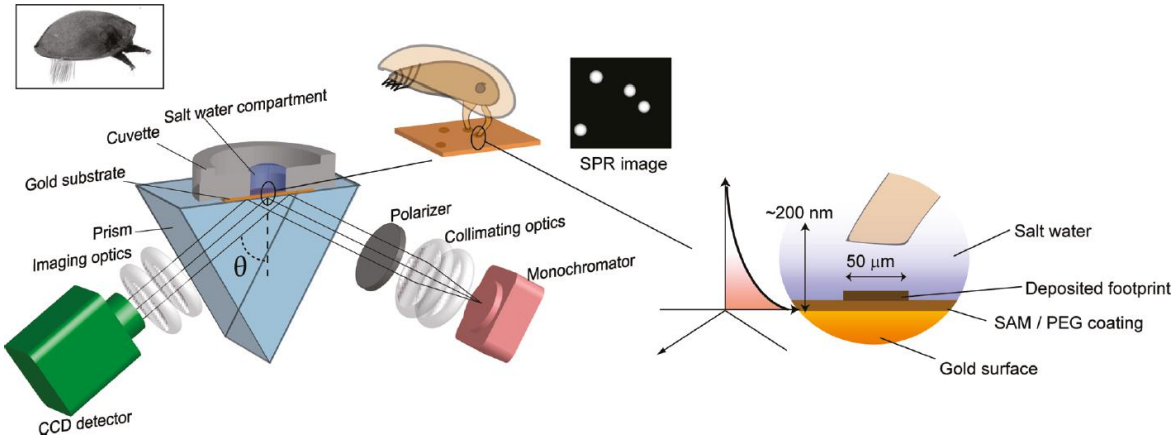

Figure 2.10.: Schematic of the iSPR setup used by Aldred et al. with the main components. If the antennules of a cyprid extend within the evanescent field this can be detected in the SPR image (right magnified view). The deposited footprint can be directly observed in the image and the amount of material left behind can be quantified by scanning of the wavelength . Image taken from [26].

chemistry influences the swimming velocity of cyprids close to surfaces, whether cyprids are decelerated when approaching surfaces and what are the regulating mechanisms.

2.4. Surface properties influencing the settlement of barnacle cyprids

As discussed earlier, cyprids test a potential substrate and rank its attractiveness for settlement based on different criteria (i.e. substrate color [58], surface chemistry [15], topography [6], presence of competitors or predators [70]). In the following sections the chemical and topographical properties of substrates are discussed with respect to their ability to influence biofouling.

2.4.1. Surface charge

Surface charge is an important factor when the interaction between surfaces and objects approaching the surfaces is considered. There have been several studies investigating the influence of surface charge on protein adsorption. In the work of Ekblad et al. [71] the authors investigated the adsorption of fibrinogen on a surface with a charge gradient and could reveal that only in the neutrally charged region the adsorption was completely suppressed. Since cyprids deploy an organic compound cement for temporary attachment, it can be expected that the same relationship between surface charge and the adhesive should be valid and surface charge should be a key factor to influ-

ence the settlement rates. This hypothesis was recently backed up by an experimental observation described in Aldred et al. [26]. The authors showed that surface charge determines the strength of temporary adhesion of cyprids of *Semibalanus balanoides* as well as the amount of adhesive deposited on surfaces during exploration. In addition, several studies have reported that high settlement can be expected on negatively charged surfaces, slightly lower amount of cyprids settle on positively charged surfaces and the lowest values can be found on surfaces with a neutral net charge (zwitterionic) [29].

As reported recently by Di Fino et al. [72] it was verified that the charge of surfaces affects their attractiveness for settlement. The authors reported that the observations on *B. amphitrite* [13] cyprids could also be confirmed for a different species - *Balanus improvisius*. The question about the mechanisms by which surface charge modulates settlement still needs to be addressed, but all evidence suggests that the temporary adhesive of cyprids is bound stronger on charged substrates than on those with a neutral net charge and this charge provides a very firm attachment, thus promoting settlement.

2.4.2. Surface wettability

Surface wettability is another factor which influences protein adsorption. In the work of Prime et al. [73] it was shown that the thickness of adsorbed protein was highest on hydrophobic surfaces and decreased with the decrease of the contact angle, meaning with increasing hydrophilicity of the surface. Originally, surface energy has been continuously stated as one of the reasons for efficacy of fouling-release coatings [1] against biofouling organisms, which was based on the work of Baier et al. [74]. Recently Di Fino et al. [72] demonstrated that surface-free energy was linked to the adhesion of marine organisms. Especially the 'Baier minimum' between $20\,\mathrm{mN/m^2}$ and $30\,\mathrm{mN/m^2}$ is believed to provide minimal adhesion.

Interestingly, reported data on cyprid adhesion differs strongly. Finlay et al. [75] have revealed that cyprids of *Balanus amphitrite* exhibit a strong preference for high-energy surfaces. These observations have been questioned by Petrone et al. [13] who found a preference of cyprids for low-energy surfaces. Also O'Connor et al. [76] found that cyprids of *Balanus improvisius* settled preferably on hydrophobic polystyrene substrates when compared to hydrophobic glass. Preferences of *Balanus amphitrite* cyprids for hydrophilic surfaces have been reported in a number of studies ([15, 76–78]. The opposite trend has been observed for cyprids of *Balanus improvisius* as reported recently by Di Fino et al. and Dahlstrom et al. [72, 79]. The mechanisms which are involved in the settlement modulation of cyprids caused by wettability properties of the substrate are still unknown. Maki et al. [80] could demonstrate that there was no direct correlation between surface wettability and the adhesion strength of *B. amphitrite* cyprids. In spite of the contradictory reports in literature, it is obvious that wettability influences the attractiveness of surfaces for settlement. For this reason, a

set of hydrophobic and hydrophilic surfaces has been selected for this thesis, in order to be able to understand pre-settlement behavior and to correlate it with well known surface properties.

2.4.3. Surface hydration

High surface hydration is a key factor in the prevention of protein and cell adhesion [81]. The main hypothesis explaining its efficacy is that the high hydration energy between the molecules prevents the water molecules within the interface of a substrate from being displaced from that interface, thus inhibiting the glue proteins secreted by marine organisms to adhere properly and permanently. Polyethylene glycol (PEG) is a known representative of this group and exhibits a high resistance towards biological substances, because of the ethylene glycol (EG) unit, which resembles the stable water environment [81]. For this reason EG terminated surfaces have been widely used in adhesion studies of different target organisms and proteins. For example, Schilp et al. [82] showed that if there were at least two EG units present on a test surface, proteins as well as *Ulva* spores did not adsorb or attach on it. While inspecting the surfaces after the experiments, the authors reported that a high settlement of spores could be observed on EG_6OH surfaces, but the adhesion strength was so low that they could be removed from the substrate by applying a minimal shear stress. This points to the conclusion that spores tried and initiated settlement, but the adhesive material could not bind properly to the surface.
Moreover, Ekblad et al. [83] showed that EG-based surfaces reduced the settlement of cyprids of *Balanus amphitrite*. The authors could demonstrate that the settlement on the EG substrate never exceeded 21 % of the settlement on the attractive (glass) surface. Since cyprids actively explore surfaces in order to find a suitable site for settlement, the proposed hypothesis was that either cyprids were deterred from settling or attempted to attach but were unable to do so effectively [83]. Because of the obvious effect of hydration on the settlement of cyprids (*Balanus amphitrite*) highly hydrated PEG surfaces have been selected for the experiments in this thesis, in order to be able to analyze pre-settlement behavior on surfaces with well-studied influence on the settlement outcome.

2.4.4. Color of the substratum

It has been long known that light is an important factor governing the attachment of biofouling organisms and the motile larvae of these organisms (responsible for settlement) are photonegative [84]. Several investigations have shown that cyprids prefer darker substrates and settle on these more readily [59, 84–86].

Visscher et al. [84] investigated the settlement stimulating efficiency of different colors. They could demonstrate that the maximum efficiency was observed for the light green color, between 530 µm-545 µm which was in the range of reports for other

marine organisms. The authors concluded that cyprids do not possess true color vision, but rather photo-sensitive cells in the compound eyes which react differently to different wave lengths [84].

Taki et al. [85] demonstrated that the tendency to prefer darker substrates disappears at nighttime. Furthermore, it was shown that cyprid larvae discriminate between different luminosities of the same hue. Interestingly, the authors did not find any different settlement behavior between hues of similarly equal and low luminosities, which could be interpreted as inability of cyprids to sense low intensities of light, irrespective of wavelength [85]. On the contrary, the settlement differed significantly for different hues at higher luminosities. The highest settlement was found on red substrates, followed by blue and finally green color [85], whereby cyprids proved to be more sensitive to green than to red. Blue substrata exhibited an intermediate effect.

Dobretsov et al. [86] could also demonstrate a general preference of several marine biofoulers to darker (black) substrates in the field which confirmed previous observations by Swain et al. [59].

As mentioned before there are several reasons explaining the preference of fouling organisms for darker colored substrates. One reason is the negative phototaxis [86] of most of them. Interestingly, it was also found that the strength of the adhesive of barnacles and *Ulva* sporelings is higher on darker substrates [87, 88], which could also contribute to the attractivity of these surfaces. Another reason could be the reflected or adsorbed energy of the radiation as well as the temperature of the substrate [86] as darker surfaces exhibit generally higher temperatures. The most probable reason for the observed differences between the substrates however is a complex combination of more than one effect [86].

2.4.5. Topography

Surface topography is another important property which has been proven to play a key role in the modulation of surface colonization by barnacle cyprids [6, 7, 89–92]. The design of biomimetic, nature-inspired coatings has been widely applied by many research groups [93–95]. Schumacher et al. [6] created surface structures on PDMS which mimicked the skin of sharks (named Sharklet ™). Briefly, the geometry of the surfaces included ridges and pillars with different sizes, lengths and heights and the distances between the elements were varied. An example of the Sharklet™ topography is shown in Figure 2.11 together with the settlement values compared to a smooth PDMS control. The settlement was reduced in some cases with up to 45 % compared to the smooth control. One explanation of this reduction was that the topographic aspect ratio was possibly related to the underwater super-hydrophobicity attained when the roughness ratio exceeded the critical limit [96].

The influence of topography on the settlement of barnacle cyprids was not part of the research directions of this thesis, and this brief overview has been included for the sake of completeness.

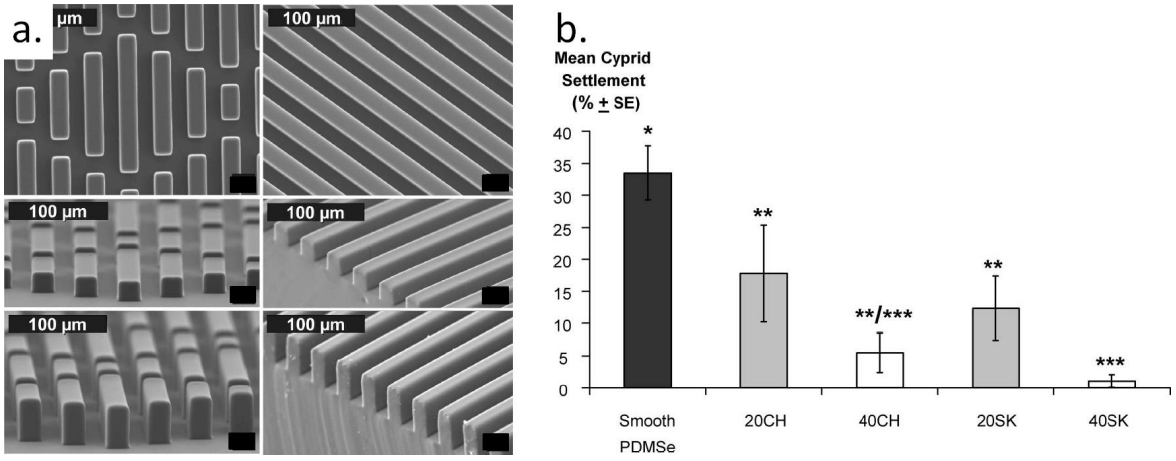

Figure 2.11.: Use of surfaces with different topography in antifouling applications. (a) SEM images of Sharklet^{TM} topographies produced on PDMSe and specially engineered to influence barnacle cyprids. (b) Settlement preferences of cyprids on the surfaces. Samples included a smooth control (Smooth PDMSe), 20 µm wide channels spaced by 20 µm wide ridges with feature height of 20 µm (20 CH) and 40 µm (40 CH). In addition a barnacle-specific Sharklet^{TM}surface with feature heights of 20 µm (20 SK) and 40 µm (40 SK, 20 µm feature width and spacing). Image taken from [6].

2.4.6. Biofilms and other chemical cues

The idea that gregariousness of cyprid settlement is being guided by chemical cues has been known for over 50 years [97]. As Clare et al. presented in their review, at least three different types of pheromones are involved in the induction of settlement of cypris larva - an adult glycoprotein (also known as settlement inducing protein complex - SIPC), a waterborne cue originating from the adult barnacle and the temporary adhesive of cyprids. The settlement inducing protein complex was shown to be sensed by cyprids through a tactile chemical sense [98], the stimulus experienced by contact with an adsorbed or insoluble material on the substratum, which means that cyprids need to contact the surface with their exploratory setae in order to perceive the presence of the SIPC on it.
In addition, the temporary adhesive which is deposited on the surface during searching in form of a 'footprint' [58, 99] was also proven to induce settlement of other cyprids [100] and is believed to either contain or to be equivalent to the SIPC [101].
The waterborne cue has proven to be a small carboxy-terminated and a neutral (or basic) amino-terminated peptide with its settlement-inducing activity mimicked by several di- and tripeptides, e.g. glycyl-glycyl-arginine (GGR) [101, 102].
In addition to the pheromones and other conspecific chemical cues, also biofilms have been demonstrated to influence the settlement behavior of barnacle cyprids. Maki et al. [103] and Wieczorek et al. [104] have reported that the settlement of cyprids

of the species *Balanus amphitrite* becomes inhibited by microbial biofilms, whereas Wieczorek et al. observed a twist in the tendency as soon as the biofilm became older with denser and more diverse microbial abundance [105]. Also here, the mechanism behind the modulation of settlement by the biofilm is not completely revealed. The chemical cues and the microbial biodiversity of the biofilms are believed to determine the discriminatory behavior of the cyprids. These factors vary temporally and spatially and depend on biotic (e.g. availability and types of species, competitors and predators, etc.) and abiotic environmental factors (e.g. depth, light conditions, season, water chemistry, turbidity, availability of nutrients, substrate characteristics, etc.) [61, 106]. Because of this wide range of factors influencing the settlement, it is believed that cyprids may evaluate the prevailing environmental conditions by interpreting the variations in the biofilm attributes, and thus attach to substrates which provide advantageous conditions for their post-metamorphic adult life [61].
Moreover, it has been verified that conditioning films influence settlement of biofouling species by covering the original chemistry of surfaces, as reported recently by Garg et al. [42] and Thome et al. [107]. In Chapter 5.5 of this thesis the influence of a conditioning film, generated following the procedure described in Thome et al. [107], on the swimming behavior of cyprids was quantified in order to detect correlations between conditioning and pre-settlement swimming patterns.

2.5. Self-assembled monolayers as model surfaces for biofouling research

As it could be shown in the previous sections, a whole range of physicochemical surface properties influences the settlement behavior of cyprids. In order to systematically investigate this influence on the exploratory behavior, a system is required which provides an easy and reliable method for realisation of surfaces with different properties. It is well known that the chemisorption of thiol molecules on gold substrates results in the formation of a well-ordered and densely packed self-assembled monolayer (SAM) [108, 109]. The commonly used organo-thiol consists of three parts - a terminal group (used to anchor the molecule to substrates), spacer group and a functional end group (Figure 2.12). SAMs are well suited for studies of interfacial phenomena, because only the outmost 5 Å-10 Å are considered to determine the surface properties and also provide an easy way to tune surface properties which can be achieved by substituting the functional group [110].
One major advantage is also that the mechanical properties of the surfaces are determined by the substrate and the physicochemical ones depend on the organic film only. The relatively easy preparation procedure, which allows to obtain stable surfaces with various properties by varying the thiol end group, made SAMs widely used in different applications [108, 111, 112]. SAMs have been frequently utilized to study protein adsorption [73, 113, 114], human cells [115], in biotechnological and medical

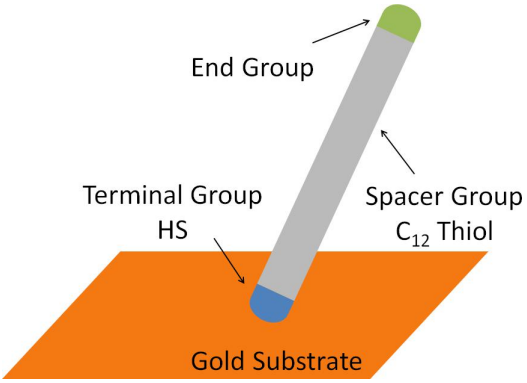

Figure 2.12.: Structure of self-assembled monolayer molecules. The schematic presents the structure of an organo-thiol molecule, including the main parts - a terminal, spacer and head group. This molecule is referred to as self-assembled monolayer (SAM).

applications [116–118] and in marine biofouling [82, 119–122].
In the case of marine biofouling, the response of marine organisms to the physicochemical attributes of the surfaces was investigated, utilizing the fact that SAMs can provide a uniform set of surfaces which only differ in the nature of the outmost (end) group. Different representatives of the biofouling community have already been tested: algal spores, diatoms and bacteria [121–127]; mussels [128, 129] and cyprids [13, 27, 72].
The SAM system applied in the course of the thesis consisted of monolayers of alkanethiols on ultra smooth gold substrates, because it has been studied quite well since it was first reported by Nuzzo et al. [110]. For the experiments described in this work, the end functional group was varied in order to prepare model surfaces with different chemical properties, i.e. wettability, hydration and charge, as these have been shown to possess a high impact on cyprids (Section 2.4).

2.6. Theoretical basics of computer stereo vision

This chapter presents briefly the mathematical fundamentals of computer stereoscopic vision, which is the main technique applied in the course of the thesis for the extraction of 3-D trajectories of swimming cyprids. In the following sections the theoretical basics required in order to understand the procedures and methods utilized for the extraction of these three-dimensional traces are presented. A more generalized and detailed information on computer vision can be found in several textbook sources (e.g. [130–132]).

2.6.1. Pinhole camera model

The pinhole camera model is a mathematical model describing the relationship between a three-dimensional point in real space and the two-dimensional projection of this point onto the image plane of an ideal pinhole camera. The ideal pinhole camera is a first order approximation of a real camera which has an aperture described as a point and does not consider lenses for focusing of light. This simplification allows to discard problems caused by blurring of unfocused objects or geometric distortions. In Figure

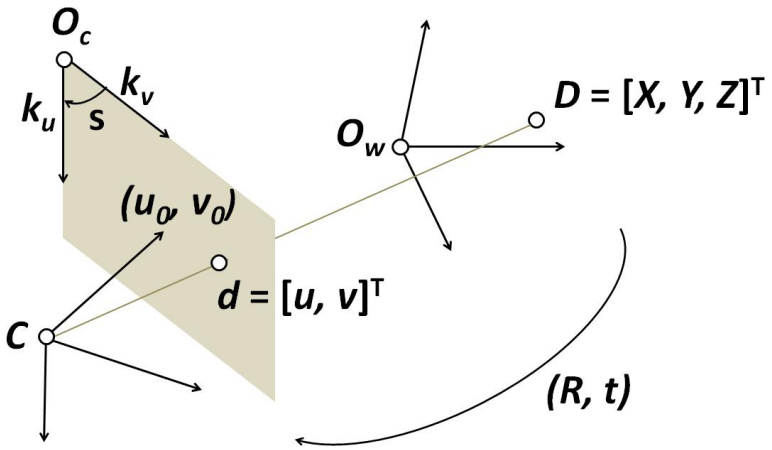

Figure 2.13.: Graphical representation of the pinhole camera model. The points O_w and O_c denote the origins of the world coordinate system and image coordinate system respectively, C marks the camera projective center. D is the point in 3-D space and d is the 2-D projection of D onto the image plane. u_0 and v_0 are the coordinates of the image principal point, s is the skew and k_u and k_v the magnification. Finally, the $\mathbf{R}$ and $\mathbf{t}$ denote the projection and translation matrices. Image inspired by [131].

2.13 a schematic representation of the pinhole camera model is shown. In the figure, a two-dimensional point is denoted as $d = [u, v]^{\mathrm{T}}$ and a point in three-dimensional space is represented with $D = [X, Y, Z]^{\mathrm{T}}$. The homogeneous notations of the 2-D and 3-D

point are $\tilde{d}$ and $\tilde{D}$ respectively. According to the pinhole camera model, the projection of the 3-D point D onto the image plane, denoted by d, is formed by an optical ray originating at D, passing through the optical center of the camera C and intersecting the image plane. The three points D, d and C are collinear [131].

2.6.2. Intrinsic and extrinsic camera parameters

The three-dimensional point $\tilde{D}$ and its two-dimensional image projection $\tilde{d}$ (Figure 2.13) are related mathematically as [131]

$$c\tilde{\mathrm{d}} = \underbrace{\mathbf{K}[\mathbf{R} \quad \mathbf{t}]}_{\mathbf{P}} \tilde{D} \equiv \mathbf{P}\tilde{D}, \tag{2.1}$$

$$\text{with } \mathbf{K} = \begin{bmatrix} k_u & s & u_0 \\ 0 & k_v & v_0 \\ 0 & 0 & 1 \end{bmatrix}. \tag{2.2}$$

The parameter c in Equation 2.1 represents a scaling factor, $\mathbf{R}$ is the rotation matrix and $\mathbf{t}$ a translation vector. These parameters define the rotation of the camera and its translational shift with respect to the world coordinate system and are referred to as the extrinsic camera parameters. Internal camera properties are denoted by the intristic camera matrix $\mathbf{K}$ with scale factors k_u and k_v, coordinates of the principal point u_0 and v_0 and a skew between the two image axes s. The internal and external camera parameters can be combined in matrix form ($\mathbf{P}$), which is then referred to as the projection matrix (sometimes projective matrix) of the camera. This matrix contains all parameters needed to project a world space 3-D point and map it onto the 2-D image plane of the camera. To obtain the mathematical relationship between image- and world-coordinates Equation 2.1 can be developed in a matrix form to become

$$\begin{pmatrix} u_i c \\ v_i c \\ c \end{pmatrix} = \begin{bmatrix} p_{00} & p_{01} & p_{02} & p_{03} \\ p_{10} & p_{11} & p_{12} & p_{13} \\ p_{20} & p_{21} & p_{22} & 1 \end{bmatrix} \begin{bmatrix} X_i \\ Y_i \\ Z_i \\ 1 \end{bmatrix} \tag{2.3}$$

with (u_i, v_i) being the 2-D image coordinates of the 3-D point (X_i, Y_i, Z_i). Following Equation 2.3, the 2-D point coordinates can be expressed as

$$u_i = \frac{p_{00}X_i + p_{01}Y_i + p_{02}Z_i + p_{03}}{p_{20}X_i + p_{21}Y_i + p_{31}Z_i + 1} \tag{2.4}$$

$$v_i = \frac{p_{10}X_i + p_{11}Y_i + p_{12}Z_i + p_{13}}{p_{20}X_i + p_{21}Y_i + p_{31}Z_i + 1} \tag{2.5}$$

$$u_i(p_{20}X_i + p_{21}Y_i + p_{31}Z_i + 1) = p_{00}X_i + p_{01}Y_i + p_{02}Z_i + p_{03} \tag{2.6}$$

$$v_i(p_{20}X_i + p_{21}Y_i + p_{31}Z_i + 1) = p_{10}X_i + p_{11}Y_i + p_{12}Z_i + p_{13}. \tag{2.7}$$

Equations 2.6 and 2.7 can be utilized to obtain the 2-D image coordinates (u_i, v_i) of a three-dimensional point with world coordinates (X_i, Y_i, Z_i) if the projection matrix $\mathbf{P}$ of the camera is known.

2.6.3. Camera calibration

In order to be able to extract quantitatively relevant information from image data of a stereoscopic system, the intrinsic and extrinsic camera parameters for all cameras need to be known, i.e. position of the image center, focal length, scaling factors, skew factor, camera orientation, etc. These can be estimated by a procedure called calibration, which calculates the parameters based on the relationship between a set of known points in 3-D space and their 2-D correspondences in the imaging planes of the cameras. There are four main categories of standard calibration methods known in the literature which can be applied: 3-D reference object based calibration, 2-D plane based calibration, 1-D line calibration and self-calibration [131]. Additionally, there exist also other techniques like calibration from pure rotation and vanishing points for orthogonal directions [131].

In the course of this thesis, a calibration object with known geometry in three-dimensional space was used. It possessed a high amount of calibration points, of which the 3-D coordinates in world space, as well as the corresponding 2-D coordinates in image space, were known. Since the projection matrix shown in Equation 2.3 contains 11 unknown parameters, at least 6 correspondences (point pairs) needed to be identified in order for the system of equations (Equation 2.8), obtained by rewriting Equations 2.6 and 2.7 in a matrix form for N points, to be determined.

$$\underbrace{\begin{bmatrix} X_1 & Y_1 & Z_1 & 1 & 0 & 0 & 0 & 0 & -u_1X_1 & -u_1Y_1 & -u_1Z_1 \\ 0 & 0 & 0 & 0 & X_1 & Y_1 & Z_1 & 1 & -v_1X_1 & -v_1Y_1 & -v_1Z_1 \\ \vdots & \vdots & \vdots & \vdots & \vdots & \vdots & \vdots & \vdots & \vdots & \vdots & \vdots \\ X_N & Y_N & Z_N & 1 & 0 & 0 & 0 & 0 & -u_NX_N & -u_NY_N & -u_NZ_N \\ 0 & 0 & 0 & 0 & X_N & Y_N & Z_N & 1 & -v_NX_N & -v_NY_N & -v_NZ_N \end{bmatrix}}_{G} \underbrace{\begin{bmatrix} p_{00} \\ p_{01} \\ p_{02} \\ p_{03} \\ p_{10} \\ p_{11} \\ p_{12} \\ p_{13} \\ p_{20} \\ p_{21} \\ p_{22} \end{bmatrix}}_{p_v} = \underbrace{\begin{bmatrix} u_1 \\ v_1 \\ \vdots \\ u_N \\ v_N \end{bmatrix}}_{e}. \tag{2.8}$$

Several approaches exist for solving the overdetermined system of equations which can be found in Xu et al. [132]. For the purposes of this work a linear method was

applied [133]. This method suggests the use of a linear least-squares technique as the pseudo-inverse (Equation 2.9) in order to solve the system in the form $\mathbf{Gp_v} = \mathbf{e}$.

$$\mathbf{min}\,\|\mathbf{Gp_v} - \mathbf{e}\|^{\mathbf{2}} \Leftrightarrow \mathbf{G^T}(\mathbf{Gp_v} - \mathbf{e}) = \mathbf{0} \Leftrightarrow \mathbf{p_v} = (\mathbf{G^T G})^{-\mathbf{1}}\mathbf{G^T e} \tag{2.9}$$

To obtain the projection matrix $\mathbf{P}$ the vector $\mathbf{p_v}$ should be rearranged in a 4×3 matrix as shown in Equation 2.10.

$$\begin{bmatrix} p_{00} \\ p_{01} \\ p_{02} \\ p_{03} \\ p_{10} \\ p_{11} \\ p_{12} \\ p_{13} \\ p_{20} \\ p_{21} \\ p_{22} \end{bmatrix} \Rightarrow \begin{bmatrix} p_{00} & p_{01} & p_{02} & p_{03} \\ p_{10} & p_{11} & p_{12} & p_{13} \\ p_{20} & p_{21} & p_{22} & 1 \end{bmatrix} \tag{2.10}$$

The projection matrix $\mathbf{P}$ can be further decomposed into an intrinsic and extrinsic part [131]. Briefly, if the first 3×3 sub-matrix of $\mathbf{P}$ is denoted by $\mathbf{B}$ and the last column of $\mathbf{P}$ is denoted by $\mathbf{b}$ then $\mathbf{P} = [\mathbf{B} \quad \mathbf{b}]$. Because, as shown in Equation 2.1, $\mathbf{P} = \mathbf{K}[\mathbf{R} \quad \mathbf{t}] = \mathbf{KR}[\mathbf{I} \quad \mathbf{R^T t}]$, $\mathbf{B}$ and $\mathbf{b}$ become

$$\mathbf{B} = \mathbf{KR} \tag{2.11}$$

$$\mathbf{b} = \mathbf{Kt} \tag{2.12}$$

Developing Equation 2.11, $\mathbf{M}$ is calculated to be

$$\mathbf{M} \equiv \mathbf{BB^T} = \mathbf{KK^T RR^T} = \mathbf{KK^T} = \begin{bmatrix} \underbrace{k_u^2 + s^2 + u_0^2}_{m_u} & \underbrace{k_v s + u_0 v_0}_{m_c} & u_0 \\ \underbrace{k_v s + u_0 v_0}_{m_c} & \underbrace{k_v^2 + v_0^2}_{m_v} & v_0 \\ u_0 & v_0 & 1 \end{bmatrix} \tag{2.13}$$

with $\mathbf{RR}^{\mathrm{T}}$=$\mathbf{I}$, because of the orthogonal rotation matrix. Subsequently, the projection matrix should be normalized in such manner that the last element of $\mathbf{M} = \mathbf{BB}^{\mathrm{T}}$ becomes equal to one ($\mathbf{M}_{33} = 1$), because $\mathbf{P}$ is defined only up to a scale factor. After normalization the intrinsic parameters can be calculated as follows [131]:

$$u_0 = \mathrm{M}_{13} \tag{2.14}$$

$$v_0 = \mathrm{M}_{23} \tag{2.15}$$

$$k_v = \sqrt{\mathrm{M}_{22} - v_0^2} = \sqrt{m_v - v_0^2} \tag{2.16}$$

$$s = \frac{M_{21} - u_0 v_0}{k_v} = \frac{m_c - u_0 v_0}{k_v} \tag{2.17}$$

$$k_u = \sqrt{\mathrm{M}_{11} - u_0^2 - s^2} = \sqrt{m_u - u_0^2 - s^2} \tag{2.18}$$

Once the intrinsic parameters have been determined (matrix $\mathbf{K}$), the rotation matrix $\mathbf{R}$ and the translation vector $\mathbf{t}$ can be estimated using Equations 2.11 and 2.12 as follows:

$$\mathbf{R} = \mathbf{K}^{-1}\mathbf{B} \tag{2.19}$$

$$\mathbf{t} = \mathbf{K}^{-1}\mathbf{b}. \tag{2.20}$$

2.6.4. Epipolar geometry

In this section, the intrinsic projective geometry between the two camera views, referred to as epipolar geometry, is described. Epipolar geometry plays an important role during stereo matching, when point correspondences from left and right camera frames need to be identified. This relationship does not depend on scene parameters and is only influenced by the intrinsic camera matrix and relative pose between the cameras [130].

As discussed above, if a point of interest is imaged with two cameras as shown in Figure 2.14, a projection of the point is found on the image plane of each camera. As obvious from the Figure 2.14, the point in world coordinates, its projections on both camera images as well as the camera projective centers ($\mathrm{O_L}$ and $\mathrm{O_R}$) are coplanar [134] and the plane is called the epipolar plane. The line connecting the projective centers of the two cameras is referred to as baseline. It intersects the image planes of the cameras in the epipoles, marked as $\mathbf{e}$ and $\mathbf{e}'$ in Figure 2.14. Additionally, the intersection of the epipolar plane with the image plane is a line called epipolar line. All epipolar lines pass through the epipoles ($\mathbf{e}$ and $\mathbf{e}'$).

As mentioned above, object matching, or the identification of an object of interest from one camera in the other camera, is a challenging step in stereoscopy. With help of the epipolar geometry, and the mathematical and geometric relations of the points, the search region for a corresponding point from one camera can be limited to a line in the other one. For example, if a point of interest is detected in the left camera (e.g. Figure 2.14 in grey), it logically would lie on the line connecting the projective center of the left camera and the real world position of the point. This line together with the baseline define the epipolar plane, which intersects the image plane of the right camera. The epipole $\mathbf{e}$ and the unknown corresponding point are collinear and lie on the intersecting line (epipolar line). With this knowledge, an object matching algorithm could scan this line and detect the point evaluating further features (e.g. morphology, etc.). This reduction of the search space from two dimensions to one dimension is often referred to as the epipolar constraint [135].

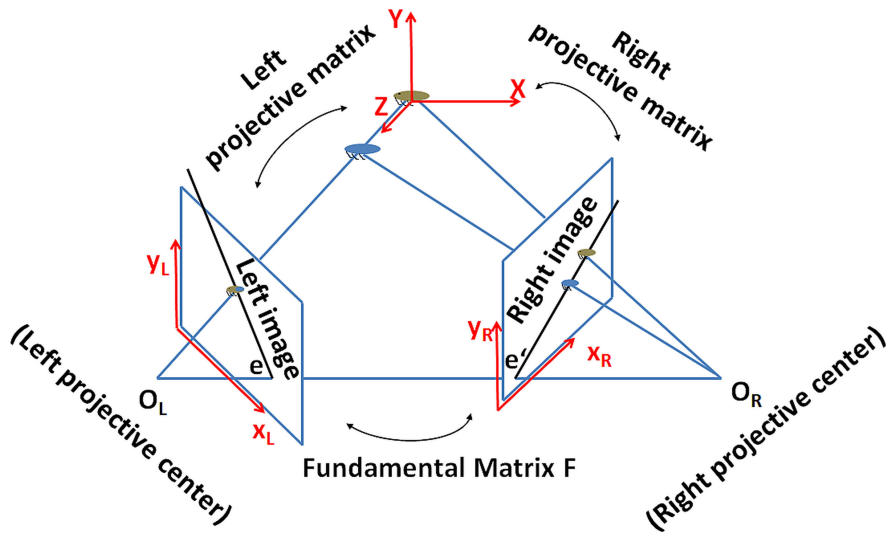

Figure 2.14.: Sketch with the basics of epipolar geometry. The main matrices used for transformations between world and image coordinates (left and right projective matrix), as well as between left and right image (fundamental matrix) are presented. Image adapted from [130].

The algebraic representation of the epipolar geometry in pixel (image) coordinates is the fundamental matrix $\mathbf{F}$. Generally, a 3-D point X is projected into a point x in the first and into a point x' in the second image, which is referred to as transfer via the epipolar plane. The fundamental matrix $\mathbf{F}$ satisfies the equation

$$x'^{\mathrm{T}}\mathbf{F}x = 0 \tag{2.21}$$

with the constraint $det[\mathbf{F}] = 0$. Additionally, the epipolar line corresponding to x can be calculated using $l' = \mathbf{F}x$ and for x' as $l = \mathbf{F}^{\mathrm{T}}x'$. One important application of the fundamental matrix is that the epipole $\boldsymbol{e}$ can be obtained by applying the following relationship $\mathbf{F}\boldsymbol{e} = 0$ and $\mathbf{F}^{\mathrm{T}}\boldsymbol{e'} = 0$. The fundamental matrix possesses two important properties [130]:

1. *Transposing:* If $\mathbf{F}$ is the fundamental matrix of a pair of cameras with projection matrices ($\mathbf{P}$, $\mathbf{P}'$), then $\mathbf{F}^{\mathrm{T}}$ is the fundamental matrix of the same pair in the opposite order: ($\mathbf{P}'$,$\mathbf{P}$).

2. *Epipolar lines:* For a point x in the first image, the corresponding epipolar line is $l' = \mathbf{F}x$. In addition, $l = \mathbf{F}^{\mathrm{T}}x'$ represents the epipolar line corresponding to x' in the second image.

Several algorithms exist for the calculation and estimation of the fundamental matrix. For the experiments presented in this thesis, in which an automatic matching was

applied, the 8-point algorithm was used. Briefly, it utilizes the relationship shown in Equation 2.21, which can be extended to

$$x'xf_{11} + x'yf_{12} + x'f_{13} + y'xf_{21} + y'yf_{22} + y'f_{23} + xf_{32} + yf_{32} + f_{33} = 0 \qquad (2.22)$$

with (x, y) being the 2-D point coordinates in one camera and (x', y') the 2-D coordinates in the other one. Written in a matrix form for N point correspondences the equation becomes

$$\underbrace{\begin{bmatrix} x'_1x_1 & x'_1y_1 & x'_1 & y'_1x_1 & y'_1y_1 & y'_1 & x_1 & y_1 & 1 \\ \vdots & \vdots & \vdots & \vdots & \vdots & \vdots & \vdots & \vdots & \vdots \\ x'_Nx_N & x'_Ny_N & x'_N & y'_Nx_N & y'_Ny_N & y'_N & x_N & y_N & 1 \end{bmatrix}}_{\mathbf{A}} \underbrace{\begin{bmatrix} f_{11} \\ f_{12} \\ f_{13} \\ f_{21} \\ f_{22} \\ f_{23} \\ f_{32} \\ f_{32} \\ f_{33} \end{bmatrix}}_{\mathbf{f}} = \underbrace{\begin{bmatrix} 0 \\ \vdots \\ 0 \end{bmatrix}}_{\mathbf{0}} \qquad (2.23)$$

or simply

$$\mathbf{Af} = \mathbf{0}. \qquad (2.24)$$

When at least 8 point correspondences have been identified (manually or automatically) the system of equations becomes overdetermined and can be solved using a least-squares or a singular value decomposition approach [136]. Often, because of measurement inaccuracies or erroneous matched points, the resulting matrix $\mathbf{F}$ would not be of rank 2, and an internal constraint needs to be enforced [136]. To achieve this, as described by Hartley, matrix $\mathbf{F}$ is replaced by a matrix $\mathbf{F}'$ which minimizes the Frobenius norm, and for which it is valid $det[\mathbf{F}'] = 0$. The Singular Value Decomposition of this matrix is $\mathbf{F}' = \mathbf{UDV^T}$ and substituting $\mathbf{D}$, being a diagonal matrix, with $\mathbf{D}$= diag(r, s, t) satisfying $r \geq s \geq t$, $\mathbf{F}'$ becomes $\mathbf{F}' = \mathbf{Udiag(r,s,0)V^T}$ [136]. This simple method for minimization of the Frobenius norm $\mathbf{F}$-$\mathbf{F}'$ has been originally suggested by Tsai et al. [137].

It is worth mentioning that, as proposed by Hartley [136], a simple normalization of the input prior to application of the 8 point algorithm improves its performance significantly. For this purpose, first, by applying translation, the origin of the coordinate system is centered at the coordinates of the centroid of the input points. Then, the coordinates of the points are uniformly scaled in order to obtain a mean distance from each point to the origin of $\sqrt{2}$. With these operations, the calculation results of the 8 point algorithm become comparable to results of the best iterative algorithms, which involve more computational power and time.

2.6.5. 3-D reconstruction and triangulation

As soon as the projection matrices have been obtained (via calibration) and the 2-D coordinates of an object of interest have been identified in both cameras (manually or using automated object matching algorithm and the fundamental matrix), the 3-D coordinates of the object of interest can be calculated. In order to obtain the 3-D coordinates of points in real space, a reconstruction of the 2-D coordinates of the two views is performed. Generally, this is achieved by back-projecting the 2-D points to a projection ray (3-D line) for both cameras [130]. The coordinates of the intersection point of the projection rays are the corresponding 3-D coordinates. To back-project the 2-D point to a ray, the 2-D coordinates of the point x in the image and the camera projection matrix are needed. Furthermore, to define the projection ray, the coordinates of two points, belonging to it, need to be known. In the approach described by Hartley et al. [130] the camera projective center and a point on the ray at infinity are used for this purpose. The second point is advantageous because it represents also the direction vector of the line [130] of the ray. Alternatively, any other arbitrary point can be selected, but then an additional calculation needs to be performed (e.g. subtraction of the coordinates of the points) to obtain the direction of the ray. Using the Hartley et al. approach, the camera optical center is defined as $C = -\mathbf{B}^{-1}\mathbf{b}$ with $\mathbf{B}$ and $\mathbf{b}$ being parts of the projection matrix $\mathbf{P} = [\mathbf{B}|\mathbf{b}]$ ($\mathbf{B}$ is a 3×3 sub-matrix and $\mathbf{b}$ denotes the last column vector of $\mathbf{P}$) [130]. An image point x back-projects to a ray intersecting the plane at infinity at the point $D = [(\mathbf{B}^{-1}x)^T, 0]^T$ [130]. The two points C and D are sufficient to represent the 3-D line. In order to allow an easy computation of point-to-line distances, the 3-D lines were represented in *Pluecker* coordinates as described in [138], which is an efficient implicit 3-D line representation. Briefly, a *Pluecker* line $L = (\boldsymbol{n}, \boldsymbol{m})$ is described by a normalized 3-D vector $\boldsymbol{n}$ (representing the direction of the line) with $\|\boldsymbol{n}\| = 1$ and a 3-D vector $\boldsymbol{m}$, called moment, which is defined by $\boldsymbol{m} := x' \times \boldsymbol{n}$ for a given point x' lying on the line. Using *Pluecker* representation, the direction of the back-projection line could be described as $\boldsymbol{n} = D$ (the point at infinity) and the moment of the line would be the cross product of the two points lying on the line $\boldsymbol{m} = C \times D$ [130]. Using this procedure and knowing the 2-D coordinates of an image point x and the camera projection matrix, the point can be back-projected to a ray. Repeating the process for the point x' in the other camera, the second 3-D projection ray is estimated. The coordinates of the intersection of both rays represent the 3-D coordinates X in real space of the 2-D point x. If collinearity of a point x to a line L is expressed by $x \in L \Leftrightarrow x \times \boldsymbol{n} - \boldsymbol{m} = 0$ and the distance between a 3-D point X and a line L $distance(X, L) = \|X \times \boldsymbol{n} - \boldsymbol{m}\|$, then the intersection 3-D point between two lines $L_1 = (n_1, m_1)$ and $L_2 = (n_2, m_2)$ can be computed as

$$X = L_1 \wedge L_2 = \left(\frac{n_1 \cdot (n_2 \times m_2)}{\|n_1 \times n_2\|^2} - \frac{(n_1 \cdot n_2)(n_1 \cdot (n_2 \times m_1))}{\|n_1 \times n_2\|^2} \right) n_1 + (n_1 \times m_1), \quad (2.25)$$

It is important to mention here, that Equation 2.25 results in a point on the first line

L_1, which lies closest to the second line L_2. For skewed lines, in order to improve the performance and minimize the projection error, a simple approach was used which computed the midpoint of the common perpendicular to the two rays as

$$X_C = 0.5(L_1 \wedge L_2 + L_2 \wedge L_1) \tag{2.26}$$

which is the arithmetic mean of both distances. This method proved to be reliable and allowed a fast 3-D reconstruction speed. Further triangulation methods can be found in literature [139, 140].

3. Surface preparation and characterization

The details regarding surface preparation and the characterization results are presented in this chapter in order to verify the quality of the materials used for experimentation.

3.1. Preparation of the test surfaces

3.1.1. Self-assembled monolayers on quadriPERM culture vessels

Gold substrates, purchased from Georg-Albert-PVD (PVD-Beschichtungen, Germany), were used as substrates for the self-assembly system.

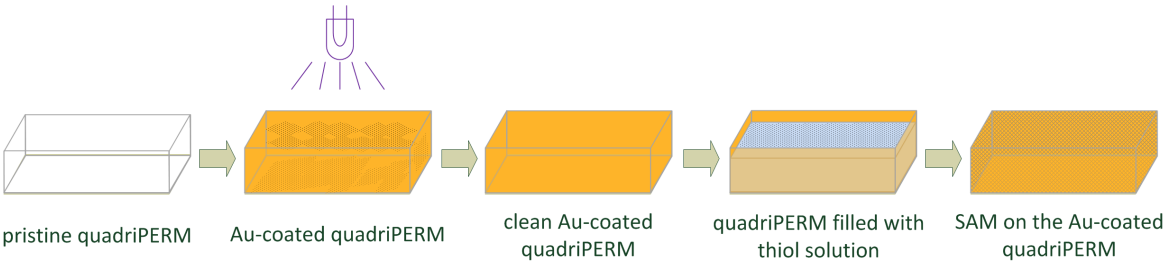

Figure 3.1.: Schematic representation of the SAM preparation protocol. First, the pristine quadriPERM was coated with a gold layer after applying a titanium adhesion promoter. Then, the substrate was cleaned by UV light, rinsed with ethanol and subsequently filled with thiol solution for 24 h / 48 h. After this period, the surfaces were cleaned again, rinsed with ethanol and stored in argon atmosphere until usage.

The preparation procedure of the SAMs is schematically shown in Figure 3.1. First, thin gold films were deposited onto quadriPERM polystyrene culture vessels using thermal vapor deposition after applying a titanium adhesion promoter of 5 nm thickness. The thickness of the gold films was ca. 100 nm (99.99 % purity) at the base of the quadriPERM and thinner on the walls, due to the geometry of the used coating apparatus. Evaporation was performed at a pressure of 2×10^{-7} bar and a deposition rate of 0.5 nm/s [141]. The prepared gold substrates were stored under ar-

gon atmosphere until used for the SAM preparation. Prior to preparation, the gold coated quadriPERMs were radiated by an ozone-generating UV lamp for 2 h. Afterwards, the substrates were subsequently rinsed with absolute ethanol, ultrasonicated for 3 min in ethanol, rinsed again and dried with nitrogen. Then the clean, substrates were filled with a 1 mmol freshly prepared thiol solution. The chemicals used for self-assembly were 1-dodecanethiol (DDT, $HS-(CH_2)_{11}-CH_3$)) and 11-hydroxy-undecanethiol (HUDT, $HS-(CH_2)_{11}-OH$), purchased from Sigma-Aldrich (Munich, Germany), hydroxy-PEG2000-thiol (PEG, $HS-(CH_2)_2(OCH_2CH_2)_{44}OH$) purchased from Rapp Polymere GmbH (Tübingen, Germany), trimetyl-ammonium-undecan-thiol (TMA, $HS-(CH_2)_{11}-NMe_3Cl$), as well as mercapto-undecanoic-acid (MUDA, $HS-(CH_2)_{11}-COOH$) and a 50/50 mixture of TMA/MUDA SAM (TMA+MUDA). All chemicals were used as obtained from the companies, without further purification. Ethanol *p.a.* was purchased from Sigma-Aldrich.
24 h after immersion (48 h for PEG surfaces) the substrates were rinsed with ethanol, treated in an ultrasonic bath for 3 min to remove non chemisorbed thiols and rinsed again. Finally, they were dried with argon and were either instantly used or kept under argon atmosphere until used.

3.1.2. Surface conditioning

The preparation of the conditioning layer on the surfaces followed the procedure described by Thome et al. [107]. The quadriPERMs were filled with filtered natural seawater from the "raft" test site in the Indian River Lagoon (belonging to the Florida Institute of Technology, located at the east coast of Florida about 5 km north of the Sebastian inlet, Florida (27°53′59.18″N; 80°28′28.34″W)). The containers were covered and left in the dark for 24 h to allow the conditioning film to form. In a next step, the solution in the containers was diluted with 500 ml of MilliQ® water, rinsed with it and dried in a stream of nitrogen. Subsequently, the thickness of the conditioning layer was quantified using ellipsometry (mean conditioning film thickness on HUDT was ca. 5 Å) and the quadriPERM samples were stored under argon until video experiments were initiated. For the experiments, the pre-conditioned surfaces were used in the same manner as the pristine samples following the experimental procedure described in Chapter 4.5.

3.2. Surface characterization

The geometry of the quadriPERMs did not allow direct ellipsometry, contact angle or XPS measurements, since they did not fit in the respective chamber or their shape did not allow the characterization. In order to be able to quantify the samples, the base of a quadriPERM was cut in 1 cm × 1 cm pieces and these were coated with the SAMs following the procedure described in Section 3.1, thus providing representative samples

with an advantageous geometry for the measurements. All measurements described in this chapter have been performed using the representative reference samples if not stated otherwise.

3.2.1. Contact angle goniometry

Contact angle goniometry is a technique used to determine the wettability of surfaces. The contact angle (CA) Θ_Y is defined as the angle between the tangent to the solid-liquid interface and the tangent to the liquid-gas interface as shown in Figure 3.2 [142]. This parameter classifies surfaces in hydrophobic ($\Theta_Y > 90°$) and hydrophilic ($\Theta_Y < 90°$) if water is used during the measurement. A small contact angle denotes high wettability and therefore a strong interaction of the liquid with the solid. Extreme values in both cases indicate superhydrophobic and superhydrophilic surfaces respectively.

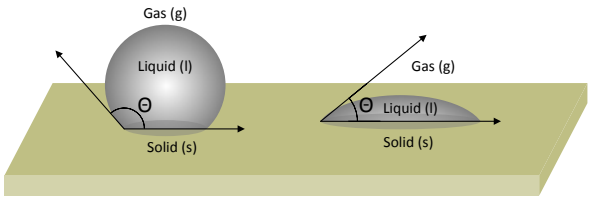

Figure 3.2.: Definition of the contact angles (CA). The CAs of a polar liquid are shown on a hydrophobic and a hydrophilic surface.

The contact angle Θ_Y of an ideal system can be described using the Young equation [143]

$$cos(\Theta_Y) = \frac{\gamma_{SL} - \gamma_{SG}}{\gamma_{LG}} \tag{3.1}$$

where γ_{SL}, γ_{SG} and γ_{LG} represent the interfacial tensions between solid-liquid, solid-gas and liquid-gas respectively. Equation 3.1 is only valid for atomically smooth and chemically homogeneous surfaces and for small droplets, in order gravitational force to have neglectable effects. Additionally, the surfaces have to be inert. The chemical structure has a high impact on the contact angle as well as the surface topography, which plays a key role in the wetting behavior and can be described using the Wenzel equation (Figure 3.3, left) [144]. The Wenzel contact angle Θ_W is determined by the

Figure 3.3.: Wenzel vs. Cassie model. The main wetting models aiming to describe the wetting of textured surfaces.

surface roughness ratio r which is defined as the ratio between actual and projected surface area ($r = 1$ for smooth surfaces, $r > 1$ for rough surfaces) and the Young contact angle Θ_Y of a flat surface from the same material (Equation 3.2).

$$cos(\Theta_W) = r \cdot cos(\Theta_Y) \tag{3.2}$$

As it can be seen from Equation 3.2 the hydrophobicity is increased by roughness ($\Theta_W > \Theta_Y$) when Θ_Y is larger than 90° and decreased (which increases the hydrophilicity) when the Θ_Y is smaller than 90°. If the structure of the surface does not allow a full wetting (e.g. Figure 3.3, right, lotus effect), wetting is best described by the Cassie Baxter equation (Equation 3.3).

$$cos(\Theta_{CB}) = \phi \cdot [cos(\Theta_Y) + 1] - 1 \tag{3.3}$$

The Cassie contact angle Θ_{CB} depends on the surface contact fractions ϕ of the liquid droplet and the surface characteristic contact angle Θ_Y, since in the small porous parts of the surface a hydrophobic air pocket is embedded beneath the droplet. This introduces an artificial bias and these contact angle values are generally higher than the ones measured on a flat substrate with an identical chemical composition. The static

Chemical formula	Short name	Contact angle [°]
HS-$(CH_2)_{11}$-CH_3	DDT	106 ± 3
HS-$(CH_2)_{11}$-OH	HUDT	33 ± 3
HS-$(CH_2)_{11}$-NMe_3^+	TMA	36 ± 3
HS-$(CH_2)_{11}$-COO^-	MUDA	46 ± 3
50% HS-$(CH_2)_{11}$-NMe_3^+ : 50% -COO^-	TMA+MUDA	19 ± 3
HS-$(CH_2)_2$-(O-$(CH_2)_2)_{44}$-OH	PEG	32 ± 3

Table 3.1.: Typical contact angles of the SAM surfaces used for the experiments in the thesis, based on static contact angle measurements on reference 1 cm × 1 cm quadriPERM pieces. The error represents the standard deviation.

water contact angles of the prepared SAM surfaces were measured using a custom built goniometric device under ambient conditions. The setup consisted of a light source positioned in front of a camera and illuminating the stage with the test surface at 90°. The droplet was released and positioned on the surface via a syringe mechanism. The camera recorded the image of the droplet on the sample and the contact angle was calculated by the MATLAB program CAM 3.02.01 (Koelsch, P.; Motschmann, H.; Orendi, H.), which modeled the geometric shape of the droplet by the Young-Laplace equation and estimated the angles applying simple thresholding and geometric moment calculations. For some experiments, where the measurement of the contact angle with this software was not possible, the DropSnake plugin [145] for ImageJ ver. 1.46r [146], based on B-spline snakes (active contours) to shape the drop, was used to obtain the

values. The reported values shown in Table 3.1 are the average of three measurements at three different positions on the samples, whereat the tip releasing the droplet was retracted before measurement.

3.2.2. Spectral ellipsometry

Spectral ellipsometry is a technique often applied to measure optical properties and thicknesses of substrates using polarized light in the visible and near infrared region. The main principle of the method is that light changes its polarization state when traveling through or being reflected on a sample and this change is a function of the optical properties and the thickness of the materials used. Usually, the incident beam directed onto the sample is polychromatic light, which is linearly polarized to an s- and p-wave (perpendicular and parallel to the plane of incidence). It interacts with the sample and is reflected, and the reflected light is collected in a detector. As a consequence of the interaction and reflection, the phases of the s- and p-polarized parts are shifted and the light becomes elliptically polarized [147] as shown in Figure 3.4. The properties of the reflected light are measured and the change in polarization

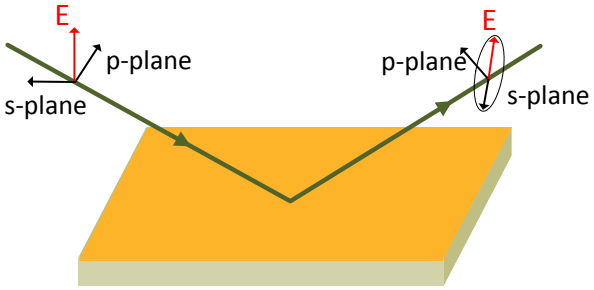

Figure 3.4.: Principles of spectral ellipsometry. A polarized beam of light is reflected from a surface, which changes its polarization. This mechanism is used in ellipsometric measurements. Image inspired by [148].

can be expressed by the ratio r of the reflection coefficients r_p and r_s (denoting the normalized reflection amplitudes of the p and s components) as described by the basic equation of ellipsometry [148]:

$$r = \frac{r_p}{r_p} = tan(\Psi)e^{(i\Delta)} \tag{3.4}$$

where $tan(\Psi)$ is the amplitude ratio upon reflection and Δ denotes the phase shift between the s- and p-polarized wave. Since the ellipsometric parameters cannot be converted directly into optical constants, a regression analysis needs to be performed. The analysis models a layer considering the optical properties and constants of all individual layers of the sample. Using an iterative, least-square minimization approach

and varying optical constants and thickness parameters the Ψ and Δ values can be estimated with the Fresnel equation [149] (with n_0 and n_1 being the refractive indices):

$$r_p = \frac{n_1 cos\Theta_0 - n_0 cos\Theta_1}{n_0 cos\Theta_1 + n_1 cos\Theta_0} \tag{3.5}$$

$$r_s = \frac{n_0 cos\Theta_0 - n_1 cos\Theta_1}{n_0 cos\Theta_0 + n_1 cos\Theta_1} \tag{3.6}$$

From the calculated values for Ψ and Δ, which best match the experimental data, the optical constants can be obtained and used for the calculation of different optical properties or thicknesses of the substrate. It is worth mentioning that in the case of a multilayer sample each layer needs to be modeled separately. In order to predict the material's behavior at each wavelength, it proved to be convenient to adjust the whole range of wavelengths simultaneously. The relationship between the optical constant shape and the wavelength can be used to allow the overall optical constant shape to match the observed experimental results. This simplifies the effort when compared to fitting individual n and k values for every wavelength. The refractive index for transparent materials can be described using the Cauchy equation [150]:

$$n(\lambda) = A + \frac{B}{\lambda^2} + \frac{C}{\lambda^4} + \cdots \tag{3.7}$$

where the variables A, B and C are adjusted until a match with the refractive index of the material is achieved.

The thicknesses of the SAMs used in the course of this thesis were determined using a M-44 multiple wavelength ellipsometer from J. A. Woollam Co. Inc. (Lincoln, USA). The incident angle was fixed at 75° to the surface normal plane. The light source was a high pressure Xe discharge point source lamp with wavelengths in the range of 200-1000 nm. For data analysis and modeling the provided software was used (WVASE^{TM}, J. A. Woollam Co. Inc.). The prepared self-assembled monolayers were modeled as a single Cauchy layer model with an estimated refractive index of A = 1.45, B = 0.01 [151]. The layer thicknesses measured on the reference quadriPERM samples are

Chemical formula	Short name	Thickness [Å]
HS-$(CH_2)_{11}$-CH_3	DDT	11 ± 2
HS-$(CH_2)_{11}$-OH	HUDT	11 ± 2
HS-$(CH_2)_{11}$-NMe_3^+	TMA	15 ± 2
HS-$(CH_2)_{11}$-COO^-	MUDA	16 ± 2
50% HS-$(CH_2)_{11}$-NMe_3^+ : 50% -COO^-	TMA+MUDA	15 ± 2
HS-$(CH_2)_2$-(O-$(CH_2)_2)_{44}$-OH	PEG	38 ± 2

Table 3.2.: Typical thicknesses of the SAMs used in this thesis, determined by ellipsometric measurements on reference 1 cm × 1 cm quadriPERM pieces.

shown in Table 3.2. The presented values are the mean of three measurements on three different positions of the reference quadriPERM piece and the error shows the standard error of the device.

3.2.3. X-ray photoelectron spectroscopy (XPS)

X-ray photoelectron spectroscopy (XPS) is a surface analysis technique which allows to determine the chemical composition of surfaces, relying on the photoelectric effect. As soon as a surface is irradiated with X-rays, electrons from the core of the surface atoms can absorb the X-ray photon energy $h\nu$ as shown in Figure 3.5.

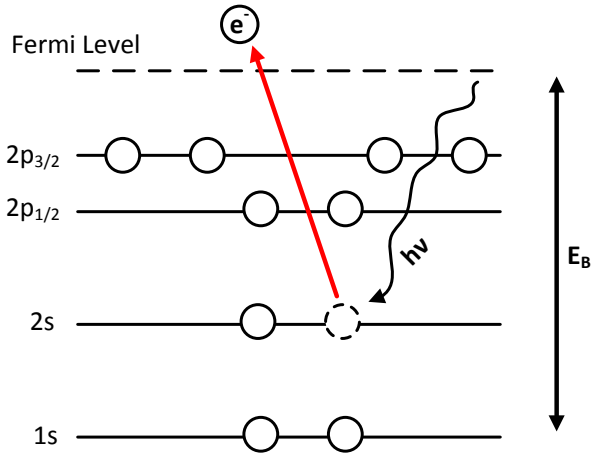

Figure 3.5.: The photoelectric effect. This photoelectric effect is used to perform X-ray photoelectric spectroscopy [152].

If the X-ray photon energy $h\nu$ is higher than the binding energy (E_B), electrons with a defined kinetic energy E_{kin} are emitted [152], which is described by the Einstein equation (Equation 3.8):

$$E_{kin} = h\nu - E_B - \Psi \tag{3.8}$$

with Ψ being the work function of the instrument. The Ψ is an instrumental parameter, which is adjusted by setting the Fermi edge emission of a pristine metallic sample to $E_B = 0$ as an energy calibration.

An analyzer measures the kinetic energy E_{kin} of the emitted electrons, which is used to calculate the binding energy (E_B) of the core level electrons, an element specific constant value. Thus, the XP-spectrum of a material contains peaks of the elements present on the surface. The amplitudes of the peaks are proportional to the concentration of each element. Usually, elemental ratios or atomic percentages are calculated, thus only relative values need to be determined and not the absolute amounts. The

peak intensity ratio of two elements (A and B) can be determined by applying Equation 3.9

$$\frac{N_A}{N_B} = \frac{I_A}{I_B} \cdot \frac{\sigma_B}{\sigma_A} \cdot \frac{\lambda_B}{\lambda_A} \tag{3.9}$$

where N represents the element ratio, I the area of the peak, σ the photoionization cross-section and λ_A and λ_B are the inelastic mean-free paths which can be obtained from databases [152].

The signal attenuation of an electromagnetic wave traveling through a medium is described by the Lambert-Beer's law:

$$I(d) = I_0 \cdot e^{-\epsilon c d} \tag{3.10}$$

with I(d) denoting the resulting intensity, I_0 is the initial intensity of the signal before entering the medium, ϵ is the adsorption constant of the material, c and d are the concentration and thickness of the medium [152]. Using this mathematical relation, the thickness of a thin film deposited on a substrate can be determined, by measuring the attenuation of the signal caused by this additional layer using Equation 3.11

$$d = \lambda_{att} \cdot cos(\theta) \cdot ln\frac{I_0}{I(d)}, \tag{3.11}$$

where I_0 is the intensity before and $I(d)$ after transmission through the material, θ is take-off angle and λ_{att} is the attenuation length of photoelectrons with a given kinetic energy and in a specific material.

To verify the quality of the surfaces and the presence of the respective SAMs, XP-spectra were recorded. The measurements were performed by Stella Bauer (University of Heidelberg, Germany) on a MAX 200 with an LHS 12 spectrometer (Leybold-Heraeus GmbH, Germany) equipped with Mg Kα X-ray source (1253.6 eV) and a Specs EA200 multi-channeltron detector. The measurement with the Mg-Anode at 250 W (13 kV, 18 mA), 48 eV pass-energy and a resolution of 0.7 eV was performed with a step size of 0.2 eV for each element. At the beginning of each measurement, a survey spectrum was recorded to verify the signal positions which are potentially shifted through charging of the sample and furthermore to detect possible impurities on the surface. Subsequently, a detailed spectrum was recorded for quantification of each atomic species of interest. The data was evaluated using SPECSLAB software which was used to normalize the peaks of Au4f signal to 84.00 eV. The XPSPEAK software was used to determine the signal intensity using the Shirley background subtraction method [153]. Because the position of the photoelectron peaks shifts by several eV if the tested surface is electrically isolated, the binding energy scale of the spectrum has to be calibrated by the position of a standard peak. The layer thicknesses obtained with spectral ellipsometry (Table 3.2) were confirmed by comparing them with the layer thicknesses calculated according to Lambert Beers law (Equation 3.10) using the attenuated integral signal intensities. For the qualitative analysis the parameters shown in Table 3.3 were used.

-	**Au4f**	**Si2p**	**C1s**	**N1s**	**F1s**	**S2p**	**P2p**	**Ca2p**
σ	18.98	0.86	1	1.77	4.27	1.73	1.23	5.15
E_{Kin} [eV]	1169.5	1150.1	969.5	853.5	568.5	1091.5	1120.3	905.0
λ_{Bain}[Å]	26.1	25.5	21.4	18.7	12.3	24.2	24.8	19.9

Table 3.3.: Parameters used for the analysis of the XP spectra (application of a Mg anode, 1253.5 eV) . Orbital cross section σ, kinetic energy E_{Kin} and inelastic mean free path of the photoelectrons λ_{Bain} normalized with the C 1s peak [154–156].

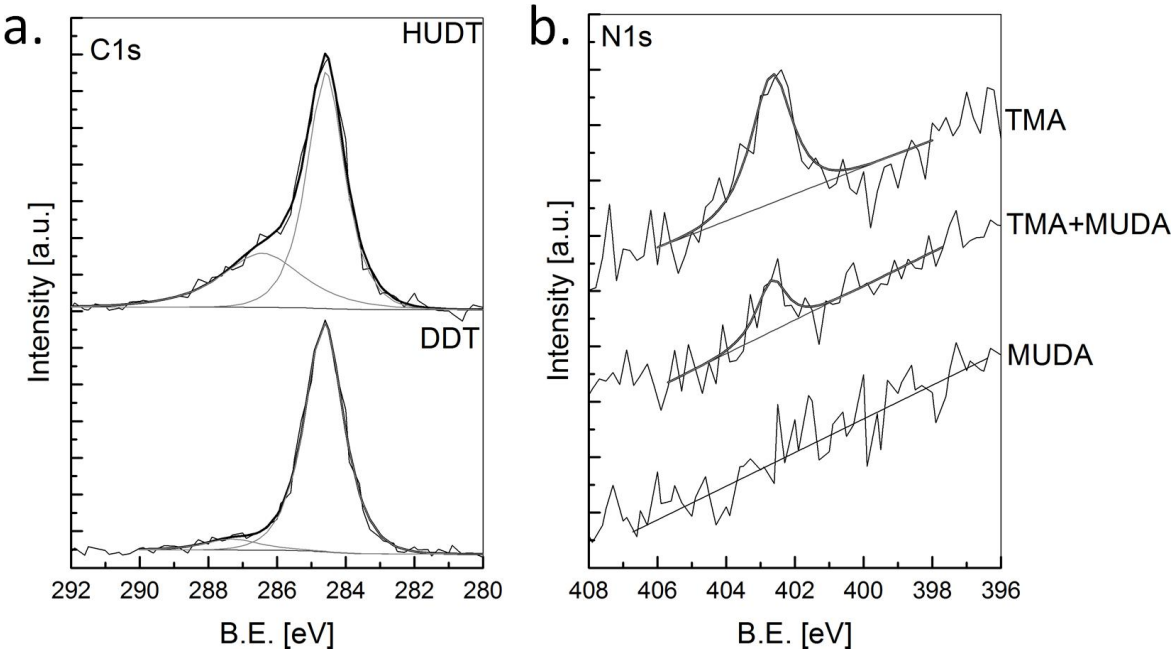

Figure 3.6.: XP spectra of the prepared surfaces. (a) the C 1s peak for DDT and HUDT and (b) the N 1s peak for TMA, MUDA and TMA+MUDA are shown.

Exemplary spectra are shown in Figure 3.6 where only the specific regions of the binding energy axis, significant for the particular molecule are presented. In Figure 3.6a the C 1s peak is shown for the DDT and HUDT SAMs. Both amplitudes have been normalized to the amplitude of the C-H peak at 284.5 eV. As it can be seen from the figure, the signal consisted of two peaks - the stronger one (at lower binding energy) originated from the C-H species, the peak at higher binding energy originated from the S-bound carbon. In the case of HUDT, an additional contribution at the higher binding energy was detectable, which occurred because of the presence of the hydroxy group (-OH). In Figure 3.6b, the N1s core region (402.5 eV) of the XPS spectra for TMA, MUDA and TMA+MUDA are shown. As expected, for the MUDA no signal originating from the nitrogen could be detected whereas for the TMA ($-NMe_3^+$) a strong peak was present. In the case of the TMA+MUDA surface, this peak was decreased

because the surface consisted of only ≈50% of the TMA molecules.

4. Stereoscopic imaging system for three-dimensional tracking

In this chapter the stereoscopic system used for measurement and extraction of the 3-D swimming patterns is discussed in detail. For this purpose, first the requirements on the setup are presented, followed by a description of the hardware components. The performance and achieved accuracy are tested and characterized using error analysis techniques. Finally, the experimental procedure is introduced.

4.1. Demands on the setup

Generally, the developed system was required to be capable of providing technical means for accurate detection, imaging and extraction of three-dimensional swimming trajectories of multiple marker-less moving objects (cyprids). Apart from modularity, flexibility and cost efficiency, there were special demands on the software and hardware parts of the setup in order to obtain reliable qualitative and quantitative information on the exploratory behavior of cyprids.

- *Hardware requirements:* Maximal accuracy and resolution were the main requirements for the design of the setup as well as for the selection of electronic devices. For the detection of swimming cyprids imaging devices with sufficiently high temporal (at least 25 frames per second) and spatial resolution (or imaging chip resolution of at least 1280 x 720 pixel, not interlaced) were required. A correct synchronization was also essential, because of the procedure for obtaining of 3-D data, involving the combination of two 2-D images. A temporal synchronization guaranteed minimal 3-D reconstruction errors. An additional aspect which was considered, was the performance and reliability of the imaging devices. Due to the large number of measurements during the experiments, it was important that the cameras were capable of recording for several hours with short interruptions without any decrease of the image quality because of overheating or oscillation in the electronic parts. Furthermore, a constant, regular and evenly distributed illumination was required to assure an optimal lighting of the scene in the field of view and to avoid shadows or illumination gradients. Such environmental conditions contributed to a decrease in processing time of the 3-D merging procedure and the tracking algorithms. Finally, for an easy exchange of the calibration object with a test surface / container,

without the risk of interfering the operation of the setup and introducing misalignments, the geometrical arrangement of the setup was important. Compliance with this requirement allowed to skip calibration procedures before every measurement, thus immensely reducing experimental time.

The special demands on the underwater version of the setup are discussed in Chapter 5.7.1.

- *Software requirements:* The challenges on the software side included noise reduction and performance optimization. Although the effort during experimentation was always to provide optimal conditions for the imaging system, there still existed sources of noise which could not be fully attenuated. Because of this fact, it was essential to design software algorithms resistant to noise and to implement pre-processing routines filtering and adjusting the quality of the input images, and thus minimizing the probability for an erroneous output of the following, more complex, mathematical procedures. Furthermore, in a long observation period, a high number of frames needed to be processed, scanned for objects of interest and detected position points needed to be connected with preceding and following frames. To reduce processing speed, performance optimized implementation of the algorithms was required. In addition to performance, also numerical stability played an important role in the development. Since several numerically unstable operations were included (e.g. matrix inversion) it was necessary that the code handled these operations appropriately.

  Because the development of the software was not the main objective of this thesis, the concrete details on how these requirements were considered during implementation of the software routines will not be further discussed in the course of this thesis.

4.2. Hardware components

The stereoscopic system exists in two modifications depending on the main application domain: a laboratory version and a setup for field experiments underwater. In the following sections the hardware components of the laboratory setup are described along with the specifics of the calibration object. The modifications of the laboratory setup necessary to allow measurements under field conditions are presented in Chapter 5.7.1.

4.2.1. Laboratory setup

The hardware components of the system were partly selected by Hernan Sendra (University of Heidelberg, Germany). A schematic representation of the setup is shown in Figure 4.1. As discussed in Section 4.1, the main requirements for the laboratory version of the setup were flexibility and cost efficiency. The imaging devices with best cost efficiency proved to be off-the-shelf camcorders. The model Sony HDR-XR550

(Manufacturer: Sony Corporation, Japan) possesses a CCD chip with square pixels and a maximal spatial resolution of 1920 × 1080 pixels (for experiments a 1440 × 1080 pixel resolution was used, depicting a field of view of ca. 47 mm × 35 mm) at a frame rate of 25 fps when operated in `TELEMACRO` mode. The focal distance of the objectives was 3.8 mm-38 mm, depending on the zoom, and the cameras were manually focused on a sample using telephoto (`TELEMACRO`) operating mode. Two camera settings ought to be mentioned at this point, because of their importance for the measurements. One special feature of the model Sony HDR-XR550 was that it did not automatically switch into the `TELEMACRO` mode. In order to enable the macro resolution the setting `TELEMACRO` needs to be selected manually. Special attention should be payed to the fact that as soon as the zoom keys are pressed, the camera switches the `TELEMACRO` mode automatically off. Another setting which is to be handled with caution is the `AUTOFOCUS`. To obtain optimal focusing on the object of interest, experience has shown, that it is best to use the calibration object, and switch the `AUTOFOCUS` on, thus letting the camera adjust the focal length accordingly. As soon as a sharp image is visible on the preview window the `AUTOFOCUS` should be switched off, in order to avoid automatic adjustments by the camera during an active measurement.

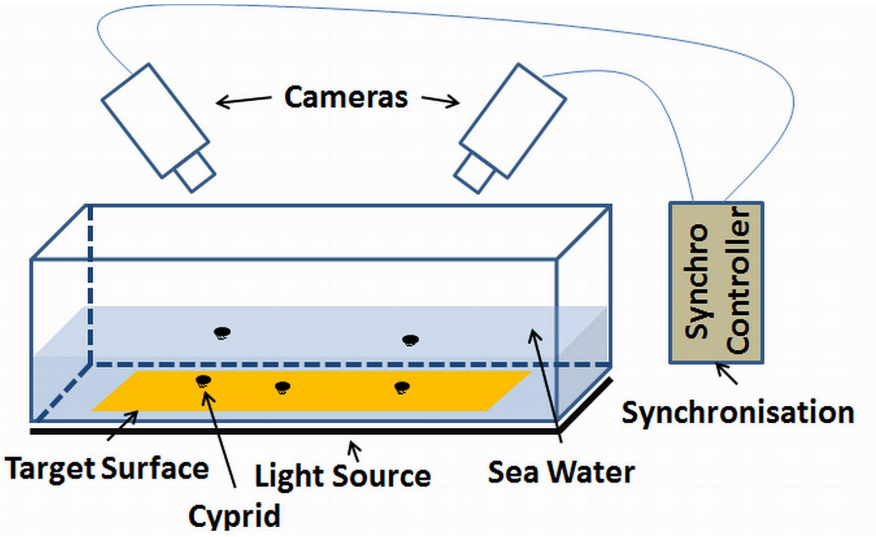

Figure 4.1.: Schematic representation of the laboratory version of the stereoscopic setup. The components included two cameras, a synchronization device, containers coated with test surfaces, a light source and cyprids.

As mentioned before, the synchronization of the video recording of both cameras was essential in order to obtain correctly reconstructed 3-D coordinates. Several techniques were discussed to guarantee an accurate synchronization between the cameras:

- *Temporal synchronization using video markers:* cameras are started manually and a short, bright flash is used to mark the beginning of the video. In the post processing

step, the user manually adjusts the frames of both cameras according to this video mark.

- *Temporal synchronization using audio markers:* Here, the two cameras are also started manually and a short, loud and easily detectable audio signal is used to mark the start of the recording [157]. In the post processing step, the user manually adjusts the frames of both cameras according to the audio marker.
- *Temporal synchronization using an external shared trigger:* With this technique an external trigger signal is used to start the recording sequence in a synchronized manner on both cameras simultaneously.

Figure 4.2.: The LANC controller synchronizing the cameras. The LANC controller purchased was used as an external synchronization and trigger device.

The last technique was applied for the setup, using a stereo LANC remote controller (Model: ste-fra LANC V3.0M, Manufacturer: digi-dat, Germany). The controller (Figure 4.2) offered a hardware clock synchronization with a low synch error of maximum 2 ms. This value proved to be acceptable for the experiments, because at a frame rate of 25 fps, it corresponded to 0.05 frames.
Several setup arrangements with different positions of the light source were used. Illumination from bellow (3.5" × 6" LED area backlight, Manufacturer: Metaphase Tech, USA) proved to be beneficial if surfaces of transparent material (polystyrene) were imaged. As described in Chapter 3.1, the test surfaces used in this thesis were mainly SAMs attached to a gold substrate. In this case, the illumination from bellow could not provide sufficient light through the gold coated containers and a light source from top was chosen, offering an optimal lighting with the lowest number of reflections. The light used for the experiments was, due to the selected camera hardware, in the visible range. It possessed a low light intensity which was just sufficient for tracking, in order not to influence the exploratory behavior of the cyprids. In addition, the positive phototaxis of cypris larvae seems to be controversially discussed in literature (Prendergast et al. [158] vs. Crisp et al. [159]). Also, it was indicated by Wolf et al. [160] that cyprids exhibit frequent reversals of phototaxis response. Because of this partly contradictory information in literature about phototactic behavior of the

larvae, no further investigation concerning the effect of light was performed, but rather all experiments were run under the same illumination conditions.

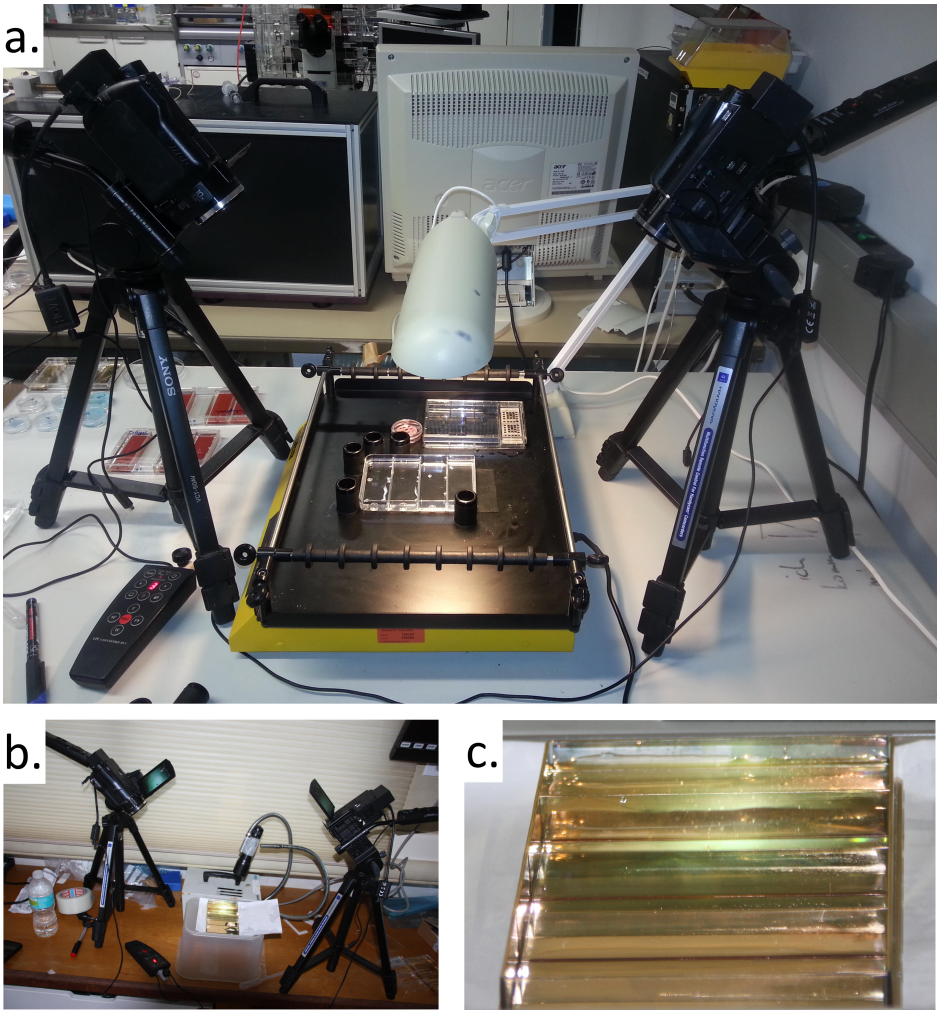

Figure 4.3.: The laboratory version of the stereoscopy setup used for the experiments. (a) Image of the system consisting of the two cameras with tripods, a synchronization device (lower left corner), the light source and the calibration object in the container. (b) Another configuration of the setup using a LED-torch as a light source and (c) the test container coated with gold.

The laboratory setup is shown in Figure 4.3 in two versions depending on the light source - a cold light source (Figure 4.3a) and a LED torch light (Figure 4.3b). Even though the position and type of the light source were varied, the general format of the setup was kept constant, because this alignment proved to be beneficial for a maximal field of view, depth resolution and flexibility during loading and unloading of test samples.

4.2.2. Calibration object

The calibration object played an important role during estimation of external and internal camera parameters and was used for scene characterization. The main properties of the calibration object were to provide geometric features allowing a fast automatic detection of the calibration points. One version of the calibration object, providing enough orthogonal planes and a high amount of reference points to be detected by the calibration routine is presented in Figure 4.4 (CAD design by Sebastian A. Weisse, University of Heidelberg, Germany). This calibration object possessed 128 points

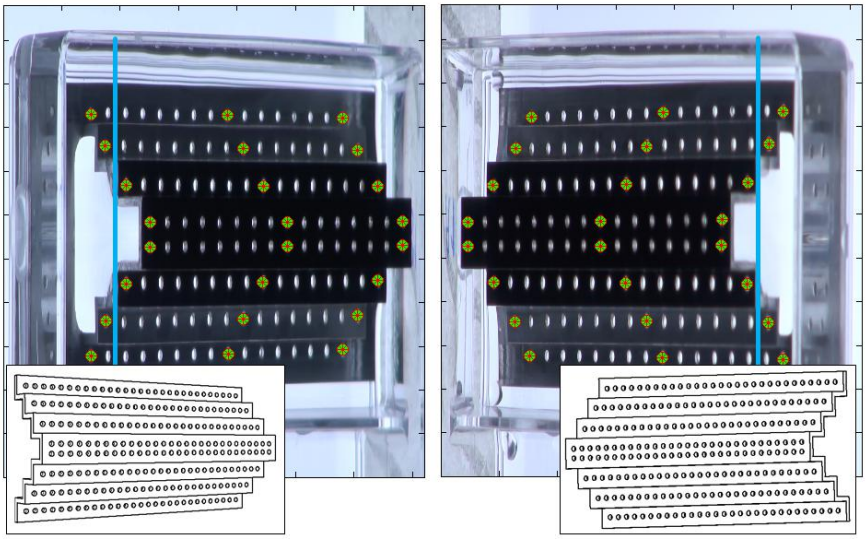

Figure 4.4.: Images and schematics of the calibration object. The images were extracted from videos taken by the left and right camera of the setup. The blue lines represent the water level during experimentation. The CAD-drawings of the object, which were used for its manufacturing, are also shown.

(holes with a diameter of 1 mm) distributed across four planes. It was designed with the same dimensions as an objective slide (75 mm× 25 mm) used in the experimental part, which allowed an easy substitution by a coated sample slide after calibration and minimized the probability of introduction of misalignments during the procedure.

An alternative version of the calibration object (Figure 4.5a) was used during measurements in round containers (e.g. during the iSPR measurement described in Chapter 5.4). Furthermore, during development it became clear that detection of corners seemed to be more accurate, than detection of centroid of perspectively distorted circles and for that reason, another version of the calibration object was designed (Figure 4.5b). This generation of objects used rectangular patterns to provide a high number of corners and edges for an efficient automated calibration point detection.

The mathematical details of the algorithms used for camera calibration are discussed in Chapter 2.6.3.

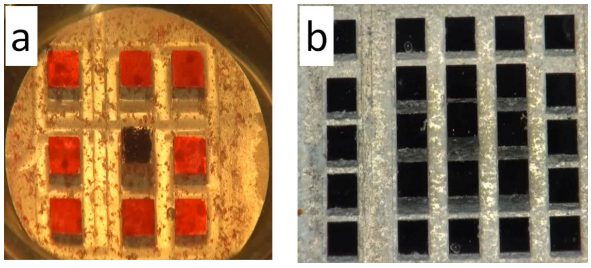

Figure 4.5.: Variations of the calibration objects used for various experimental setups. (a) The circular calibration object applied during iSPR measurements and (b) an alternative rectangular version of the calibration object, allowing the easier identification of calibration points using automated edge detection algorithms.

4.3. Tracking software

The 2-D trajectories from frames of the left and right cameras were generated using the tracking software. The self-developed MATLAB application quantumCAT (**QU**antitative **AN**alysis of **T**wo-dimensional **U**ndirected **M**otion by **C**omputer **A**ssisted **T**racking) implements a modified version of a tracking kernel developed by Prof. B. Rosenhahn (Leibniz-University of Hannover, Germany) and allows simultaneous tracking of multiple label-free objects. In this chapter, a brief introduction to the tracking procedure is presented and a full user's guide can be found in Appendix A.

4.3.1. Graphical user interface (GUI)

The graphical user interface of the software is shown in Figure 4.6. The GUI consists of four main parts which grouped different functions together.

The 'Main preview window' visualizes the currently processed frame from the input stream (a directory of images or a video). In the 'Controls' section, the navigation between frames as well as switching between trajectories and selection of points of each trajectory for a potential manual position refinement can be achieved. The right group of the GUI, 'Settings', contains the main options controlling the tracking procedure. Finally, the 'Magnified preview window' shows a magnified version of the current frame portion in the search window, which is aimed to assist the supervision of the accuracy of the tracking by the user.

4.3.2. Tracking basics

There are three working modes available in the application - automatic, semiautomatic and manual. In the automatic, the software requires an initial point, which is defined by the user, and the object is followed until leaving the field of view or the last frame is reached. For each frame, the search window in which the object has been detected

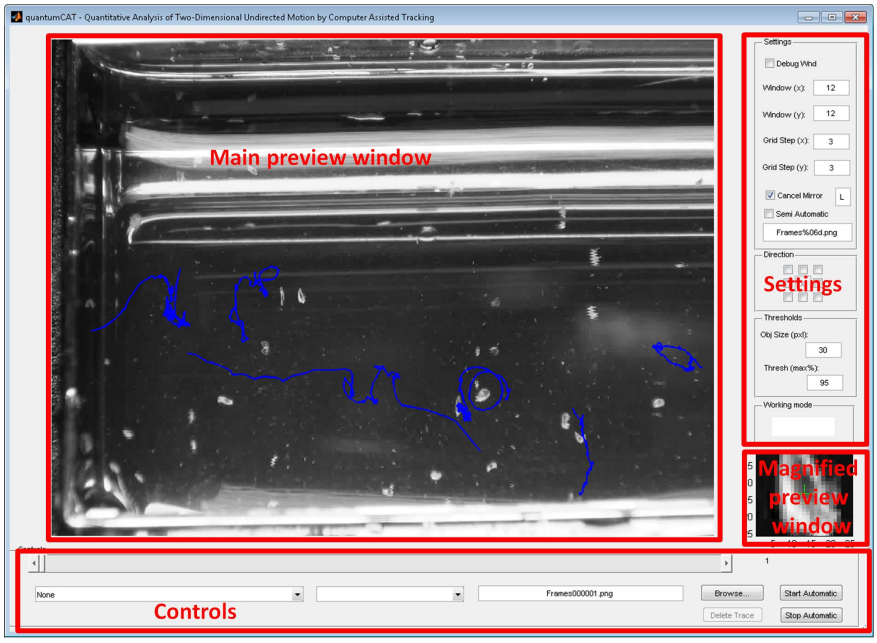

Figure 4.6.: Graphical user interfaces of quantumCAT. The software used for tracking of cyprids, quantumCAT, was developed as part of this thesis.

is shown in the 'magnified preview window'. If several points have been defined, each of them is tracked simultaneously until the last one has left the field of view or end of the image stream is reached. For each manually defined point a separate trajectory file is generated.

In semiautomatic mode, the object of interest if tracked, but for each frame a magnified view of the search windows is presented to the user. It is expected to manually refine the centroid of the detected object, by clicking in the magnified window. The input is evaluated and a centroid of the object positioned bellow the selection of the user is calculated. This 'double-refining' strategy is advantageous if two or more objects appear in the same search window area. It provides the opportunity of a user intervention and manual identification of an object of interest, for which in a subsequent step the centroid is automatically calculated, thus eliminating the manually introduced tracking error. Finally, the following frame is selected and the procedure is repeated from the beginning. In the manual mode of operation, the user tracks the object of interest in the main window and the software automatically refines the selection and switches to the next frame. This procedure is repeated until terminated by the user.

The tracking kernel utilized statistical classificators describing the object of interest based on values from past frames and used this information to identify the same object in subsequent frames. In addition, an adaptive search window size was implemented in the course of this thesis, which monitored the values of velocity and direction of the

object in order to minimize the probability of identifying a wrong object of interest, since all objects in the field of view possessed similar geometric shape and color. Furthermore, in order to improve the accuracy in finding the object of interest, a scanning raster method was introduced as shown in Figure 4.7. The raster structure fragmented

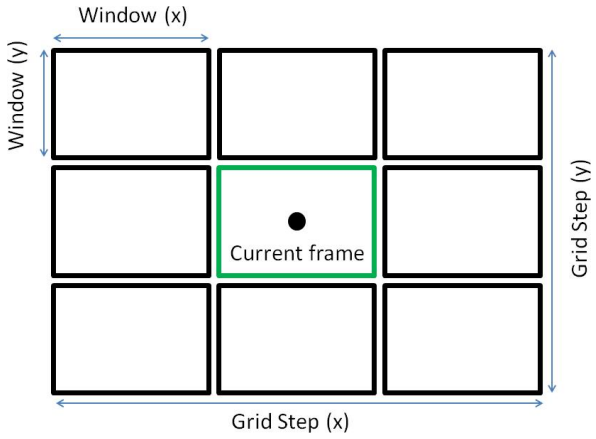

Figure 4.7.: Structure of the scanning raster of the tracker. It denotes the main scanning parameter which can be selected in the GUI of the software.

the search area, and thus provided the possibility for selection of the tracking direction, which was controlled by the parameters in the 'Settings' section, in the subsection 'Direction'. E.g. when tracking objects of interest in a flow environment with a predefined motion direction, this setting can be selected to accelerate the search algorithm by discarding directions in which no movement can be expected.
One important feature of the software is the 'cancel mirror' check box which allowed the user to define a direction in which potential mirror images to be discarded. On highly reflective substrates (e.g. gold) this setting, together with the control of the threshold of the binarization procedure as well as the minimal size of an object of interest, improved the accuracy of the detection algorithm considerably.

4.4. Error analysis of the system

Analysis of the results of first feasibility tests with the system revealed that an exact estimation of the coordinates of calibration points at sub-pixel level is challenging and can lead to calculation uncertainties. In addition, illumination and contrast between swimming objects and background affected the exact estimation of the object's coordinates. Depending on the reflectivity of the surface, mirror aberrations occurred, which, combined with the morphing of the non-spherical objects of interest, could induce inaccuracies in the detected position. To characterize how the system responses to erroneous inputs, tests with artificially distorted object coordinates were performed.

Analyzing the outcome of the 3-D merging algorithm, the relationship between the error in the coordinates of the object in the left and the right frames (in pixel) and the error in the real position (in mm) was empirically determined.

4.4.1. Random errors in the pixel coordinates

In order to obtain the 3-D coordinate of an object, its 2-D coordinates in the two camera images need to be known. In the software processing pipeline these points were estimated using the tracking software and then merged with the reconstruction algorithm (details follow in Chapter 4.5). Because of several sources of noise which influenced the estimation of the 2-D coordinates, the calculated 3-D coordinate contained a component of uncertainty (Figure 4.8). To statistically quantify how the

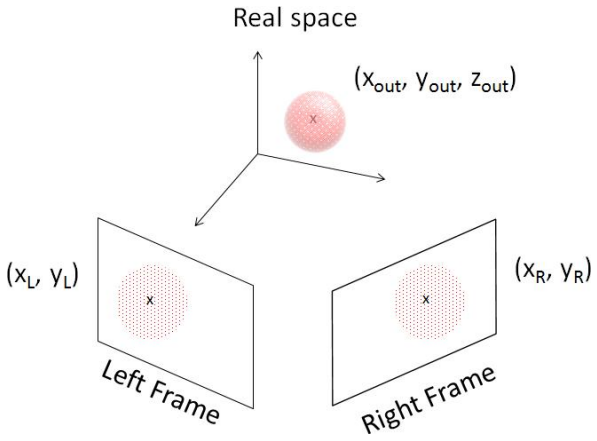

Figure 4.8.: Relationship between the errors in image and real world space. The error regions in image coordinates, marked by a red circle, caused an error in real space depicted schematically as a red sphere.

algorithms react to distortions, a random error component was introduced to the 2-D coordinates of correctly tracked cyprid positions. To obtain a random signal which is representative of potential errors in real life applications, two assumptions needed to be made: (i) the error signal was normally distributed and (ii) the inaccuracies in frame [*k*] were statistically independent from the inaccuracies in frame [*k-1*]. The resulting distorted coordinates, contained the error signal which was added to already correctly tracked coordinates (Figure 4.9). The error signal was generated to possess normally distributed values between ±36 pixels as shown in Figure 4.10c. The parameters of the distribution were μ=0 pixels and σ=14 pixels. Since the size of a cyprid in the frames was ca. 24-28 pixels (Figure 4.10a), this meant that all error values higher than ±14 pixels distorted the coordinates of the center of mass to such extent that they lay completely outside of the cyprid body. A data set containing the artificially distorted 2-D coordinate arrays for both cameras was processed with the 3-D reconstruction

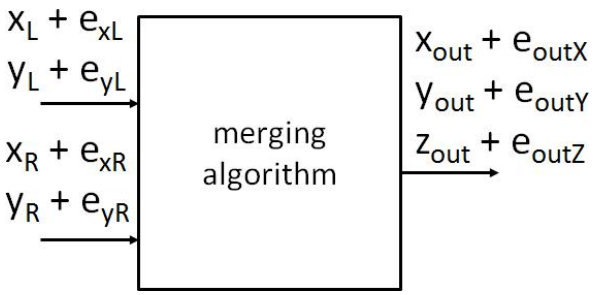

Figure 4.9.: Inputs and outputs of the merging algorithm. The variable names are denoted to visualize the process of coordinate distortion.

algorithm in order to obtain the 3-D coordinates. Finally, the known 3-D coordinates (obtained using the correctly tracked positions) were subtracted from the 'distorted' 3-D coordinates to estimate and visualize only the error signal. The output of the test is shown in Figure 4.10d and 4.10e. As it can be seen from Figure 4.10d, the error of the 3-D coordinates of the object of interest in real space was in worst case ±2 mm.

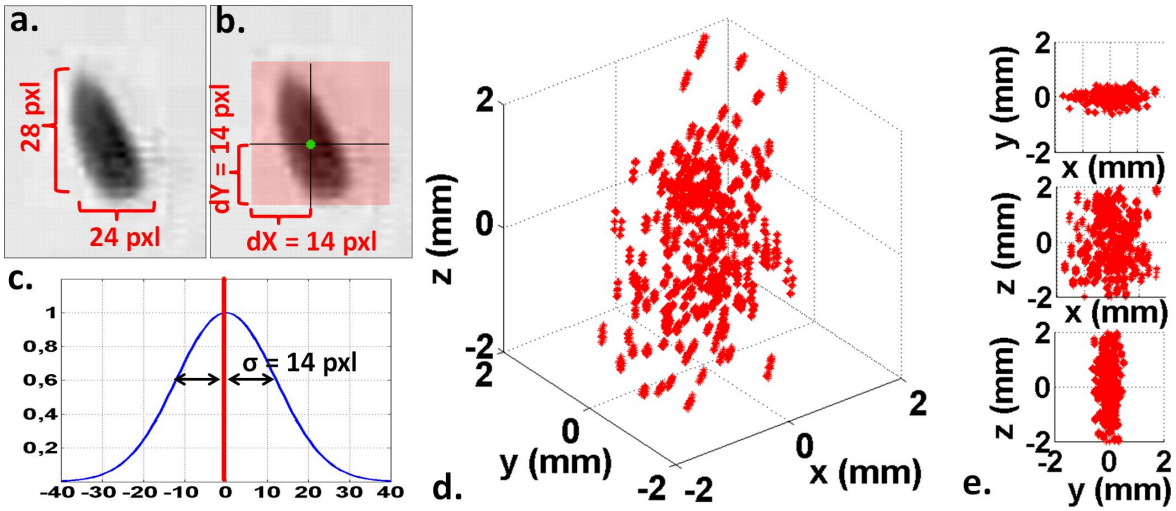

Figure 4.10.: Characteristics of the random error signal. (a) The size of a cyprid in the frames in pixels and (b) the region in which the error signal moves the coordinates of the center of mass. (c)The distribution function of the input error signal which lead to the (d, e) error signal.

4.4.2. Systematic error in the pixel coordinates

The analysis in the previous section characterized the worst case scenario, evaluating the output of the algorithms caused by an error signal with normally distributed values of up to ± 36 pixels. A value which carries more practically relevant information is the

typical error of the system. It is an empirical variable, based on the evaluation of the input of an experienced tracking user working with the software in the manual tracking mode. To quantify this error, an expert user tracked a trajectory with already known coordinates in a manual mode, whereby the coordinates were refined by the software which calculated the center of mass of the object in the region identified by the user, thus providing sub-pixel accuracy. This value represented a more realistic parameter for the evaluation of the expected error and was referred to as 'typical error'. The

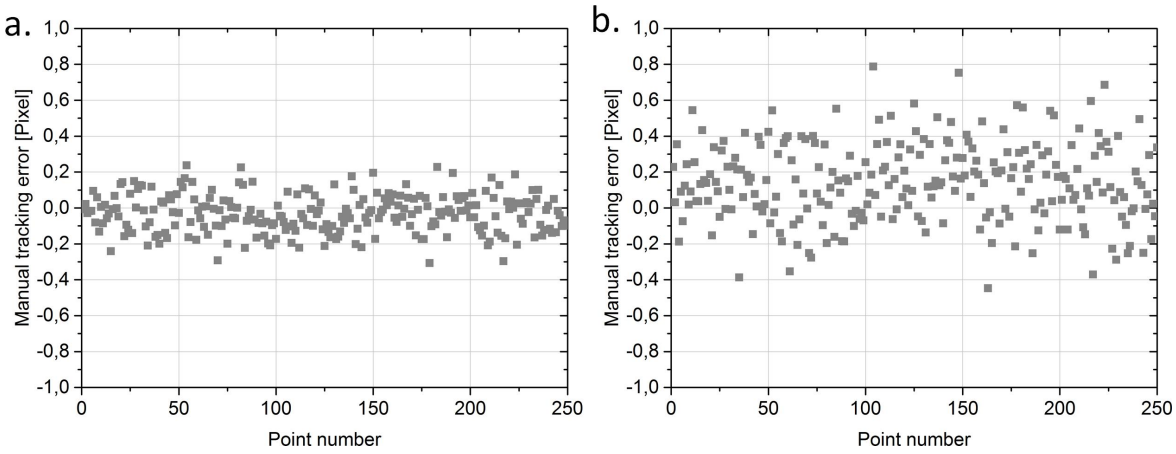

Figure 4.11.: Typical error of the system. Error in pixels in the center of mass calculation algorithm for 250 frames in (a) x and (b) y direction.

mean values of the typical error were, as visible from Figure 4.11, $\mu_{\delta x} = -0.02$ pixel in x direction and $\mu_{\delta y} = 0.16$ pixel in y direction.

In order to systematically characterize the error response of the system to errors with magnitude in the range of the typical error and to estimate the corresponding typical error in mm, another artificial error signal was added to the coordinates of an object of interest. As it can be seen in from the results in Figure 4.12, the error signal was increased stepwise from 0 pixels up to 2 pixels for both frames (from the left, Figure 4.12a and right, Figure 4.12b camera) and both directions, represented by the x and y axis of the graphs. The z axis showed the magnitude of the resulting error in real space and the three planes were the x, y and z component of this error in mm. It is obvious from the Figure 4.12 that the errors in the left and right camera resulted in similar values in real space. If the typical error was considered ($\pm$ 0.2 pixels) it became obvious that it introduced an error in the real world coordinates of ca. 0.01 mm-0.02 mm. This value was ca. 5 % of the real dimensions of cyprids (e.g. *Balanus amphitrite* ca. 500 µm), which proved to be sufficient for the planned application of cyprid tracking.

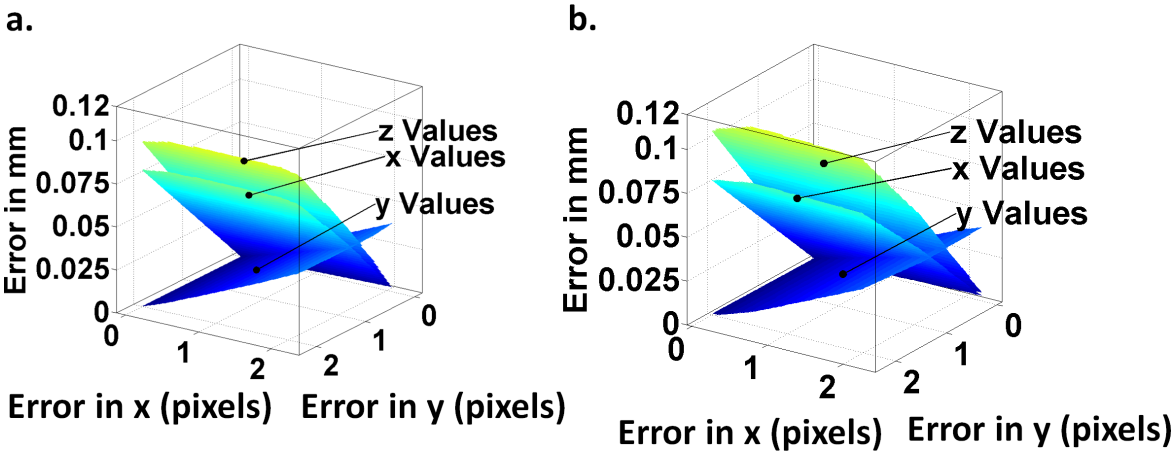

Figure 4.12.: Characteristics of the random error signal. Results of the systematic error analysis showing the error planes for the (a) left and (b) right cameras. The z coordinate represents the magnitude of the error in mm, whereas x and y coordinates represent the magnitude of the error in pixels.

4.4.3. Conclusions

The software part in which inaccuracies were most likely to occur was the tracking algorithm. In order to characterize its behaviour in case of an erroneous input data, three evaluations were performed. First, the reaction of the system to a random, normally distributed noise signal was investigated and it could be demonstrated that the output was also normally distributed. In the worst-case, a tracking error of $\pm$ 36 pixels moving the centroid outside of the cyprid body, resulted in an error in real space of $\pm$ 2 mm.
Further more, it was investigated what is the typical error an experienced user introduced during manual tracking. For this purpose the user manually tracked 250 points, whereby the object of interest was selected, and the algorithm refined its center of mass. It became obvious that this 'typical error' was ca. $\pm$ 0.2 pixels.
Finally, in order to obtain the connection between the typical error and the resulting error in real space, the algorithm was tested with a systematically distorted signal. The error component was linearly varied, in order to systematically obtain all values for errors in the region between 0-2 pixels. Using this information, the value for the typical error of the tracking algorithm in mm could be revealed to be ca. 0.01 mm-0.02 mm, which fulfilled the requirements for accurate tracking of cyprids in 3-D.
At this point it should be noted, that the dimensions of the errors of the stereoscopic system depend on the geometric alignment of the cameras. The errors described in this chapter, were calculated using the most common alignment of the setup - cameras imaging the scene from top, distance from camera to sample of interest ca. 40 cm and relative angle between both cameras of ca. 80°.

4.5. Experimental procedure

Figure 4.13 summarizes the general measurement pipeline of the experimental procedure. After surface coating, tracking experiments were performed and the settlement

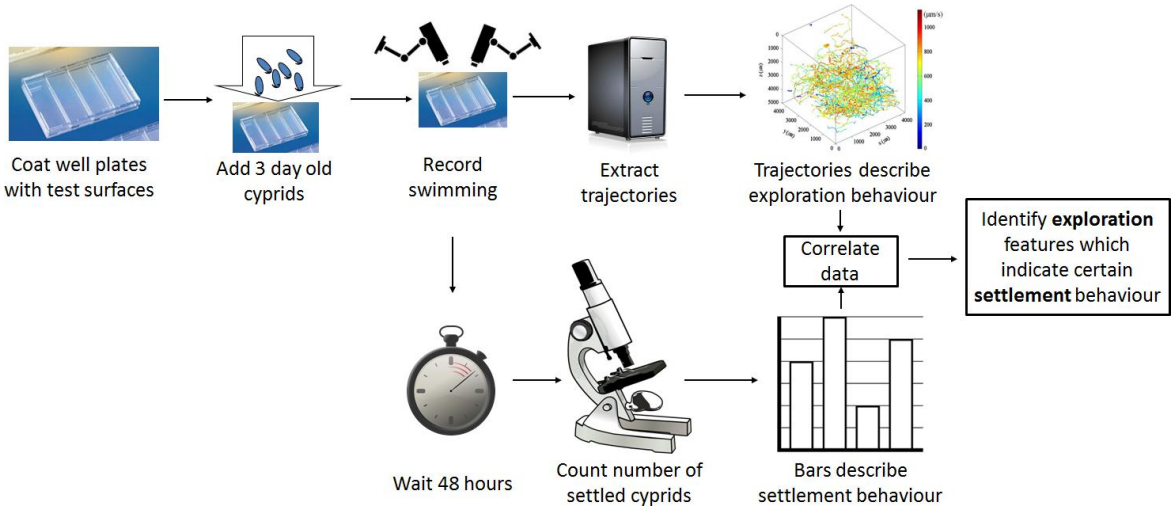

Figure 4.13.: Schematic representation of the experimental procedure. The two main paths are shown - tracking and settlement assays. The advantage of this procedure is that it allows a direct combination of the results of exploratory and settlement behavior.

of the cyprids was quantified 48 h after tracking in the same containers. The extracted swimming and exploration behavior features were then correlated with the settlement preferences in order to identify potential motility parameter in the exploratory behavior which indicated the settlement preferences.

The main steps of the measurement and experimental procedure can be found in the following sections. First, the specifics of the cyprid culture handling are presented, followed by a description of the camera calibration approach. Then, the process of obtaining the videos is shown. Finally, the post-processing of the videos and the process from video file to the extraction of 3-D trajectories are briefly explained, together with the special form of settlement assays developed in the course of this thesis.

4.5.1. Handling of cyprids

Cyprids of the species *Balanus amphitrite* were cultured and harvested at the University of Newcastle following established protocols. Briefly, as described by Elbourne et al. [161] and Imbesi et al [162] the adult barnacles (from brood stock originally from Beaufort, North Carolina, USA [29]) were bred in the laboratories of the University of Newcastle in a static-renewal seawater environment at 24.8 °C and were fed with

Artemia sp. nauplii and the diatom *Skeletonema costatum*. After culturing in filtered seawater (filter pore size 0.7 mm) containing antibiotics, the cyprids were transferred into a new environment at 28.8 °C and a 12:12 light-dark cycle. After 4 days, nauplii had metamorphosed into cyprids which were filtered out through a plankton mesh. After cleaning and removing remaining alga, cyprids were transferred to filtered natural seawater (0.2 µm) and stored at 6 °C for 2-3 days prior to shipping. Then, they were shipped overnight in a cooling box to the Karlsruhe Institute of Technology, Germany and the experiments were performed on the following days. In the time between arrival and experiments, the larvae were stored at 6 °C in a fridge in filtered natural seawater. At the beginning of each experimental day, the cyprids were allowed to slowly adapt to the ambient temperature for 60 min. After inoculation into the test containers convection effects occurred and cyprids were left for additional 5 min before the recording procedure was started. After experimentation, if settlement assays were required, cyprids remained in the containers, which were placed in an incubator, to guarantee stable temperature (28 °C) conditions and settlement was quantified after 24 h and 48 h via light microscopy.

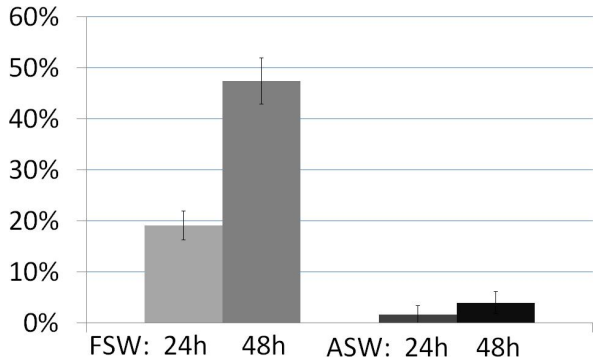

Figure 4.14.: Comparison of settlement in fresh and artificial seawater. The settlement [%] of *Balanus amphitrite* cyprids on polystyrene in filtered fresh seawater (FSW) proved to be considerably higher than in artificial seawater (ASW, Instant Ocean™).

Experiments were performed, unless stated otherwise, in filtered natural seawater (0.2 µm), provided from the University of Newcastle and stored at 6 °C prior to use. This was necessary, because as it can be seen in Figure 4.14, in the course of this thesis it was found that, the type of water strongly influences the settlement of cyprids on the attractive polystyrene control. The settlement after 48 h in filtered natural seawater was ≈50 %, whereas in artificial seawater it remained bellow 10 %.

4.5.2. Camera calibration

As mentioned in Chapter 2.6.3, for the accurate reconstruction of three dimensional trajectories out of two 2-D files the camera projection matrices need to be estimated. For this purpose, a camera calibration was performed after every adjustment of the setup. Briefly, the calibration procedure involved the imaging of a calibration object (as the one described in Chapter 4.2.2), the transformation of the video files, extraction of the PNG frames and definition of the (x, y) coordinates of at least 8 calibration point pairs in both camera frames. Once the two calibration files containing the 2-D coordinates of the points, as well as the file containing the coordinates of the calibration points in real space in 3-D had been generated, they were used as an input of the calibration graphical user interface (GUI) to start the calibration procedure as shown in Figure 4.16. The calibration GUI is depicted in Figure 4.15. After the coordinate

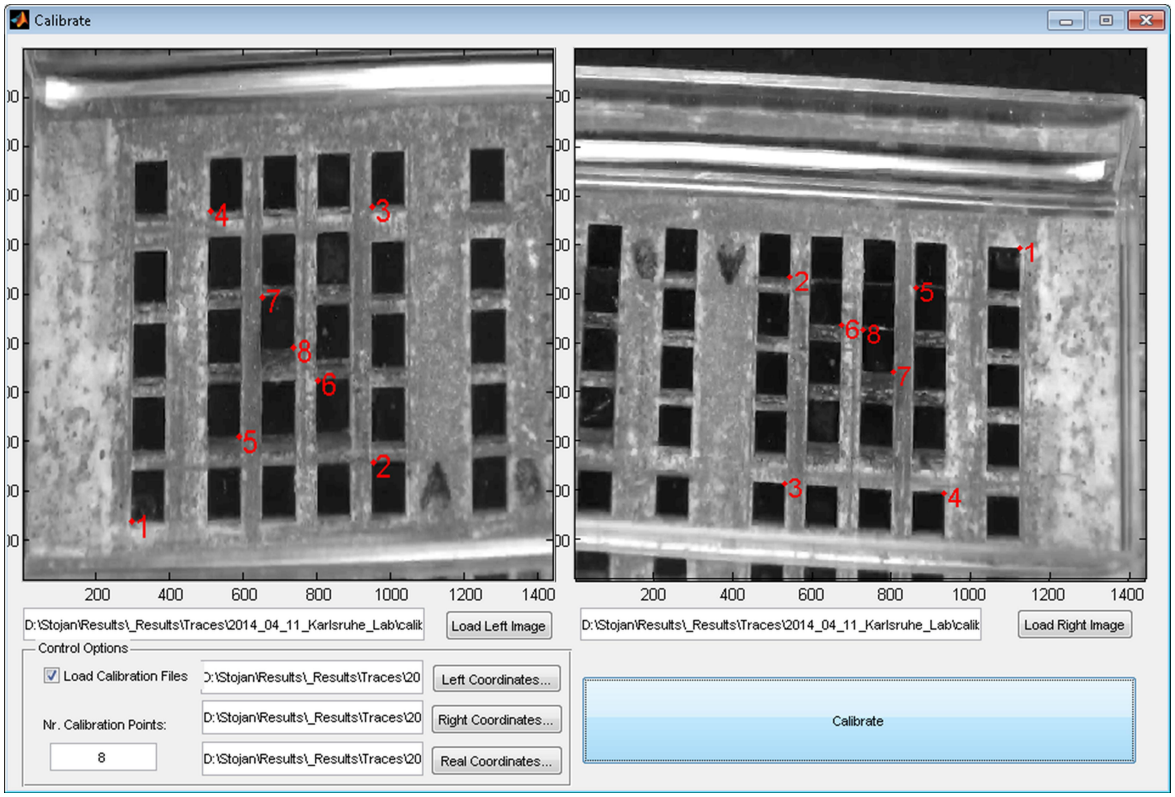

Figure 4.15.: Graphical user interface of the calibration software. This software, developed under MATLAB, was used for calculation of the camera projection matrices. As an input the script expects a file with the calibration points for each camera and a file containing the real space coordinates of the calibration points.

files have been loaded, the coordinates are loaded and marked in the GUI (8 numbered readings in red). As mentioned earlier, the minimal number of coordinate point pairs

needed for the calculation is 8, which can be increased, thus over-determining the system. In this case an enhancement algorithm is activated, which uses a least-squares method to optimize the output.

After the calibration has been performed, the software outputs both calibration matrices in a single m-file (MATLAB). Using the information contained in this file, any two 2-D trajectories originating from the same alignment of the setup, which was used during calibration, can be merged into a three dimensional trajectory, containing the coordinates in real space.

4.5.3. Video recording

After calibration the actual measurement followed. For this purpose, the container with the calibration object was carefully removed and a new chamber with the test surface was placed at its position. The horizontal alignment was controlled in the displays of the cameras to guarantee, that the whole portion of the compartment of interest was visible for both cameras. A horizontal misalignment of the measurement chamber (e.g. by placing it not at the same position as the calibration object) did not influence the measurement, since only an output with a relative (x, y) error was produced.

Once the container with the surface of interest was positioned, it was filled with filtered natural seawater (unless stated otherwise) using a Pasteur pipette. Based on the observations, the amount of water which proved to be advantageous for settlement and measurements was $\approx$10 ml. Then, 20-30 cyprids were taken out from the petri dish, in which they were stored before usage, and inoculated into the chamber. Additional 5 min were given to the larvae to adapt to the new environment and the convex effects in the water volume to settle. Finally, the recording was initiated through the synchronization device. Recording times differed for the different experiments, but for each replicate at least 10 min of video material was recorded.

A detail which needs to be mentioned at this point is, that even though the cameras were synchronized with an external synchronization device, they started to drift apart after 1h of continuous recording or operation. This desynchronization was indicated by blinking of the red LED of the LANC controller (see Figure 4.2). To avoid this problem, the cameras needed to be restarted, which, because of the new adjustment of zoom and focus, required a new calibration cycle. Calibration was also necessary, when the batteries of the cameras were exchanged, during longer experimental days (maximum capacity of the batteries was observed to be ca. 5 h, differing from the specification in the technical data sheet, which could probably be attributed to the fact, that the LANC controller operated also supplied by the batteries).

4.5.4. Settlement assays in quadriPERM culture vessels

To reveal the correlation between the results of the tracking with a specific settlement outcome, the cyprids were left in the containers after the recording of the exploration process. As a next step the chambers were placed in an incubator, where a stable temperature environment of 28 °C was adjusted. After 24 h and 48 h the containers were inspected under the microscope, in order to quantify the number of settled cyprids.

Usually, as described in Section 2.3.1, a droplet of seawater containing ca. 20 cyprids is pipetted onto a test surface and the number of settled cyprids is determined using microscopy. The advantage of the approach presented here is, that it reveals the direct correlation of the exploratory and settlement behavior, because for the estimation of these, the same physical samples were used. Of course, with this method the overall volume available for swimming and exploration, as well as the area of the water/liquid interface ([14]) become larger than the conventional droplet assay which makes a direct comparison with literature values (e.g. [10–13, 19, 72]) impossible, and only trends should be compared.

4.5.5. Post-processing pipeline

The post-processing pipeline contains the steps involved in the generation and visualization of the three-dimensional trajectories, starting at the time point where the two videos have been generated by the cameras. The process is shown schematically in Figure 4.16 (right side). After each experimental cycle, two video files were available - one from each camera. The output MTS (MPEG Transport System) videos were recorded in advanced video codec high definition (AVCHD) format containing a video (720p coded in AVC/H.264) and an audio stream (coded in AC3 format). The videos were converted into AVI format with the freely available software XMedia Recode (Author: Sebastian Dörfler, Source: www.xmedia-recode.de) in order to allow further processing with MATLAB (MathWorks, USA).

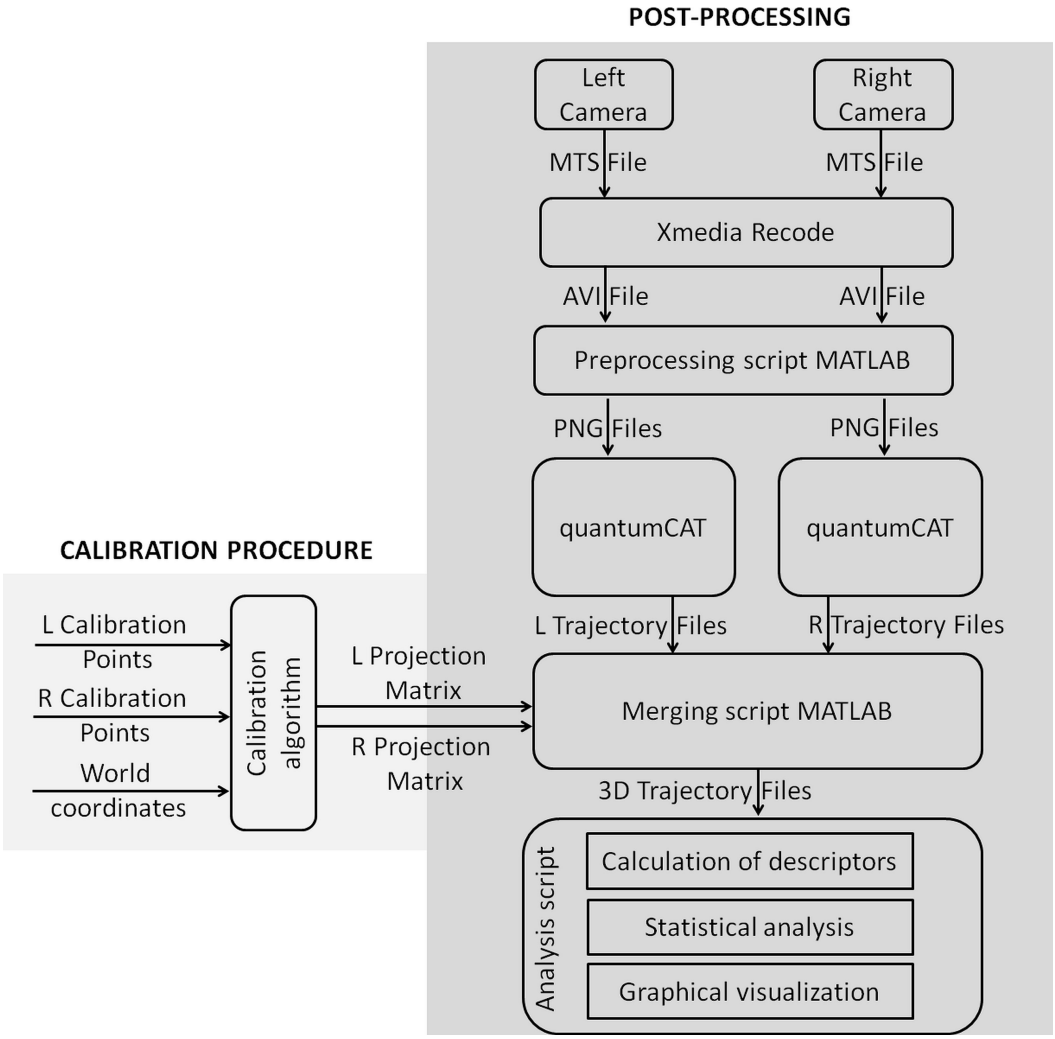

Figure 4.16.: The post-processing pipeline. The pipeline includes the processing steps from video acquisition to graphical visualization and quantitative analysis of the results.

As it can be seen from the figure, in the next step the AVI video files were processed with a self-developed MATLAB script which extracted each frame and saved it in a PNG format. Subsequently, for each of the videos a directory with PNG files representing the frames, was generated.
Using quantumCAT (Chapter 4.3) the objects of interest were tracked in both cameras separately, in order to generate two-dimensional trajectory files. In a next step, the files were merged into three-dimensional trajectories. For this purpose a self-coded MATLAB software was used, which combined two 2-D trajectories into a 3-D trajectory utilizing the projective matrices of the cameras (see Chapter 2.6.3). These matrices were obtained from the calibration procedure as described in Section 4.5.2. The three-

dimensional trajectories described the swimming of the cyprids in the containers and were used by the analysis algorithm to calculate different descriptors (swimming velocity, swimming depth, swimming angle, etc.). The analysis script provided functions for the statistical analysis and graphical representation of the data. Some newly defined parameters and descriptors to quantify the behavior of the cyprids are discussed in the following section.

4.6. Description and analysis of cyprid behavior

This section introduces some special data processing descriptors which were used for the analysis of the data and for quantification of the exploratory behavior of the cyprids.

4.6.1. Evaluation and description of data with box plots

Box plots are a graphical tool for the visualization of descriptive statistical parameters used for the quantification of a set of data [163]. A standard box plot is shown in Figure 4.17. From the figure it can be seen that the box represents the 1st (lower

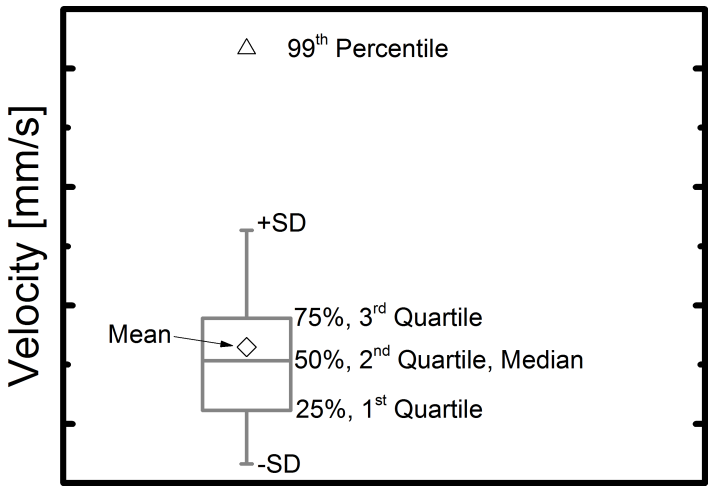

Figure 4.17.: Introduction to box plots. The box plot is a standard tool for visualization of descriptive statistical parameters in data sets. The horizontal lines of the box represent the 1st, 2nd (median) and 3rd quartile of the data. A △ is the 99th percentile. The ◇ is the mean value of the data set and the whiskers denote the standard deviation.

box margin), 2nd (middle line) and 3rd (upper margin) quartile of the data. The quartile can be expresses also as the 25th, 50th and 75th percentile. A **p**-th percentile originates from the cumulative distribution function [164] of the analyzed data set and

represents a value which is higher than **p** percent of all values in the data set. For example the 25th percentile (1st quartile) of the data set is a value below which 25 % of all data points are found. A special percentile is the 50th percentile (2nd quartile). This percentile is also referred to as the median and 50 % of the values in the data set are lower than this percentile and at the same time, 50 % are higher. It is marked by the middle horizontal line of the box in Figure 4.17. The 99th percentile represents the value which is higher than 99 % of all values in the data set and demonstrates the upper limit of the data distribution. In the Figure 4.17 it is marked by a $\triangle$. The arithmetic mean of the data, denoted by a $\diamond$ in the Figure 4.17, is calculated by

$$\bar{x} = \frac{\sum_{i=1}^{n} x_i}{n}, \tag{4.1}$$

with x_i being the values in the data set, n the size of the data set and $\sum$ is the summation operator. The standard deviation of the data set (whiskers in Figure 4.17) is calculated as

$$\sigma = \sqrt{\frac{\sum_{i=1}^{n} (x_i - \bar{x})^2}{n-1}}, \tag{4.2}$$

where x_i are the values of the data set, $\bar{x}$ is the mean value and n is the sample size.

4.6.2. Empirical cumulative distribution function for detection of swimming region borders

In statistics, the probability density function (pdf), describes mathematically the relative likelihood that a random test variable will exhibit a given value. A histogram represents the occurrence frequencies of classes of values (bins) of the test variable, obtained via observation (sampling). The accuracy of the histogram is influenced by the sample size (number of observations). Normalizing the discrete histogram (area under the curve equals 1) and selecting an infinite number of classes (bins) transforms it into a continuous pdf. The probability that the value of a random variable with a known pdf falls in a range of values is given by the integral of the density of the variable. Furthermore, a special function, the cumulative distribution function (cdf, F_{cdf}) describes the probability ($\mathbf{P}$) that the random variable (X) will exhibit values less than or equal a given threshold (χ) [165]

$$\mathrm{F}_{cdf} := \mathbf{P}(X \leq \chi). \tag{4.3}$$

The empirical cdf (ECDF) describes the integrated form of a discrete histogram rather than that of a continuous pdf. The ECDF was used in the course of this thesis to automatically detect the borders of vertical regions in the water column which exhibited a high concentration of cyprids. To perform this, first the histogram of the z positions of cyprids in the water column was calculated. Such histogram, which is

presented as a curve connecting the bar values of the distribution, is shown in Figure 4.18 (black curve). For low values of the z position (vicinity of the coated substratum, 0 mm-1 mm) and for high z positions (close to the water surface, 3.5 mm-4 mm), the probability to observe cyprids was strongly increased, whereas the occurrence values in between were much lower. Subsequently, the empirical cumulative distribution function of the histograms was calculated. The ECDFs visualized the accumulated occurrence (0 %-100 %) of z positions (integrated representation) within the data set. For the estimation of the ECDFs from the histograms the Equation 4.4 was used [164].

$$\mathrm{F}_{ECDF}[\chi] = 100 \cdot \frac{1}{n} \sum_{i=1}^{n} \mathbf{1}\{X_i \leq \chi\}, \text{where } \mathbf{1}\{X_i \leq \chi\} = \begin{cases} 1 \text{ if } X_i \leq \chi \\ 0 \text{ otherwise} \end{cases} \tag{4.4}$$

To determine the borders of the regions, the ECDF gradient was analyzed. In the case of the LSR, as soon as the ECDF reached a plateau (denoted by a red vertical line, Figure 4.18) and the absolute occurrence values of the histogram became lower than 5 % (depleted bulk region), the corresponding z position was defined as the border of the region. For the USR, the ECDF was analyzed from higher to lower values, and as soon as the plateau (Figure 4.18, green vertical line) was reached and occurrences were lower than 5 %, the z value was used for a lower border of the USR.

4.6.3. Swimming area coefficient

The fraction of the area (swimming area, SA) visited by a cyprid within the field of view during measurement either by swimming or by close surface inspection is described by the coefficient C_{SA} (swimming area coefficient) as shown in Equation 4.5.

$$C_{SA} = \frac{N_{Pixels}}{N_{Datapoints}} \tag{4.5}$$

To calculate this coefficient, the trajectories were mapped on a 2-D plane and the number of pixels used to visualize the motion (N_{Pixels}) was related to the total number of points in the data set ($N_{Datapoints}$). Since 2-D visualization was applied, overlapping positions were represented with the same pixel. C_{SA} can vary between 0 and 1. Very localized motions including a more convoluted swimming path would lead to small C_{SA} values (close to 0) and extended motions without overlapping points and more straight swimming paths would result in C_{SA} values close to 1. The swimming area coefficient describes all motions, including close surface inspections and swimming in the water column as well as close to the surface. An example with two different surfaces, where cyprids swam in a different manner is shown in Figure 4.19. In Figure 4.19a the observed trajectories were straighter with less overlapping regions, which led to a higher swimming area coefficient ($C_{SA} = 0.72$). On the contrary, the movements in Figure 4.19b were more convoluted and a high amount of data points overlapped, indicating a more focused swimming area, which resulted in a lower value of the swimming area coefficient ($C_{SA} = 0.41$).

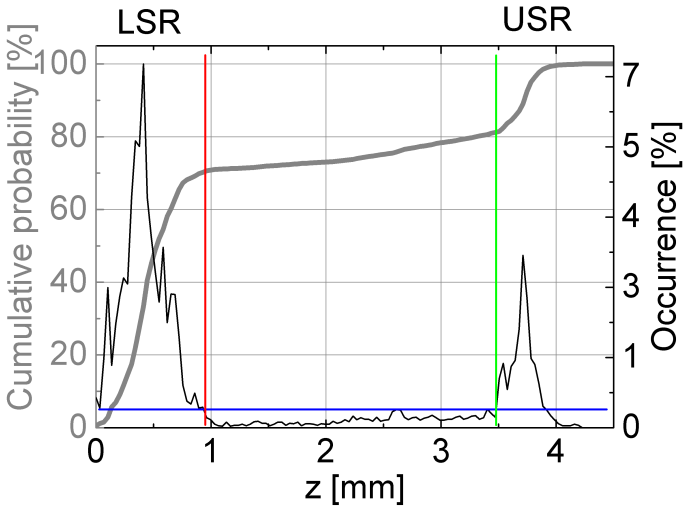

Figure 4.18.: Estimation of the swimming region borders. A histogram of the z position of cyprids is presented as a black curve. The corresponding ECDF function is depicted in gray and the two borders of the LSR and USR are marked with a red and a green line respectively. As soon as the values of the histogram decreased under a given value (5 %) and the plateau of the ECDF was reached, the border of the corresponding swimming region was defined. The blue horizontal line marks the threshold for values of the histogram which were considered too small to belong to the corresponding region (5 %).

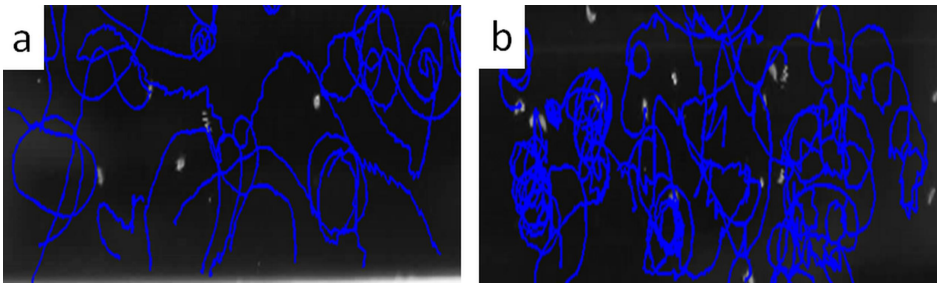

Figure 4.19.: Swimming area coefficient. Example of two types of swimming behaviors of cyprids on different surfaces with (a) more straight and (b) more convoluted swimming paths.

4.6.4. Transition frequency between swimming regions

As it is going to be discussed in the main part of the thesis, cyprids were proven to accumulate in several distinct swimming regions in z direction above the test surface (see Chapter 5.1). The transition frequency expressed the number of transitions between the different regions per unit time in relation to the availability of cyprids in

the region. It can be described mathematically with Equation 4.6.

$$f_{Trans}[\frac{Transitions}{min}] = \frac{N_{Trans} \cdot 60}{t_{obs} \cdot N_{Cyprids}} = \frac{N_{Trans} \cdot 60}{t_{obs} \cdot \frac{\sum t_N}{t_{obs}}} = \frac{N_{Trans} \cdot 60}{\sum \frac{N_{Datapoints}}{f_{Video}}} \tag{4.6}$$

The transition frequency f_{Trans} into or out of a given swimming region was calculated by estimating the number of transitions (N_{Trans}) and dividing them by the product of the observation time (t_{obs}) and the mean number of cyprids present in the field of view ($N_{Cyprids}$). As shown in Equation 4.6, this equals the number of transitions divided by the sum of obtained data points in a single frame ($N_{Datapoints}$) divided by the acquisition frequency of the video (f_{Video}). The minimal value for the transition frequency is 0 transitions$\times$min^{-1} and reflects the situation where cyprids neither leave nor enter the analyzed volume. High values reflect a high probability for a cyprid entering or leaving the region. It is important to point out, that this is a pure frequency parameter, which describes the transitions per minute and cyprid. Due to the normalization to the number of cyprids, the parameter has little sensitivity to the total number of transitions. E.g. if transitions are seldom observed out of the region close to the surface, but cyprids spent only little time in that region, the frequency value will be still high, because the time component is in the denominator. On the contrary, if cyprids spent a long time in this region with few transitions, a very low transition frequency would be obtained.

4.6.5. Occurrence value of cyprids in the swimming regions

Another identifier used in the analysis was the occurrence value. Here, a test variable, e.g. the distance to the surface (swimming depth), was analyzed by calculating the probability to find the cyprids in a certain region. This value was proportional to the duration of the time cyprids spent swimming in this particular region. This probability was calculated from the histogram by integrating the relative occurrence (normalized histogram) between the upper boundary of the range and the lower boundary of the range:

$$OV[\%] = \frac{\sum_{n=rlb}^{n\leq rub} Counts(n)}{\sum_{n=mih}^{n\leq mah} Counts(n)} \cdot 100 \tag{4.7}$$

with rub $\equiv$ range upper boundary, rlb $\equiv$ range lower boundary (Figure 4.20 in blue), mah $\equiv$ max value of the test variable in the histogram, mih $\equiv$ min value of the test variable in the histogram (in red in Figure 4.20), Occurrence $\equiv$ the histogram value at the specific position and n $\equiv$ index variable.

4.6.6. Calculation of the body density of cyprids

For the calculation of the body density of cyprids using their sedimentation or sinking velocity, a modified form of the Stoke's equation was applied as described by Komar

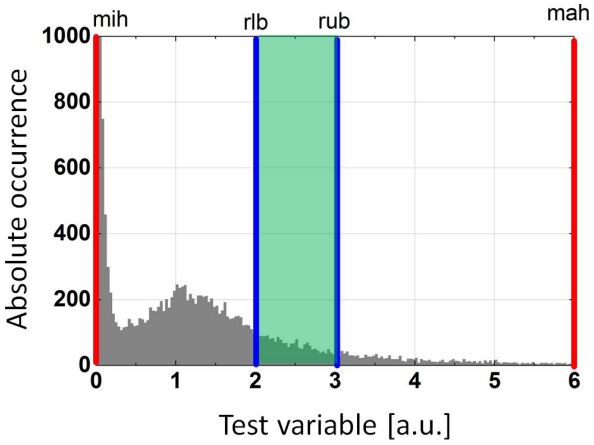

Figure 4.20.: Calculation of the occurrence value. An exemplary histogram of a test variable, demonstrating the meaning of the parameters in the occurrence value equation (Equation 4.7)

et al. [166]. The modification is necessary as the Stokes law strictly applies only to spherical objects. The authors could prove that objects with shapes that deviate from spheres showed different sinking speeds. Komar et al. have derived semi-empirical equations which apply to ellipsoidal and cylindrical particles. For the calculations in this thesis it was assumed that the body of cyprids has an ellipsoidal shape. In this case, the equation for calculating the sinking velocity w_s (also settling rate) of cyprids is

$$w_s = \frac{1}{18} \cdot \frac{1}{\mu} \cdot (\rho_{cyprid} - \rho_{fluid}) \cdot g \cdot D_n^2 \cdot E^{0.380}. \tag{4.8}$$

Re-writing Equation 4.8 in order to calculate the density of cyprids it becomes

$$\rho_{cyprid} = \frac{18 \cdot \mu \cdot w_s}{g \cdot D_n^2 \cdot E^{0.380}} + \rho_{fluid} \tag{4.9}$$

with E being the "measure of shape" of the cyprid [167], defined as

$$E = D_s \cdot \left[\frac{D_s^2 + D_i^2 + D_l^2}{3} \right]^{-\frac{1}{2}}, \tag{4.10}$$

D_n denoting the nominal diameter of the cyprid (the diameter of a sphere having the same volume and weight as the non-spherical cyprid). D_l, D_i and D_s are the dimensions of the cyprid (longest, intermediate, and smallest axial diameters of the ellipsoid [166]), μ the viscosity of seawater (1.085 g/ms), ρ_{fluid} the density of seawater (1.028×10^6 g/m^3) for the experimental conditions (temperature of seawater ≈20 °C and salinity 39‰) and g - the gravitational acceleration (9.81 m/s^2).

4.7. Statistical analysis

Trends in the obtained results, observed throughout the thesis, were analyzed in order to reveal their statistical significance. For example, to statistically determine how significantly different two groups of data representing the same variable were (e.g. settlement on different surfaces, velocity on different surfaces, etc.) a Students t-test was used as described in [168]. Because the values included in the comparison originated from data sets with the same size and the distributions of the values had similar variance, a two-sided t-test was applied. As established in literature, a p-value of $p \leq 0.001$ indicated a highly significant difference, $p \leq 0.05$ was considered to indicate a significant difference and $p > 0.05$ marked not significantly different groups.

5. Exploratory behavior of *Balanus amphitrite* cyprids

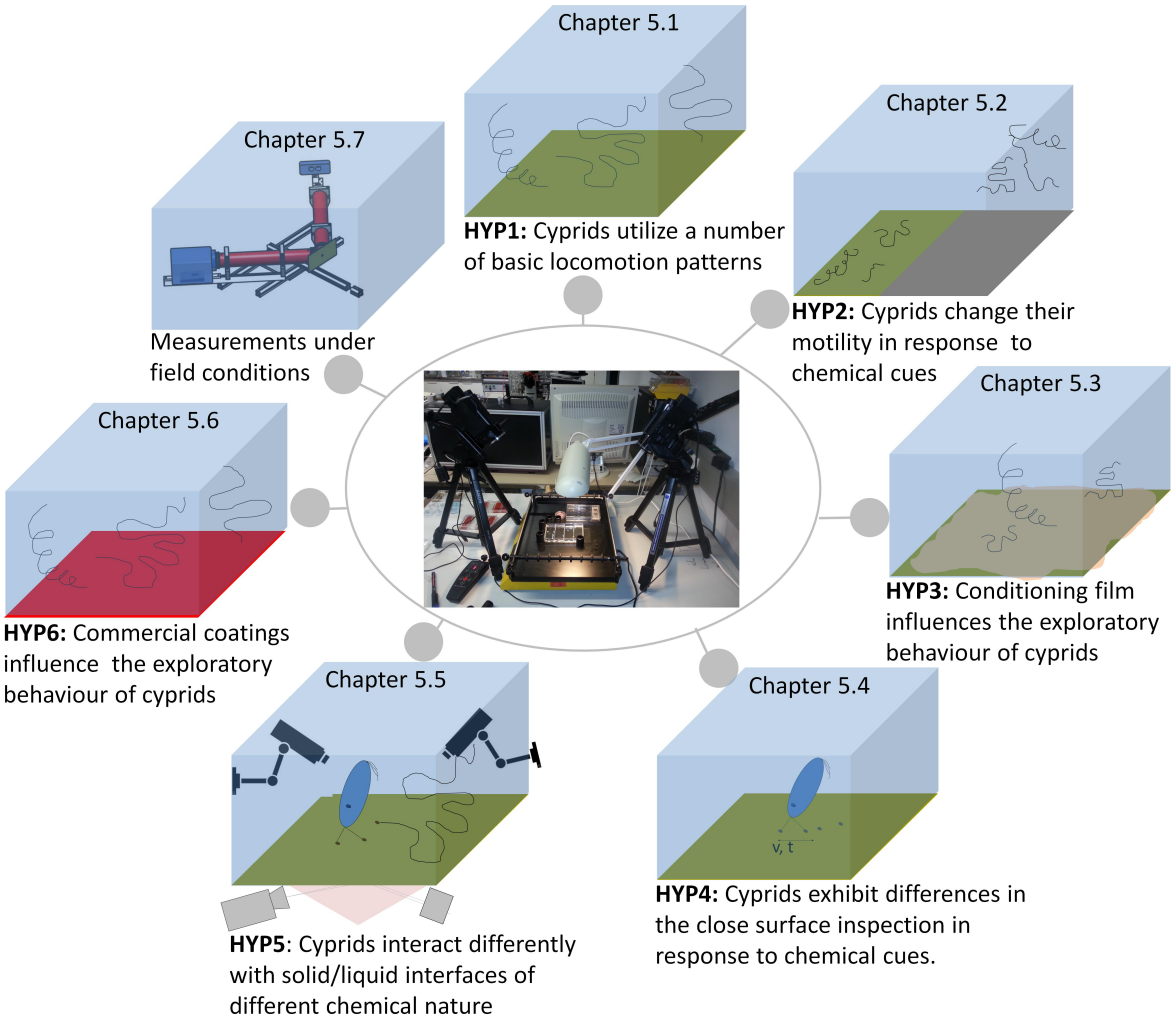

Figure 5.1.: Overview of the main working hypotheses. Each research aspect, investigated in the course of this thesis, is denoted by a sketch, a summary of the hypothesis and a reference chapter in which the discussion details can be found.

An overview of the main research directions of the thesis is shown in Figure 5.1.

The first chapters investigate the exploratory behavior of barnacle cyprids on model surfaces (SAMs) under laboratory conditions. Since behavior is directly projected onto the way of locomotion, Chapter 5.1 discusses the identification and quantification of the basic locomotion patterns which occur in the swimming trajectories. In addition to the general knowledge on these patterns, a novel 'macroscopic' analysis on the exploratory behavior is presented in Chapter 5.2 and it is demonstrated that settlement preferences can be indicated already in the pre-settlement stage by several motility parameters. To further quantify the motions during this stage, events in close proximity to the substratum are investigated and the question how surface chemistry influences the close surface inspection is discussed in Chapter 5.3. Subsequently, a novel setup for the quantification of the cyprid-interface interactions is presented in Chapter 5.4.
The remaining chapters deal with the exploratory behavior in real-life situations. For this purpose, first the influence of conditioning films on the motility parameters is analyzed (Chapter 5.5). Then, the locomotion of the larvae is investigated on commercially available foul-release (FR) coatings rather than model surfaces (Chapter 5.6). Finally, in Chapter 5.7, a modification of the laboratory setup is presented allowing the recording and extraction of three-dimensional trajectories of marine biofouling and planktonic organisms under water - *in situ*.

5.1. General description of cyprid locomotion

In this chapter swimming trajectories of barnacle cyprids of *Balanus amphitrite* exploring surfaces are analyzed. The basic reocurring patterns are quantified and their distribution in the data set as well as their transitions are discussed in order to answer the question whether any sequential order exists between patterns during locomotion. Finally, a detailed look is provided on one special form of locomotion - *sinking*. The quantitative information contained in the pattern is utilized to calculate the body density of the cyprids, a parameter which is normally difficult to obtain, because of methodological challenges involved in quantification of the body weight. Finally, the changes in the sinking velocity are analyzed for cyprids of different ages and dead ones, in order to indirectly investigate how body density values shift with cyprid age.

5.1.1. Basic locomotion patterns

Figure 5.2 shows the basic locomotion patterns which were observed in a data set of ca. 300 trajectories. The differentiation and identification of the patterns was done by visual analysis of the trajectories and manual segmentation, where a new pattern was defined and assigned to every uniquely observed shape in the set. This procedure led to the definition of two main categories and patterns were assigned to a category based on their position in relation to the substrate surface. Thus, in the first group, denoting patterns used for general locomotion and occasional surface

contacts, *spiraling*, *swimming* and *sinking* (Figure 5.2a, b, c) were included. *Swimming*

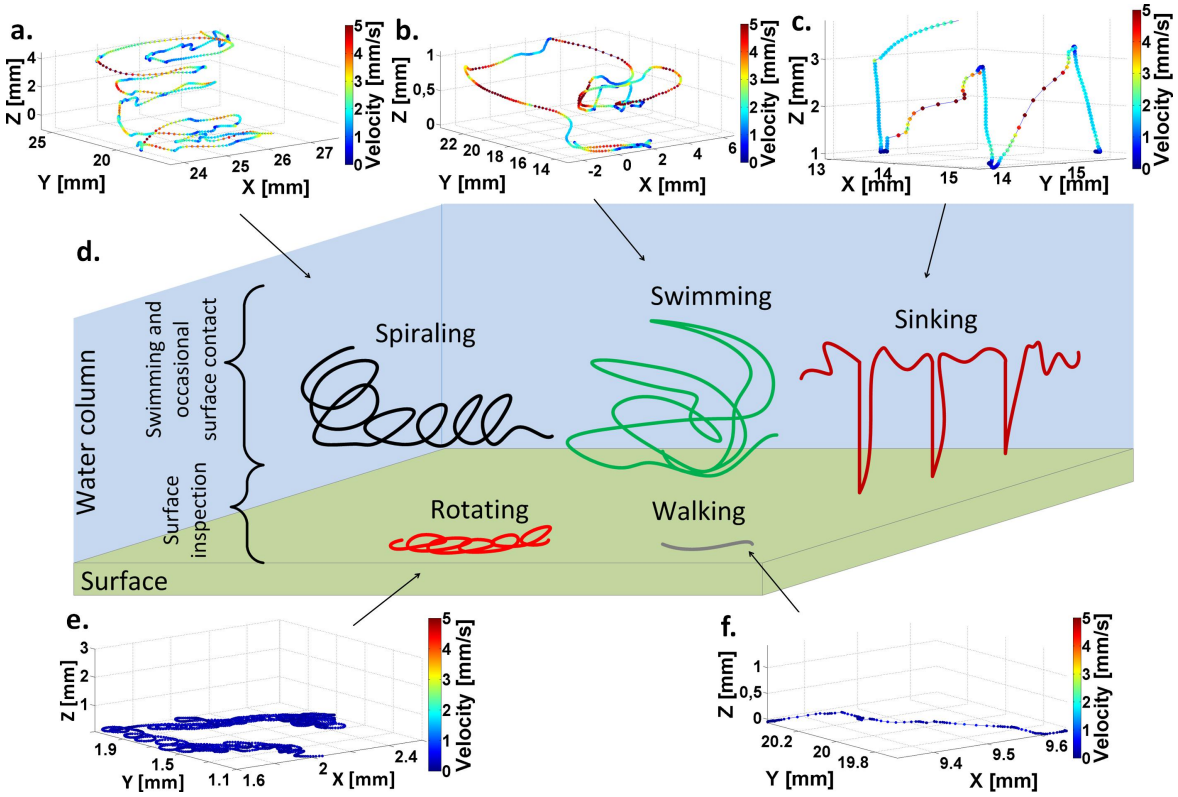

Figure 5.2.: The main motion patterns of cyprids of *B. amphitrite*. (d) Overview of the patterns observed for cyprids, active during recording. Furthermore, examples are shown for (a) spiraling, (b) swimming, (c) sinking, (e) rotating (special form of spiraling) and (f) walking.

(Figure 5.2b) was the most frequently observed pattern, deployed for moving across the water volume over wider distances. It included smooth movements with portions of fast unidirectional locomotion or slower turns and the velocities fell in a broad range. *Swimming* occurred as soon as the thoracopods of the cyprid started beating in the specific 'burst-like' mode, thus functioning as a motor for the movement. At the same time, one antennule was maximally extended by the larvae, probably involved in determining the swimming direction [53].
A special form of the *swimming* pattern, which included pseudo-helical movements, was *spiraling* (Figure 5.2a). It also occurred in the water volume and the axis of helical rotation was found to change rapidly causing an alternation of the swimming direction. Similar to *swimming*, also *spiraling* was driven by the 'burst-like' beating of the thoracopods. In contrast to *swimming*, the rotation moment in *spiraling* occurred probably due to a changed center of mass of the cyprid body, caused by an extension of the antennule outwards.

Because of the metachronous nature [53] of the beating of the thoracopods, the larva started to sink in the water column during the periods when no beating was active, driven by gravity. This movement was termed *sinking* and although it seemed to have a passive character, it was often observed. Furthermore, according to the observations, it was the main pattern leading to a contact with the horizontally positioned substrates.

In the second group of patterns, locomotion in close proximity to the surface was included. The corresponding patterns were referred to as *rotating* and *walking* (Figure 5.2e, f). There have been earlier reports on these patterns, e.g. by Lagersson et al. [53], who have termed the close surface inspection of cyprids "wide search" and "close search", as discussed in Section 2.2.3. Because the resolution of the setup applied in the experiments, described in this thesis, did not allow a 'microscopic' observations, i.e. single steps were not resolved, all movements exhibiting a low velocity profile and high linearity (cyprids moving in a straight-line manner) were classified as *walking*. *Walking* was, thus, generally analogous to both patterns "wide search" and "close search" identified by Lagersson et al. [53]. The pattern *rotating* was perceived as a special form of *spiraling*, which extended to the liquid/solid interface and involved circular movements at intermediate velocities.

Figure 5.3 shows the histograms of the velocities of the four active patterns (*swimming*, *spiraling*, *walking* and *rotating*). Interestingly, all histograms showed a pronounced peak at velocities of 0 mm/s. These values originated from periods of inactivity during locomotion and apparently such phases were present to different extents for all of the patterns. In the water column representatives, the amplitude of the peak was below 10 % for *swimming* and ca. 15 % for *spiraling*. Histograms of the surface patterns showed in turn, a higher occurrence of velocities close to 0 mm/s (30 % for *walking* and 20 % for *rotating*, Figure 5.3c, d). Furthermore, it became obvious that the width of the distributions differed. In order to better quantify this parameter, the box plots of the histograms are shown in Figure 5.4a. To allow a more clear representation of the velocities higher than 0 mm/s, the strong peak at 0 mm/s was removed from the distributions. The resulting histograms are visualized in Figure 5.4b. From Figure 5.4a it can be seen that the values of the 99th percentile, or the upper limit of the distributions, were different for the water column and surface patterns. For *swimming* and *spiraling* these lay at ca. 7 mm/s and ca. 5 mm/s respectively, indicating the highly active type of locomotion used to move across the water volume. On the contrary, *walking* velocities reached only around 1.5 mm/s and the *rotating* values were ca. 2.5 mm/s. Furthermore, during *walking* cyprids seemed to exhibit a nearly constant velocity, which became obvious from the low height of the corresponding box plot. In contrast, during *swimming* the velocity values were in a broader range, indicating more changes, reflected also in the higher box plot of this pattern. The *swimming* pattern also possessed the highest standard deviation, confirming the different velocity magnitudes present during locomotion across the water volume. The occurrence of resting phases in combination with lower velocities was typical for motions close to the surface and seemed to confirm the previously described inspective nature of these

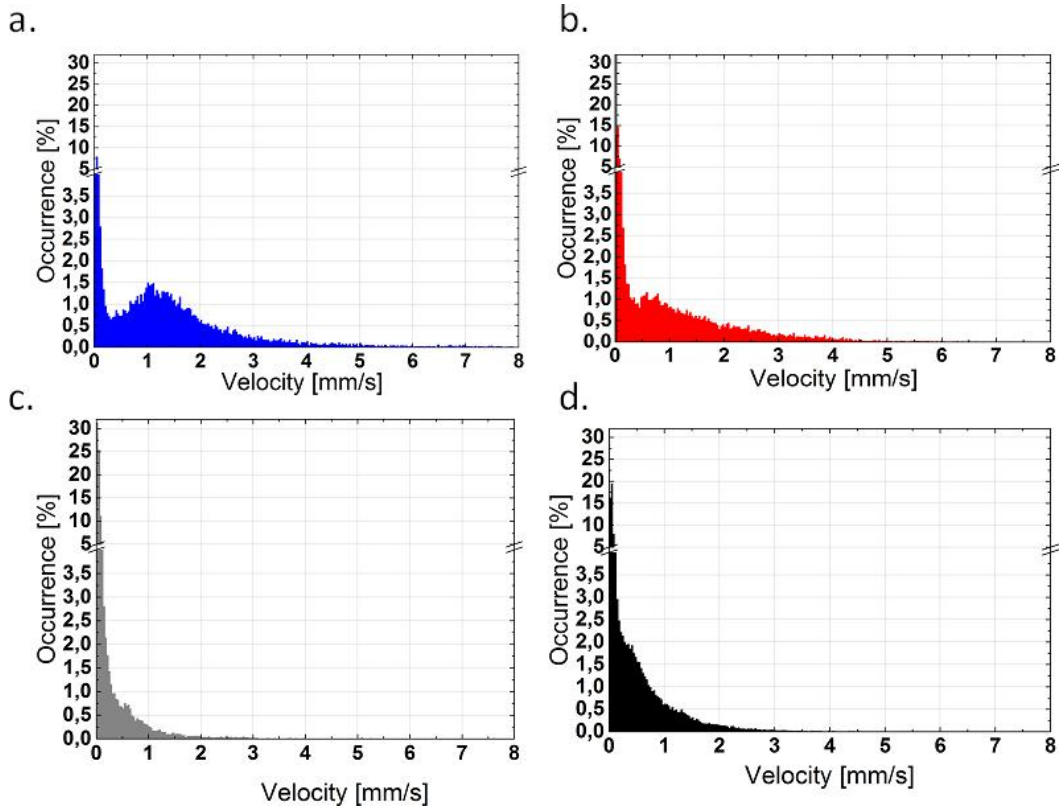

Figure 5.3.: Velocity histograms of different locomotion patterns. The distributions are provided for (a) swimming, (b) spiraling, (c) walking and (d) rotating. Note the two different scales on the y-axis, in order to visualize all trends present in the histograms.

patterns.

Additionally, the linearity of the patterns was investigated. The term described how directed was the spatial displacement of cyprids moving in a given locomotion pattern. The linearity of a single segment of a trajectory was calculated as the quotient of the absolute displacement of the cyprid in space during this segment (straight line connecting coordinates of the cyprid at the start and endpoint of the segment) and the actual covered swimming distance (see Figure 5.5a). Thus, a low linearity marked a locomotion pattern involving a convoluted path and a limited effective spatial displacement of the cyprid. On the contrary, a high linearity value was characteristic for locomotion patterns involving a directed and linear way of locomotion. A linearity of 1 described a straight line path. The linearity values for the locomotion patterns *rotating*, *spiraling*, *swimming* and *walking* are presented in Figure 5.5b. These values were obtained from the analysis of representative parts of trajectories, containing only the investigated locomotion patterns. Each of the selected exemplary trajectories contained a minimal duration of 30 s and it was divided into 20 segments, for which

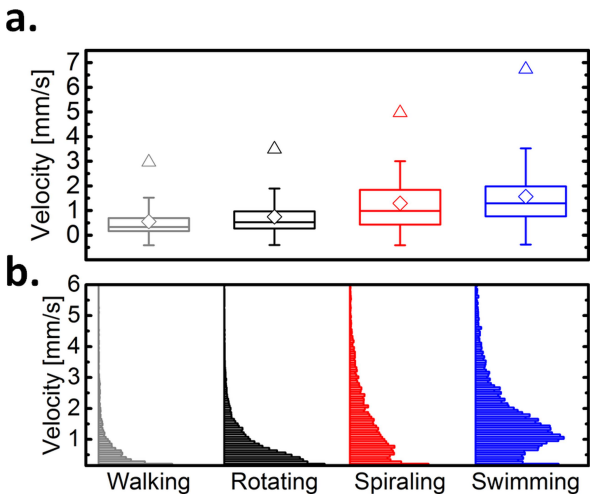

Figure 5.4.: Statistical description of the velocity distributions. (a) Box plot diagrams of the velocity values of the patterns. ◇ shows the mean velocity. The box plots give the 1st (lower box margin), 2nd (middle line; median), 3rd (upper box margin) and 99th (the △ symbol) quartile of the data. The whiskers represent the standard deviation. (b) The histograms of the velocity, excluding values close to 0 mm/s.

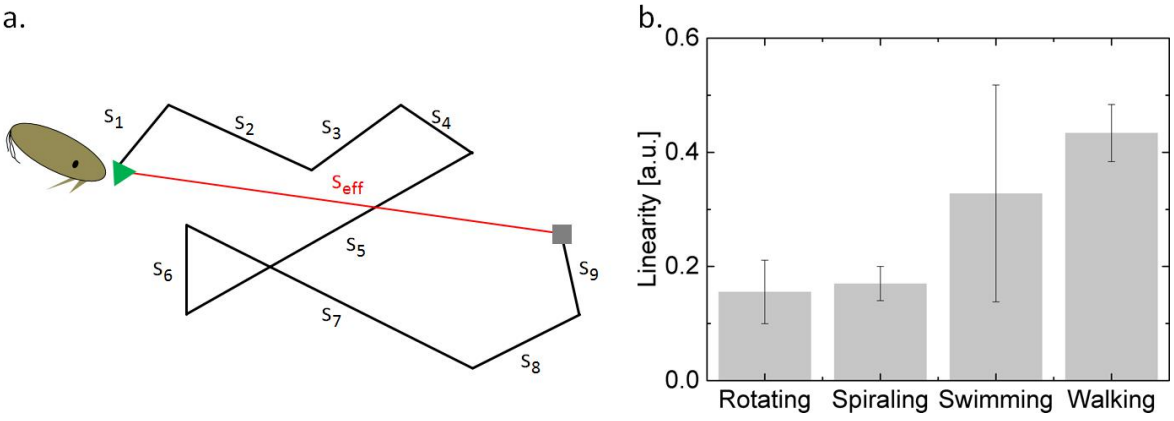

Figure 5.5.: Linearity analysis of the patterns. (a) Schematic representation of the linearity of a given trajectory segment. The start and endpoint of the segment are marked by a green triangle and a gray rectangle respectively. The linearity is the quotient of the displacement of the cyprid in space (s_{eff}) and the actual path (sum of the partial path vectors s_1 ... s_9). (b) Values for the linearity parameter for exemplary trajectories describing the locomotion patterns - *rotating*, *spiraling*, *swimming*, *walking*. Error bars represent the standard deviation of the linearity of a single pattern over the segments in the trajectory.

the linearity was calculated. Thus, each segment had a length of 1.5 s, which, at the frame rate of 25 fps equaled to 37 consecutive data points. The patterns with low linearity were *rotating* (0.15±0.06) and *spiraling* (0.17±0.03). This can be explained by the fact, that these patterns exhibited mainly circular and helical movements, which involved a high covered swimming distance with a limited actual displacement of the cyprid in space. On the contrary, high linearity was observed for the *walking* pattern (0.43±0.05). During *walking* cyprids moved on the substrate in a bipedal manner and tested it for permanent settlement, with directed and linear movements. Interestingly, the linearity of *swimming* was shown to be high as well, probably because the pattern was used mainly for locomotion across the water column and cyprids did not concentrate on a certain spot in a limited spatial area. The high variance of the linearity value for the *swimming* pattern in the different segments of the representative trajectory, expressed by the error bar in Figure 5.5b, could be attributed to the fact that this pattern involved parts with directed and linear as well as more convoluted swimming.

5.1.2. Distribution and transition of locomotion patterns

In order to quantify how often a pattern occurred in the data set, the distribution of the patterns was analyzed. For this purpose, the trajectories were manually segmented and the occurrence of each of the patterns, shown in Figure 5.6, was counted. Since for the occurrence analysis the trajectories were used, only cyprids which were active during the observation period were considered. Therefore, the *resting* pattern described only the inactive parts of these trajectories and did not provide a general quantification value of cyprids which remained inactive throughout the whole recording time. In the data set, the *swimming* pattern was most frequently observed occurring around 1/3rd of the time (31 %) and allowing cyprids to freely explore a broad perimeter and to move across the water volume. Since the cyprids used in the experiments were 3-4 days old during recording, it was not surprising that such a high value was observed for this pattern representing the motility in the water volume. As expected, the counterpart of *swimming*, *sinking*, demonstrated also a high absolute occurrence (26 %). As stated earlier, these values were interconnected because of the biomechanical process involved in swimming leading to a periodic sequential order of active swimming and sinking phases (see Section 2.2.3). Generally, it could be observed that the passive patterns, *resting* and *sinking*, amounted to 41 % of all patterns, which suggested that motion of cyprids was frequently interrupted by stops. At the same time, the occurrence values for the active patterns (*swimming*, *spiraling*, *walking* and *rotating*) were slightly higher (59 %). The overall occurrence of the surface patterns remained below 17 %, of which *rotating* (4 %) was less frequently observed compared to *walking* (13 %). As shown in Figure 5.6, the behavior was dominated by patterns in the water column (68 %). Although not further quantified, we noted a general trend that older cyprids (8 days or more) tended to exhibit more surface patterns. This trend is in a good agreement with the "desperate larvae theory" which states that older non-feeding larvae tend to

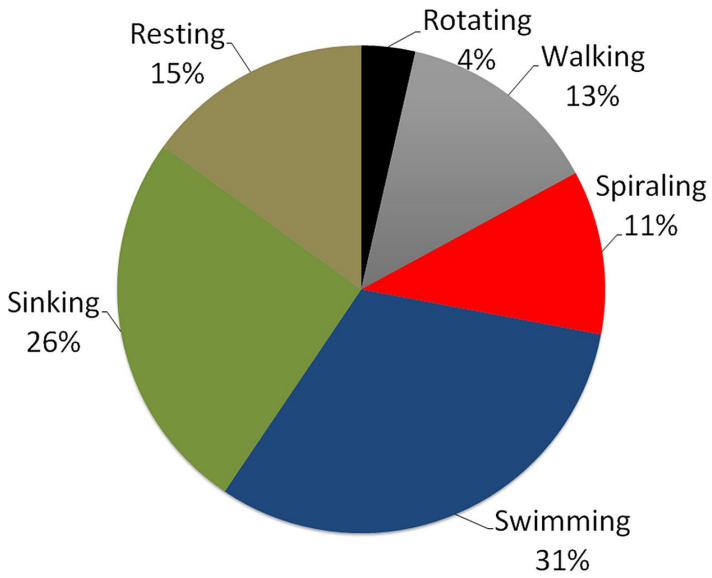

Figure 5.6.: Occurrence of the patterns in the data set. The occurrence values were obtained, by manual analysis of the number of occurrences of each pattern in the data set.

decrease selectivity on settlement site, as discussed by Elkin et al. [16]. It is worth mentioning that *spiraling* occurred only during 11 % of the time. Beside the active motions, *sinking* was an important component during motion involving vertical (in this setup alignment) movements with a relatively constant and low speed as shown in Figure 5.2c. The sinking phases were followed by active *swimming*, enabling the cyprid to gain its original swimming depth, followed by a new sinking period. This constant alternation agrees with previous investigations which discussed, that it is an energy efficient way of locomotion under wavy conditions [24, 169, 170].

The distribution of the locomotion patterns was a consequence of an active selection of the current pattern by the larvae, rather than the result of a random process. In order to gain a better insight on the possible transitions between patterns and their sequential order, a qualitative analysis was performed and the results are shown in Figure 5.7. Each of the five locomotion patterns is shown in the figure in a different color. A self-reference arrow stands for the probability that the pattern observed at time point $t_0 = N$ will be still observable at time point $t_1 = (N+1)$. 'Surface contact' was a pseudo-pattern, which was used to represent the moment of the arrival of the cyprids at the chemical interface. Based on the observations, the main pattern in the water column, *swimming* (Figure 5.7 in blue), was followed frequently by a *sinking* or a *spiraling* pattern. Interestingly, the *swimming* pattern itself seldom led directly to surface contacts, which supports the statement that it was mainly used for locomotion across the water volume and during which, less particular interest in the nature of the test surface was exhibited. *Spiraling* (Figure 5.7 in red) proved to mainly transform

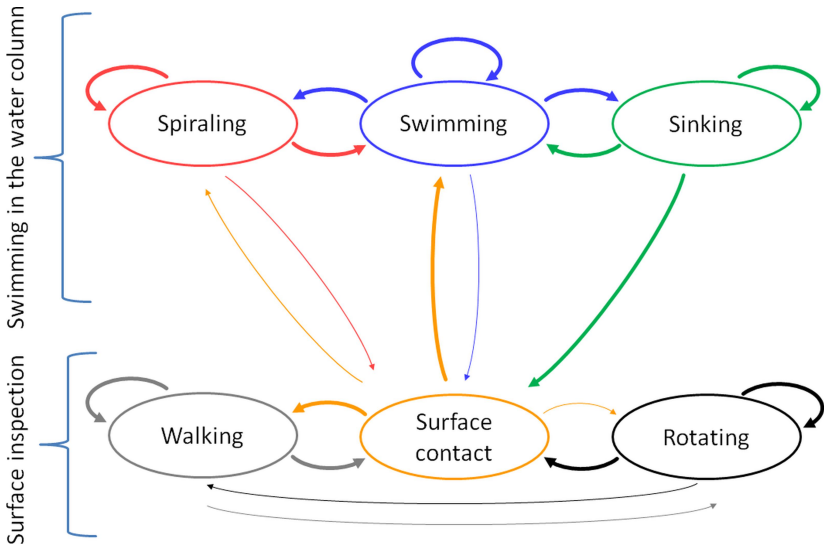

Figure 5.7.: Qualitative representation of the possible transitions between the locomotion patterns. The arrows mark the possible transitions out of a given pattern, a thick line denotes a high probability and a thin line represents a low probability for the transition to be observed.

into *swimming* and again less freuqently random surface contacts were observed. Most of the contacts with the horizontal surface originated from a *sinking* motion (Figure 5.7 in green). This pattern demonstrated an equally probable transition back to *swimming*. Once on the surface, cyprids often remained there *resting* which was reflected in the high occurrence value of this pattern in the data set (15 % as shown in Figure 5.6). *Resting* is not depicted in Figure 5.7 because potentially all of the locomotion patterns were observed to originate from *resting*. If the cyprids remained on the surface, they preferred the *walking* pattern, which also contributed to its highest occurrence among the surficial patterns (13 % in Figure 5.6). It was probably the pattern which cyprids used during inspection of the surface and evaluation of its properties for permanent settlement. *Rotating* was rarely observed except on hydrophilic ethylene glycols (EGs). Both *rotating* and *walking* seldom switched between each other and cyprids preferred to rather switch back into *swimming*.

5.1.3. Quantification of sinking velocity

As discussed in the previous section, *sinking* was a frequently observed pattern in the locomotion of cyprids (26 % of time as seen in Figure 5.6). Figure 5.8a shows a representative three-dimensional trajectory which includes several sinking phases followed by active swimming. During these vertical movements (one typical sinking phase is highlighted by the black circle), it changed its swimming depth from ca. 3 mm above the surface to below 1 mm. This short phase occurred at low velocities of only

≈1.6 mm/s (indicated by the blue color). After the sinking, the cyprid accelerated and

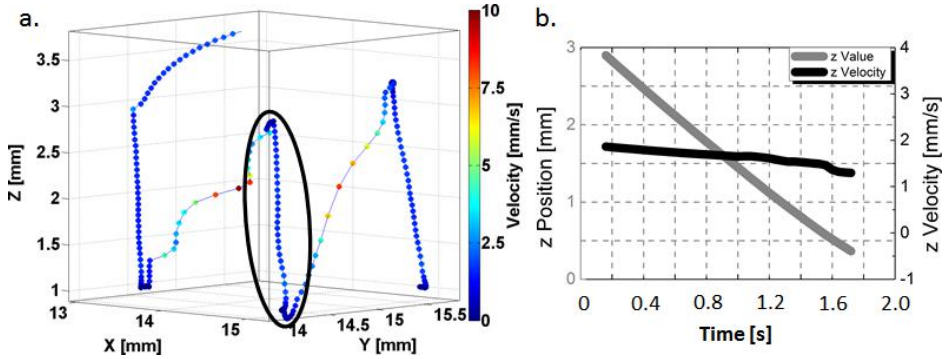

Figure 5.8.: Analysis of the sinking velocity of an exemplary trajectory. The typical swim-sink switching can be observed in the (a) trajectory including three sinking phases (black marks the segment selected for quantification). The changes of (b) the z position (gray) and z velocity (black) during the sinking phase of the selected sinking phase are shown.

returned at a velocity of ≈7.8 mm/s to its initial swimming depth. Subsequently, a new sinking period was initiated. It is worth mentioning that at the end of the sinking, the cyprid seemed to actively counteract it and reduced its speed before accelerating again and swimming upwards. Figure 5.8b shows the change in z position (grey) and the corresponding velocity (black) during a sinking phase with a total duration of ca. 2 s (labeled by a black circle in Figure 5.8a). To better quantify the sinking velocity, 28 swimming trajectory parts containing sinking phases were manually segmented. The condition which a pattern needed to fulfill in order to be considered a sinking pattern, was that at least for 15 sequential frames the change in the x and y direction was low and at the same time the change in z direction was negative. Figure 5.9a shows the sinking parts, and it can be seen that the cyprids decreased their swimming depth at low velocities (indicated by the blue color) while moving in vertical direction. The direction of these patterns was always the same, starting at a higher distance to the substratum and moving towards the liquid/solid interface and no locomotion in the xy plane was detected. Figure 5.9b shows the histogram of the velocity in z direction, which was fit using a Gaussian distribution function. The mean sinking velocity was −1.11 mm/s with a standard deviation of 0.39 mm/s. It can be seen that the sinking velocity identified in Figure 5.8 lies in the region given by the Gaussian curve.

5.1.4. Empirical estimation of the body density of cyprids

Beyond characterizing the sinking motion, the information contained in the trajectories could be further utilized to extract physical properties of the barnacle cyprids. One value which could be obtained by applying a modified version of Stokes law (described

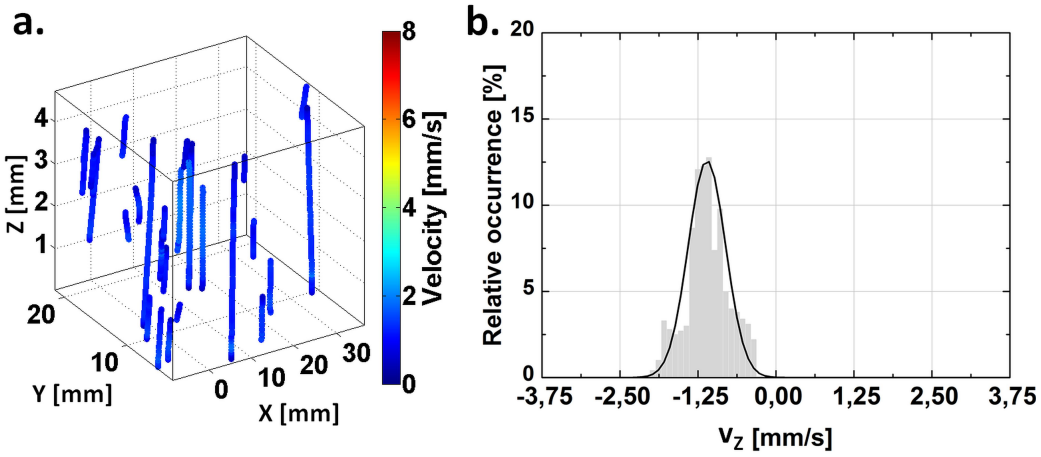

Figure 5.9.: Quantification of the sinking velocity. In order to define parameters to describe the sinking velocity, (a) 28 sinking phases of manually-segmented trajectories were used. The values were analyzed based on (b) a histogram of the velocity in z fit using a Gaussian distribution function (μ=−1.11 mm/s, σ^2=0.39 mm/s), which was used as a 'model' distribution for sinking velocity.

in Chapter 4.6.6) is the body density. Due to the fact that the motion during the sinking phase contained almost no x and y components, and barely body motions of the cyprid, it could be anticipated, that this motion was only determined by the gravitational force and the counteracting hydrodynamic Stokes force. For this approach, a detailed analysis of the velocity of active 3-day old cyprids was performed and the histogram of the z component of the velocity vector is presented in Figure 5.10. As it can be seen from the histogram there was an enhanced occurrence of v_Z values close to −1.25 mm/s. The data was fit using a mix of Gaussian function and an exponential decay. The resulting fit is shown as a black curve in Figure 5.10 (parameters of the Gaussian contribution: μ_{mean} =−1.23 mm/s, σ^2 =0.357 mm/s). For comparison, the Gaussian fit of the segmented sinking phases from Figure 5.9 is also added in the histogram (red curve). The velocity of 1.23 mm/s as well as the form of the Gaussian of both fits were very similar and indicated that this peak could be assigned to the sinking phases.

For the calculation of the body density, in addition to the sinking velocity, also the dimensions of the cyprid were important. Several reports determined the dimensions of cyprids of *Balanus amphitrite* to be $r_x \approx 300\,\mu m$ and $r_y \approx 125\,\mu m$, e.g. [7, 12, 54]. For the third dimension of the cyprid body no reference value could be found in the literature, and this was assumed to be $r_z \approx 60\,\mu m$ based on own microscopy observations. From these values, the average dimension parameters D_n and E could be calculated to be 262 µm and 0.314 respectively. Using the measured mean value for the sinking velocity (also settlement velocity, w_s) $\overline{w_s} = -1.23$ mm/s (with $\sigma^2_{w_s} = \pm$

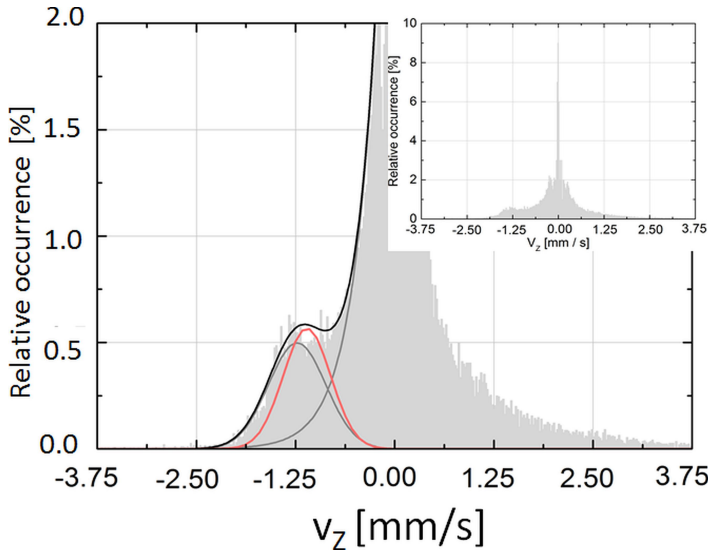

Figure 5.10.: Histogram of the velocity in z direction (v_Z). Inset: Complete histogram across all occurrence values which was dominated by velocities close to 0 mm/s. Main figure: Magnified view of the histogram showing only the region of interest . The fit on the left side is composed of a Gaussian contribution and an exponential decay. The parameters (μ=−1.23 mm/s, σ^2=0.357 mm/s) of the Gaussian function characterize the sinking motion. In red, the "model" distribution describing sinking, which perfectly matched the Gaussian used here, thus proving this region of the histogram contained the sinking velocity values.

0.36 mm/s, Figure 5.10) and the modified form of the Stokes law for elliptical objects [166], the density of the cyprids was calculated with Equation 5.2 and the experimentally determined values of the dimension parameters D_n and E to be

$$\overline{\rho_{cyprid}} = \frac{18 \cdot \mu \cdot \overline{w_s}}{g \cdot D_n^2 \cdot E^{0.380}} + \rho_{fluid} = 1.083\,39 \times 10^6\,\mathrm{g/m^3} \tag{5.1}$$

$$\text{with } \sigma^2_{\rho_{cyprid}} = \pm 1.607\,78 \times 10^4\,\mathrm{g/m^3}. \tag{5.2}$$

The viscosity and density of seawater were μ=1.085 g/(m s) and ρ_{fluid}=1.028 g/cm^3 for the experimental conditions (temperature of the water 20 °C and salinity 39‰) [171]. The gravitational acceleration constant was g=9.81 m/s^2. The dimensions of the obtained value could be verified using literature reports on the weight of cyprids. The dry-body mass of cyprids of *Balanus balanoides* has been reported to be $m_{cyprid} \approx$ 38 µg [172] which corresponds to a wet weight of $m_{cyprid} \approx$126 µg considering a general percentage of water in the body of zooplankton of ca. 70 % [173, 174]. The dimensions for *B. balanoides* cyprids, although measured in species from arctic waters (74°N), were shown by Crisp et al. to be $r_x \approx$663 µm and $r_y \approx$346 µm [175]. In older literature reports it has been discussed that the size of these cyprids varies with latitude [175–

177] due to the temperature differences during egg maturation, food supply, slowed metabolism, etc. The recent work of Pineda et al. [178] demonstrated that also cyprids from warmer regions (41°N), as the ones used for the experiments in this work, exhibit the described dimensions. For that reason the values of Crisp et al. [175] have been used for the calculations. The third dimension was again assumed to be $r_z \approx 90\,\mu m$ based on our microscopy observations. From these values, and an ellipsoid model for the geometry of the cyprid body, the density could be calculated to be

$$\rho_{cyprid} = \frac{m_{cyprid}}{V_{cyprid}} = \frac{3 \cdot m_{cyprid}}{4 \cdot \pi \cdot r_x \cdot r_y \cdot r_z} = 1.451\,23 \times 10^6\,g/m^3 \tag{5.3}$$

Although the value contained several approximations, the density of cyprids of *Balanus balanoides* was very similar to the one obtained from the sinking analysis for *Balanus amphitrite* presented in Equation 5.2 ($1.083\,39 \times 10^6\,g/m^3$). Interestingly several other marine organisms have densities in the same range, e.g. *Cerastoderma edule* larvae $\rho = 1.1 \times 10^6\,g/m^3$ [179], *Calanus finmarchicus* $\rho = 1.08 \times 10^6\,g/m^3$ [180]. This further supports the conclusion, that the sinking analysis according to the Stokes law yields an accurate density value. As expected the body density values of these marine organisms were higher than the density of seawater at 20 °C ($\rho = 1.03 \times 10^6\,g/m^3$) so that they had to actively use swimming upwards in order to avoid sedimentation [181].

5.1.5. Change in the body density as a function of cyprid age

The previous section described the calculation of the body density of 3-day old cyprids from their sinking velocity. Because, as long known in literature [182, 183], cypris larvae use lipids as the main energy reserve, accounting for up to ca. 1/3rd of their total body weight, and the amount of these lipid cells decreases with age, it can be hypothesized that also the body density of the larvae changes. To investigate this, the sinking velocity of 4-day, 8-day and 12-day old cyprids as well as of dead ones was analyzed. Then, the velocity was used together with Equation 5.2 to calculate the densities.

The z component of the velocity vector is shown in Figure 5.11. The mean value of the Gaussian contribution decreased with cyprid age. The 4-day old cyprids exhibited a value of $\mu = -1.13\,mm/s$, which was similar to the mean of the 8-day old ones ($\mu = -1.03\,mm/s$). After 12 days, the mean of the Gaussian was found to be considerably smaller ($\mu = -0.75\,mm/s$). The shape of the histogram for the dead cyprids, essentially only sinking down in the water column, (Figure 5.11, top subplot) differed from the general shape found for active cyprids. The positive side was not populated due to a lack of active movements. Also the peak at $v_Z = 0\,mm/s$ was missing, as dead cyprids were only tracked until reaching the bottom of the container. Thus, the measured velocity was always negative. The mean of the Gaussian function for the dead cyprids (also 12 days old) was found to be $\mu = -0.46\,mm/s$. This value was much lower than the sinking speed of the living larvae.

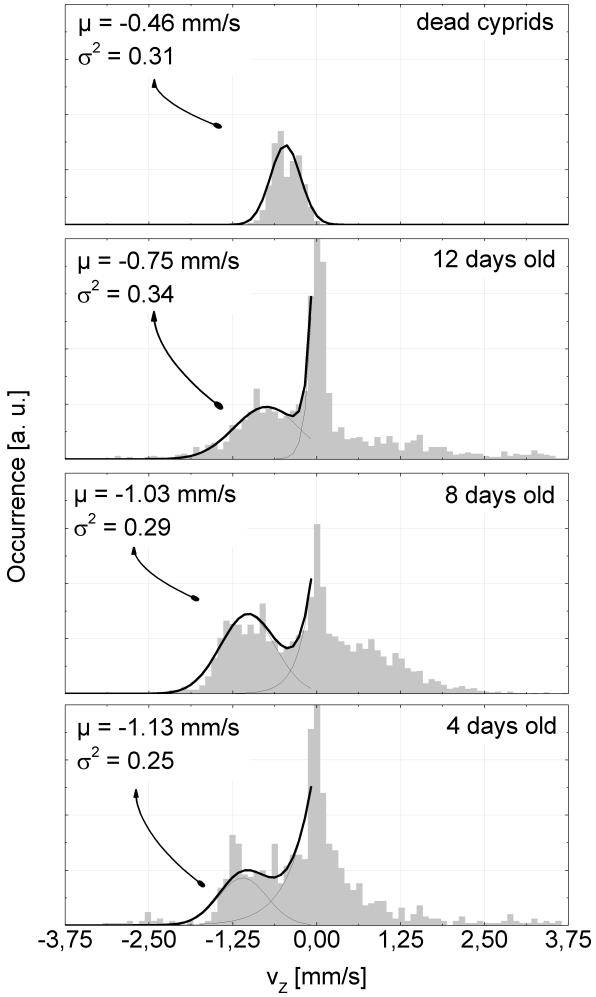

Figure 5.11.: Histogram of the velocity in z direction (v_Z) for cyprids of different ages. 4 d, 8 d and 12 d old larvae as well as dead ones (after 12 d) were used. The fit on the left side is composed of a Gaussian contribution and an exponential decay. The parameters of the Gaussian function (denoted in the respective subplot with μ and σ^2) characterize the sinking motion.

Using the modified Stokes law (Chapter 4.6.6) the cyprid body density was calculated and it could be noted that the density values also decreased (Figure 5.12, in black) and the body density of 3-day old larvae being $1.08 \times 10^6\,\mathrm{g/m^3}$ became $1.06 \times 10^6\,\mathrm{g/m^3}$ for the 12-day old and $1.04 \times 10^6\,\mathrm{g/m^3}$ for the dead cyprids, thus approaching the density value of the seawater under the experimental conditions ($1.03 \times 10^6\,\mathrm{g/m^3}$ for water temperature of 20 °C). One explanation of the observed decrease in the body density could be, as mentioned above, the changed lipid content in the larvae. The amount of the neutral protein TAG (primary used for growth, behavior and metamorphosis [182]) contributes strongly to the total body weight of cyprids of *B. balanoides* [183].

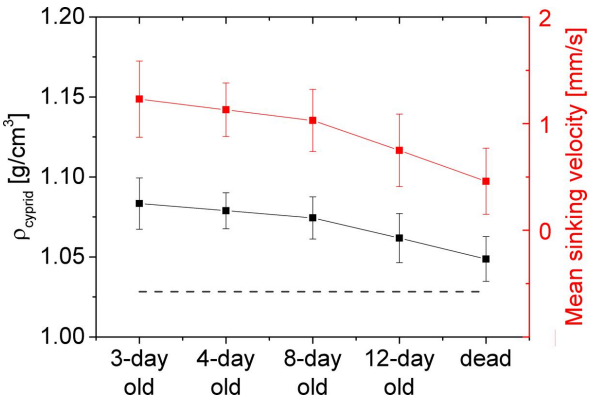

Figure 5.12.: Change in the body density of cyprids with increasing age. The black curve shows the decrease of the body density and the red one, the decrease of the mean sinking velocity of 3 d, 4 d, 8 d and 12 d old larvae and dead ones. The dashed line denotes the density of seawater at 20 °C.

Miron et al. [184] investigated the normalized quantity of the TAG protein in cyprids of *B. amphitrite* of different ages and could demonstrate that it decreased by 25 % between 1-day and 12-day old larvae. The drop in the sinking velocity between 3-day and 12-day old cyprids in our measurements was ca. 33 %, which would correlate with the change in TAG content. At this point it can be only speculated that this or related physiological changes caused the change in larvae density. The fact that the sinking velocity of dead cyprids was further decreased suggested that in addition to the body density, also physiological phenomena (e.g. stretching of thoracopods or antennules, etc.) or active osmoregulation contributed to the changed sinking velocity.

5.1.6. Summary: locomotion patterns

In this chapter a systematic classification of the patterns occurring in the swimming trajectories of barnacle cyprids of *Balanus amphitrite* was presented. The main patterns - *swimming*, *spiraling*, *sinking*, *walking* and *rotating* could be identified. Each of the patterns was characterized based on its velocities, linearity, relative occurrence in the data set and sequential order. It could be shown that *swimming* was the most commonly found pattern (31 %), involving less resting phases, and exhibiting the highest velocity values. The main pattern leading to surface contact was found to be *sinking* (occurring ca. 26 % of the time). The patterns in close proximity to the surface were both characterized by a low velocity and low occurrence in the data set. Interestingly, their linearities were quite opposite - *walking* was found to be highly linear whereas *rotating* possessed the lowest linearity value in the group.

In addition to the classification of the main patterns of the trajectories, the body density of cyprids was calculated based on the empirically obtained sinking velocity and

a modified form of Stoke's equation. Analysis of the data revealed that the mean value of the sinking velocity was 1.11 mm/s, which corresponded to a mean body density for 3 d old cyprids of 1.08×10^6 g/m^3. Finally, it could be shown that the sinking velocity of the cyprids decreased by 25 % between 3 d and 12 d old larvae, which led to a decrease in the body density. This decline could be correlated with literature reports about a reduction of 33 % of the lipid content in the body of 1 d and 12 d old larvae.

5.2. Changes in the motility in response to chemical cues on surfaces

Cyprids behavior is known to be guided by different surface properties. In Chapter 5.1 the main locomotion patterns in trajectories were identified and described quantitatively. In the following sections, a holistic approach for analysis of the exploratory behavior, based on motility, rather than the investigation of the trajectories as single entities, is presented. The method is applied to evaluate the changes in the motility of cyprids on surfaces with different wettability and charge. Furthermore, the spatial distribution of cyprids is discussed, as well as the question whether larvae swim throughout the water column randomly or they are guided by certain cues. For this purpose, the transitions between predefined regions of different swimming depths in the water column are analyzed. Finally, the temporal variations of parameters holistically describing locomotion are investigated in order to reveal potential changes in the behavior of the larvae induced by the time spent on the substrate.

5.2.1. Clustering of cyprids in the water column

During conduction of the experiments it could be observed, that immediately after being released into the test container, cyprids distributed randomly into the whole water volume, driven by the turbulence forces which were induced by the inoculation procedure. Once this artificial initial state had passed and the convections had diminished, cyprids began with the swimming and exploration of the test volume. An evaluation of the distribution of their z positions within the container during swimming revealed a concentration in three distinct regions (Figure 5.13a): the lower swimming region (LSR); the upper swimming region (USR); and the region in between - (bulk or BSR). It should be mentioned, that cyprids in a given swimming region did not necessarily remain there for the whole observation period. Regions represented solely the zones with high accumulation of positions detected during tracking and did not exclude the probability that cyprids potentially changed their z position. Thus, a high density of data points implied that cyprids spent much of their time swimming in the corresponding region. Figure 5.13b shows an example histogram of the occurrence of cyprids in the water column above a DDT surface (z position). For low values of the z position (vicinity of the coated substratum) and for high z positions (close to

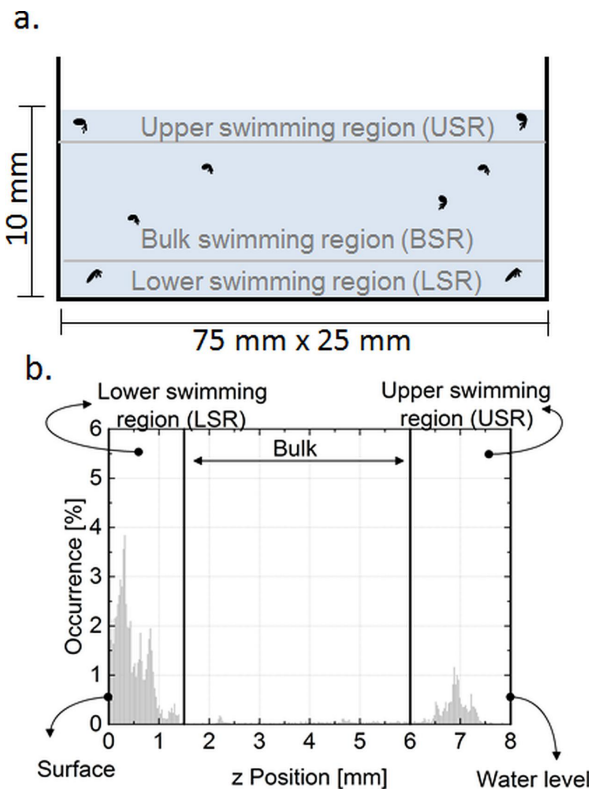

Figure 5.13.: Schematic side view of the test container and z position distribution. The dimensions of (a) the test container as well as the main swimming regions are denoted. The z position of active (V>0 mm/s) cyprids was analyzed with respect to its (b) histogram, which revealed the main swimming regions.

the water surface), the probability to observe cyprids was strongly increased, whereas the occurrence values in between were much lower. The borders of the regions were determined by analysis of the distribution of the z position of the cyprids and their empirical cumulative distribution function (ECDF). In the case of the LSR, as soon as the ECDF reached a plateau and the histogram values were lower than 5 % (depleted bulk region), the corresponding z position was defined as the border of the region. For the USR, the ECDF was analyzed from higher to lower values, and as soon as the plateau was reached and occurrences were lower than 5 %, the z-value was used for a lower border of the region. A graphical representation of this process is illustrated in Section 4.6.2.

The USR extended from the water surface down to ≈1.5 mm (for details on border definition see Figure 4.18 in Section 4.6.2) swimming depth. In Figure 5.14 (top panel, in gray), the distribution of the z velocities within the USR has been calculated. These values represent only the z component of the velocity vector describing the velocity of swimming up (positive velocities) and diving down (negative velocities).

In general, the velocity distribution was characterized by a peak in the proximity of 0 mm/s (representing around 70 % of all values), indicating movements parallel to the water surface. It is worth mentioning that there were still a substantial number of changes in the z-position (velocities ≈ 1 mm/s or -1 mm/s), indicating that the cyprids in the USR moved freely and were clearly distinguishable from those captured in the meniscus. This observation was backed up by the fact that the histogram of the xy component of the velocity vector pronounced showed a peak at around 0.5 mm/s (Figure 5.14, top panel, brown histogram), confirming the activity of the larvae in the xy plane of the USR. At this point it should be noted that cyprids, trapped at the liquid/air interface, were excluded from the analysis presented in this work.

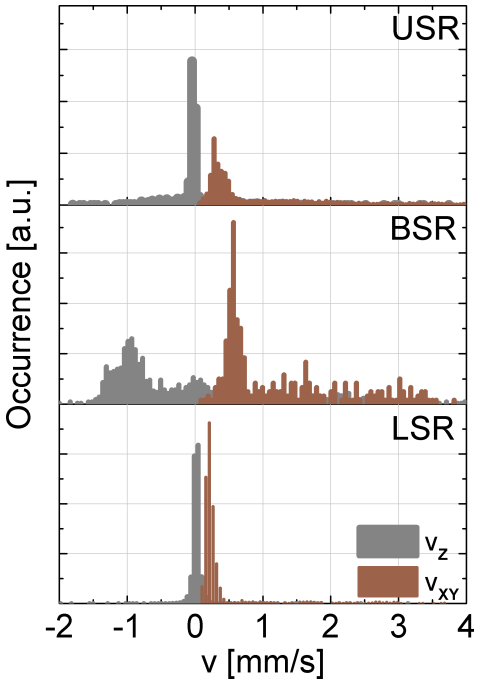

Figure 5.14.: Histograms of the components of the velocity vector for the USR, BSR and LSR. The gray values show the z component, demonstrating that in the USR and LSR most values were in the region of 0 mm/s. The brown distributions represent the velocity in the xy plane. As it can be seen, in the interfacial regions velocity values higher than 0 mm/s appeared, thus indicating that cyprids moved mostly in the xy plane when in the interfacial zones.

The 'bulk swimming region' (BSR) started bellow the USR. The transition into the BSR occurred gradually as soon as the distribution of the swimming positions in USR decayed to very low values. Those parts of trajectories, found in the BSR, originated mainly from transitions between the LSR and the USR, thus the probability of finding cyprids in this region was very low. It should be noted that the values of the z component of the velocity in this region were broadly distributed and no peak was

detectable at values $v_Z \approx 0\,mm/s$ (Figure 5.14 in gray, middle panel). Interestingly, also in the xy plane velocities higher than 0 mm/s were present (Figure 5.14 in brown, middle panel). This distribution of the velocity vector seemed to confirm that the BSR region is mainly used for transitions between the interfacial regions.

The lower swimming region (LSR) was located between the BSR and the chemically functionalized surface. Similar to the USR it extended from the surface $\approx 1.5\,mm$ into the solution with a high probability of finding cyprids. In this region, the cyprids swam slowly ($v_{XY} \approx 0.3\,mm/s$, brown histogram in the bottom panel of Figure 5.14) and mostly parallel to the surface ($v_Z \approx 0\,mm/s$, gray histogram in the bottom panel of Figure 5.14). The low velocity seemed to indicate a transition from *walking* into "close surface inspection" [19, 28, 185], but this was not further investigated due to hardware limitations of the setup resolution.

The presence of two preferred swimming regions where cyprids accumulated (USR and LSR) raised the question of whether the height of the water column affected their position. Therefore, experiments were conducted to investigate the influence of different water depths on the USR. As expected, the position of the outer regions proved to be defined by the interfaces: solid/liquid interface for the LSR and liquid/air interfaces for the USR. Figure 5.15 shows the occurrence of cyprids as a function of their swimming depth (z position) in culture vessels coated with DDT for water depths of 3.5 mm, 6.5 mm and 8 mm. It became clear that the position of the USR was determined by the water surface and it increased with increasing water depth. In all three cases, the USR extended $\approx$ 0.5 mm-1 mm beneath the water surface. This finding, combined with the observation that the occurrence value for BSR remained very low (OV_{LSR}=84 % ± 4 %, OV_{USR}=12 % ± 4 % compared to OV_{BSR}=4 % ± 1 %) for all examined depths, supports the notion that for the applied assay geometry (chemically functionalized surfaces placed horizontally below the cyprids, perpendicular to the gravitational force), cyprids expressed a clear preference for interfacial regions and spent most of their time swimming either close to the air/liquid or liquid/solid interface. In literature, different mechanisms are discussed which could be involved in sensing of the two interfacial regions, i.e. phototaxis, rheotaxis, and barokinesis [24], but these were not further investigated.

5.2.2. Motility changes in response to surface wettability and charge

After identifying different swimming regions, the question was pursued whether the exploratory behaviour of cyprids as well as their distribution in the water column above functionalized surfaces were affected by the chemical termination of the substrates. For this purpose three motility parameters were quantified: occurrence of cyprids in the swimming regions (USR, BSR and LSR), mean velocity and swimming area coefficient, describing the spatial extent of a trajectory (details in Chapter 4.6.3). In the group of surfaces attractive for settlement, DDT and TMA were selected because they have

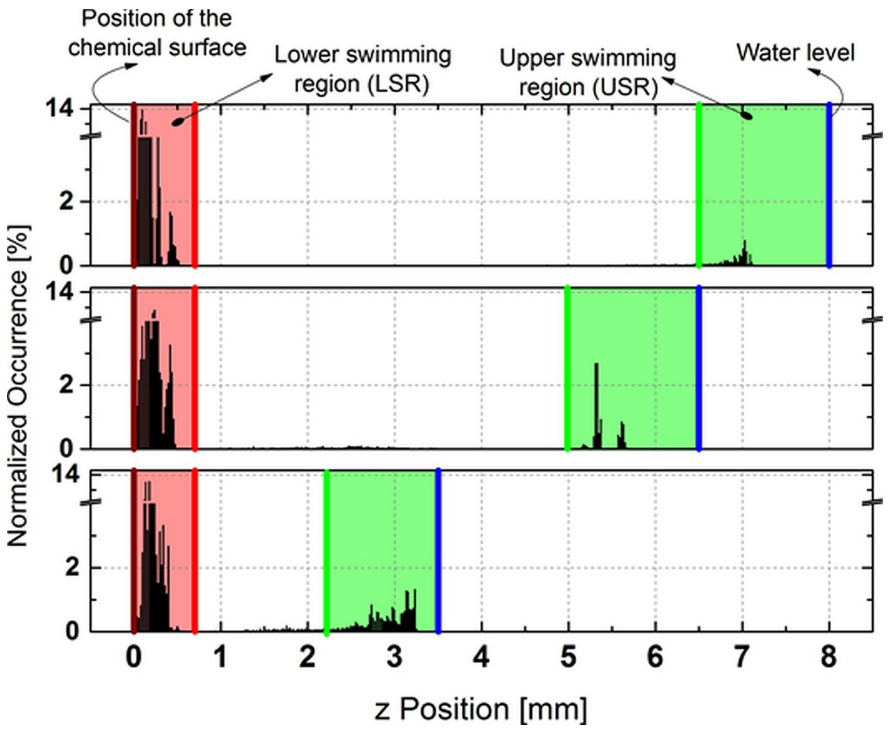

Figure 5.15.: Occurrence of cyprids in the swimming regions for containers of different water depth. The occurrence of active (v>0 mm/s) cyprids was investigate as a function of their z position in the water column ($N_{surfaces}$=3, $N_{cyprids}$ = 20). Cyprids in containers with different water depths showed a clear preference for interfacial regions (LSR marked in red and USR marked in green). A blue line represents the position of the liquid/air interface (water level).

been reported to be colonized readily by cyprids [13]. On the contrary, HUDT and TMA+MUDA have been known to exhibit less attractive properties [29]. The details on surface preparation and characterization are shown in Chapter 3.2. To verify the attractiveness of the selected surfaces a settlement assay was performed. Figure 5.16a shows the settlement results after 48 h on DDT, HUDT, TMA+MUDA, TMA and a polystyrene control. The hydrophobic DDT surface proved to be attractive for settlement (ca. 10 %) whereas the hydrophilic HUDT exhibited a much lower value (ca. 0.2 %). Similar settlement trends have been reported in literature, e.g. Petrone et al. [13] reported a 25 % settlement on a DDT surface and only ≈ 12 % on the HUDT. It should be noted, that the absolute settlement values in this thesis were generally lower than reports in literature for surfaces with the same chemical properties. The reason for these differences was the procedure applied to perform the settlement assays. While literature settlement values originate from assays conducted in droplets on a well plate, here quadriPERM containers were used, which provided a much wider area for swimming and in addition, the air/liquid interface was much broader (for details see

Chapter 4.5.4). Factors, such as water volume, size of container, etc. have been reported to influence the results of settlement assays [14], that is why trends, rather than absolute settlement values should be compared.

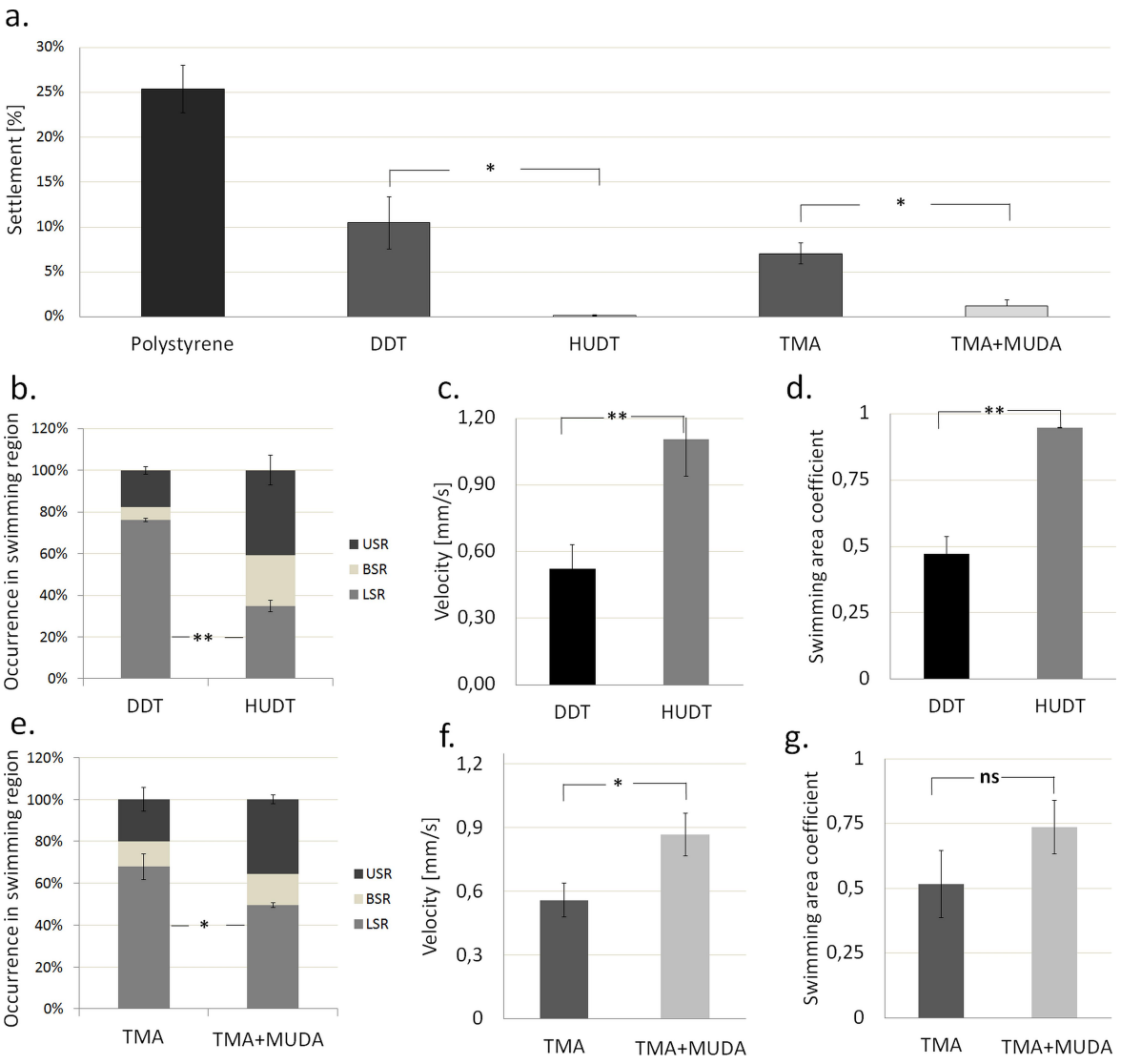

Figure 5.16.: Investigation of motility parameters for surfaces with different wettability and charge. (a) The settlement values after 48 h showed a clear preference of the cyprids for the DDT and TMA, in contract to the HUDT and TMA+MUDA. This was reflected in the (b, e) Occurrence values of cyprids in the swimming regions, (c, f) velocities and (d, g) swimming area coefficients. For the parameter calculations, values were considered only from active (v>0 mm/s) cyprids. (N=4, error bar is the standard error). Asterisk represents statistically different groups (two sided Students t-test, **: $p<0.001$; *: $p<0.05$; ns: not significantly different)

The second motility parameter, used to describe the exploratory behavior, was the occurrence of cyprids in the swimming regions. Figure 5.16b shows the values for this parameter in the swimming regions above the DDT and HUDT surfaces. In the case of the attractive, hydrophobic DDT the occurrence in the LSR (75 % ± 1 %) was more than twice as high as for the less attractive, hydrophilic HUDT (33 % ± 3 %). In both cases the lowest occurrences were observed in the BSR, with somewhat lower values for DDT (6 % ± 1 %) compared to HUDT (23 % ± 6 %). To further quantify the behaviour, the mean velocities of the cyprids were investigated over both surfaces. This parameter represented the averaged value of the locomotion velocities of all cyprids swimming in the water volume (including the three regions - USR, BSR and LSR). The velocities on the attractive surface (DDT) were around two times lower (0.5 mm/s ± 0.1 mm/s) than the velocities over HUDT (1.1 mm/s± 0.2, Figure 5.16c). Finally, after it has been established which swimming region was populated for the respective surface and the velocities detected during this swimming have been identified, the extent of surface area visited by the cyprid in the field of view either by close surface inspection or swimming was quantified. The swimming area coefficient (see Chapter 4.6.3 for details) included cyprids from the whole water volume (USR, BSR and LSR). A lower value for the swimming area coefficient originated from a more localized and convoluted path, while higher values represented a more extended and straight path. The swimming area coefficient on DDT (0.47 ± 0.06) was only half of the value for HUDT (0.94 ± 0.01) (Figure 5.16d), indicating that cyprids on DDT spent more time in a specific area while moving at lower speeds (0.5 mm/s compared to 1.1 mm/s). It is likely, that these cyprids were engaged in close inspection of the surface. This general trend, that larvae expressed lower speeds and more focused swimming in the vicinity of attractive surfaces, was in a good agreement with literature reports. Matsumura et al. [25] showed that cyprids spent more time, traversed more slowly and took a more convoluted path on attractive surfaces. Also Chaw et al. [28] noted that cyprids explored attractive surfaces (CH_3-treated glass) more thoroughly and the duration of the steps was much longer than the step duration on surfaces of no particular interest (e.g. NH_2-treated glass). In turn, on highly hydrophilic zwitterionic polymers, a fast motion across large areas has been found [29].

In addition to the surfaces with different wettability, positively charged trimethylammoniumundecanethiol (TMA) and mixed TMA+MUDA SAMs (consisting of 50 % TMA and 50 % MUDA) with a net neutral charge (Figure 5.16e-g) were compared. The results of the settlement assay are shown in Figure 5.16a. More cyprids settled on TMA compared to the TMA+MUDA SAMs. This observation was inline with reports of Aldred et al. [29] that zwitterionic materials possess settlement inhibition properties in contrast to charged surfaces. However the difference in the settlement values was not as pronounced as between DDT and HUDT. Figure 5.16e compares the occurrences of cyprids in the respective swimming regions. The probability of finding cyprids in the LSR close to the positively charged surface (TMA, ca. 67 %) was nearly as high as for DDT (ca. 75 %). Additionally, cyprids moved with low mean velocity on

the TMA ($\approx 0.55\,\mathrm{mm/s}$). The corresponding surface area coefficient on this surface was comparable to the DDT value and a smaller area was explored in a more convoluted path ($C_{SA} = 0.5$). These observations combined with the high occurrence in the LSR region correlated well with the high settlement. On the contrary, the time spent in the LSR over the TMA+MUDA surface was as expected lower (<50 %). The trend was even more apparent if the occurrence of cyprids in the USR was compared. The probability of finding cyprids in the USR above the attractive surface (ca. 20 %) was only around half of the one for the TMA+MUDA SAM (ca. 37 %). Also here, the occurrence in the BSR was very low. Furthermore, cyprids moved with higher mean velocity on the TMA+MUDA SAM ($\approx 0.85\,\mathrm{mm/s}$) compared to TMA SAM and the corresponding surface area coefficient was $C_{SA} = 0.75$ on the mixed SAM, denoting a broader and more linear way of exploration of this surface. The described findings combined with the trend that cyprids moved into the USR, away from the TMA+MUDA SAM, correlated positively with the reduced settlement. One explanation of these observations could be the influence of surface change on the adhesive system of cyprids. There have been several reports on the correlation of settlement preferences of cyprids and their interaction with the substrate via the temporary adhesive located at the end of the antennules [27, 186] which linked strong adhesion to high settlement outcome. On the contrary, it could also be shown that low settlement was observed on protein resistant surfaces, where the temporary adhesive stuck less readily [26]. In a similar way, charge equilibrium at zwitterionic interfaces caused protein resistance and low settlement of another marine biofouler - algal spores, while charge excess facilitated their binding [71, 187–189]. The lower velocity, more localized exploration and the more frequent occurrence of cyprids in the LSR on TMA surface seem to be correlated with the stronger interaction of the temporary adhesive on this surface. The high velocity and the high exploration coefficient on the surfaces with mixed, zwitterionic charges correlated well with previous findings on zwitterionic polymers which revealed extended swimming motion at high velocities [29]. In both cases - the DDT/HUDT and the TMA/TMA+MUDA - a lower velocity (Figure 5.16c, f) correlated with a smaller swimming area coefficient (Figure 5.16d, g), higher occurrences in the LSR and higher settlement.

5.2.3. Surface induced transitions between swimming regions

As already discussed, the occurrence in the bulk swimming region (BSR) exhibited the lowest values of the swimming regions for all test surfaces (see Figure 5.16b, e). This fact suggested that the region was mainly used for transitions between the interfacial zones (USR and LSR). In order to confirm this observation, the transition frequency into and out of the BSR over DDT and HUDT was determined (Figure 5.17). It can be seen that in both cases the transitions out of the bulk region (BSR) were more frequent ($15.2\,\mathrm{min^{-1}} \pm 1.8\,\mathrm{min^{-1}}$ for DDT and $14.1\,\mathrm{min^{-1}} \pm 1.8\,\mathrm{min^{-1}}$ for HUDT) than the transitions into the BSR ($1.0\,\mathrm{min^{-1}} \pm 0.1\,\mathrm{min^{-1}}$ for DDT and $3.4\,\mathrm{min^{-1}} \pm$

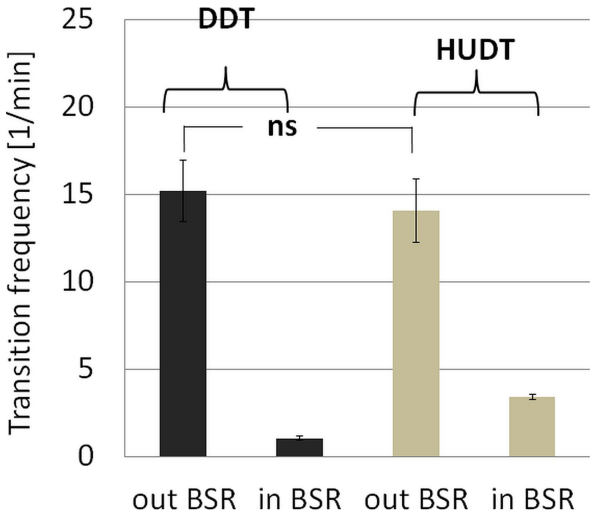

Figure 5.17.: Transition frequencies into and out of the BSR. Interestingly, mainly transitions out of the bulk swimming region could be detected for both DDT and HUDT samples (mean values shown, error bars represent standard error, N=42).

0.1 min^{-1} for HUDT). It was concluded that the distribution shown in Figure 5.16b was a consequence of an active process where cyprids left the BSR and accumulated at the interfaces, rather than accidental random inhomogeneous distributions. The fact that the experimental groups containing ca. 20 cyprids each, demonstrated a summed transition frequency into and out of the BSR of nearly 17 transitions per minute indicated a highly dynamic behaviour. Additionally, it showed that the distributions observed in Figure 5.16b were a consequence of active redistribution and not a static situation. Interestingly, no significant differences were detected for the frequencies out of BSR for DDT and HUDT.

While the transition frequencies out of the BSR explained the accumulation at the interfaces, the frequencies into and out of the lower (Figure 5.18a) and upper swimming region (Figure 5.18b) were calculated to analyze the response to the chemical surface cues in greater detail. As shown in Figure 5.18a for the DDT surface, less transitions occurred out of the LSR (1.3 min^{-1} $\pm$ 0.2 min^{-1}) and a higher frequency was observed for cyprids to enter this region (14.0 min^{-1} $\pm$ 1.0 min^{-1}). On HUDT, these two probabilities were nearly identical (3.9 min^{-1} $\pm$ 0.5 min^{-1} out of LSR and 4.2 min^{-1} $\pm$ 1.0 min^{-1} into LSR). Especially the high probability of cyprids to enter the LSR of DDT was the reason for the observed accumulation in Figure 5.16b.
In turn, the transition frequencies of cyprids into or out of the USR on the DDT surface were similar (1.5 min^{-1} $\pm$ 0.3 min^{-1} for swimming out of the USR and 3.5 min^{-1} $\pm$ 0.5 min^{-1} for swimming into it). However, the transition frequency of cyprids entering the USR above the HUDT coatings was much higher (10.9 min^{-1} $\pm$ 1.8 min^{-1}). Thus, the attractive DDT showed a high transition frequency of cyprids entering the LSR

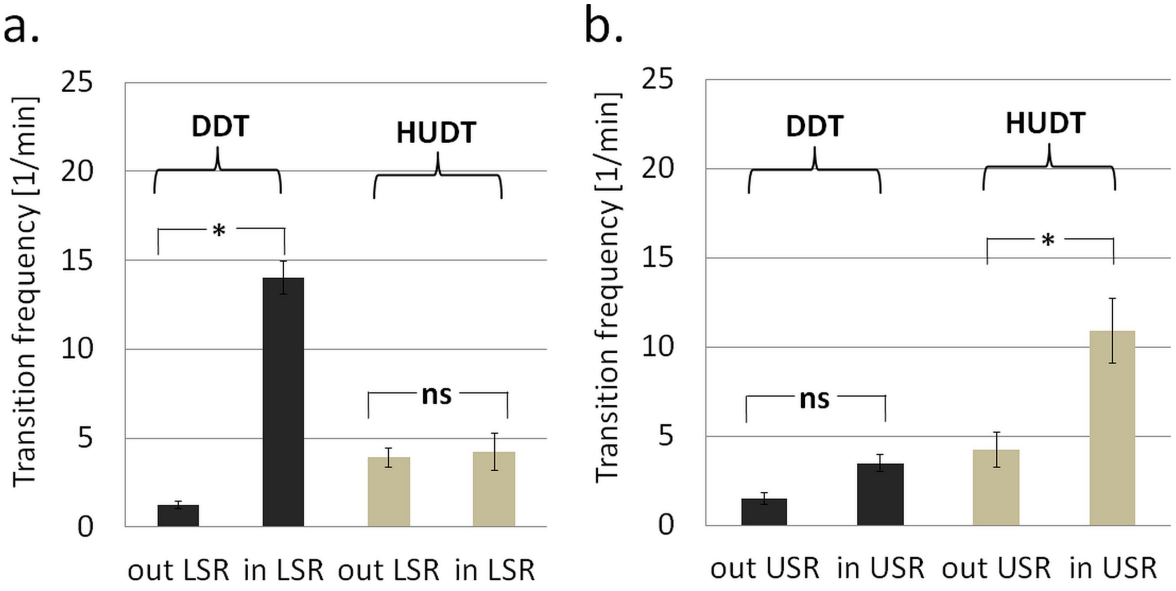

Figure 5.18.: Transition frequencies into and out of the interfacial regions. The transitions on DDT and HUDT samples into and out of the (a) lower swimming region and (b) upper swimming region revealed the re-distribution of cyprids in the interfacial regions. On the DDT, most transitions were into the LSR, while on the HUDT cyprids swam mainly into the USR. (mean values shown, error bars represent standard error, N=42).

with no marked preference for the USR. On the contrary, the unattractive HUDT surfaces obviously stimulated an accumulation in the USR as indicated by the high frequency of cyprids entering this region. Concluding, the different distributions in the water column above the DDT and the HUDT surfaces were caused by dynamic transitions and the different transition frequencies for USR and LSR were guided by the surface chemistry.

5.2.4. Temporal variations of the motility parameters on surfaces with different wettability

Since most of the trajectories were extracted from videos recorded shortly after the initial contact of cyprids with the test surfaces, it was important to investigate how the occurrences in the LSR, the mean velocity and the swimming area coefficient changed with time and whether the correlation with settlement probability remained. Again, the hydrophobic DDT and the hydrophilic HUDT were compared and Figure 5.19 shows the occurrence in the LSR at different time points - 0 h, 4 h and 12 h after initial inoculation into the containers. The values for DDT remained high for the three time points, confirming the interest of the cyprids in this surface. On the contrary, the

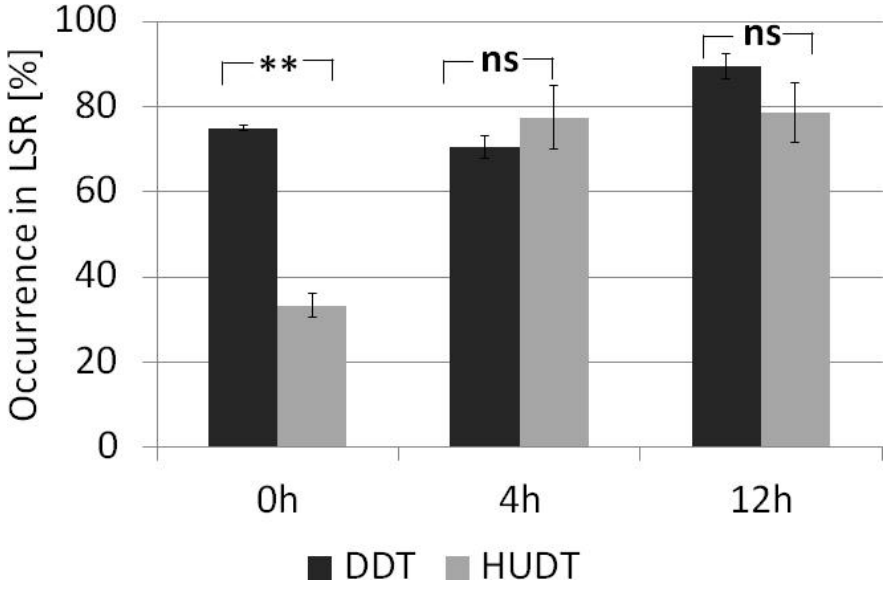

Figure 5.19.: Temporal variations of the occurrence of cyprids in the swimming regions. Occurrence values of active cyprids (V>0 mm/s) in the LSR over DDT and HUDT surfaces for three different time points: 0 h ($N_{replicates} = 4, N_{cyprids} = 4{*}20$), 4 h ($N_{replicates} = 2, N_{cyprids} = 2 * 20$) and 12 h ($N_{replicates} = 2, N_{cyprids} = 2 * 20$) after inoculation (error bar denotes the standard error). Asterisk represents statistically different groups (**: p<0.001; ns: p>0.1).

occurrences in the LSR for the HUDT, being low at point 0 h (ca. 33 %), showed an increase with time. This increase implied that the significantly different values (p<0.001, Student *t*-test) of the first experiment for the HUDT and DDT surfaces became similar already after 4 h and remained the same also after 12 h. It seemed that the initial correlation of occurrences in the LSR with the overall settlement preference disappeared after 4 hours. While it can currently only be speculated if conditioning affected the surface [42, 107] or deposits on it [101] changed the occurrence across the water column, it is important to keep the time dependence in mind if a similar probability analysis is anticipated. In addition, changes in the mean velocities were compared. Figure 5.20a shows the results for velocities obtained on the DDT and HUDT surfaces at the three time points (0 h, 4 h, and 12 h after initial exposure) in the whole container. In general, the velocity over HUDT was more than twice as high as over the attractive DDT and this ratio slightly increased with time. The increase was mainly caused by higher velocities over HUDT. Faster swimming over HUDT correlated with a reduced occurrence near the surface and lower settlement. Chaw et al. [28] demonstrated that cyprids express longer steps with shorter duration, thus higher locomotion velocities, when engaging in close surface inspection on hydrophilic surfaces. This observation is in agreement with the higher velocities close to the HUDT

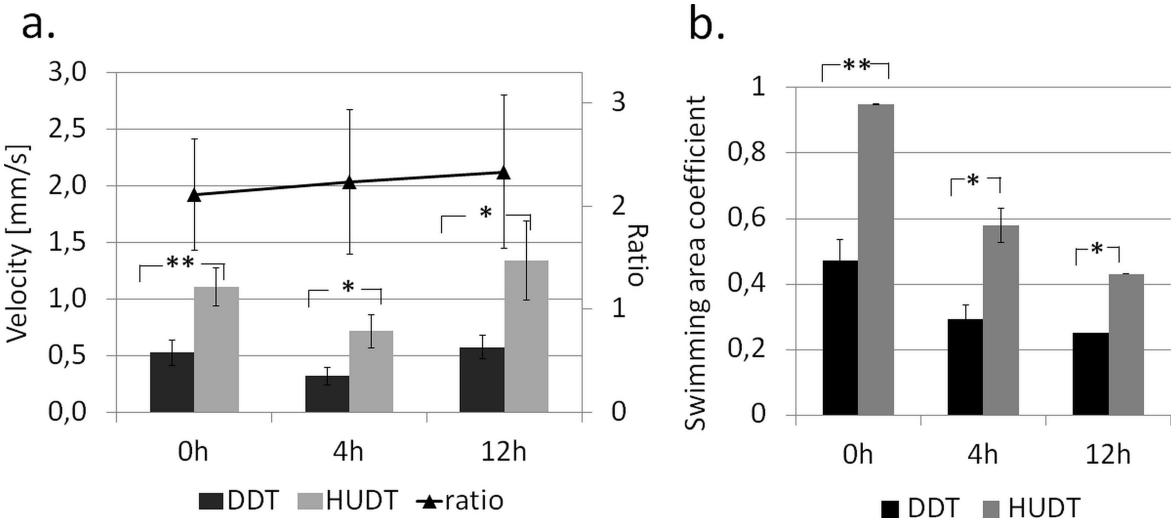

Figure 5.20.: Temporal variations of the motility parameters. (a) Velocities together with their ratio and (b) swimming area over DDT and HUDT measured at three different time points: 0 h ($N_{replicates} = 4, N_{cyprids} = 4 * 20$), 4 h ($N_{replicates} = 2, N_{cyprids} = 2 * 20$) and 12 h ($N_{replicates} = 2, N_{cyprids} = 2 * 20$) (error bars denote the standard error). Asterisk represents statistically different groups (**: $p<0.001$; *: $p<0.05$)

surfaces in this experiment. It is important to note that the resolution of the used setup was not sufficient to differentiate whether the evaluated movements originated from close surface inspection interactions or from swimming movements close to the surface.

Furthermore, it was analyzed whether cyprids swam across large areas or the movements were localized. The corresponding 'swimming area coefficient' tended to decrease with time (Figure 5.20b), indicating that the swimming became more and more localized, probably including some close surface inspection patterns. The effect of the decreasing swimming area was observed on both surfaces, DDT and HUDT and with time, the swimming area coefficients became more similar but remained different.

Combining these observations with the distribution of cyprids within the water column revealed that on DDT, where the highest cyprid occurrences were in the LSR at all three time points, the velocity remained low and the swimming area coefficient decreased. This indicated a high attractiveness of the surfaces for the larvae, causing a more focused and localized swimming motion. After 48 h, this attractiveness was confirmed by the higher settlement values found on these surfaces. On HUDT, cyprids were initially less frequently observed in the LSR (less than half of the occurrence compared to DDT). However, already after 4 h, they were found with an increased probability in the lower swimming region with occurrence values equal to the ones observed for DDT. With time the ratio between velocities on HUDT and DDT increased

and after 12 h HUDT values were more than twice as high as on DDT. Obviously, the higher velocities correlated with lower settlement on the HUDT surfaces. Interestingly, the swimming area coefficient over HUDT also decreased with time, which points towards cyprids decreasing their swimming area and probably engaging in close surface inspection, but the relative differences remained. This seems to indicate the the swimming area coefficient also correlates with settlement behavior.

5.2.5. Summary: Exploratory behavior

A new approach for the quantification of the motility and pre-settlement behavior of barnacle cyprids was presented. It relied on the utilization of motility parameters for a holistic analysis of the cyprid locomotion, rather than the investigation of individual parameters of single trajectories. This 'macroscopic' approach revealed the formation of three distinct swimming regions in the distribution of active cyprids across the water column - in the lower (LSR), bulk (BSR) and upper (USR) swimming region. Furthermore, a clear preference for the interfacial zones was observed. An analysis of the transitions between the swimming regions demonstrated that the concentration of larvae there was an active behavioral response rather than of random nature. The occurrence of the larvae was also investigated with respect to the surface attractiveness for settlement. A clear correlation between higher occurrence values in the LSR, lower velocity and swimming area coefficient on one side and high settlement values on the other was described (e.g. for the attractive, hydrophobic DDT surface or the attractive, positively charged TMA). On the contrary, lower occurrences in the LSR combined with high velocity and a higher swimming area coefficient resulted in low settlement (e.g. for the non-attractive, hydrophilic HUDT surface or the non-attractive, zwitterionic TMA+MUDA). Interestingly, the temporal variations of the parameter describing the occurrence in the swimming regions revealed that already after 4 h the correlation with the settlement preferences disappeared and cyprids spent an equally high amount of time in the LSR on both attractive and non-attractive surfaces. In contrast, the velocity and swimming area coefficient values did not vary with time and correlated with the settlement also after 12 h.

5.3. Quantification of close surface inspection

While the first two chapters described the systematic analysis and quantification of exploratory behavior of cyprids, performing a general characterization of the motility and a holistic analysis of the exploration process, in this chapter the close surface inspection, or the behavior of cyprids in contact with the substratum is analyzed. This is an important aspect of cyprid behavior because it reveals the process of surface testing at a more 'microscopic' level. Thus, in the following sections the motility of cyprids in close proximity to coatings is quantified and the changes in behavior are correlated with the attractiveness of the surfaces for settlement.

Due to hardware restrictions in the resolution of the setup described in Chapter 4, the tracking experiments were performed by Nick Aldred (Newcastle University, UK) on a system with a higher optical resolution. The test surfaces used in the experiments were prepared by Stella Bauer (University of Heidelberg, Germany) and the automated extraction and analysis of the parameters quantifying the close surface inspection of the cyprids were performed at KIT as part of this thesis.

5.3.1. Analysis of step velocity and step duration

One surface property which has been identified to be important for resistance to fouling is the ability to store water [109]. Ethylene glycol based polymers have shown remarkable antifouling properties (e.g. [83]), but have the disadvantage that they suffer from rapid degradation when in aquatic environment (e.g. [122]). An alternative system which also possesses the ability to store water are polysaccharides [190]. The highly hydrated hyaluronic acid (HA) and alginic acid (AA) have been shown to be resistant to the adhesion of some cells and bacteria [191] and recently it was demonstrated that coatings with amphiphilic properties can be used in antifouling applications [192]. For that reason, in this experiment the hydrophilic polysaccharides [109, 191] HA and AA were selected as test surfaces. The substrates were modified with hydrophobic molecules (2,2,2-trifluoroethylamine, TFEA) in order to achieve amphiphilicity [127] and thus to enhance their anti-fouling capabilities. The values of the previously defined motility parameters (i.e. step velocity and step duration [28]) were compared for the pristine and modified versions of the coatings.

Before quantification of the close surface inspection behavior, the settlement properties of the coatings were determined with a settlement assay and compared to well known controls from literature. The settlement values after 24 h and 48 h on the pristine polysaccharide surfaces (HA, AA), on the modified versions capped with hydrophobic TFEA (HA+TFEA, AA+TFEA) as well as on glass are shown in Figure 5.21. The trend was similar for both time points, with more organisms settling after 48 h. The AA coatings showed higher settlement ($\approx 59\,\%$, after 48 h). Hyaluronic acid was less populated ($\approx 40\,\%$, after 48 h), although with values still above the negative glass control ($\approx 21\,\%$, after 48 h). Settlement on the AA+TFEA was $\approx 28\,\%$ (Figure

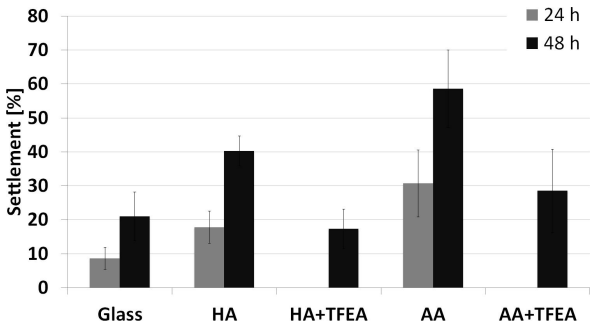

Figure 5.21.: Settlement of cyprids on polysaccharide coatings. The outcome of the settlement assay of *Balanus amphitrite* cyprids on pristine and modified (+TFEA) polysaccharide surfaces after 24 h and 48 h (unpublished data, Stella Bauer). Because of the hydrophilicity of the surfaces, settlement was measured in coated vials. 20 cyprids were examined per surface on 6 surface replicates. Error bar represents the standard error of the mean.

5.21), which was only half of the settlement observed on the pure AA coating. The same effect could be noted also on the HA+TFEA, where the settlement ($\approx$ 18 %) was ca. two times lower than on the unmodified version ($\approx$ 40 %). As inspected, the settlement values on the pristine polysaccharides, which were more attractive for settlement, were decreased with the TFEA capping, to levels comparable to glass - a non-attractive control. An additional effect worth mentioning was that on both mod-

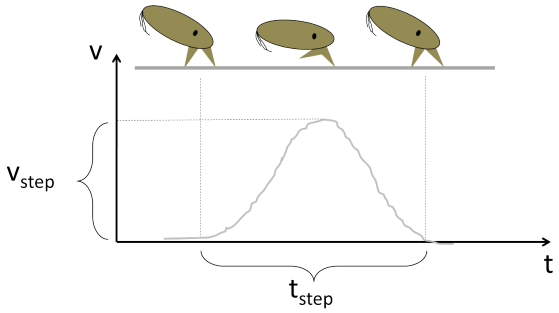

Figure 5.22.: Sketch of the performance of a single step. In order to quantify the process of walking in cyprids, during the performance of a single step, the parameter step velocity and step duration were monitored.

ified coatings, AA+TFEA and HA+TFEA, the settlement values after 24 h equaled 0 %. This could be explained by the fact that cyprids needed more time to evaluate the properties of these coatings for permanent settlement, but the reason was not a subject of this study.

To quantify the close surface inspection, the mean duration of a single step on the test surfaces was investigated together with the mean velocity of larvae during the

step, parameters schematically presented in Figure 5.22. For this purpose, the velocity profile of walking cyprids was observed in which peaks represented the step motion. The velocity of a single step was given by the amplitude of the peak and its width represented the step duration. The data set contained $\approx 7-8$ trajectories per coating, each consisting of ≈ 20 steps.

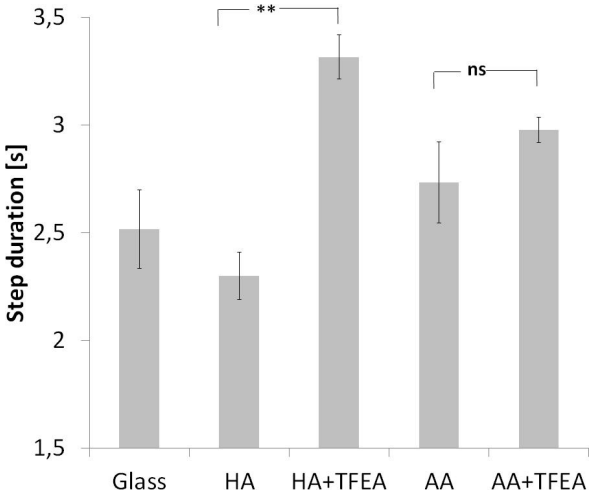

Figure 5.23.: Duration of a single step on polysaccharide coatings. The mean duration (y axis scaled) of a step on pure and modified (+TFEA) polysaccharide coatings as well as on a glass control ($\bar{N}_{cyprids} = 8$, $\bar{N}_{steps} = 20$). It could be observed that the step duration on less attractive surfaces was longer. The error bars represent the standard error of the mean. Student's t-test, **: p<0.001, ns: p>0.05.

The effect of the TFEA capping becomes obvious if the time duration of a single step is compared (Figure 5.23). The mean duration on the HA coatings was observed to be 2.29 s ± 0.06 s. This value was increased to 3.31 s ± 0.19 s after capping with TFEA. Similar response, although not as pronounced, was observed on the other test coating AA. While the mean step duration on it was 2.73 s ± 0.11 s, on the AA+TFEA coating cyprids needed 2.97 s ± 0.18 s.

In addition, the velocity of cyprids during a the performance of the steps was estimated (Figure 5.24). As it can be seen from the Figure 5.24, the mean velocity of the steps was influenced by the TFEA modification. This velocity was observed on the HA coatings to be 1.13 mm/s ± 0.03 mm/s. As soon as the hydrophobic TFEA molecule was introduced, the velocity sank to 0.92 mm/s ± 0.04 mm/s. The same trend could be observed for the AA coatings, where the mean velocity on the pristine coating was 1.11 mm/s ± 0.04 mm/s while on the one capped with TFEA it decreased to 1.00 mm/s ± 0.05 mm/s. The values of the velocity of a single step on the negative glass control were in the range of the modified coatings (0.94 mm/s ± 0.04 mm/s).

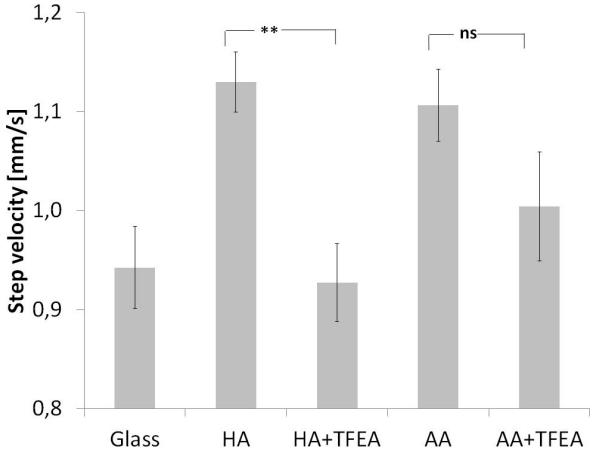

Figure 5.24.: Velocity of a single step on polysaccharide coatings. The mean velocity (y axis scaled) of steps occurring during close surface inspection on pure and modified (+TFEA) polysaccharide coatings and a glass surface as control ($\bar{N}_{cyprids} = 8$, $\bar{N}_{steps} = 20$). It could be noted that the velocity was higher on the less attractive coatings. Error bars represent the standard error of the mean. Student's t-test, **: $p<0.001$, ns: $p>0.05$.

5.3.2. Summary: Close surface inspection

Summarizing, it could be shown that the settlement on polysaccharide coatings (hyaluronic acid and alginic acid) was reduced by capping with a hydrophobic TFEA molecule and it reached levels of non-attractive glass substrates. The mean step velocity on the surfaces during close surface inspection was decreased on coatings modified with the TFEA molecule, whereas the mean step time was increased on these surfaces. One explanation of this behavior could be that cyprids were decelerated by the TFEA surfaces, since, because of the amphiphilicity, these required a longer and more extensive inspection. It should be noted, that these were preliminary results and more data needs to be analyzed in order to backup the observations, but the presented differences demonstrated already first trends.

5.4. Imaging surface plasmon resonance and stereoscopy for quantification of interfacial interactions

For a complete quantification of the exploratory behavior of larvae, in addition to the motion analysis and description, also the interaction of the cyprid with the interface needs to be investigated. In this chapter the outcome of first feasibility tests of a novel system are presented, which provides a detailed insight into the complex swimming

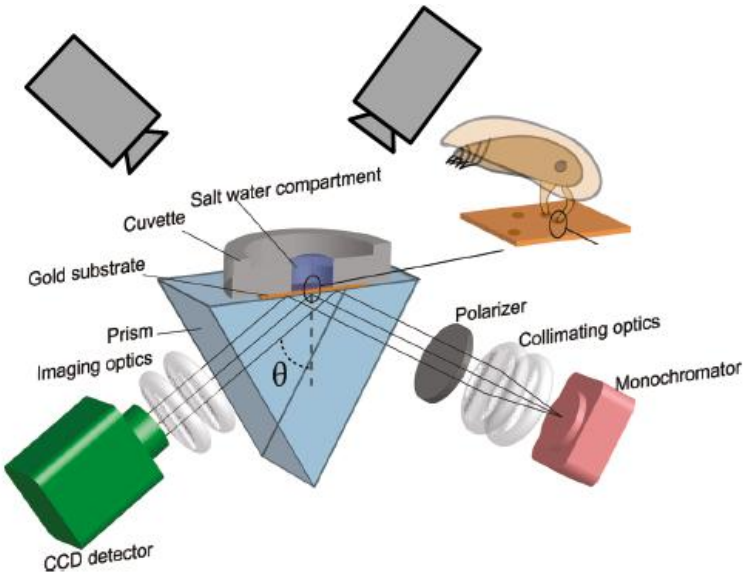

Figure 5.25.: Setup combining the stereoscopic system with the iSPR. The schematic shows the combined system including the stereoscopic setup on the top and the iSPR setup on the bottom of the container. This novel system was used to quantify the behavior of cyprids during exploration and simultaneously to investigate interactions with the interface. Adapted from [26].

and exploratory behavior of cyprids and at the same time into their interaction with the substrate at the liquid/solid interface. This is achieved by combining imaging surface plasmon resonance (iSPR), a technique used to investigate interfacial events, with the stereoscopic setup described in Chapter 4.

The experiments in this section were conducted by Hernan Sendra (University of Heidelberg, Germany) in the group of Thomas Ederth (Linköpping University, Sweden) and the data analysis was performed at KIT as part of this thesis.

5.4.1. Measurement setup combining iSPR and stereoscopy

The resolution of the stereoscopy setup (Chapter 4) did not allow to image and characterize events occurring at the interface microscopically. On the contrary, the imaging surface plasmon resonance technique enabled quantification of the amount of adhesive organic material left behind by cyprids, as well as the detection of touchdown events, but did not provide information on the swimming process and motility in close proximity to the substratum or in the water column. The combination of both techniques allowed the quantification of the macroscopic exploratory behavior together with the interfacial interactions, thus extending the information obtained with the techniques separately. The resulting setup is shown schematically in Figure 5.25. Briefly, it con-

sisted of two cameras imaging the illuminated sample container from the top. The iSPR part included a light source, a detector with imaging optics as well as a prism. The detector was a CCD camera and a lens providing a macroscopic resolution of <10 µm. For synchronization of the stereoscopy cameras an external trigger signal provided by a LANC controller was used (details in Chapter 4). The iSPR camera was started manually, and its video signal was digitally adjusted to the video of the stereoscopy cameras during the post-processing step. The theoretical background of iSPR is discussed in Chapter 2.3.3.

5.4.2. Proof of principle measurements

The objective of the initial experiments with the system was to prove the feasibility of the proposed combination. For this purpose, cyprids of *Balanus amphitrite* were placed in a test container and their swimming and exploration were quantified. The test surfaces were a negatively charged $HS-(CH_2)_{11}COO^-$ SAM surface and a hydrated $HS-(CH_2)_{11}CONH(C_2H_4O)_{11}CH_3$ SAM, referred to as MUDA and mPEG respectively, on which cyprids were reported to exhibit different interaction patterns [26].

Figure 5.26a shows a representative trajectory on the mPEG surface obtained with the stereoscopic part of the system. The cyprid swam close to the surface, did not

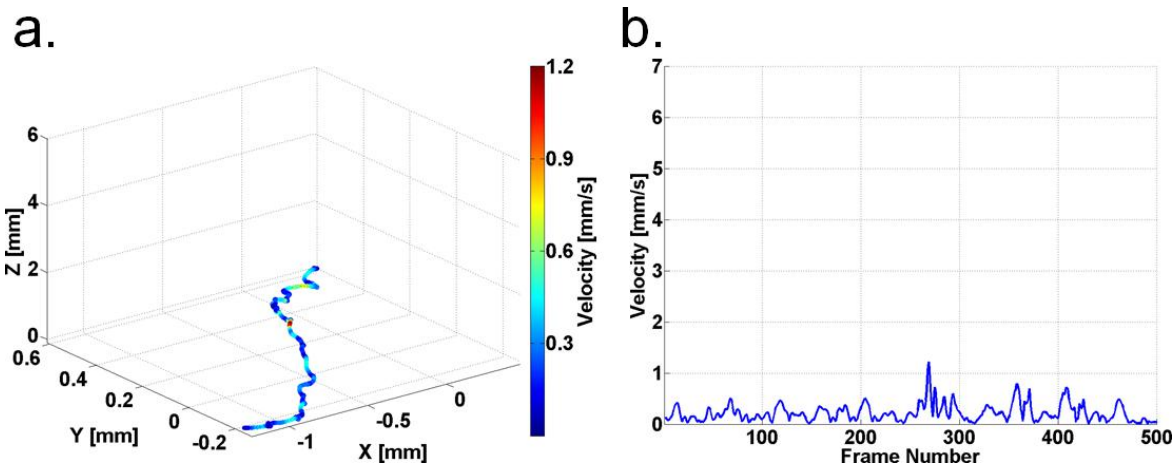

Figure 5.26.: Cyprid exploring the mPEG surface. (a) A representative trajectory of a cyprid of *Balanus amphitrite* exploring the mPEG surface and (b) the velocity profile of the trajectory. An exemplary touchdown event, detected by the iSPR during this segment of the trajectory, is shown in Figure 5.27

change swimming patterns and exhibited low velocity. In addition, the velocity profile (Figure 5.26b) did not reveal any major changes and no distinct resting phases could be detected. On the contrary, a rather continuous and linear way of moving was observed.

It seemed that the cyprid experienced the surface as non-attractive and the chemical cues did not trigger a close surface inspection behavior, but rather exploration and swimming were involved [53].

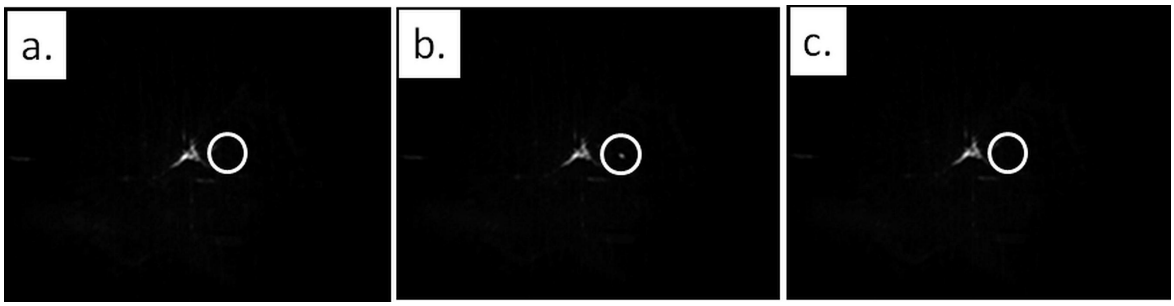

Figure 5.27.: iSPR images demonstrating a touchdown event on an mPEG surface. The image sequence shows the occurrences of a touchdown event which was not observable (a) before the event, (b) occurred for a short period of time (marked with a white circle) and (c) disappeared after the event.

In Figure 5.27 a part of the iSPR signal corresponding to the representative trajectory is shown, at three different time points around a touchdown event. As it can be seen, no iSPR signal was present before (Figure 5.27a) the touchdown. Interestingly, this event (Figure 5.27b) occurred for a very short period of time and then the signal disappeared (Figure 5.27c). The reason for this could be either that the cyprid left the field of view of the iSPR detector or it swam up in the water volume. The information from the stereoscopic system (Figure 5.26) showing that no swimming in the water volume was present proves that the cyprid left the field of view, remaining at the interface exploring and not leaving any organic deposit. The presence of touchdown events, which do not leave any footprint deposit behind has already been demonstrated by Aldred et al. [26] for non-attractive surfaces. Combining the findings from both systems it can be stated that the exploration and search triggered by the surface properties seemed to be complemented by few touchdown events which did not leave any footprints on the surface.

The other surface, MUDA, is known to be attractive for settlement and a representative trajectory is shown in Figure 5.28a. The trajectory consisted of two parts - a swimming part in the water volume and an exploration part, where the cyprid inspected the surface. The exploration part consisted of several walking segments (highly linear, with low velocity) which were connected by faster movement parts (up to $\approx$7 mm/s), shown in the velocity profile (Figure 5.28b). Additionally, the patterns contained more sharp turns compared to the mPEG surface. A part of the corresponding iSPR signal obtained on the MUDA surface is shown in Figure 5.29. As it can be seen in Figure 5.29b, the cyprids exhibited two touchdowns and left an organic deposit behind (Figure 5.29c). It has been speculated in literature whether the reason for leaving a high amount of footprints on the negatively charged surface is related to the

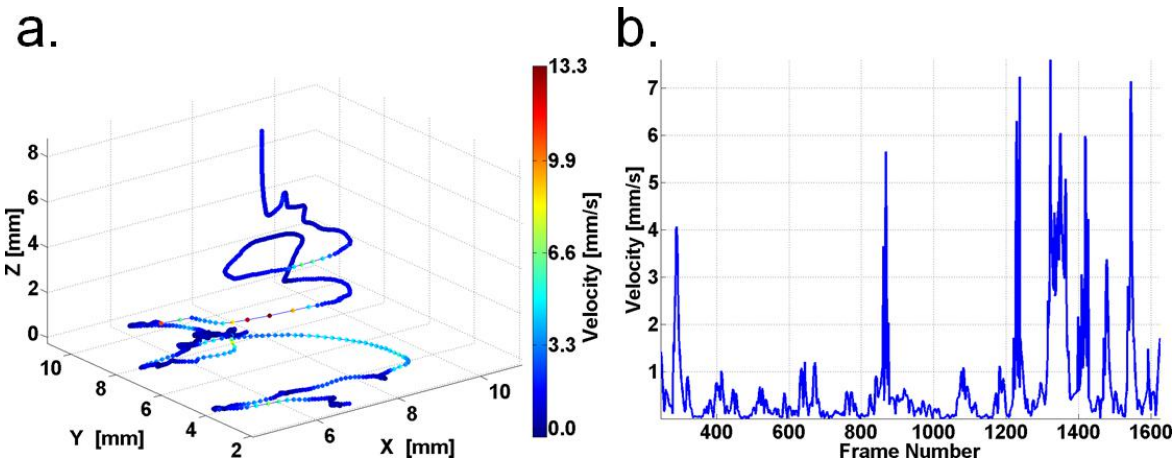

Figure 5.28.: Cyprid exploring a MUDA surface. (a) A representative trajectory of a cyprid of *Balanus amphitrite* exploring the MUDA surface and (b) the velocity profile of the trajectory. An exemplary touchdown event, detected by the iSPR during this segment of the trajectory, is shown in Figure 5.28

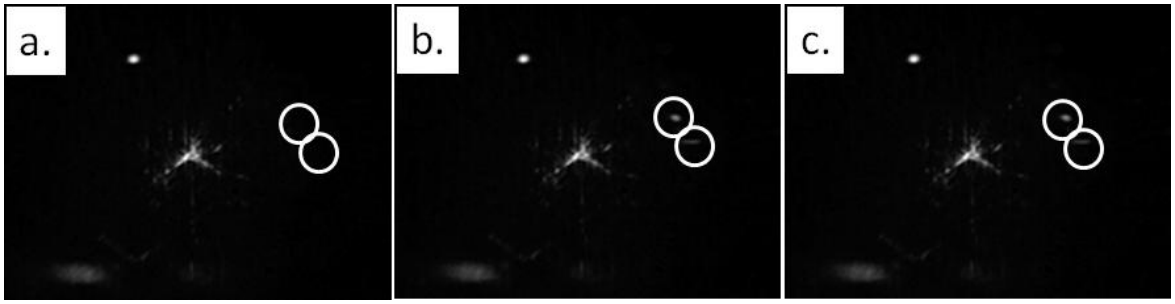

Figure 5.29.: iSPR images demonstrating a touchdown events on an MUDA surface. The image sequence shows the occurrences of the touchdown events which were not observable (a) before the event, (b) occurred for a short period of time (marked with a white circle) and (c) remained there after initial touchdown, leaving an organic material behind.

charge of the deposited material [26] but this is still not fully understood. Combining the observations from both systems it could be concluded that the cyprids exhibited a more dynamic behavior on the attractive MUDA SAM. They swam in the water volume, entered the surface inspection mode, left footprints behind and eventually settled more on these surfaces.

5.4.3. Summary: Interaction with the interface

Concluding, in this chapter it could be shown that the combination of imaging surface plasmon resonance and video stereoscopy was beneficial. This novel system can be used to gain a better knowledge on the swimming, exploratory and inspective rituals of barnacle cyprids. The advantage is that this can be observed simultaneously and the information is stored for post-processing. The behavior of larvae on two surfaces with different chemical terminations has been presented - a highly hydrated mPEG and a negatively charged MUDA surface. The mPEG surface is known to be resistant to marine biofouling whereas the negatively charged surface possesses attractive properties. In the first feasibility test, it could be shown that the system could detect behavioral differences in the swimming as well as in the close surface inspection process in response to chemical cues from the surface. E.g. on the mPEG cyprids did not change swimming patterns, exhibited low velocity and high linearity, combined with less surface contacts, which did not leave any organic material deposited on the substrate. On the contrary, on the MUDA surface the larvae demonstrated patterns characteristic for surface exploration, with several direction changes and different velocities. Interestingly, on this surface more touchdown events occurred and organic material ('footprints') was left behind. These observations still remain to be confirmed statistically, but they already demonstrate that with this system effects can be revealed which remain covered for each of the techniques separately.

One limitation, originating from the nature of the iSPR technique, was the small size of the detection field or field of view. This highly limited the observable area of the iSPR and, thus, also of the stereoscopic system. A valid direction for improvement of the setup could be an automatic stage, following cyprids with help of real-time tracking and positioning the stage at coordinates, detected by the stereoscopy system in order to provide optimal conditions for an iSPR measurement. Such an automated setup would allow to image cyprids during the whole cycle of exploration and surface inspection in the whole field of view, thus extending the knowledge of this highly dynamic process.

5.5. Influence of surface conditioning on the exploration process

As it could be shown in previous sections, cyprids interact with the interface and often leave an organic deposit ('footprints') behind. In a more general context all surfaces immersed into the ocean adsorb dissolved organic material, composed of compounds including proteins, lipids, polysaccharides and amino acids [42]. These form a layer, which is defined as a "macro molecule film or conditioning film" and it has been reported to mask the chemical end group and, thus, to strongly compromise the initial purpose of surfaces [42, 107].

In this chapter the influence of conditioning film formation on the exploratory behavior of cyprids has been quantified on pristine and pre-conditioned hydrophilic (-OH, HUDT) surfaces, evaluating the motility parameters introduced in Chapter 5.2: velocity, swimming area coefficient and the occurrences in the lower swimming region (LSR). The test surfaces were conditioned with natural seawater, collected from the "raft" test site of the FIT in the Indian River Lagoon, located at the east coast of Florida about 5 km north of the Sebastian inlet, Florida (27°53′59.18″N; 80°28′28.34″W), in collaboration with Isabel Thome (University of Heidelberg, Germany).

5.5.1. Effects on the exploratory behavior

Following the protocol described in Section 3.1.2, hydrophilic surfaces (HUDT) were pre-conditioned with filtered fresh seawater for 24 h. After carefully removing the remaining water from the quadriPERM containers, the experiments were immediately started. Figure 5.30 shows the results of the settlement assay for pristine HUDT, pre-conditioned HUDT, DDT and a PS control. The settlement values for the pris-

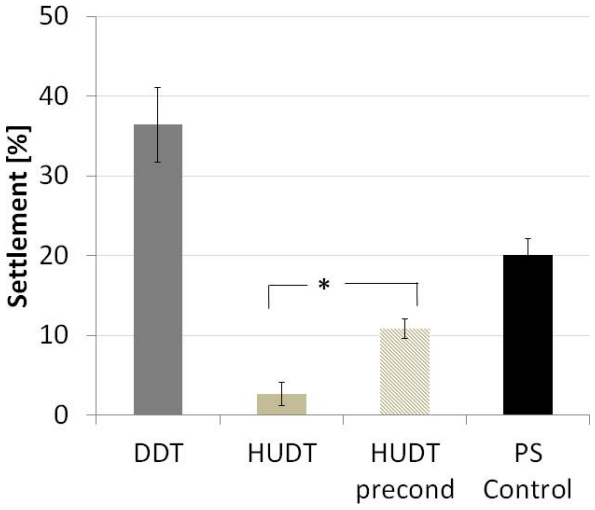

Figure 5.30.: Influence of conditioning on the settlement of *Balanus amphitrite* cyprids. The results of the settlement assay on a pristine and pre-conditioned hydrophilic surface (HUDT), a hydrophobic (DDT) surface and a polystyrene control were compared. It could be demonstrated that settlement of cyprids was enhanced on HUDT induced by preconditioning. (Error bar represents the standard error, N=3, Student's t-test, *: $p<0.05$)

tine surfaces were in line with the findings described in the previous chapter (Chapter 5.2) and confirmed the good physiological condition of the larvae (settlement on the polystyrene control 20.0 %±2.1 %). In addition, for the pristine surfaces the results were as expected. The settlement on the hydrophobic DDT (shown here as an attractive surface for comparison) was high (36.4 % ± 4.7 %), whereas the settlement

on the hydrophilic HUDT was the lowest (2.6 % ±1.4 %). The settlement on the pre-conditioned HUDT was 5 times higher than on the pristine version (10.9 %±1.3 %) and these were significantly different (Figure 5.30). Although this increased value did not reach the levels for the attractive surfaces (DDT and polystyrene control) it was still obvious that there was a settlement enhancing effect on the repellent HUDT, originating in the formation of the conditioning film. One question which arose from here was, whether such differences were also present and detectable in the exploratory behavior of cyprids. For this purpose, as shown in Figure 5.31, the occurrence values

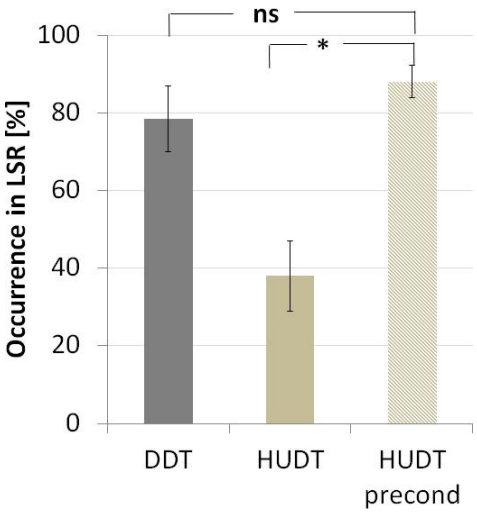

Figure 5.31.: Occurrence of cyprids in the LSR on pristine and preconditioned surfaces. The distribution of cyprids in the lower swimming region was investigated on pristine hydrophobic (DDT) and hydrophilic (HUDT) surfaces as well as a pre-conditioned hydrophilic surface (HUDT precond). The analysis of the data showed that the LSR of the pre-conditioned HUDT was higher populated than the pristine version and the occurrences were comparable to the occurrences for the attractive DDT. (Error bar represents the standard error, N=3, Student's *t*-test, *: $p<0.05$, ns: $p>0.05$)

of the cyprids in the lower swimming region (LSR) were considered. The occurrence of larvae in the LSR for the DDT surface (78.5 %±8.5 %) as well as for the pristine HUDT (38.0 %±9.0 %) were significantly different and comparable to the values discussed in Chapter 5.2. These correlated well with the respective settlement shown in Figure 5.30. The conditioning layer highly influenced the occurrence values of cyprids in LSR on the pre-conditioned HUDT surface. As it can be seen from Figure 5.31, the occurrence of 88.1 %±4.2 % was even higher than for DDT, indicating that cyprids spent more time in close proximity to the chemical interface.

In order to further quantify the motility and behavior of the cyprids, mean velocity and swimming area coefficient were calculated (Figure 5.32). The mean velocity (Fig-

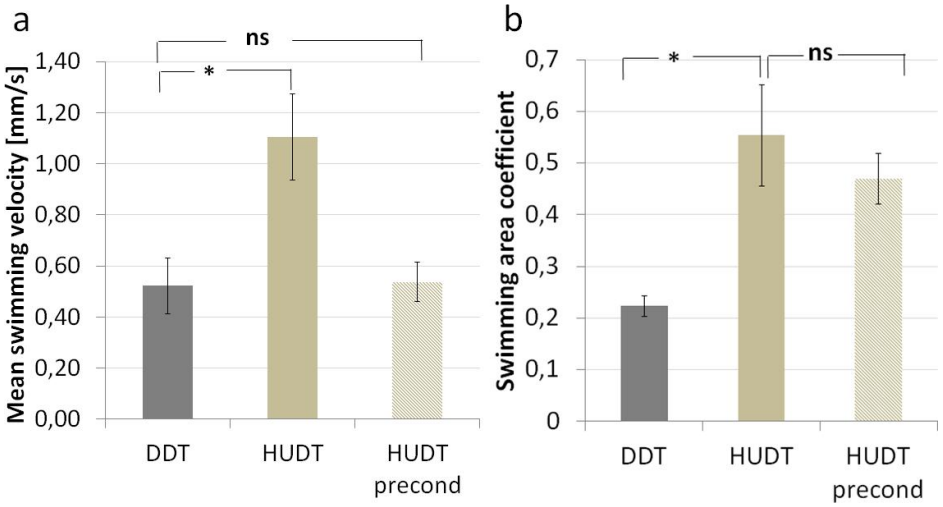

Figure 5.32.: Exploration parameters on pristine and pre-conditioned surfaces. (a) Mean velocity and (b) swimming area coefficient on pristine hydrophobic (DDT) and hydrophilic (HUDT) surfaces as well as a pre-conditioned hydrophilic (HUDT precond) surface. The parameters revealed that cyprids explored, initially unattractive, pre-conditioned HUDT surfaces in the same manner as attractive DDT. (Error bar represents the standard error, N=3, Student's *t*-test, *: $p<0.05$, ns: $p>0.05$)

ure 5.32a) on the DDT surface (0.52 mm/s ± 0.11 mm/s) was only half of the velocity on the pristine HUDT (1.10 mm/s ± 0.17 mm/s). These values were significantly different with a p-value of $p<0.005$, verified with a Student's *t*-test. Interestingly, the mean velocity on the pre-conditioned HUDT surface was highly reduced to 0.54 mm/s ± 0.10 mm/s. Another Student's *t*-test could show that the values for the velocity on the attractive DDT and the pre-conditioned unattractive HUDT became practically the same (not significantly different).
The comparison of the swimming area coefficients, describing the area visited by cyprids, is shown in Figure 5.32b. The value of 0.22 ± 0.02 on the DDT was the lowest in the group. A low coefficient described movements which were rather localized and focused. The opposite was observed on the pristine HUDT surface where a high swimming area coefficient (0.55 ± 0.09) pointed toward a more broad search region and less interest in any particular part of the surface. Interesting, although the coefficient values on the pre-conditioned HUDT (0.46 ± 0.05) were reduced, they still remained similar to the ones for the unconditioned HUDT surface.

5.5.2. Summary: Conditioning film

Conditioning influenced the exploratory and settlement behavior of cyprids. It was shown that the HUDT surface, originally non-attractive for settlement, became more attractive and settlement on it was increased up to 5 times (Figure 5.30). Additionally,

the occurrence of cyprids in the lower swimming region (close to the chemical interface) was highly increased for the conditioned HUDT and it reached levels of the attractive DDT. Although the velocity was reduced as a result of conditioning, the explored swimming area was still in the range of the pristine HUDT surface. One explanation of these effects is that the chemical end group, which determined the attractiveness of the surface for settlement, became masked by the conditioning layer, and cyprids became more attracted to explore and settle on these surfaces. Apparently cyprids were motivated to decrease their velocity and swim close to the liquid/solid interface, probably attracted by pheromones [97], or because unable to sense the original repellent chemical end group masked by the film. This change in the exploratory behavior was logically projected onto the settlement behavior, and more cyprids settled on the conditioned than on the pristine version of HUDT.

5.6. Exploratory behavior on commercial coatings

After the quantification of the basic patterns in cyprid swimming, as well as the description of the general exploratory behavior on model surfaces (SAMs), the behavior of cyprids on commercially available coatings was investigated. Because of the success of the fouling-release (FR) technology in the battle against marine biofouling, two widely spread silicone-based FR paints were selected for the experiments. Their low surface energy decreases the organism's ability to form a strong interfacial bond with the surface [22]. Since these surfaces possess a high smoothness at the molecular level, once a vessel is moving beyond a critical velocity [8], the organisms get dislodged. Additionally, they deploy shear and tensile stress to aid removal of fouling [22]. To quantify their antifouling properties, first settlement assays were performed and subsequently the motility of cyprids on surfaces coated with these paints was analyzed.

5.6.1. Experimental procedure

The experimental procedure with commercial coatings, differed form the general procedure used for model surfaces, described in Chapter 4.5:

- *Test surfaces:* Samples from two coating types were selected in order to characterize the settlement and exploratory behavior. The first coating (here denoted as HH) was, according to the description of the manufacturer, a biocide-free, two-component, fouling release silicone coating delivering a smooth hydrophobic surface with a low energy. The second surface (HGel) was a fouling release coating on which a hydrogel micro layer is generated which prevents fouling organisms from firmly adhering, thus allowing an easy and effective self-cleaning.

- *Pre-leaching of surfaces:* The experiments were performed with two batches of cyprids. For one of the batches the surfaces were pre-leached in order to discard any

remaining solvents, involved in the cross-linking and curing process of the coating. During the procedure, the samples were immersed in a container filled with Milli-Q water, steered for 48 h, using a magnetic steerer, and finally rinsed with clean Milli-Q water and air-dried.

- *Contact angle measurement:* The static contact angle, as described in Section 3.2.1, was measured for the two coatings. The HH surface, which is known to possess highly hydrophobic properties demonstrated, as expected, a contact angle of 105° ± 5° (Table 5.1). Surprisingly, the hydrogel-based coating, HGel, also showed a similarly high contact angle of 102° ± 2°. Ths could be contributed to the fact that the measurement was performed immediately after releasing the droplet on the surface, thus not accurately representing the wettability of the surface. A dynamic contact angle measurement should be used in the future in order to provide results closer to the expectations, especially if the HGel exhibits a high hysteresis in the contact angle.

Surface name	**Contact angle**
HH	105° ± 5°
HGel	102° ± 2°

Table 5.1.: Measured contact angles for the tested surfaces. The error values represent the standard deviation of 3 samples measured at 3 different spots.

- *Settlement assay:* The settlement assays were performed following the protocol described in Section 4.5.4, but cyprids were placed in a droplet, rather than a container filled with seawater. The procedure was as follows: 20-30 cyprids were inoculated in a droplet either on the quadriPERM culture vessels (polystyrene control) or on glass slides with the coatings of interest (HH or HGel). The samples were kept in an incubator to ensure stable environmental conditions allowing the cyprids to metamorphose and settle permanently. After 48 h the amount of settled cyprids was quantified by common light microscopy.

- *Motility analysis:* For quantification of the motility of the cyprids on the coatings an activity analysis was performed. First, a median of N subsequent frames was calculated and then subtracted from each of them, thus eliminating static points and detecting only signal from active larvae. Then, the N frames were binarized and projected on a single frame using summation. The standard deviation of the pixels of the resulting image was used as a parameter describing the activity of the cyprids, because only if the larvae moved between the frames, they were detectable in the image. In this experiment the number of frames for the calculation was $N = 1500$, thus representing the combined motility for 1 min. The total time quantified with this approach was 240 min.

5.6.2. Settlement and motility analysis

In order to obtain descriptive values for the antifouling properties of the tested surfaces, settlement assays were performed and results are shown in Figure 5.33. As it can

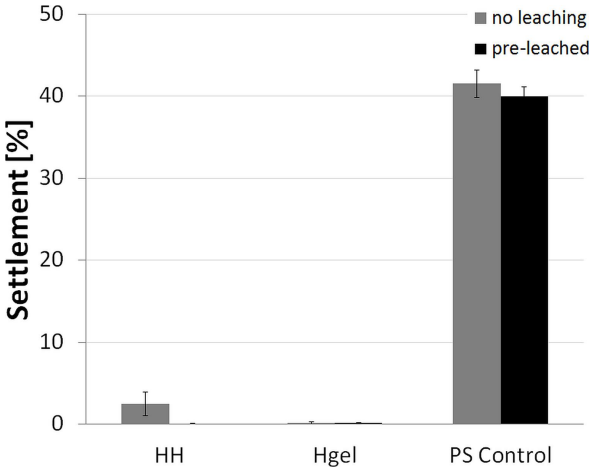

Figure 5.33.: Settlement of cyprids on commercially available coatings. Results of the settlement assays after 48h, performed with two different batches of cyprids for the fouling release HH and HGel surfaces and a polystyrene control. The two series show the results for unleached and surfaces preleached for 3 weeks. It was confirmed that commercially available coatings have an excellent antifouling properties. (N = 3, error bar representing the standard error of the mean).

be seen from the high settlement on the control (polystyrene) for both experiments (ca. 40 %), the cyprids were in a good physiological condition and the values were comparable to literature reports [13]. The settlement on the HH proved to be very low (<5 %). Also the settlement on the HGel surface was extremely low for both batches of cyprids. As expected, these coatings exhibited excellent anti-fouling properties, even under the static experimental conditions in the laboratory. It should be noted, that preleaching did not influence the settlement values as shown in Figure 5.33.

To test how the exploratory behavior of the cyprids was influenced on the surfaces, and to compare it to behaviours observed on the model surfaces (SAMs, Chapter 5.2), the motility was characterized and the results are shown in Figure 5.34. The value for the first time point was used to normalize the data and to obtain the relative motility. In the first part of the figure (0 min-12 min), the activities for all of the surfaces seemed to have similar values. The activity decreased with time for all samples, including the highly attractive polystyrene control, which could be interpreted as an increased interest of the larvae in the surfaces. After 240 min (second part of the x axis), the experiment showed, that the activity on the control surface remained similar to the activity at the beginning. Surprisingly, the values for HGel and HH were very low and remained constant for the whole duration of this observation period. Since it

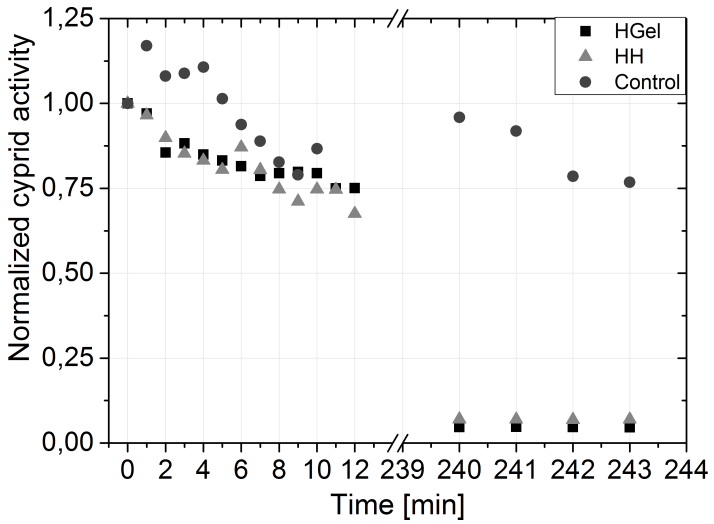

Figure 5.34.: Analysis of the cyprid motility on commercially available coatings. The cyprid activity was normalized with the first point, thus demonstrating only the change of motility with respect to this point. The values were measured for the test surfaces as well as for polystyrene control and represent the measurement in the first 12 min after initial surface exposure and 4 h after that (mind the different scales of the x axis).

was determined during the settlement experiment, that cyprids did not settle on these surfaces, the lack of activity could not be contributed to settlement and it rather meant that the condition of the cyprids had changed. When inspected under the microscope, two different behavioral patterns could be observed: cyprids which had a contact with the surface were completely non-motile and inactive. From a first look also the internal body movements seemed to have ceased functioning. In turn, cyprids which were caught in the meniscus (at the air-liquid interface) were grouping and swam actively on the water surface as shown in Figure 5.35, even 4 h after inoculation. These cyprids were excluded from the motility analysis shown in Figure 5.34, but were used to prove that the mortality was related to surface contact and did not originate in a bad cyprid condition.

5.6.3. Summary: Commercially available coatings

During the experiments, with different batches of cyprids, the motility analysis showed that as soon as the cyprids contacted the silicon based test surfaces (HH and HGel) they remained at the interface and the motility gradually decreased during the first 10 min, leading to a complete stop 4 h after first exposure. None of the typical exploration patterns (i.e. *swimming* and *sinking*, *spiraling*, ect.) was observed. Interestingly, those cyprids never attempted settlement or metamorphosis as the settlement data

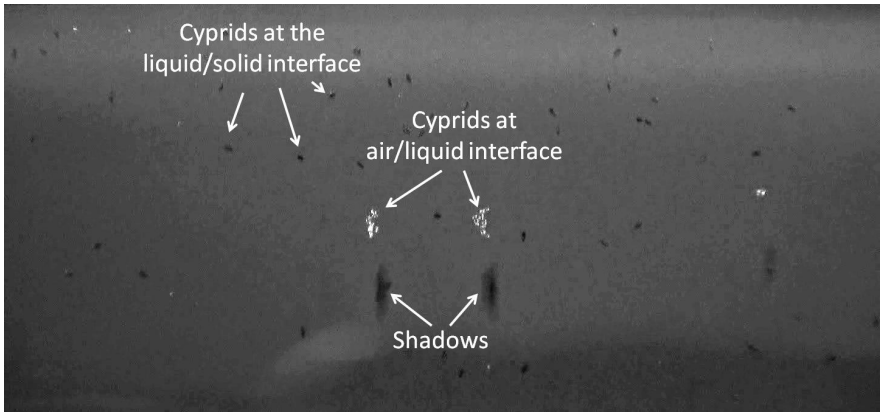

Figure 5.35.: Cyprids captured in the meniscus. These larvae floated at the liquid/air interface and were active also 4 h after inoculation, whereas cyprids on the surface became non-motile shortly after first surface contact.

was very low on both HH and HGel compared to the polystyrene control. In contrast, cyprids which never had contact with the surface would float up and join the ones trapped in the meniscus, where their motility remained relatively constant even after 48 h (optical inspection). Both, the rapid reduction in cyprid activity and the inhibition of settlement and metamorphosis pointed towards an adverse (if not toxic) effect upon surface contact. One reason for that could be the short pre-leaching procedure (48 h) which did not completely remove the remaining curing agent. For the future, in order to guarantee the complete removal of any toxic components from the coatings, a 90 d pre-leaching should be applied. Furthermore, as stated by Thomason et al. [66] a curing period of 3 weeks should be considered rather than the 24 h applied here. Under such conditions, it would be interesting to compare the results described in this study with results obtained using these new technological parameters in order to investigate the reason for the toxic effect on the cyprids.

5.7. Measurements under field conditions

Experiments under field conditions, overcome the limitations of laboratory measurements, i.e. lack of natural water movements and static micro environment, and thus provide a more realistic view on the exploratory behavior of cyprids. It is known that hydrodynamic forces influence the settlement behavior of larvae (discussed by e.g. Mullineaux et al. and DiBacco et al. [24, 193]). Miron et al. [194] have presented several models describing settlement of cyprids as a function of larval supply, immersion duration and hydrodynamic properties of the environment and could demonstrate that the presence of water movements is a major factor in settlement enhancement. Because of these findings, literature reports have questioned the validity of extrapolation of laboratory settlement results to cypris larvae settlement in field situations [195]. As a consequence, field experiments are normally used for the test of coatings against biofouling (see [25, 196–200]) although most of these experiments still rely only on post-settlement approaches, e.g. settlement assays, colonization quantification, etc.

In this chapter the challenges for extraction, quantification and description of exploratory behavior underwater are discussed and a modification of the stereoscopy setup is presented which allows measurements in the field. Finally, underwater setup is discussed with respect to its feasibility, analyzing the outcome of the proof of principle experiments.

5.7.1. Stereoscopy setup for field applications

The presence of factors influencing the performance of the stereoscopy setup in field conditions, e.g. by decreasing the quality of the video signal, introduced additional challenges for the system. To counteract these factors a new version of the setup was designed in collaboration with Hernan Sendra (University of Heidelberg, Germany) and Klaus Schmitt (Workshop of the University of Heidelberg, Germany), and a CAD model is shown in Figure 5.36.

Since the cameras were submerged and operated underwater, a waterproof case was used, which is schematically presented in Figure 5.36 in blue (Official name: Sports Pack Waterproof Case; Model: SPK-HCG; Producer: Sony). During the measurement, the cameras were placed in the housings and then the setup was aligned and submerged underwater. Because of the temperature difference inside and outside of the water, anti-fog inserts (Official name: GoPro Anti-Fog Insets; Producer: GoPro) were applied in order to avoid condensation on the housings and the objectives. To guarantee a stable distance between sample and camera objectives and a constant angle at which the cameras imaged the sample, thus minimizing the error of the coordinate extraction algorithm, a rigid, modular and extendable frame (Figure 5.36 in grey) was constructed. The frame kept the camera positions and orientations fixed and allowed to avoid misalignment after calibration, thus eliminating erroneous tracking results. It is important to point out that in addition to the standard settings of the

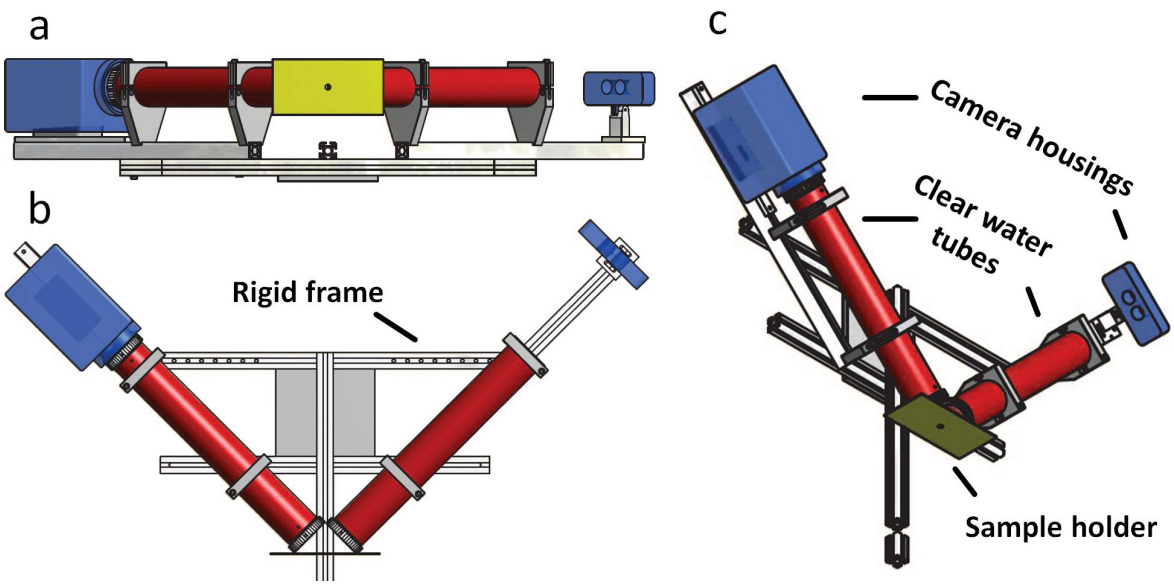

Figure 5.36.: CAD model of the underwater setup. The main parts of the setup, designed in collaboration with the Workshop of APC / University of Heidelberg, are shown ((a) front, (b) top, (c) side view).

camera described in Chapter 4 (`AUTOFOCUS`, `TELEMACRO`), for the measurements under water the values of two new parameters needed to be adjusted: `STEADYSHOT` and `AUTO WHITEBALANCE`. The first mode activates an image stabilisation algorithm developed by Sony (Sony Corporation, Tokio, Japan), which compensates for movements introduced by the user, by adjusting the internal optics or the image sensor. This setting should be switched **off** for measurements underwater, because, due to the wavy environment it artificially distorts the input signal. The second parameter is the `AUTO WHITEBALANCE`. It automatically adjusts the colors of the input signal, thus often degrading its quality. In addition, because of the constantly changing lighting situation of the underwater environment (presence of waves, reflections, etc.), the automatic adjustment of white balance introduces a considerably high amount of consecutive frames with different brightness properties, which complicates further processing. This setting needs to be switched **off** during measurements in the field.

One major factor influencing the quality of the video signal was the poor lighting situation underwater. It was improved by introducing 4 underwater lights (each consisting of four 7 Watt LEDs, gun-lux GmbH, Germany) as it can be seen in Figure 5.37a. The turbidity of seawater was challenging for the image quality as well, since it filled the space between camera objective and objects of interest and introduced additional noise (e.g. back scattering, reflections, absorption of light, etc.). In order to compensate the influence of these factors, tubes filled with air (or clear water) were installed between camera objective and the sample surface (Figure 5.36 in red). They guaranteed controlled environmental conditions and enhanced the quality of the video

signal drastically. The different types of media between camera and sample, introduced by the tubes, were compensated by the calibration procedure.

Since the deployment of the system underwater was normally performed from a boat, a live preview of the camera images needed to be available and transmittable to a remote visualization device in order to control the recording and imaging procedure. For this purpose the `A/V` interface of the cameras, as well as the `DC IN` port were connected to a laptop with an external graphic adapter and a power source respectively. The `A/V` interface was used for life preview transmission as well as for the synchronization of the cameras, since the LANC controller was connected to it as well.

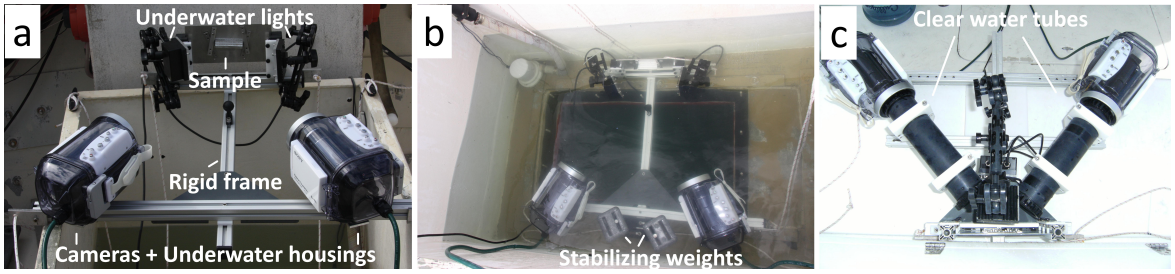

Figure 5.37.: Images of the underwater setup and deployment procedure. (a) The underwater setup with sample holder, underwater lights, camera housings and a rigid frame. (b) Deployment of the setup from the wet well of the boat. (c) An updated version of the setup including the clear water tubes for enhancement of image quality.

The underwater setup is shown in Figure 5.37a without the clear water tubes and in Figure 5.37c with the tubes installed. As it can be seen, the cameras imaged the sample placed in the sample holder at an angle of ≈80°-85°. The underwater lights were placed to illuminate the sample from four directions and to provide a regular lighting and simultaneously not to prevent marine organisms from exploring the surface by blocking the access to it. One additional feature of the setup, which ought to be mentioned, was the uneven distribution of weight in the system. Especially when it was operated with tubes filled with air, it tended to float. Furthermore, the camera underwater housings induced floating or tilting in vertical direction, letting the sample holder sink deeper and leave the cameras at the water surface. To overcome these effects, diver weights were attached to the rigid frame (Figure 5.37b), which retained the stability of the setup and it sank perpendicular to the direction of gravitational force.

5.7.2. Test sites

To test the feasibility of the setup for experiments under field conditions, several measurement trips to two test sites with different environmental conditions and predominant cyprid species were performed. The first site was Cape Canaveral Marina (Figure

5.38), Port Canaveral, Florida, USA ($N28°24'26.03''$, $W80°37'24.436''$), belonging to Florida Institute of Technology. This site has been used by the group of Prof. G. Swain for several years for the investigation of marine biofouling organisms and the efficacy of antifouling coatings [59, 196, 200–204]. The fact, that the diversity of the available organisms together with their seasonal availability were studied in detail was very advantageous during experimental planing. In addition, as it can be seen on Figure 5.38a, the group provided a boat for accommodation of the equipment.

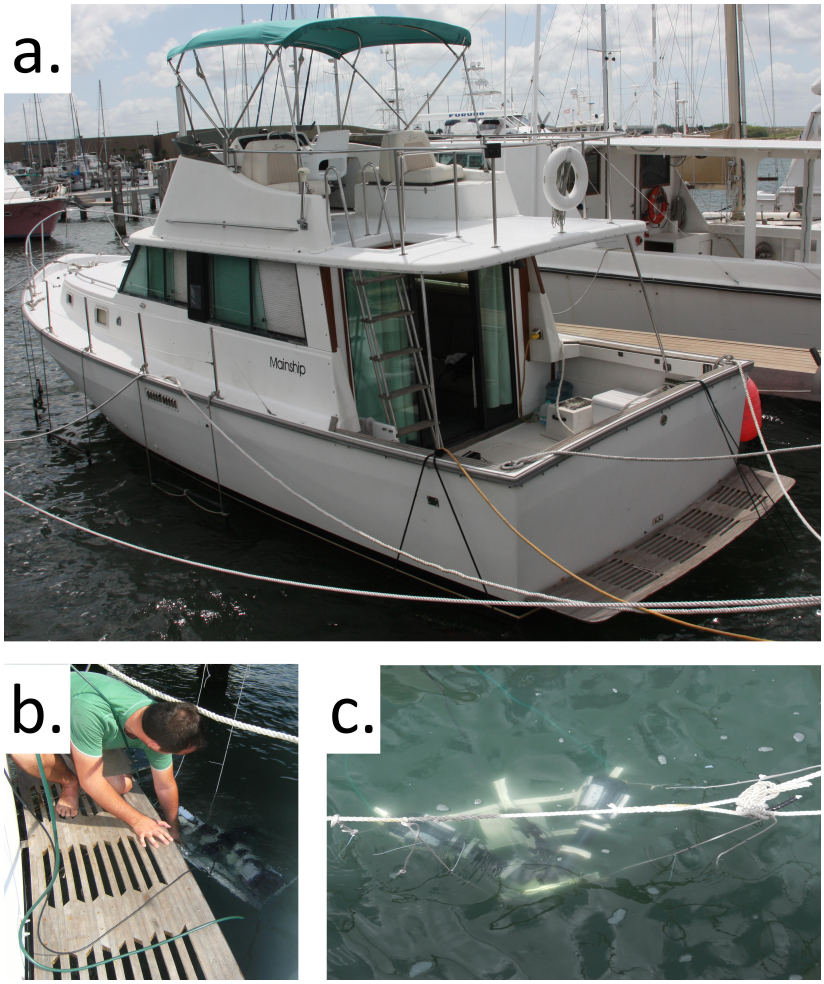

Figure 5.38.: Deployment procedure at Cape Marina test site. (a) The stereoscopy setup at Cape Marina test site was deployed underwater from a boat, provided by the group of Prof. G. Swain. (b) The boat with the platform for easier deployment of the setup were used to submerge the system underwater. (c) Once underwater the setup was stabilized with ropes and diving weights.

In addition, the 'Mainship' vessel possessed a platform (Figure 5.38b) for direct submersion of the setup underwater and a power source to supply the underwater

lights and cameras. The cyprids available at this test site were shown to be of *Balanus amphitrite*, but also a high variety of other marine biofouling organisms were available [201]. The main reason for this diversity was the high nutrient level in the sub-tropical waters of the Atlantic ocean near Florida and this made tracking and pre-processing challenging.

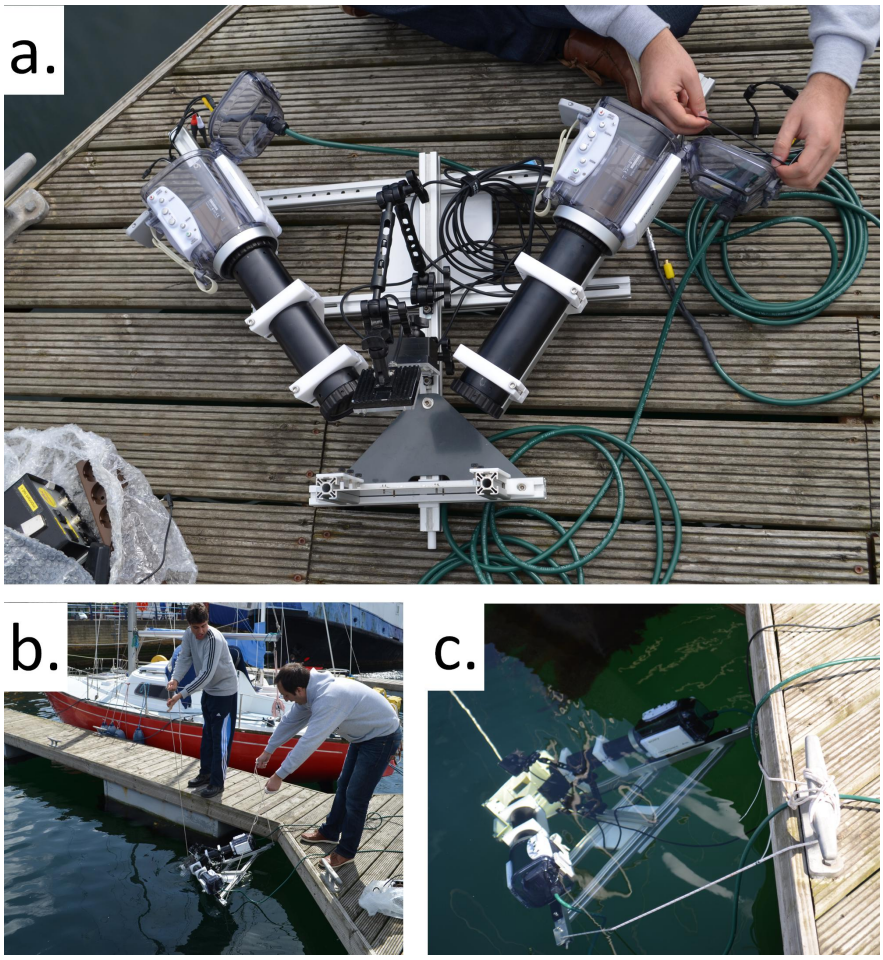

Figure 5.39.: Deployment procedure at Hartlepool Marina test site. At the test site in Hartlepool Marina (access provided by International Paints - Akzo Nobel) (a) the underwater setup was submerged directly from (b, c) the pier.

The second test site was Hartlepool Marina (shown in Figure 5.39), Hartlepool, UK ($N54°41'31.884''$, $W1°11'55.211''$), belonging to International Paint - Akzo Nobel. The measurements there were performed directly from the pier of the marina as shown in Figure 5.39b. One major advantage of the boreo-arctic region [183] was that the water was more clear because of the fewer organisms swimming in the field of view. The main barnacle species, which was observed at the test site was *Semibalanus balanoides*. From experimental point of view, the environmental conditions at the Hartlepool Marina test

site were more favorable, because of the low turbidity of the water, the lack of highly dynamic wavy conditions in the marina and the size of the cyprid species (*Semibalanus balanoides* are $\approx 2\times$ bigger than *Balanus amphitrite*). In contrast, the occurrence of cyprids at this test site was much lower than the sub-tropical site and their seasonal availability was limited to a short period of 1-2 months between April-June. The Cape Marina test site had a higher cyprid population, but the quality of the water (from an image processing point of view) was not optimal.

5.7.3. Proof of principle measurements

To visualize the effects of the underwater turbidity on the quality of the video recordings, frames from a laboratory experiment (Figure 5.40b) and from a measurement in the field (Figure 5.40a taken at Cape Marina) are shown. The contrast between

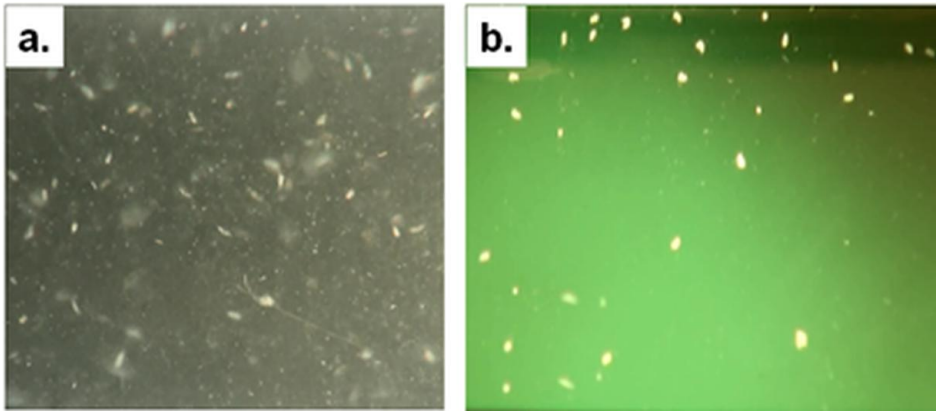

Figure 5.40.: Image quality from field and in the lab. Comparison of the image quality for a frame (a) from the field and (b) from a video in the laboratory. The number of sources of noise in the field was higher, which can be seen from the artifacts in the image.

the green-yellow background and the objects of interest in the lab (Figure 5.40b) was higher and during tracking and post-processing a more accurate and time optimized outcome was produced. On the contrary, in the underwater frame (Figure 5.40a), there were several artifacts: blurred objects caused by dirt spots on the camera housing, lower lighting which decreased the contrast between background and cyprids and several elongated objects representing different marine organisms. It is worth mentioning that the frame shown in Figure 5.40a was obtained with the clear-water tube system installed, and the quality proved to be sufficient for the tracking experiments.

To demonstrate the advantage of the setup for the extraction of the dynamics of the biofouling process, surfaces coated with a PEG SAM and a positively charged (TMA, $-NMe_3^+$) SAM were kept underwater for 60 min (Cape Marina test site), during which the swimming movements of the biofouling organisms were recorded and the frames

were extracted from the videos. Then, the amount of biomass on the surfaces was quantified using a simple thresholding method and evaluating the central moments (area, form, orientation) of the objects in the remaining binary image. To quantify the accumulation of organisms on the surfaces, the amount of material was evaluated every 2 min and the results are shown in Figure 5.41. In addition, a negatively charged MUDA surface was included in the comparison. It is obvious that the biomass on PEG

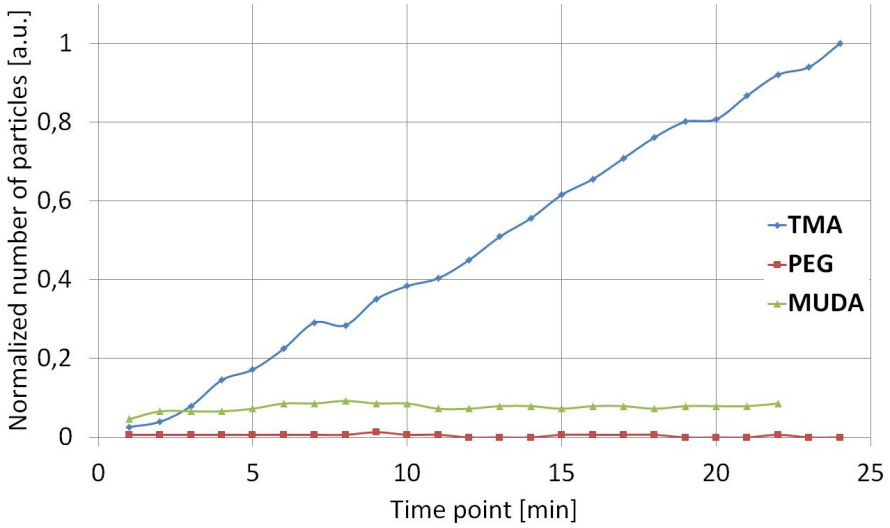

Figure 5.41.: Normalized accumulation of organic material. The amount of accumulated organic material (organisms) is shown for a repellent PEG surface, a positively charged TMA surface and a negatively charged MUDA surface.

was very low. It can also be seen that while the MUDA SAM behaved similar to a repellent surface, the amount of biomass on the positive one increased with time and was the highest. Figure 5.42 shows a section of the two test surfaces after 60 min and it can be noted that on the TMA the accumulation of biofouling organisms was much higher than on PEG. These observations were in good agreement with reports that surfaces with a positive charge induce [71] and PEG surfaces inhibit [205] colonization.

The results demonstrated the general applicability of the system to reveal the dynamics of colonization under field conditions. In order to prove the feasibility in behavioral analysis applications, two exemplary trajectories were extracted from organisms swimming over the MUDA and the PEG surface and are shown in Figure 5.43. The color code represents the swimming velocity on the respective surface. On the MUDA SAM (Figure 5.43a) the magnitudes of the velocity vectors were higher in contrast to the lower values for PEG. In both trajectories an oscillatory component was observable originating from the wavy environment. To further quantify the swimming, histograms of the velocities of the trajectories on both surfaces were calculated and are shown in Figure 5.44. The velocities of the marine microorganisms on the two surfaces revealed certain differences in the behaviors of the organisms. It became obvious that

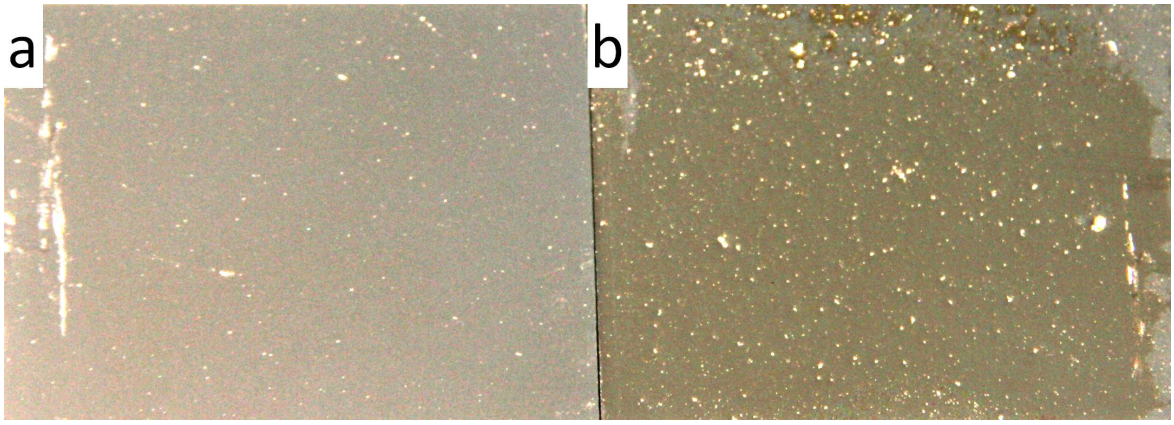

Figure 5.42.: Images of the accumulated organic material. The amounts of material (organisms) on (a) a repellent PEG surface and (b) a positively charged TMA surface after 60 min differed. On the TMA surface more objects were found to accumulate.

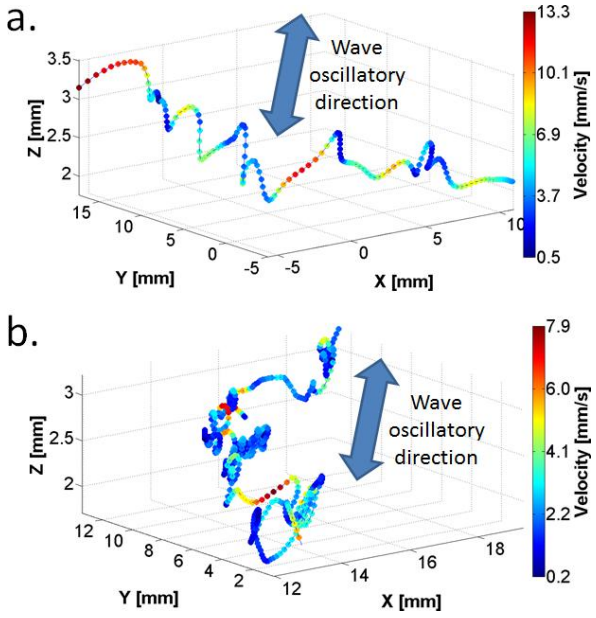

Figure 5.43.: Exemplary trajectories extracted from field experiments. The experiments were performed at Cape Marina test site for (a) a negative MUDA SAM and for (b) a PEG SAM. Color represents velocity values and the direction of the oscillations originating from the wave front is marked with a blue arrow.

the velocity distribution over the MUDA surface was broader and less values close to zero were observed. On the contrary, the distribution over the protein-resistant PEG was narrower with a high peak in the region of velocities close to 0 mm/s.

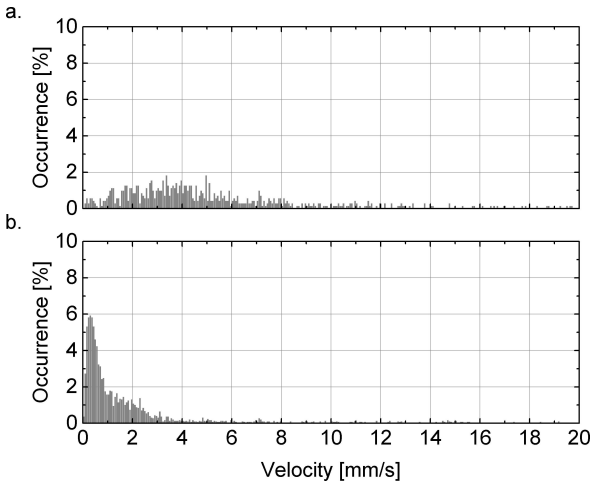

Figure 5.44.: Histograms of the velocities underwater. The distributions of the velocities of swimming cyprids obtained underwater on (a) MUDA and (b) PEG SAMs revealed different profiles.

5.7.4. Summary: Field experiments

The presented setup proved to be capable of imaging marine organisms underwater with sufficient accuracy and efficacy. The proposed form and design, together with the selected parts, were demonstrated to be able to overcome limiting factors like noise, wavy conditions, turbidity of the water, limited lighting, etc. In addition, the possibility to follow the imaging procedure live with an external monitor assured the effective imaging. Finally, it should be noted that the setup was constructed to be highly modular, which allows upgrades as well as transportation and reparation during field experiments.

The data shown in this chapter, although of exemplary nature, could already demonstrate some differences in the swimming of marine organisms. The swimming velocity was a vector consisting of the combined velocities of waves and objects of interest. Further investigations need to verify these initial observations in order to be able to conclude on the exploratory behavior based on statistically backed-up data. Two challenges still remain to be solved in order to improve the performance of the system under field conditions. Firstly, because of the unlimited water volume being investigated in the ocean, the occurrence of events is decreased. During some experiments, even the evaluation of 60 min video contained a low amount of swimming events. This posed a problem, because in order to collect statistically relevant data the duration of measurements was increased. Secondly, the identification of the objects of interest, proved to be a tedious task. Because of the similar sizes, forms and colors of the marine organisms in the field of view it was difficult to differentiate between species. One potential solution for both challenges is offered by analysis of the way of locomotion of the organisms. The presence of the swimming patterns described in Chapter

5.1 could be utilized as an indicator of cyprid behavior in the future, and thus any organism in the field of view not exhibiting these patterns during locomotion could be discarded. In addition, the cameras could sample the field of view periodically remaining in a standby mode during the rest of the time and only if the patterns typical for cyprids have been detected a long-term recording could be automatically initiated. This upgrade would assist the identification of unidentified swimming objects (USO) and at the same time automate the recording process, thus increasing the yield of the experiments.

6. Summary and outlook

The objective of this thesis was the investigation and quantification of the behavior of *Balanus amphitrite* barnacle cyprids during surface exploration, based on the extraction and evaluation of three-dimensional swimming trajectories. The main findings of the work are summarized in Table 6.1.

Table 6.1.: Summary of the main findings and a keyword for easier reference in text.

Key word	Main findings
Swimming patterns (HYP1)	The main reoccurring motion patterns *swimming*, *sinking*, *spiraling*, *rotating* and *walking* were identified along with their occurrence and sequential order during locomotion (Chapter 5.1).
General motility (HYP2)	Cyprids concentrated in three distinct regions - lower, bulk and upper swimming region, at which the interfacial ones were higher populated. Attractive surfaces were explored at lower velocity, locomotion was mostly in the lower swimming region and in a limited spatial extent (Chapter 5.2). On non-attractive substrates the opposite trend was observed.
Close surface inspection (HYP3)	Cyprids step velocity was higher and step duration lower on attractive than on less attractive surfaces (Chapter 5.3).
Interaction with interfaces (HYP4)	A higher number of touchdowns, leaving footprints behind, were detected on attractive than on non-attractive surfaces (Chapter 5.4).
Commercial coatings (HYP5)	Commercially available coatings had a lethal effect on cyprids, probably due to insufficient preleaching applied prior to the experiments (Chapter 5.6).
Conditioning film (HYP6)	The parameters of the exploratory behavior of cyprids were influenced by the presence of conditioning film and these explored a preconditioned non-attractive surface in the same manner as an attractive one (Chapter 5.5).
Field experiments	First feasibility tests, revealed the applicability of the system underwater and demonstrated the biological relevance of the extracted results (Chapter 5.7).

To enable the extraction of 3-D swimming trajectories, a stereoscopic setup was developed. Its hardware consisted of two cameras, a synchronization device, a calibration object and a light source. All components were selected to be widely available (i.e. off-the-shelf camcorders as imaging devices or an LED torch light source). The software provided a pre-processing and calibration script, a semi-automated tracking application and 3-D merging, analysis and visualization software, all developed under MATLAB (The Mathworks Inc., USA). Analysis of the systematic, random, and typical errors of the system proved, that it was sufficiently accurate to track cyprids of the species *Balanus amphitrite* (typical error in the calculated 3-D positions was <5 % of the body size of the organisms).

With the stereoscopic setup, locomotion trajectories of larvae exploring model surfaces under laboratory conditions were collected. The evaluation of trajectories allowed a general characterization of swimming. Five basic **patterns** could be identified, which cyprids exhibited during locomotion: *spiraling*, *swimming*, *sinking*, *rotating* and *walking*. Furthermore, the distribution of these patterns in the data set revealed that *swimming* and *sinking* were most frequently observed. *Spiraling* and *rotating* were defined to be the same pattern, and differed only by the position of the cyprids in the water volume, at which helical movements in the water column were termed *spiraling* and on the surface - *rotating*. *Walking* could be identified as the main surface inspection pattern, although the resolution of the setup did not allow its detailed quantification. In addition, it could be shown that surface contact occurred mainly after the *sinking* pattern. The quantification of the velocity during the *sinking* pattern and the application of a modified version of Stokes law allowed the calculation of the body density of larvae of *B. amphitrite*. Furthermore, with this indirect approach, it could be demonstrated that the body density decreased with age (by 33 % between 3 d and 12 d old cyprids), which was attributed to the decreased concentration of lipid cells in the body of older larvae.

A holistic analysis of the **motility** of the cyprids in the water column revealed, that they accumulated at three water depths relative to the chemical substrate - the lower, bulk and upper swimming region, at which the interfacial regions were higher populated. Utilizing this finding and combining it with the analysis of mean velocity and swimming area coefficient, it could be shown that the accumulation of cyprids in the regions correlated with the attractiveness of the surface for settlement. E.g. on hydrophobic surfaces (higher settlement values) cyprids swam mostly in the lower swimming region with decreased velocities and exhibited a more focused swimming path (a lower swimming area coefficient). On the contrary, on the hydrophilic surfaces (non-attractive), cyprids exposed an opposite behavior: they swam mostly in the upper swimming region, with higher speeds in a broader area. Interestingly, the correlation between the occurrences in the swimming region and surface attractiveness for settlement was proven to disappear after 4 h, but the remaining two parameters retained their settlement indication properties.

Subsequently, the walking motion, or **close surface inspection**, was investigated.

With the developed algorithm for automatic step detection, a faster accumulation of statistically relevant data was achieved. Analysis of the collected data from experiments with pristine and modified (amphiphilic, less attractive) polysaccharide coatings revealed that cyprids tended to increase the step duration and at the same time decrease the step velocity on less attractive substrates. On the contrary, the step parameters on attractive surfaces were opposite - decreased step duration and higher velocity. Especially, the increased step duration on the less attractive coatings suggested a more thorough inspection of these coatings.

A combination of the stereoscopy system with an imaging surface plasmon resonance setup could reveal the specifics of the motility of cyprids and their **interaction with the interface** simultaneously. First feasibility tests demonstrated the quantification of the swimming on polyethylene glycol surfaces and the presence of touchdowns but no deposition of organic material. On the contrary, on the attractive negatively charged SAM, touchdowns as well as footprints were present involving several resting phases, which seemed to indicate the existence of surface cues inducing settlement.

Furthermore, the influence of a **conditioning film** on the behavior was investigated. It could be demonstrated that the presence of such film increased the settlement on non-attractive hydrophilic surfaces. Using the three-dimensional swimming trajectories, it was revealed that on the pristine surfaces, cyprids swam in a linear manner mostly in the upper swimming region with high speeds. The conditioned hydrophilic surfaces were explored in a similar manner as attractive hydrophobic surfaces - swimming was mostly in the lower swimming region with lower speeds and in a focused and localized area. These observations supported the notion that conditioning masks the initial chemical composition of surfaces, thus potentially decreasing the performance of anti-fouling coatings.

Following the investigation on model surfaces, experiments with **commercial coatings** were performed. Analysis of the swimming trajectories demonstrated that the motility decreased gradually on hydrogel-based coatings resulting in a complete loss of motility after 4 h. Since, the settlement on these coatings was 0 % it did not cause the lack of motility. An optical analysis under the microscope revealed that cyprids had died. On the contrary, cyprids captured in the meniscus, which did not have a contact with the coating, remained active for the whole observation period. One explanation for these effects could be the short pre-leaching procedure of 48 h. For the future the surfaces should be allowed to cure for 3 weeks and subsequently should be preleached for at least 3 months in order to remove any toxic components from the cross-linking process. Results on such surfaces could reveal whether current commercial coatings follow the approach to use tethered rather than soluble components to prevent cyprids from settling. Furthermore it can be investigated, by analysis of the motion parameters described in the previous chapters, whether the effects of high performance antifouling coatings on cyprids are detectable already during the exploration phase.

Finally, an upgrade of the setup was applied which allowed the imaging of marine biofouling organisms underwater. The stereoscopic system was adapted using a rigid

frame, underwater housings for the cameras, underwater lights, a specially designed sample holder and clear water / air tubes to overcome difficulties with highly turbid seawater. The first experiments in the **field** in collaboration with the group of Prof. G. Swain in FIT, Florida and International Paint Akzo Nobel in Hartlepool, UK confirmed the feasibility of the system and the capability of extracting trajectories of swimming organisms. Additionally, it could be successfully demonstrated that utilizing the system can provide insights in the settlement dynamics of marine organisms and detect changes in the motion of marine organisms over surfaces with different chemical properties.

For the future, more field experiments should be performed, in order to collect a larger data set and to compare the behavior of cyprids in the sub-tropical region with cyprids available in the cold waters in northern UK. One important task for the analysis of the underwater experiments will be to create technical means for identification of swimming objects. Because of the presence of numerous swimming organisms in the field of view, it is challenging even for an experienced user, to identify cyprids. For this purpose, an automatic classification algorithm should be created which analyzes the swimming patterns of objects in the field of view and classifies as cyprids only those exposing swimming patterns and movements as described in Chapter 5.1.

Moreover, to overcome the highly limited field of view of the iSPR technique, an automatic stage could be developed, which follows cyprids of interest and automatically positions the stage at the optimal coordinates for the iSPR setup. In order to achieve this, the data from the stereoscopy cameras needs to be analyzed live and the coordinates to be forwarded to the stage controller. This would allow the tracking and following of cyprids through the whole cycle of exploration: swimming, surface inspection, interaction with the interface and settlement.

Summarizing, the utilization of the basic findings described in this thesis presents a step forward in the quantification of the exploratory behavior of cyprids. Understanding the complex motility of cyprids and how behavior is involved in surface selection will accelerate the identification of surface cues that moderate or counteract settlement. Applying this knowledge, a new generation of specially designed anti-fouling coatings can be developed, which interfere intelligently and more focused with the settlement of organisms only during the substrate selection and exploration stages. Such coatings would, thus, prevent settlement without influencing other coexisting species and would be totally environmentally benign - intelligent anti-fouling coatings 2.0.

Bibliography

[1] J. A. Callow and M. E. Callow.
Trends in the development of environmentally friendly fouling-resistant marine coatings.
Nature Communications, 2:244, 2011.

[2] M. P. Schultz.
Effects of coating roughness and biofouling on ship resistance and powering.
Biofouling, 23(5):331–341, 2007.

[3] R. L. Townsin.
The ship hull fouling penalty.
Biofouling, 19:9–15, 2003.

[4] D. M. Yebra, S. Kiil, and K. Dam-Johansen.
Antifouling technology - past, present and future steps towards efficient and environmentally friendly antifouling coatings.
Progress in Organic Coatings, 50(2):75–104, 2004.

[5] International Maritime Organization (IMO).
International convention on the control of harmful antifouling systems on ships.
Technical report, International Maritime Organization, 2003.

[6] J. F. Schumacher, N. Aldred, M. E. Callow, J. A. Finlay, J. A. Callow, A. S. Clare, and A. B. Brennan.
Species-specific engineered antifouling topographies: correlations between the settlement of algal zoospores and barnacle cyprids.
Biofouling, 23(5):307–317, 2007.

[7] N. Aldred, A. Scardino, A. Cavaco, R. de Nys, and A. S. Clare.
Attachment strength is a key factor in the selection of surfaces by barnacle cyprids (Balanus amphitrite) during settlement.
Biofouling, 26(3):287–299, 2010.

[8] R. F. Brady and I. L. Singer.
Mechanical factors favoring release from fouling release coatings.
Biofouling, 15(1-3):73–81, January 2000.

[9] J.-F. Briand.
Marine antifouling laboratory bioassays: an overview of their diversity.
Biofouling, 25(4):297–311, January 2009.

[10] D. Rittschof, E. S. Branscomb, and J. D. Costlow.
Settlement and behavior in relation to flow and surface in larval barnacles, Balanus amphitrite Darwin.
Journal of Experimental Marine Biology and Ecology, 82(23):131–146, 1984.

[11] D. Rittschof, A. S. Clare, D. J. Gerhart, S. A. Mary, and J. Bonaventura.
Barnacle in vitro assays for biologically active substances: Toxicity and Settlement inhibition assays using mass cultured Balanus amphitrite amphitrite darwin.
Biofouling, 6(2):115–122, 1992.

[12] J.-P. Maréchal and C. Hellio.
Antifouling activity against barnacle cypris larvae: Do target species matter (Amphibalanus amphitrite versus Semibalanus balanoides)?
International Biodeterioration & Biodegradation, 65(1):92–101, 2011.

[13] L. Petrone, A. Di Fino, N. Aldred, P. Sukkaew, T. Ederth, A. S. Clare, and B. Liedberg.
Effects of surface charge and Gibbs surface energy on the settlement behaviour of barnacle cyprids (Balanus amphitrite).
Biofouling, 27(9):1043–1055, 2011.

[14] J.-W. Qiu, O. S. Hung, and P.-Y. Qian.
An improved barnacle attachment inhibition assay.
Biofouling, 24(4):259–266, 2008.

[15] D. Roberts, D. Rittschof, E. Holm, and A. R. Schmidt.
Factors influencing initial larval settlement: temporal, spatial and surface molecular components.
Journal of Experimental Marine Biology and Ecology, 150(2):203–221, 1991.

[16] C. Elkin and D. J. Marshall.
Desperate larvae: influence of deferred costs and habitat requirements on habitat selection.
Marine Ecology Progress Series, 335:143–153, 2007.

[17] N. Aldred, J. T. Høeg, D. Maruzzo, and A. S. Clare.
Analysis of the Behaviours Mediating Barnacle Cyprid Reversible Adhesion.
PLoS ONE, 8(7):e68085, 2013.

[18] D. Maruzzo, S. Conlan, N. Aldred, A. S. Clare, and J. T. Hoeg.
Video observation of surface exploration in cyprids of Balanus amphitrite: the movements of antennular sensory setae.
Biofouling, 27(2):225–239, 2011.

[19] J.-P. Maréchal, C. Hellio, M. Sebire, and A. S. Clare.
Settlement behaviour of marine invertebrate larvae measured by EthoVision 3.0.
Biofouling, 20(4-5):211–217, 2004.

[20] N. N. Pradhan, N. V. Gohad, B. Orihuela, T. C. Burg, S. T. Birchfield, D. Rittschof, and A. S. Mount.
Development of an automated algorithm for tracking and quantifying Barnacle cyprid settlement behavior.
Journal of Experimental Marine Biology and Ecology, 410:21–28, 2011.

[21] M. O. Amsler, C. D. Amsler, D. Rittschof, M. A. Becerro, and J. B. McClintock.
The use of computer-assisted motion analysis for quantitative studies of the behaviour of barnacle (Balanus amphitrite) larvae.
Marine and Freshwater Behaviour and Physiology, 39(4):259–268, 2006.

[22] L. Chambers, K. Stokes, F. Walsh, and R. Wood.
Modern approaches to marine antifouling coatings.
Surface and Coatings Technology, 201(6):3642–3652, December 2006.

[23] G. S. Prendergast, C. M. Zurn, A. V. Bers, R. M. Head, L. J. Hansson, and J. C. Thomason.
Field-based video observations of wild barnacle cyprid behaviour in response to textural and chemical settlement cues.
Biofouling, 24(6):449–459, 2008.

[24] C. DiBacco, H. L. Fuchs, J. Pineda, and K. Helfrich.
Swimming behavior and velocities of barnacle cyprids in a downwelling flume.
Marine Ecology-Progress Series, 433:131–148, 2011.

[25] K. Matsumura, J. M. Hills, P. O. Thomason, J. C. Thomason, and A. S. Clare.
Discrimination at settlement in barnacles: Laboratory and field experiments on settlement behaviour in response to settlement-inducing protein complexes.
Biofouling, 16(2-4):181–190, November 2000.

[26] N. Aldred, T. Ekblad, O. Andersson, B. Liedberg, and A. S. Clare.
Real-Time Quantification of Microscale Bioadhesion Events In situ Using Imaging Surface Plasmon Resonance (iSPR).
ACS Applied Materials & Interfaces, 3(6):2085–2091, 2011.

[27] O. Andersson, T. Ekblad, N. Aldred, A. S. Clare, and B. Liedberg.
Novel application of imaging surface plasmon resonance for in situ studies of the surface exploration of marine organisms.
Biointerphases, 4(4):65–68, 2009.

[28] K. C. Chaw and W. R. Birch.
Quantifying the exploratory behaviour of Amphibalanus amphitrite cyprids.
Biofouling, 25(7):611–619, 2009.

[29] N. Aldred, G. Li, Y. Gao, A. S. Clare, and S. Jiang.
Modulation of barnacle (Balanus amphitrite Darwin) cyprid settlement behavior by sulfobetaine and carboxybetaine methacrylate polymer coatings.
Biofouling, 26(6):673–683, 2010.

[30] M. Heydt, A. Rosenhahn, M. Grunze, M. Pettitt, M. E. Callow, and J. A. Callow.
Digital in-line holography as a three-dimensional tool to study motile marine organisms during their exploration of surfaces.
Journal of Adhesion, 83(5):417–430, 2007.

[31] M. Heydt, P. Divós, M. Grunze, and A. Rosenhahn.
Analysis of holographic microscopy data to quantitatively investigate three-dimensional settlement dynamics of algal zoospores in the vicinity of surfaces.
The European physical journal. E, Soft matter, 30(2):141–8, October 2009.

[32] M. Heydt, M. Pettitt, X. Cao, M. Callow, J. Callow, M. Grunze, and A. Rosenhahn.
Settlement Behavior of Zoospores of Ulva linza During Surface Selection Studied by Digital Holographic Microscopy.
Biointerphases, 7(1):1–7, 2012.

[33] S. M. Vater, S. Weiße, S. Maleschlijski, C. Lotz, F. Koschitzki, T. Schwartz, U. Obst, and A. Rosenhahn.
Swimming Behavior of Pseudomonas aeruginosa Studied by Holographic 3D Tracking.
PLoS ONE, 9(1):e87765, January 2014.

[34] J. Sheng, E. Malkiel, J. Katz, J. Adolf, R. Belas, and A. R. Place.
Digital holographic microscopy reveals prey-induced changes in swimming behavior of predatory dinoflagellates.
Proceedings of the National Academy of Sciences of the United States of America, 104(44):17512–17517, 2007.

[35] B. Rosenhahn, U. Kersting, K. Powell, R. Klette, G. Klette, and H.-P. Seidel.
A system for articulated tracking incorporating a clothing model.
Machine Vision and Applications, 18(1):25–40, 2007.

[36] L. Leal-Taixé, G. Pons-Moll, and B. Rosenhahn.
Branch-and-price global optimization for multi-view multi-object tracking.
In *IEEE Conference on Computer Vision and Pattern Recognition (CVPR)*, 2012.

[37] H. G. Maas, A. Gruen, and D. Papantoniou.
Particle tracking velocimetry in 3-dimensional flows. 1. Photogrammetric determination of partacle coordinates.
Experiments in Fluids, 15(2):133–146, 1993.

[38] M. Himpel, B. Buttenschon, and A. Melzer.
Three-view stereoscopy in dusty plasmas under microgravity: a calibration and reconstruction approach.
The Review of scientific instruments, 82(5):53706, 2011.

[39] F.-G. Michalec, M. Holzner, J. S. Hwang, and S. Souissi.
Three dimensional observation of salinity-induced changes in the swimming behavior of the estuarine calanoid copepod Pseudodiaptomus annandalei.
Journal of Experimental Marine Biology and Ecology, 438:24–31, 2012.

[40] F.-G. Michalec, M. Holzner, D. Menu, J.-S. Hwang, and S. Souissi.
Behavioral responses of the estuarine calanoid copepod Eurytemora affinis to sub-lethal concentrations of waterborne pollutants.
Aquatic toxicology (Amsterdam, Netherlands), 138-139:129–138, 2013.

[41] N. Aldred and A. S. Clare.
The adhesive strategies of cyprids and development of barnacle-resistant marine coatings.
Biofouling, 24(5):351–363, 2008.

[42] A. Garg, A. Jain, and N. B. Bhosle.
Chemical characterization of a marine conditioning film.
International Biodeterioration & Biodegradation, 63(1):7–11, 2009.

[43] D. Rittschof.
Research on Environmentally Benign Antifouling Coatings.
In S. Durr and J. C. Thomason, editors, *Biofouling*. Wiley-Blackwell, 2009.

[44] A. S. Clare, D. Rittschof, D. J. Gerhart, and J. S. Maki.
Molecular approaches to nontoxic antifouling, 1992.

[45] A. Clare and N. Aldred.
Surface colonisation by marine organisms and its impact on antifouling research.
In C. Hellio and D. Yebra, editors, *Advances in marine antifouling coatings and technologies*, pages 46 – 79. Woodshead Publishing, Cambridge, 2009.

[46] A. S. Clare and J. T. Høeg.
Balanus amphitrite or Amphibalanus amphitrite? A note on barnacle nomenclature.
Biofouling, 24(1):55–7, January 2008.

[47] C. Hellio, C. Simon-Colin, A. S. Clare, and E. Deslandes.
Isethionic acid and floridoside isolated from the red alga, Grateloupia turuturu, inhibit settlement of Balanus amphitrite cyprid larvae.
Biofouling, 20(3):139–45, June 2004.

[48] L. J. Walley.
Studies on larval structure and metamorphosis of Balanus balanoides (L.).
Philosophical Transactions of the Royal Society of London Series B-Biological Sciences, 256(807):237–280, 1969.

[49] D. Maruzzo, N. Aldred, A. S. Clare, and J. T. Høeg.
Metamorphosis in the cirripede crustacean Balanus amphitrite.
PloS one, 7(5):e37408, January 2012.

[50] D. Marshall and M. Keough.
Variation in the dispersal potential of non-feeding invertebrate larvae: the desperate larva hypothesis and larval size.
Marine Ecology Progress Series, 255:145–153, 2003.

[51] I. Y. Phang, N. Aldred, A. S. Clare, J. A. Callow, and G. J. Vancso.
An in situ study of the nanomechanical properties of barnacle (Balanus amphitrite) cyprid cement using atomic force microscopy (AFM).
Biofouling, 22(3-4):245–50, January 2006.

[52] V. Thiyagarajan, T. Harder, and P.-Y. Qian.
Relationship between cyprid energy reserves and metamorphosis in the barnacle Balanus amphitrite Darwin (Cirripedia; Thoracica).
Journal of Experimental Marine Biology and Ecology, 280(1-2):79–93, November 2002.

[53] N. Lagersson and J. Høeg.
Settlement behavior and antennulary biomechanics in cypris larvae of Balanu s amphitrite (Crustacea: Thecostraca: Cirripedia).
Marine Biology, 141(3):513–526, September 2002.

[54] H. D. Doochin.
The Morphology of Balanus improvisus Darwin and Balanus amphitrite niveus Darwin During Initial Attachment and Metamorphosis.
Bulletin of Marine Science, 1(1):15–39(25), 1951.

[55] H. Glenner and J. T. Høeg.
Scanning Electron Microscopy of Cypris Larvae of Balanus amphitrite (Cirripedia: Thoracica: Balanomorpha).
Journal of Crustacean Biology, 15(3):523–536, August 1995.

[56] J. Bielecki, B. K. K. Chan, J. T. Hoeg, and A. Sari.
Antennular sensory organs in cyprids of balanomorphan cirripedes: standardizing terminology using Megabalanus rosa.
Biofouling, 25(3):203–14, January 2009.

[57] J. T. Høeg.
Cypris Settlement, Kentrogon Formation and Host Invasion in the Parasitic Barnacle Lernaeodiscus porcellanae (Müller) (Crustacea: Cirripedia: Rhizocephala).
Acta Zoologica, 66(1):1–45, March 1985.

[58] A. B. Yule and G. Walker.
The temporary adhesion of barnacle cyprids - effects of some differing surface characteristics.
Journal of the Marine Biological Association of the United Kingdom, 64(2):429–439, 1984.

[59] G. Swain, S. Herpe, E. Ralston, and M. Tribou.
Short-term testing of antifouling surfaces: the importance of colour.
Biofouling, 22(5-6):425–9, January 2006.

[60] D. J. Crisp.
Two settlement responses in marine organisms.
In *Newell RC (ed) Adaptation to enviroment. Essays on the physiology of marine animals.*, pages 83– 124. Butterworths, London, 1976.

[61] V. Thiyagarajan.
A review on the role of chemical cues in habitat selection by barnacles: New insights from larval proteomics.
Journal of Experimental Marine Biology and Ecology, 392(1-2):22–36, 2010.

[62] M. Faimali, F. Garaventa, V. Piazza, G. Greco, C. Corrà, F. Magillo, M. Pittore, E. Giacco, L. Gallus, C. Falugi, and G. Tagliafierro.
Swimming speed alteration of larvae of Balanus amphitrite as a behavioural end-point for laboratory toxicological bioassays.
Marine Biology, 149(1):87–96, 2006.

[63] R. S. Wu, P. K. Lam, and B. Zhou.
A settlement inhibition assay with cyprid larvae of the barnacle Balanus amphitrite.

Chemosphere, 35(9):1867–1874, November 1997.

[64] L. Petrone, S. S. C. Lee, S. L. M. Teo, and W. R. Birch.
A novel geometry for a laboratory-based larval settlement assay.
Biofouling, 29(2):213–221, 2013.

[65] E. W. Knight-Jones and D. J. Crisp.
Gregariousness in Barnacles in Relation to the Fouling of Ships and to Anti-Fouling Research.
Nature, 171(4364):1109–1110, June 1953.

[66] J. C. Thomason, J. M. Hills, and P. O. Thomason.
Field-based Behavioural Bioassays for Testing the Efficacy of Antifouling Coatings.
Biofouling, 18(4):285–292, January 2002.

[67] R. Head, K. Berntsson, M. Dahlström, K. Overbeke, and J. Thomason.
Gregarious settlement in cypris larvae:the effects of cyprid age and assay duration.
Biofouling, 20(2):123–8, April 2004.

[68] L. P. J. J. Noldus, A. J. Spink, and R. A. J. Tegelenbosch.
EthoVision: A versatile video tracking system for automation of behavioral experiments.
Behavior Research Methods Instruments and Computers, 33(3):398–414, 2001.

[69] H. E. de Bruijn, R. P. Kooyman, and J. Greve.
Surface plasmon resonance microscopy: improvement of the resolution by rotation of the object.
Applied optics, 32(13):2426–30, May 1993.

[70] A. B. Yule and D. J. Crisp.
Adhesion of cypris larvae of the barnacle, Balanus-balanoides, to clean and arthropodin treated surfaces.
Journal of the Marine Biological Association of the United Kingdom, 63(2):261–271, 1983.

[71] T. Ekblad, O. Andersson, F.-I. Tai, T. Ederth, and B. Liedberg.
Lateral Control of Protein Adsorption on Charged Polymer Gradients.
Langmuir, 25(6):3755–3762, 2009.

[72] A. Di Fino, L. Petrone, N. Aldred, T. Ederth, B. Liedberg, and A. S. Clare.
Correlation between surface chemistry and settlement behaviour in barnacle cyprids (Balanus improvisus).
Biofouling, pages 1–10, December 2013.

[73] K. Prime and G. Whitesides.
Adsorption of proteins onto surfaces containing end-attached oligo (ethylene oxide): a model system using self-assembled monolayers.
Journal of the American Chemical Society, 115(23):10714–10721, 1993.

[74] R. E. Baier and A. E. Meyer.
Surface analysis of fouling resistant marine coatings.
Biofouling, 6(2):165–180, November 1992.

[75] J. A. Finlay, S. M. Bennett, L. H. Brewer, A. Sokolova, G. Clay, N. Gunari, A. E. Meyer, G. C. Walker, D. E. Wendt, M. E. Callow, J. A. Callow, and M. R. Detty.
Barnacle settlement and the adhesion of protein and diatom microfouling to xerogel films with varying surface energy and water wettability.
Biofouling, 26(6):657–666, 2010.

[76] N. J. O'Connor and D. L. Richardson.
Comparative attachment of barnacle cyprids (Balanus amphitrite Darwin, 1854; B. improvisus Darwin, 1854; & B. ebumeus Gould, 1841) to polystyrene and glass substrata.
Journal of Experimental Marine Biology and Ecology, 183(2):213–225, November 1994.

[77] D. Rittschof and J. D. Costlow.
Bryozoan and barnacle settlement in relation to initial surface wettability a comparison of laboratory and field studies.
Scientia Marina, 53:411–416, 1989.

[78] D. J. Gerhart, D. Rittschof, I. R. Hooper, K. Eisenman, A. E. Meyer, R. E. Baier, and C. Young.
Rapid and inexpensive quantification of the combined polar components of surface wettability: Application to biofouling.
Biofouling, 5(4):251–259, May 1992.

[79] M. Dahlstrom, H. Jonsson, P. R. Jonsson, and H. Elwing.
Surface wettability as a determinant in the settlement of the barnacle Balanus improvisus (Darwin).
Journal of Experimental Marine Biology and Ecology, 305(2):223–232, 2004.

[80] J. S. Maki, A. B. Yule, D. Rittschof, and R. Mitchell.
The effect of bacterial films on the temporary adhesion and permanent fixation of cypris larvae, balanus amphitrite darwin.
Biofouling, 8(2):121–131, October 1994.

[81] A. Rosenhahn, S. Schilp, H. J. Kreuzer, and M. Grunze.
The role of "inert" surface chemistry in marine biofouling prevention.
Physical Chemistry Chemical Physics, 12(17):4275–4286, 2010.

[82] S. Schilp, A. Rosenhahn, M. E. Pettitt, J. Bowen, M. E. Callow, J. A. Callow, and M. Grunze.
Physicochemical properties of (ethylene glycol)-containing self-assembled monolayers relevant for protein and algal cell resistance.
Langmuir, 25(17):10077–82, September 2009.

[83] T. Ekblad, G. Bergström, T. Ederth, S. L. Conlan, R. Mutton, A. S. Clare, S. Wang, Y. Liu, Q. Zhao, F. D'Souza, G. T. Donnelly, P. R. Willemsen, M. E. Pettitt, M. E. Callow, J. A. Callow, and B. Liedberg.
Poly(ethylene glycol)-containing hydrogel surfaces for antifouling applications in marine and freshwater environments.
Biomacromolecules, 9(10):2775–83, October 2008.

[84] J. Visscher and R. Luce.
Reactions of the Cyprid Larvæof Barnacles to Light with Special Reference to Spectral Colors.
Biological Bulletin, 54(4):336–350, 1928.

[85] Y. Taki, Y. Ogasawara, Y. Ido, and N. Yokoyama.
Color factors influencing larval settlement of barnacles, Balanus amphitrite subspp.
Nippon Suisan Gakkaishi, 46(2):133–138, 1980.

[86] S. Dobretsov, R. M. M. Abed, and C. R. Voolstra.
The effect of surface colour on the formation of marine micro and macrofouling communities.
Biofouling, 29(6):617–27, January 2013.

[87] J. A. Finlay, B. R. Fletcher, M. E. Callow, and J. A. Callow.
Effect of background colour on growth and adhesion strength of Ulva sporelings.
Biofouling, 24(3):219–25, January 2008.

[88] M. A. Robson, D. Williams, K. Wolff, and J. C. Thomason.
The effect of surface colour on the adhesion strength of Elminius modestus Darwin on a commercial non-biocidal antifouling coating at two locations in the UK.
Biofouling, 25(3):215–27, January 2009.

[89] J. M. Hills, J. C. Thomason, and J. Muhl.
Settlement of barnacle larvae is governed by Euclidean and not fractal surface characteristics.

Functional Ecology, 13(6):868–875, 1999.

[90] D. J. Crisp and H. Barnes.
The Orientation and Distribution of Barnacles at Settlement with Particular Reference to Surface Contour.
Journal of Animal Ecology, 23(1):142–162, May 1954.

[91] E. Bourget.
Barnacle Larval Settlement: the Perception of Cues at Different Spatial Scales.
In G. Chelazzi and M. Vannini, editors, *Behavioral Adaptation to Intertidal Life SE - 12*, volume 151 of *NATO ASI Series*, pages 153–172. Springer US, 1988.

[92] M. Andersson, K. Berntsson, P. Jonsson, and P. Gatenholm.
Microtextured surfaces: Towards macrofouling resistant coatings.
Biofouling, 14:167–178, 1999.

[93] M. Salta, J. A. Wharton, P. Stoodley, S. P. Dennington, L. R. Goodes, S. Werwinski, U. Mart, R. J. K. Wood, and K. R. Stokes.
Designing biomimetic antifouling surfaces.
Philosophical transactions. Series A, Mathematical, physical, and engineering sciences, 368:4729–4754, 2010.

[94] A. J. Scardino and R. de Nys.
Mini review: Biomimetic models and bioinspired surfaces for fouling control.
Biofouling, 27(1):73–86, 2011.

[95] G. Greco, T. S. Lanero, S. Torrassa, R. Young, M. Vassalli, A. Cavaliere, R. Rolandi, E. Pelucchi, M. Faimali, and J. Davenport.
Microtopography of the eye surface of the crab Carcinus maenas: an atomic force microscope study suggesting a possible antifouling potential.
Journal of the Royal Society Interface, 10(84):20130122, July 2013.

[96] L. Xiao.
Influence of Surface Topography on Marine Biofouling.
PhD thesis, University of Heidelberg, 2014.

[97] A. S. Clare and K. Matsumura.
Nature and perception of barnacle settlement pheromones, 2000.

[98] D. J. Crisp and P. S. Meadows.
Adsorbed Layers: The Stimulus to Settlement in Barnacles.
Proceedings of the Royal Society of London. Series B, Biological Sciences, 158(972):364–387, 1963.

[99] C. Dreanno, R. R. Kirby, and A. S. Clare.
Smelly feet are not always a bad thing: the relationship between cyprid footprint protein and the barnacle settlement pheromone.
Biology Letters, 2(3):423–425, 2006.

[100] A. S. Clare, R. K. Freet, and M. McClary.
On the antennular secretion of the cyprid of Balanus amphitrite amphitrite, and its role as a settlement pheromone.
Journal of the Marine Biological Association of the United Kingdom, 74(01):243–250, February 1994.

[101] P. D. Elbourne and A. S. Clare.
Ecological relevance of a conspecific, waterborne settlement cue in Balanus amphitrite (Cirripedia).
Journal of Experimental Marine Biology and Ecology, 392(1):99–106, 2010.

[102] K. Tegtmeyer and D. Rittschof.
Synthetic peptide analogs to barnacle settlement pheromone.
Peptides, 9(6):1403–6, 1988.

[103] J. S. Maki, D. Rittschof, J. D. Costlow, and R. Mitchell.
Inhibition of attachment of larval barnacles, Balanus amphitrite, by bacterial surface films.
Marine Biology, 97(2):199–206, February 1988.

[104] S. Wieczorek, A. Clare, and C. Todd.
Inhibitory and facilitatory effects of microbial films on settlement of Balanus amphitrite amphitrite larvae.
Marine Ecology Progress Series, 119(1-3):221–228, 1995.

[105] M. G. Hadfield.
Biofilms and Marine Invertebrate Larvae: What Bacteria Produce That Larvae Use to Choose Settlement Sites.
Annual Review of Marine Science, 3(1):453–470, January 2011.

[106] S. K. Wieczorek, A. W. A. Murray, and C. D. Todd.
Seasonal variation in the effects of hard substratum biofilming on settlement of marine invertebrate larvae.
Biofouling, 10(4):309–330, December 1996.

[107] I. Thome, M. E. Pettitt, M. E. Callow, J. A. Callow, M. Grunze, and A. Rosenhahn.
Conditioning of surfaces by macromolecules and its implication for the settlement of zoospores of the green alga Ulva linza.
Biofouling, 28(5):501–510, 2012.

[108] C. D. Bain and G. M. Whitesides.
Molecular-Level Control over Surface Order in Self-Assembled Monolayer Films of Thiols on Gold.
Science (New York, N.Y.), 240:62–63, 1988.

[109] P. Harder, M. Grunze, R. Dahint, G. M. Whitesides, and P. E. Laibinis.
Molecular conformation in oligo(ethylene glycol)-terminated self-assembled monolayers on gold and silver surfaces determines their ability to resist protein adsorption.
Journal of Physical Chemistry B, 102(2):426–436, 1998.

[110] R. G. Nuzzo and D. L. Allara.
Adsorption of bifunctional organic disulfides on gold surfaces.
Journal of the American Chemical Society, 105(13):4481–4483, June 1983.

[111] C. D. Bain and G. M. Whitesides.
Modeling Organic Surfaces with Self-Assembled Monolayers.
Angewandte Chemie International Edition in English, 28(4):506–512, April 1989.

[112] L. H. Dubois and R. G. Nuzzo.
Synthesis, Structure, and Properties of Model Organic Surfaces.
Annual Review of Physical Chemistry, 43:437–463, 1992.

[113] K. L. Prime and G. M. Whitesides.
Self-assembled organic monolayers: model systems for studying adsorption of proteins at surfaces.
Science (New York, N.Y.), 252:1164–1167, 1991.

[114] R. Chelmowski, S. D. Köster, A. Kerstan, A. Prekelt, C. Grunwald, T. Winkler, N. Metzler-Nolte, A. Terfort, and C. Wöll.
Peptide-based SAMs that resist the adsorption of proteins.
Journal of the American Chemical Society, 130:14952–14953, 2008.

[115] N. Faucheux, R. Schweiss, K. Lützow, C. Werner, and T. Groth.
Self-assembled monolayers with different terminating groups as model substrates for cell adhesion studies.
Biomaterials, 25:2721–2730, 2004.

[116] J. C. Love, D. B. Wolfe, M. L. Chabinyc, K. E. Paul, and G. M. Whitesides.
Self-assembled monolayers of alkanethiolates on palladium are good etch resists.
Journal of the American Chemical Society, 124:1576–1577, 2002.

[117] J. C. Love, L. A. Estroff, J. K. Kriebel, R. G. Nuzzo, and G. M. Whitesides.
Self-assembled monolayers of thiolates on metals as a form of nanotechnology.
Chemical reviews, 105(4):1103–69, April 2005.

[118] D. G. Castner and B. D. Ratner.
Biomedical surface science: Foundations to frontiers.
Surface Science, 500:28–60, 2002.

[119] L. K. Ista, H. Fan, O. Baca, and G. P. López.
Attachment of bacteria to model solid surfaces' oligo(ethylene glycol) surfaces inhibit bacterial attachment.
FEMS Microbiology Letters, 142:59–63, 1996.

[120] P. D. Steinberg, R. De Nys, and S. Kjelleberg.
Chemical cues for surface colonization.
Journal of Chemical Ecology, 28:1935–1951, 2002.

[121] M. E. Callow, J. A. Callow, L. K. Ista, S. E. Coleman, A. C. Nolasco, and G. P. Lopez.
Use of Self-Assembled Monolayers of Different Wettabilities To Study Surface Selection and Primary Adhesion Processes of Green Algal (Enteromorpha) Zoospores.
Applied and Environmental Microbiology, 66(8):3249–3254, August 2000.

[122] S. Schilp, A. Kueller, A. Rosenhahn, M. Grunze, M. E. Pettitt, M. E. Callow, and J. A. Callow.
Settlement and adhesion of algal cells to hexa(ethylene glycol)-containing self-assembled monolayers with systematically changed wetting properties.
Biointerphases, 2(4), 2007.

[123] L. K. Ista, M. E. Callow, J. A. Finlay, S. E. Coleman, A. C. Nolasco, R. H. Simons, J. A. Callow, and G. P. Lopez.
Effect of substratum surface chemistry and surface energy on attachment of marine bacteria and algal spores.
Applied and environmental microbiology, 70:4151–4157, 2004.

[124] T. Ederth, P. Nygren, M. E. Pettitt, M. Ostblom, C. X. Du, K. Broo, M. E. Callow, J. Callow, and B. Liedberg.
Anomalous settlement behavior of Ulva linza zoospores on cationic oligopeptide surfaces.
Biofouling, 24(4):303–312, 2008.

[125] J. A. Finlay, M. E. Callow, L. K. Ista, G. P. Lopez, and J. A. Callow.
The influence of surface wettability on the adhesion strength of settled spores of the green alga enteromorpha and the diatom amphora.
Integrative and comparative biology, 42:1116–1122, 2002.

[126] J. A. Callow, M. E. Callow, L. K. Ista, G. Lopez, and M. K. Chaudhury.

The influence of surface energy on the wetting behaviour of the spore adhesive of the marine alga Ulva linza (synonym Enteromorpha linza).
Journal of the Royal Society Interface, 2:319–325, 2005.

[127] S. Bauer, M. P. Arpa-Sancet, J. A. Finlay, M. E. Callow, J. A. Callow, and A. Rosenhahn.
Adhesion of marine fouling organisms on hydrophilic and amphiphilic polysaccharides.
Langmuir, 29(12):4039–47, March 2013.

[128] N. Aldred, L. K. Ista, M. E. Callow, J. A. Callow, G. P. Lopez, and A. S. Clare.
Mussel (Mytilus edulis) byssus deposition in response to variations in surface wettability.
Journal of the Royal Society Interface, 3:37–43, 2006.

[129] L. Petrone, N. L. C. Ragg, L. Girvan, and A. J. McQuillan.
Scanning Electron Microscopy and Energy Dispersive X-Ray Microanalysis of Perna canaliculus Mussel Larvae Adhesive Secretion.
Journal of Adhesion, 85:78–96, 2009.

[130] R. I. Hartley and A. Zisserman.
Multiple View Geometry in Computer Vision.
Cambridge University Press, second edition, 2004.

[131] Z. Zhang.
Camera Calibration.
In G. Medioni and S. Kang, editors, *Emerging Topics in Computer Vision*, pages 4–43. Prentice Hall Professional Technical Reference, 2004.

[132] G. Xu and Z. Zhang.
Epipolar Geometry in Stereo, Motion, and Object Recognition: A Unified Approach.
Kluwer Academic Publishers, October 1996.

[133] E. L. Hall, J. B. K. Tio, C. A. McPherson, and F. A. Sadjadi.
Measuring Curved Surfaces for Robot Vision.
Computer, 15(12):42–54, December 1982.

[134] H. C. Longuet-Higgins.
A computer algorithm for reconstructing a scene from two projections.
Nature, 293(5828):133–135, September 1981.

[135] Z. Zhang and T. Kanade.
Determining the Epipolar Geometry and its Uncertainty: A Review.
International Journal of Computer Vision, 27:161–195, 1998.

[136] R. I. Hartley.
In defense of the eight-point algorithm.
IEEE Transactions on Pattern Analysis and Machine Intelligence, 19(6):580–593, 1997.

[137] R. Y. Tsai and T. S. Huang.
Uniqueness and Estimation of Three-Dimensional Motion Parameters of Rigid Objects with Curved Surfaces.
IEEE Transactions on Pattern Analysis and Machine Intelligence, PAMI-6(1):13–27, January 1984.

[138] F. Shevlin.
Analysis of Orientation Problems Using Plucker Lines.
In *ICPR '98 Proceedings of the 14th International Conference on Pattern Recognition - Volume 1*, page 685. IEEE Computer Society, August 1998.

[139] R. I. Hartley and P. Sturm.
Triangulation.
Computer Vision and Image Understanding, 68(2):146–157, November 1997.

[140] T. Brox, B. Rosenhahn, J. Gall, and D. Cremers.
Combined region and motion-based 3D tracking of rigid and articulated objects.
IEEE transactions on pattern analysis and machine intelligence, 32(3):402–15, March 2010.

[141] G. Albert.
Herstellung Und Charakterisierung Polykristalliner Goldschichten Zur Verwendung in Der Nanolithographie.
Master thesis, University of Heidelberg, 1996.

[142] P. de Gennes.
Wetting: statics and dynamics.
Reviews of Modern Physics, 57(3):827–863, July 1985.

[143] T. Young.
An Essay on the Cohesion of Fluids.
Royal Society of London Philosophical Transactions Series I, 95:65–87, 1805.

[144] R. Wenzel.
Resistance of solid surfaces to wetting by water.
Industrial & Engineering Chemistry, 28(8):988–994, August 1936.

[145] A. Stalder, G. Kulik, D. Sage, L. Barbieri, and P. Hoffmann.
A snake-based approach to accurate determination of both contact points and contact angles.

Colloids and Surfaces A: Physicochemical and Engineering Aspects, 286(1-3):92–103, September 2006.

[146] C. A. Schneider, W. S. Rasband, and K. W. Eliceiri.
NIH Image to ImageJ: 25 years of image analysis.
Nature Methods, 9(7):671–675, June 2012.

[147] V. G. Bordo and H. G. Rubahn.
Optics and Spectroscopy at Surfaces and Interfaces.
Wiley & Sons, 2008.

[148] H. Tompkins.
A User's Guide to Ellipsometry.
Academic Press, 1992.

[149] D. H. Goldstein.
Polarized Light.
Optical Engineering Series, Dekker, M., 2003.

[150] J. Singh.
Optical Properties of Condensed Matter and Applications.
In *Wiley Series in Materials for Electronic & Optoelectronic Applications*, chapter 1. Wiley & Sons, 2006.

[151] H. Fujiwara.
Spectroscopic ellipsometry: principles and applications.
Wiley & Sons, 2007.

[152] B. D. Ratner and G. D. Castner.
Electron spectroscopy for chemical analysis.
In *Vickerman, J. C. and Gilmore, I., Surface Analysis: The Principal Techniques.*, chapter 7. Wiley & Sons, 2011.

[153] D. Shirley.
High-Resolution X-Ray Photoemission Spectrum of the Valence Bands of Gold.
Physical Review B, 5(12):4709–4714, June 1972.

[154] J. Scofield.
Hartree-Slater subshell photoionization cross-sections at 1254 and 1487 eV.
Journal of Electron Spectroscopy and Related Phenomena, 8(2):129–137, January 1976.

[155] J. Yeh and I. Lindau.
Atomic subshell photoionization cross sections and asymmetry parameters: 1 Z 103.
Atomic data and nuclear data tables, 32(1):1–155, January 1985.

[156] N. Meyerbröker.
Präparation und Charakterisierung ultradünner, biokompatibler Filme und Membranen auf Basis von Polyethylenglykolen.
PhD thesis, Ruprecht-Karls-Universität Heidelberg, 2012.

[157] N. Hasler, B. Rosenhahn, T. Thormahlen, M. Wand, J. Gall, and H.-P. Seidel.
Markerless Motion Capture with unsynchronized moving cameras.
In *2009 IEEE Conference on Computer Vision and Pattern Recognition*, pages 224–231. IEEE, June 2009.

[158] G. Prendergast, C. Zurn, A. V. Bers, R. Head, L. Hansson, and J. Thomason.
The relative magnitude of the effects of biological and physical settlement cues for cypris larvae of the acorn barnacle, Semibalanus balanoides L.
Biofouling, 25(1):35–44, 2009.

[159] D. J. Crisp.
The behaviour of barnacle cyprids in relation to water movement over a surface.
Journal of Experimental Biology, 32(3):569–590, 1955.

[160] P. D. Wolf.
Ecological observations on the mechanisms of dispersal of barnacle larvae during planktonic life and settling.
Netherlands Journal of Sea Research, 6(12):1–129, 1973.

[161] P. D. Elbourne, R. A. Veater, and A. S. Clare.
Interaction of conspecific cues in Balanus amphitrite Darwin (Cirripedia) settlement assays: continued argument for the single-larva assay.
Biofouling, 24(2):87–96, January 2008.

[162] P. M. Imbesi, J. A. Finlay, N. Aldred, M. J. Eller, S. E. Felder, K. A. Pollack, A. T. Lonnecker, J. E. Raymond, M. E. Mackay, E. A. Schweikert, A. S. Clare, J. A. Callow, M. E. Callow, and K. L. Wooley.
Targeted surface nanocomplexity: two-dimensional control over the composition, physical properties and anti-biofouling performance of hyperbranched fluoropolymerpoly(ethylene glycol) amphiphilic crosslinked networks.
Polymer Chemistry, 3(11):3121, October 2012.

[163] J. W. Tukey.
Exploratory Data Analysis, volume 2.
Pearson, New York, NY, 1977.

[164] A. W. van der Vaart.
Asymptotic Statistics.
Cambridge University Press, 1998.

[165] R. B. Ash.
Real Analysis and Probability.
Academic Press, New York, 1972.

[166] P. D. Komar, A. P. Morse, L. F. Small, and S. W. Fowler.
An Analysis of Sinking Rates of Natural Copepod and Euphausiid Fecal Pellets.
Limnology and Oceanography, 26(1):172–180, January 1981.

[167] N. C. Janke.
Effect of shape upon the settling vellocity of regular convex geometric particles.
Journal of Sedimentary Research, 36(2):370–376, June 1966.

[168] STUDENT.
The probable error of a mean.
Biometrika, 6(1):1–25, March 1908.

[169] E. W. Knightjones and S. Z. Qasim.
Responses of some marine plankton animals to changes in hydrostatic pressure.
Nature, 175(4465):941–942, 1955.

[170] L. Haury and D. Weihs.
Energetically efficient swimming behavior of negatively buoyant zooplankton.
Limnology and Oceanography, 21(6):797–803, 1976.

[171] H. T. El-Dessouky and H. M. Ettouney.
Fundamentals of salt water desalination.
Elsevier, 2002.

[172] H. Barnes.
Size variations in the cyprids of some common barnacles.
Journal of the Marine Biological Association of the United Kingdom, 32(02):297–304, 1953.

[173] T. Ikeda, A. Yamaguchi, and T. Matsuishi.
Chemical composition and energy content of deep-sea calanoid copepods in the Western North Pacific Ocean.
Deep Sea Research Part I: Oceanographic Research Papers, 53(11):1791–1809, November 2006.

[174] H. Barnes and M. Barnes.
The relation of water uptake and oxygen consumption of body tissues to the moulting cycle in Balanus balanoides (L.).
Crustaceana, 6(1):62–68, 1963.

[175] D. Crisp.
The planktonic stages of the Cirripedia Balanus balanoides (L.) and Balanus balanus (L.) from north temperate waters.
Crustaceana, 3(3):207–221, 1962.

[176] D. J. Crisp.
Factors Influencing the Time of Breeding of Balanus balanoides.
Oikos, 10(2):275–289 CR – Copyright © 1959 Nordic Society, January 1959.

[177] E. Norris, L. W. G. Jones, T. Lovegrove, and D. J. Crisp.
Variability in Larval Stages of Cirripedes.
Nature, 167(4246):444–445, March 1951.

[178] J. Pineda, D. Riebensahm, and D. Medeiros-Bergen.
Semibalanus balanoides in winter and spring: larval concentration, settlement, and substrate occupancy.
Marine Biology, 140(4):789–800, 2002.

[179] P. R. Jonsson, C. Andre, and M. Lindegarth.
Swimming Behavior of Marine Bivalve Larvae in a Flume Boundary-Layer Flow - Evidence for near-Bottom Confinement.
Marine Ecology-Progress Series, 79(1-2):67–76, 1991.

[180] M. Zarubin, V. Farstey, A. Wold, S. Falk-Petersen, and A. Genin.
Intraspecific Differences in Lipid Content of Calanoid Copepods across Fine-Scale Depth Ranges within the Photic Layer.
PLoS ONE, 9(3):e92935, 2014.

[181] G. Walker.
Swimming speeds of the larval stages of the parasitic barnacle, Heterosaccus lunatus (Crustacea : Cirripedia : Rhizocephala).
Journal of the Marine Biological Association of the United Kingdom, 84(4):737–742, 2004.

[182] D. L. Holland.
Lipid reserves and energy metabolism in the larvae of benthic marine invertebrates.
In D. Sargent and J. Malins, editors, *Biochemical and Biophysical Perspectives in Marine Biology*, pages 85–123. Academic Press, London, 1978.

[183] D. L. Holland and G. Walker.
Biochemical composition of cypris larva of barnacle Balanus-balanoides L.
Journal Du Conseil, 36(2):162–165, 1975.

[184] G. Miron, L. Walters, R. Tremblay, and E. Bourget.
Physiological condition and barnacle larval behavior: a preliminary look at the relationship between TAG/DNA ratio and larval substratum exploration in Balanus amphitrite.
Marine Ecology Progress Series, 198:303–310, 2000.

[185] D. J. Crisp.
Overview of research in marine invertebrate larvae.
In J. D. Costlow and R. Tipper, editors, *Marine Biodeterioration: an Interdisciplinary Study*, pages 103–126. Naval Institute Press, MD, 1984.

[186] M. Berglin and P. Gratenholm.
The barnacle adhesive plaque: morphological and chemical differences as a response to substrate properties.
Colloids and Surfaces B-Biointerfaces, 28(2-3):107–117, 2003.

[187] R. E. Holmlin, X. Chen, R. G. Chapman, S. Takayama, and G. M. Whitesides.
Zwitterionic SAMs that Resist Nonspecific Adsorption of Protein from Aqueous Buffer.
Langmuir, 17(9):2841–2850, 2001.

[188] S. Chen, F. Yu, Q. Yu, Y. He, and S. Jiang.
Strong resistance of a thin crystalline layer of balanced charged groups to protein adsorption.
Langmuir : the ACS journal of surfaces and colloids, 22(19):8186–91, September 2006.

[189] S. Bauer, M. Alles, J. A. Finlay, J. A. Callow, M. E. Callow, and A. Rosenhahn.
Influence of zwitterionic SAMs on protein adsorption and the attachment of algal cells.
Journal of Biomaterials Science. Polymer edition, pages 1–10, June 2014.

[190] T. Fyrner, H.-H. Lee, A. Mangone, T. Ekblad, M. E. Pettitt, M. E. Callow, J. A. Callow, S. L. Conlan, R. Mutton, A. S. Clare, P. Konradsson, B. Liedberg, and T. Ederth.
Saccharide-functionalized alkanethiols for fouling-resistant self-assembled monolayers: synthesis, monolayer properties, and antifouling behavior.
Langmuir : the ACS journal of surfaces and colloids, 27(24):15034–47, December 2011.

[191] M. Morra and C. Cassineli.
Non-fouling properties of polysaccharide-coated surfaces.
Journal of Biomaterials Science. Polymer edition, 10(10):1107–24, January 1999.

[192] S. Krishnan, C. J. Weinman, and C. K. Ober.
Advances in polymers for anti-biofouling surfaces.
Journal of Materials Chemistry, 18(29):3405, July 2008.

[193] L. S. Mullineaux and C. A. Butman.
Initial contact, exploration and attachment of barnacle (Balanus amphitrite) cyprids settling in flow.
Marine Biology, 110(1):93–103, February 1991.

[194] G. Miron, B. Boudreau, and E. Bourget.
Intertidal barnacle distribution: a case study using multiple working hypotheses.
Marine Ecology Progress Series, 189:205–219, 1999.

[195] J. M. Hills, J. C. Thomason, H. Davis, J. Kohler, and E. Millett.
Exploratory behaviour of barnacle larvae in field conditions.
Biofouling, 16(2-4):171–179, 2000.

[196] K. A. Zargiel, J. S. Coogan, and G. W. Swain.
Diatom community structure on commercially available ship hull coatings.
Biofouling, 27(9):955–65, October 2011.

[197] G. S. Prendergast, C. M. Zurn, A. V. Bers, R. M. Head, L. J. Hansson, and J. C. Thomason.
Field-based video observations of wild barnacle cyprid behaviour in response to textural and chemical settlement cues.
Biofouling, 24(6):449–459, 2008.

[198] D. Rittschof, T.-M. Sin, S.-M. Teo, and R. Coutinho.
Fouling in natural flows: Cylinders and panels as collectors of particles and barnacle larvae.
Journal of Experimental Marine Biology and Ecology, 348(1-2):85–96, September 2007.

[199] O. Frederic, R. Tremblay, E. Bourget, and D. Rittschof.
Barnacle settlement: field experiments on the influence of larval supply, tidal level, biofilm quality and age on Balanus amphitrite cyprids.
Marine Ecology Progress Series, 2000.

[200] G. W. Swain, J. R. Griffith, J. D. Bultman, and H. L. Vincent.
The use of barnacle adhesion measurements for the field evaluation of nontoxic foul release surfaces.
Biofouling, 6(2):105–114, November 1992.

[201] E. A. Ralston and G. W. Swain.

The ghost of fouling communities past: the effect of original community on subsequent recruitment.
Biofouling, 30(4):459–71, April 2014.

[202] C. J. Kavanagh, G. W. Swain, B. S. Kovach, J. Stein, C. Darkangelo-Wood, K. Truby, E. Holm, J. Montemarano, A. Meyer, and D. Wiebe.
The effects of silicone fluid additives and silicone elastomer matrices on barnacle adhesion strength.
Biofouling, 19:381–390, 2003.

[203] M. P. Schultz and G. W. Swain.
The Effect of Biofilms on Turbulent Boundary Layers.
Journal of Fluids Engineering, 121(1):44–51, 1999.

[204] G. W. Swain, W. G. Nelson, and S. Preedeekanit.
The influence of biofouling adhesion and biotic disturbance on the development of fouling communities on non-toxic surfaces.
Biofouling, 12:257–269, 1998.

[205] A. Rosenhahn, S. Schilp, H. J. Kreuzer, and M. Grunze.
The role of 'inert' surface chemistry in marine biofouling prevention.
Physical chemistry chemical physics : PCCP, 12(17):4275–86, May 2010.

Financial support

The research work described in this thesis was funded by the German Research Foundation (DFG grant: RO 2524/2-2).

Acknowledgments

Finally, I would like to take the opportunity to express my gratitude to the people who were directly or indirectly involved in my work and to everyone who supported me during my time as a PhD student.

Zunächst möchte ich mich ganz besonders bei Prof. Axel Rosenhahn für die Aufnahme in seine Arbeitsgruppe, seine unzähligen Ideen, die gute Betreuung, die vielen Gespräche und Diskussionen und den Freiraum meine Arbeit zu gestalten. Danke auch für die Möglichkeit an dem tollen interdisziplinären Projekt in einem internationalen Umfeld teilnehmen zu dürfen. Vielen Dank außerdem für die Geduld bei der Erklärung der chemischen Zusammenhänge, die Unterstützung, Korrektur und Ratschläge bei der Verfassung der Publikationen und auch dieser Dissertation.

Bei Prof. Hans-Robert Volpp bedanke ich mich herzlich für die bereitwillige Übernahme des Zweitgutachtens.

Prof. Bodo Rosenhahn gilt mein großer Dank für die freundliche und kompetente Unterstützung bei den algorithmischen Fragen. Danke außerdem für die Einführung in die Welt der Stereoskopie, den freundlichen Empfang in Hannover, sowie die Korrektur vom stereoskopischen Teil der Arbeit.

Thanks to Prof. Geoffrey Swain for his support during my research stays at the Florida Institute of Technology. Thank you also for providing the terrific boats for the experiments in the Cape Marina, the possibility to perform the experiments in the scenic landscape of Florida and for recommending the delicious Mahi-Mahi burger.

I thank Prof. Anthony S. Clare for his hospitality during my research stays in the University of Newcastle and the possibility to perform experiments with cyprids in his lab.

Ein spezieller Dank geht an Dr. Urban Liebel, Dr. Felix Loosli und Prof. Matthias Franzreb für die Teilnahme an meinem TAC (thesis advisory comitee). Danke für die Diskussionen und vielen hilfreichen Ratschläge für meine Arbeit.

An dieser Stelle möchte ich mich ganz herzlich bei Dr. Gudrun Knedlitschek für Ihr Vertrauen und die Unterstützung während meiner Zeit an der Graduiertenschule des KIT bedanken. Danke auch an das ganze Biointerfaces Team für die zahlreichen

Möglichkeiten zur Weiterbildung und Horizonterweiterung.

A special thanks to Dr. Nicholas Aldred and Dr. Alessio Di Fino for providing the infinite number of cyprids for the experiments. Often even on a very short notice. Thank you also for your patience to discuss biological details to an IT guy.

Thanks to Dr. Emily Ralston, Abe Stephen and the whole team of the Center for Corrosion and Biofouling Control at FIT for the technical, moral and experimental support during the field tests at the Cape Marina test site and in open sea.

I would like to thank Dr. Laura Leal-Taixé for the friendly discussions on stereoscopy, providing core functions for the classification software and the correction of parts of this thesis.

I am thankful to my 'postdoc' Dr. Hernan Sendra, for all the support with the work and for performing the iSPR experiments. Thanks for the fun times during the measurement trips to Newcastle, Linköpping and Berlin and the long (not only) scientific discussions. Also, thanks for helping me carry around the diesel generator along the whole northern coast of England.

Vielen Dank an Dr. Isabel Thome und Stella Bauer für die Präparation der unzähligen SAMs, die in dieser Arbeit verwendet wurden.

Ein ganz herzlicher Dank geht an den fleißigen Korrekturlesern, vor allem Stella Bauer, Dr. Linlin Xiao, Dr. Svenja Vater, Dr. Isabel Thome und Maximilian Hanke.

Für die Zeit in Florida möchte ich mich bei Dr. Isabel Thome und Stella Bauer bedanken. Ein spezieller Dank auch an Prof. Axel Rosenhahn und Prof. Geoffrey Swain, für die Messungen auf dem 'Mainship', mit live-Übertragung von EM Spielen über W-LAN. Eine tolle Zeit!

I would like to thank Linlin not only for the scientific discussions, but also for the company on the KIT Shuttle, the delicious Chinease treats and the help in the lab.

Max danke ich für die hilfreichen Diskussionen und Vorschläge und dass er öfters mal sein mitgebrachtes Mittagessen zum Abendessen gemacht hat.

Isabel und Stella möchte ich für die Einführung und Unterstützung in den vielen chemischen Angelegenheiten danken. MilliQ Wasser respektiere ich immer noch.

Andreas danke ich für die Diskussionen und die Fahrradtouren zwischen Eggenstein und Karlsruhe und dass er den Glauben an meine sportlichen Fähigkeiten nie verloren

hat.

Ich danke auch Svenja für die hilfreichen Diskussionen und das Testen der Software.

Bei allen ehemaligen Mitgliedern der AK Rosenhahn, insbesondere bei Sebastian, möchte ich mich bedanken für die vielen nützlichen Ratschläge für die Durchführung der Arbeit.

Ein spezieller Dank geht an die ganze Gruppe für die herzliche Aufnahme eines Nachrichtentechnikers und die Motivation während der Arbeit. Die Pausen, der Ausflug zum Europa Park, die Konferenzen, die Grills, die Weihnachtsfeier mit Feuerzangenbowle, das “Heute ist Geburtstag”-Lied sind nur einige Highlights, die die vier Jahre zu etwas ganz Besonderem gemacht haben. Danke!

Prof. Michael Grunze, dem Team des PCI, der Verwaltung und der Elektronik und EDV danke ich für die Unterstützung während der ganzen Zeit als Doktorand. Ein besonderer Dank an Herrn Schmitt von der feinmechanischen Werkstatt der Universität Heidelberg für die vielen Ideen, und die (oft sehr) kurzfristige Anfertigung der benötigten Teilen.

Danke auch an das ganze Institut für funktionelle Grenzflächen am KIT für die Bereitstellung der Infrastruktur sowie die freundliche Aufnahme.

Ein großer Dank gilt Prof. Bernhard Wirnitzer von der HS Mannheim, der durch tolle Projekte mein Interesse an digitaler Signal- und insbesondere an Bildvearbeitung geweckt hat.

Reinhold danke ich für die Motivation während der Promotion und dass er mir öfters den Weg gezeigt hat.

I would like to thank my parents and brother for always believing in me and for the support and help during my whole studies. A special thanks also to my aunt for being always a moral supporter.

Ein ganz spezieller Dank an meine süße kleine Maus Lena Marie dafür, dass sie mich immer mit viel positiver Energie aufgeladen hat. Aber der größte Dank geht an meine Frau Kamelia, die mich immer unterstützt hat, mir Kraft gegeben hat weiter zu machen, mich inspiriert hat und sehr viel Geduld während dieser Zeit entgegengebracht hat. Danke dass du immer da warst in den guten und nicht so guten Phasen. Ohne euch Beide wäre die vergangene Zeit nicht im geringsten so schön gewesen... Ich freue mich auf die neue Herausforderungen. Обичам ви!

A. User manual: quantumCAT

A.1. Introduction and GUI overview

The MATLAB application quantumCAT (**qu**antitative **an**alysis of **t**wo-dimensional **u**ndirected **m**otion by **c**omputer **a**ssisted **t**racking) can be used to track multiple, marker-less objects in two-dimensional frame sets or videos. The software provides functionality for an automated, semi-automated and manual tracking. The tracking kernel has been developed by Prof. B. Rosenhahn (Leibniz-University Hannover, Germany) and relies on statistical parameters for the tracing of objects of interest.

The graphical user interface of the software is shown in Figure A.1. The GUI consists of four main parts which grouped different functions together.

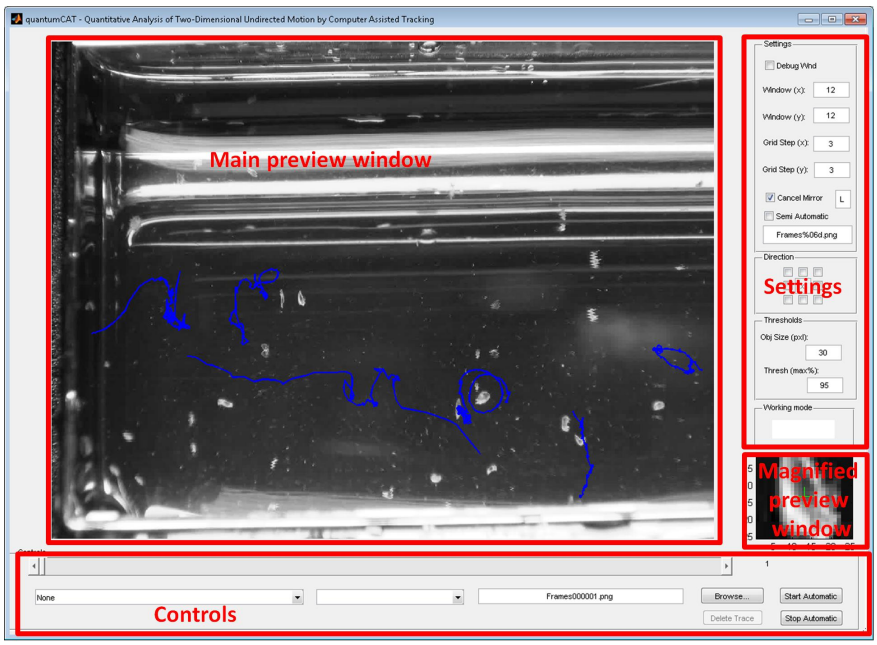

Figure A.1.: General overview of the quantumCAT GUI. The tracking software quantumCAT used for the tracking of cyprids, consisting of four main groups of functions.

The 'Main preview window' visualizes the currently processed frame from the frame set or the video. The frames are shown as grayscale image and the trajectories, con-

tained in the working directory, are visualized by blue lines. During tracking, the borders of the current tracking window are denoted by a red rectangular structure. The position of the object of interest, for which the coordinates have been determined in the current frame, is denoted by a green cross.
In the 'Controls' section, a navigation scroll bar can be found. It allows the user to navigate between different frames in the data set (or different frames of the video). The sequential number of the visualized frame is denoted in the field next to the scroll bar. A click in the scroll bar field results in a jump of 100 frames in either direction. In addition, in this group the buttons for selection of the working directory as well as for initiation and termination of an automatic tracking cycle are found. Once a working directory has been selected and it passes the plausibility check (image files or a video can be found, conform with the input in the name format field in the 'Settings' section), the first frame in the data set is shown in the 'main preview window'. The file name is output in the field next to the browse button.
If any text files are contained in the selected directory, they are loaded and visualised on the current main preview window. As it can be seen in Figure A.2, the contents of

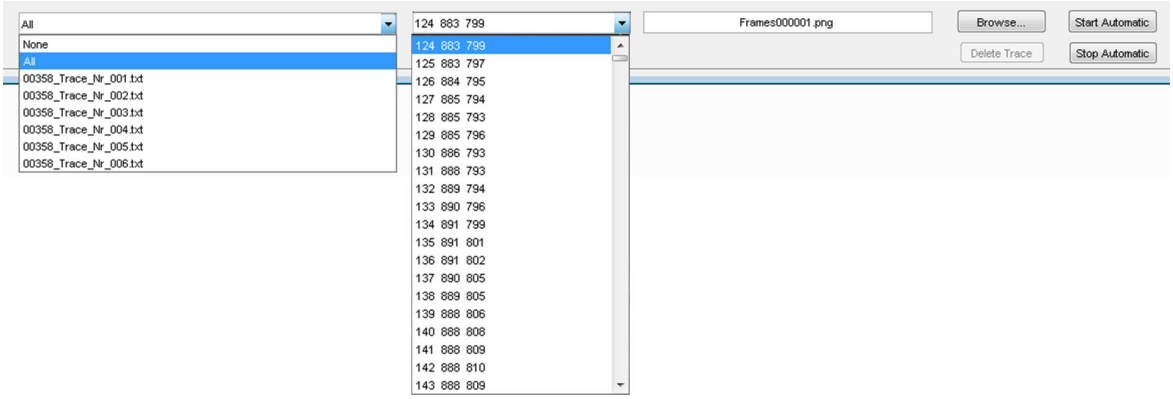

Figure A.2.: 'Controls' section of the main GUI window. The dropdown menus from the left used for switching between trajectories and between the single points of the trajectories. On the right the start/stop automatic control buttons as well as the button for selection of the current working directory.

the dropdown menus are filled with the trajectory information in the working directory. The left dropdown menu shows the file names of all trajectories found in the directory, as well as two additional options - 'None' and 'All' allowing the user to unselect or select all trajectories for visualisation and modification. The right dropdown menu is updated on every change of the selection in the trajectories menu. It is populated with the coordinates of all points contained in the selected trajectory and can be used to scroll and select individual points. Navigation through the points, automatically updates the current working frame in the main preview window. These menus can be utilized to select a whole trajectory or a point of it for modification or deleting.

The right group of the GUI, 'Settings', contains the main options controlling the tracking procedure. In Figure A.3 the main settings of the tracking algorithm are shown.

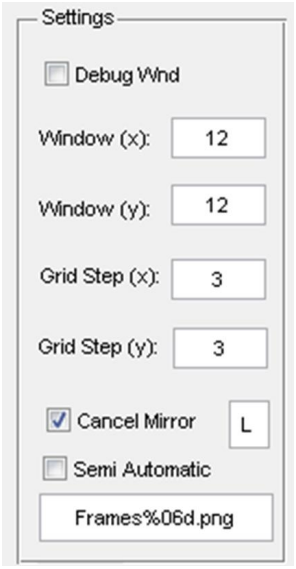

Figure A.3.: 'Settings' section of the main GUI window. In this part of tha main dialog, the options controlling the tracking algorithm can be found. In addition, in the edit field at the bottom of the section, the name convention for the input data search algorithm can be specified, thus allowing an easy adaption to new naming conventions of the input stream.

The tracking kernel used statistical classificators describing the object of interest based on values from past frames and used this information to identify the same object in following frames. In addition, an adaptive search window size was implemented in the course of this thesis, which utilized statistical parameters like velocity and direction of the object in order to minimize the probability of identifying a wrong object of interest, since all objects in the field of view possessed similar geometric shape and colour. The window sizes define the dimensions of the search area in which the cyprid is tried to be located. A higher area increases the probability to detect the cyprid of interest, but also to detect a different one. These parameters have to be adjusted in accordance to the motion velocity of the objects. Furthermore, in order to improve the accuracy in finding the object of interest, a scanning raster method was introduced as shown in Figure A.4. The raster structure fragmented the search area, and thus provided the possibility for selection of the tracking direction, which was controlled by the parameters in the 'Settings' section, in the subsection 'Direction'. E.g. when tracking objects of interest in a flow environment with a predefined motion direction, this setting can be selected to accelerate the search algorithm by discarding directions in which no movement can be expected. The properties of the raster network are controlled by the 'Grid step' parameters.

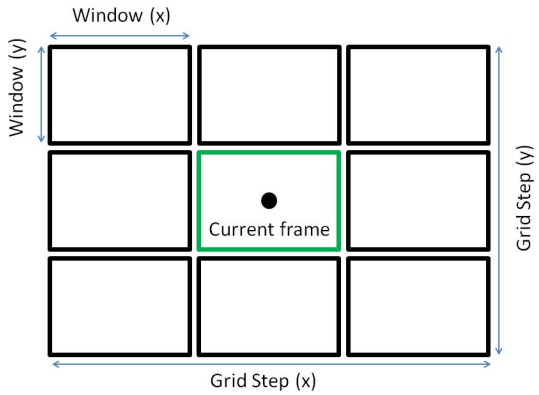

Figure A.4.: Structure of the scanning raster of the tracker. The main parameters controlling the search direction, size of the search window as well as the step size can be found in this section.

One important feature of the software is the 'cancel mirror' check box, which allows the user to define a direction in which potential mirror images should be discarded. On highly reflective substrates (e.g. gold) this setting, together with the control of the threshold of the binarisation procedure as well as the minimal size of an object (Figure A.5) of interest, improved the accuracy of the detection algorithm considerably. Finally, the 'Magnified preview window' shows a magnified version of the current frame

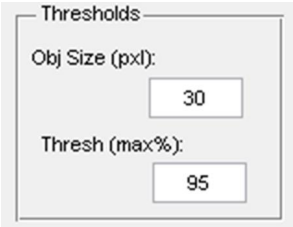

Figure A.5.: Search window parameters. The edit fields for the minimal object size as well as the threshold for the search window binarisation are located in this section of the main dialog.

portion in the search window, which is aimed to assist the user during supervision of the accuracy of the system.

In order to start the tracking procedure, starting points defining the object of interest need to be selected. Point definition during tracking in the manual mode is achieved by a left click on an object of interest during working mode 'DEFINE'. To switch in this mode, the Ctrl (Strg on German keyboards) key has to be kept pressed and the selection is confirmed by 'DEFINE' text on a green background in the working mode group (Figure A.6). The 'REFINE' mode is used to modify an already tracked point, e.g. if generated by the automated tracking procedure. To switch in the refine

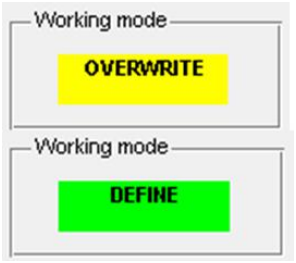

Figure A.6.: Point definition / update functions. The tracking software allowed to either define points (top panel) or edit already existing points (low panel). The first mode was mainly used to define starting points for the tracking algorithm, whereas the second one was useful to update the coordinates of points, which were wrongly detected by the tracker.

mode, the Shift (Umschalt on German keyboards) key has to be kept pressed and the selection is confirmed by an 'OVERWRITE' text box on a yellow background in the group working mode (Figure A.6 in yellow).

A.2. General tracking procedure

The general purpose of the software is the tracking of moving objects in videos obtained via 2-D video recording. Figure A.7, contains a flow chart of an object tracking procedure.

As mentioned earlier in order to select the working directory the user selects a folder containing the image data and trajectories, tracked in previous runs. The file names should be conform with the naming format which is defined in the 'Settings' section of the GUI. After a successfully passed plausibility check, the image data is loaded and the software iterates through potential text files located in the directory and loads their contents. At the same time the folder is selected as the destination folder for new trajectory definitions. If trajectory files are found, they are visualised in the main preview window.

Once the initial loading is finished, the user normally scrolls through the frames manually in order to find an object of interest. After an object of interest is found, the user defines a new point by holding the Ctrl key and a left click on the object. After the click, a magnified version of the search window is shown in the lower right corner of the dialog, which is used for a manual refinement of the selection. As a result of the click, the software runs an automatic centroid procedure to refine the selection even further. If 'None' was selected in the trajectory dropdown menu, a new trajectory file is created and the coordinates of the current point are saved. If, on the contrary, a trajectory was selected in the dropdown menu, the last tracked point is appended to the current trajectory.

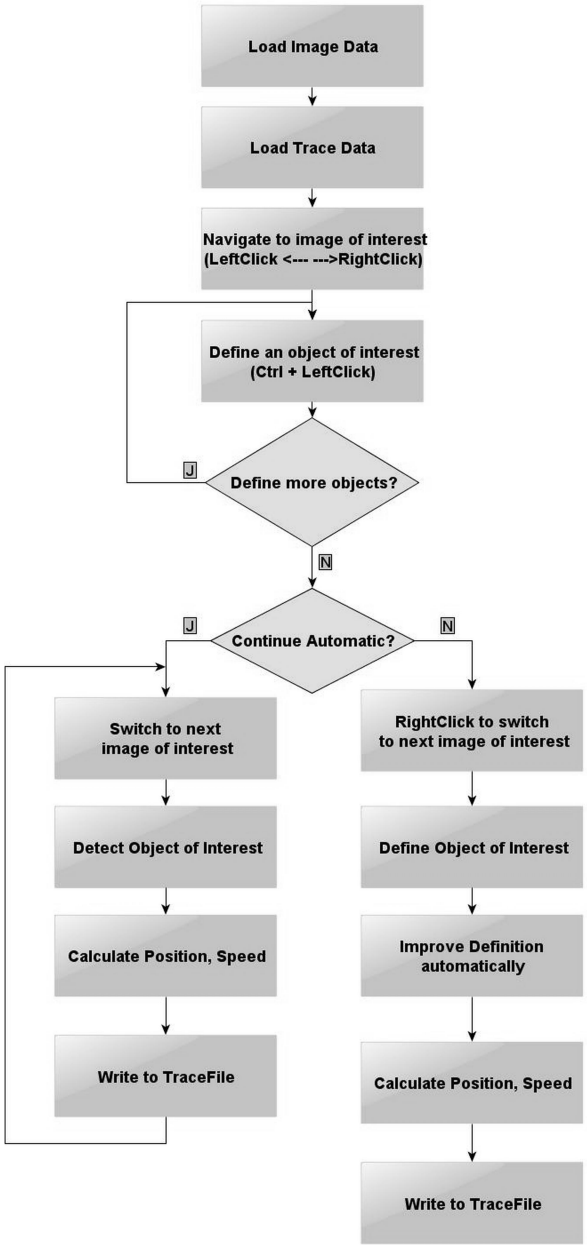

Figure A.7.: General overview of the tracking algorithm. The flowchart shows the main steps the tracking algorithm applies in order to follow the object of interest in the tracking window.

A.3. Operation modes

In the following, the main operating modes for point and trajectory generation are reviewed. Each of the modes is possible to be used for parts of trajectories (e.g.

automatic tracking until objects cross paths, then semi-automatic until objects move from each other to a sufficient distance and finally automatic tracking for the rest of the trajectory).

A.3.1. Manual tracking

Manual tracking is usually selected when an automated procedure is not possible because of a high number of objects in the field of view or low image quality. Because in that case, numerous points have to be defined a three-step tracking algorithm has been developed: 1. An object of interest is selected in the main preview window (left click + holding the Ctrl key);
2. The selection is confirmed / refined in the magnified view in the lower right corner of the dialog, by clicking on the object;
3. The right mouse button click switches to the next frame in the data set;

These three simple steps are repeated until the object of interest has left the field of view or the end of the stream has been reached.

A.3.2. Automatic tracking

In the automatic mode the software continues until it is aborted by the user or internal abort criteria have been reached. The automatic tracking uses the three steps described in the previous chapter adding the monitoring of statistical parameter such as size and speed persistence, etc. The user needs to select a point in the Trace dropdown menu and click on the Start Automatic button. If 'All Traces' are selected in the dropdown menu, the software iteratively starts an automatic tracking for all of the loaded trace files sequentially. After the automatic tracking of a single trace has been aborted, the next trace file is selected and the tracking continues from the last point in the list.

A.3.3. Semi-automatic tracking

A drawback of the fully automatic tracking is that it can easily switch to a different object of interest as soon as it crosses the path of the tracked one. For this purpose the semi-automatic mode was designed. It performs step 1 through 3 from the manual algorithm in an automated manner. For the refinement / confirmation of the selection, a user input is required, thus ensuring that the object of interest continues to be tracked. This mode is advantageous if objects of interest cross paths in the field of view and the automatic procedure does not track the object of interest, but rather switches to a different object.

B. User manual: Holography tracking software

B.1. Introduction

The software package `TraceMaster` can be used to track particles, microorganisms, bacteria and generally all kinds of moving objects that can be found in the holograms. The software works with the reconstructed stack images of holographic data. The software can be used in two main operating modes: MANUAL THREE CLICK tracking and SEMI-AUTOMATIC tracking. The program comes in the pipeline just after the image reconstruction and makes it possible to manipulate the reconstructed images and detect potential objects of interest. The package is capable of tracking the moving

Figure B.1.: Pipeline of the holographic processing. The TraceMaster application is represented in the context of the working packages and it appears just after the image reconstruction module.

object in the following frames, using a couple of descriptors from the preceding frames which are monitored. These descriptors include the velocity, the size of the object in XY plane, the size of the object in the Z projection planes and the position in XY / Z planes. The limits for these descriptors can be defined in the Advanced Settings part of the main dialog, because they vary drastically depending on the type of particle / microorganism which is tracked. The MANUAL and the AUTOMATIC tracking use the same particle detection algorithm. The idea is to use a fast but not perfect algorithm to roughly detect a potential particle candidate (in the automatic mode) or click on a potential candidate particle (in the manual mode). In the second step, the algorithm calculates the centroid of the object to correct its exact position, after which a statistical parameter based on the descriptors described earlier is calculate giving the information if the current particle belongs to the trace in which it has been tracked.

This step makes sure that at crossing points the algorithm will keep tracking the object of interest and not other colliding objects which are in near proximity. The software package contains a folder with example hologram reconstructions, a parameter file, a time stamp file and some already tracked organism trajectories.

B.2. Main Functions

B.2.1. Interface of the program

The software expects the input parameters shown on Figure B.2.

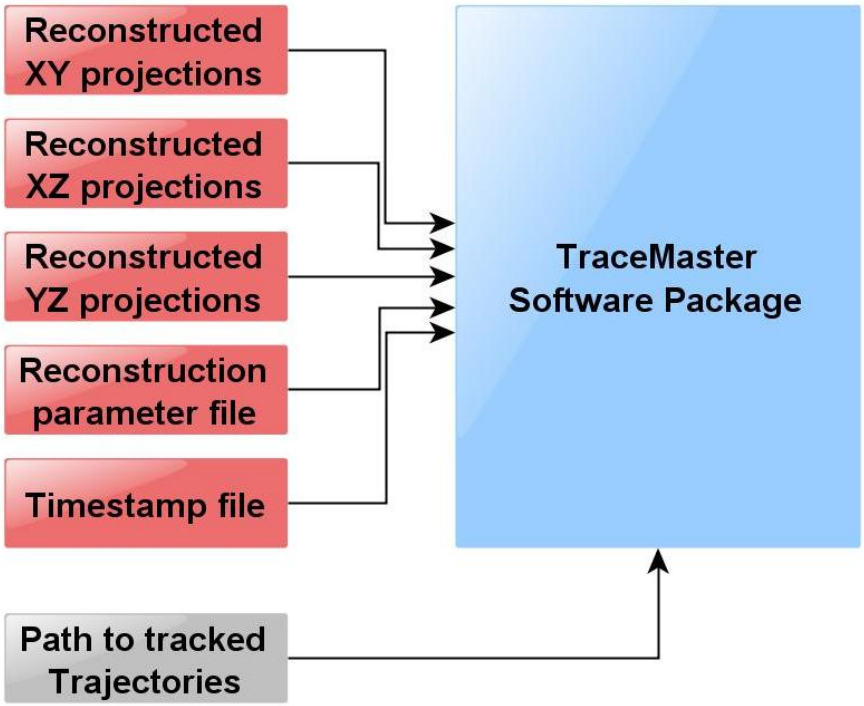

Figure B.2.: Input parameters of the TraceMaster. In addition to the image files, a reconstruction parameter file as well as a time stamp file are required. A destination path is an optional parameter (in gray) and can be used to specify an output folder, different from the working directory.

a) Reconstructed XY Projections: These files contain the movement data of the particles in the xy plane. There is one requirement for the file name (because of compatibility issues with previous versions) - `IMG_FILENAME_XY = ‘‘*xy_*.png’’`

b) Reconstructed XZ Projections: The projection file names in the XZ plane have the format - `IMG_FILENAME_XZ = ‘‘*xz_*.png’’`

c) Reconstructed YZ Projections: The projection file names in the YZ plane have the format - `IMG_FILENAME_YZ = ‘‘*yz_*.png’’`

d) Reconstruction parameter file: Contains important parameters used for the reconstruction of the images from the histograms. It has the following name convention - `REC_PARAM_FILENAME = *.rf`. An exemplary content of the parameter file is shown in Figure B.3.

e) Time stamp file: This file contains the time information which can be used to calculate the speed and other describing parameters. The name convention here is - `TIME_STAMP_FILENAME = ‘‘*.ts’’`. Figure B.4 shows an exemplary time stamp file.

f) Tracked trajectories: This parameter is a path, where the trajectory files are saved / loaded. Figure B.5 shows the contents of a trajectory file.

B.3. Graphical user interface overview

The main dialog of the program consists of the following groups of graphical user interface elements:

a) Image Preview group
This is the main part of the control dialog. On the left (big image) are presented the reconstructed XY projection photos. On the right (upper two images) represent the XZ and YZ projections with a red line indicating the position in Z where a matching object has been detected. The lower image shows a zoomed version of the region around the potential clicked point, which allows the user to verify and refine a selection which he previously made on the big XY image plane.

b) Trace Manipulation group
This group shows information about the loaded traces (the left list) and the points in each trace file (the right list). The loaded trace list is automatically generated after the user has selected a folder containing the trace files. If there are no files in the folder only NONE will be in the list. The list allows a selection of single traces, all traces or none trace. The exclude points selection will load all the defined exclude points and present them on the XY image plane. The right list shows all the points belonging to a selected trace from the left menu. If the selection is on the exclude points, on the right will appear a list of all points which are defined as exclude points. The Button Delete Selected Trace deletes the selected trace file also from the hard disk. Concatenate Traces can be used to merge two trace files together. The only requirement to do this is that the last image number in the first trace file is equal to the first image number 1 in

```
mainfolder          F:\Samples\
filename            ParameterFile
fileext             .rf
RP_version          RP_SM-1
setupfile           Samples_3.txt
source              SourceRange_410-459.png
inputext            png
outputext           png16
outputtype          0
Outputbits          16
from                410
to                  3000
skip                1
L11                 1.6
L12                 3
steps               0.005
coswindow           80
NF                  20
lambda              5.32e-007
n0                  1
L                   22.6
pp                  12
d_sample            [1.925 2.725]
n_sample            1.33
d_before            1.00
n_before            1.47
d_after             [1 5 0.78]
n_after             [1.51 1.51 1.53]
starttime           [2011 4 1 13 19 22]
size                1024
N                   1024
endtime             [2011 4 1 13 24 28]
```

Figure B.3.: Reconstruction parameter file. In addition to the input / output folder information, the file contains the physical properties of the medium, laser and important distances, as well as range of files to be used.

the second one. In this manner it is guaranteed that no traces will exist with missing points in certain frames. Delete Point allows the user to delete a certain point in a trace file. If the point is in the middle of the trace the software would automatically ask whether the trace should be tracked automatically or the rest of the points should be deleted. The Define Manually allows a manual correction

Image number	Time	Timestamp
00001	10.09.08_15:21:14.359609	14.359609
00002	10.09.08_15:21:14.426269	14.426269
00003	10.09.08_15:21:14.492930	14.492930
00004	10.09.08_15:21:14.559590	14.559590
00005	10.09.08_15:21:14.626251	14.626251
00006	10.09.08_15:21:14.692911	14.692911
00007	10.09.08_15:21:14.759571	14.759571
00008	10.09.08_15:21:14.826232	14.826232
00009	10.09.08_15:21:14.892892	14.892892
00010	10.09.08_15:21:14.959553	14.959553
00011	10.09.08_15:21:15.026213	15.026213
00012	10.09.08_15:21:15.092873	15.092873
00013	10.09.08_15:21:15.159534	15.159534
00014	10.09.08_15:21:15.226194	15.226194
00015	10.09.08_15:21:15.292855	15.292855
00016	10.09.08_15:21:15.359515	15.359515
00017	10.09.08_15:21:15.426175	15.426175

Figure B.4.: Time stamp file. The exact recording time of each image in the path is recorded in this file. The software uses the image number to locate the file on the hard drive and assigns the time stamp value found in the file. This is an important feature, since many cameras cannot provide a reliable constant frame rate of image recording.

```
Version: 1.0
Bild Xst[Pix] Yst[Pix] Xopt[Pix] Yopt[Pix] Z_ebenen Zst[mm] Fehler Z [µm] Z_x [Ebene] Z_y [Ebene] Xµm[µm] Yµm[µm] Zµm[µm] time[s] V[µm/s]
#00800 NaN NaN 652.72798 276.98854   66.66500 01.93333 02.01525 66.95000 66.38000  164989.48135 -275527.43288 1933.32500 NaN     NaN
#00801 NaN NaN 647.43732 285.32883   67.70500 01.93853 01.44957 67.50000 67.91000  159213.75660 -266463.99120 1938.52500 67.688 187902.73621
#00802 NaN NaN 646.33534 293.19240   66.26500 01.93133 00.60104 66.18000 66.35000  157331.83355 -256264.66246 1931.32500 67.755 139562.84815
#00803 NaN NaN 642.44964 301.45154   64.76000 01.92380 00.98995 64.90000 64.62000  152187.98840 -245634.60844 1923.80000 67.821 159744.56442
#00804 NaN NaN 648.99194 303.91994   64.53500 01.92268 00.81317 64.65000 64.42000  159729.28568 -242616.31500 1922.67500 67.888 122295.60801
#00805 NaN NaN 645.05356 308.88690   64.82500 01.92413 00.10607 64.81000 64.84000  155251.42987 -236999.28441 1924.12500 67.955 111012.60788
#00806 NaN NaN 639.12095 304.13723   60.93000 01.90465 00.49497 60.86000 61.00000  146863.36937 -240144.73066 1904.65000 68.021 131712.42777
#00807 NaN NaN 629.44685 295.20447   61.06000 01.90530 00.49497 60.99000 61.13000  135732.04255 -250548.22672 1905.30000 68.088 228282.01708
```

Figure B.5.: Trajectory file. The contents of the output trajectory file are shown. It contains a header with the version number, for compatibility issues, and the swimming parameters corresponding to a given frame number.

of the selected tracking point from the list.

c) Info group
This group has only informative meaning. The Status field gives information on the success of the tracking algorithm and is used for communication with the user. The Q Parameter is for the moment for debugging use only and gives internal

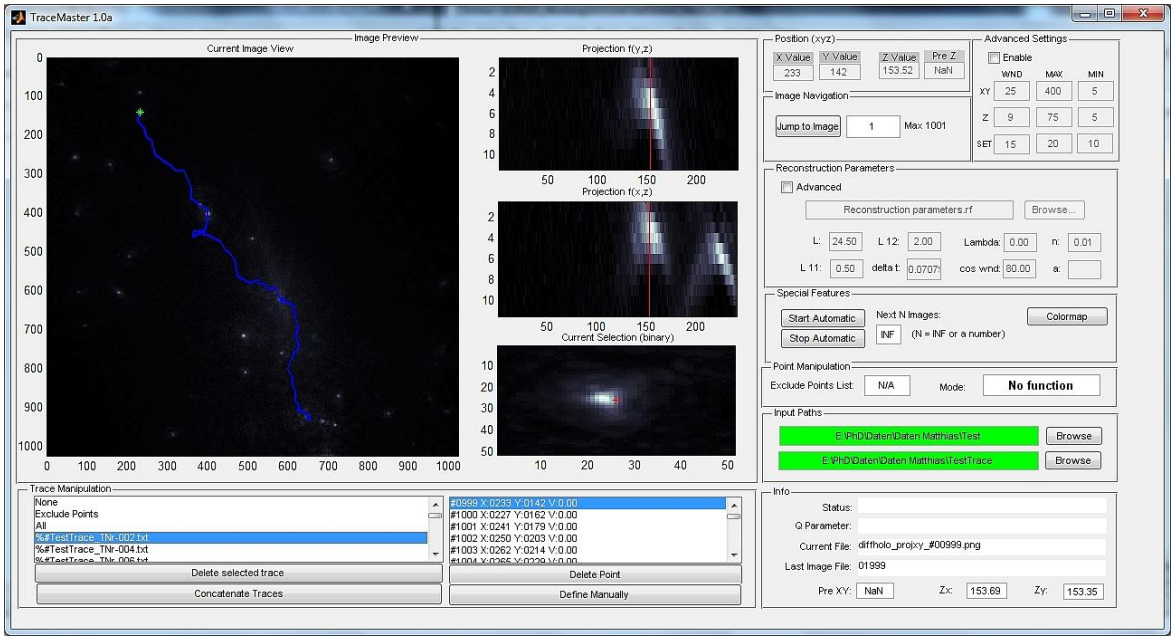

Figure B.6.: TraceMaster GUI overview. The GUI of the program contains several parts, responsible for either output of results or input and control of the tracking process.

information about the quality of the detection. Current File gives information on which projection file is being visualized in the XY projection plane. Last Image File, Pre XY, Z_x and Z_y are for internal use.

d) Input Paths group
This is the main input for the software. The first folder gives the location of the image sequences, where the reconstructed holographic image data can be found. The second folder gives the location where the trace files are saved / loaded. The naming convention of the trace files is as follows: `TRACE_FILENAME = '%#TraceFolder_TNr-XXX.txt'`. In the example from above the traces will be called %#TestTrace_TNr-001.txt etc.

e) Point Manipulation group
This group has informative role. It gives information which input mode is active in the moment and whether there is an active exclude points list loaded in the memory. The input modes are: Define Points and Exclude Points. In the point definition point (holding the Ctrl Key) each click on the XY-Plane defines a point in the current trace. If there is no trace file selected, each click defines a new trace file. In the definition of exclude points mode each clicked point on the XY-Plane is defined as an exclude point and it is substituted by background pixels in order to exclude fixed pattern noise points from the potential candidates

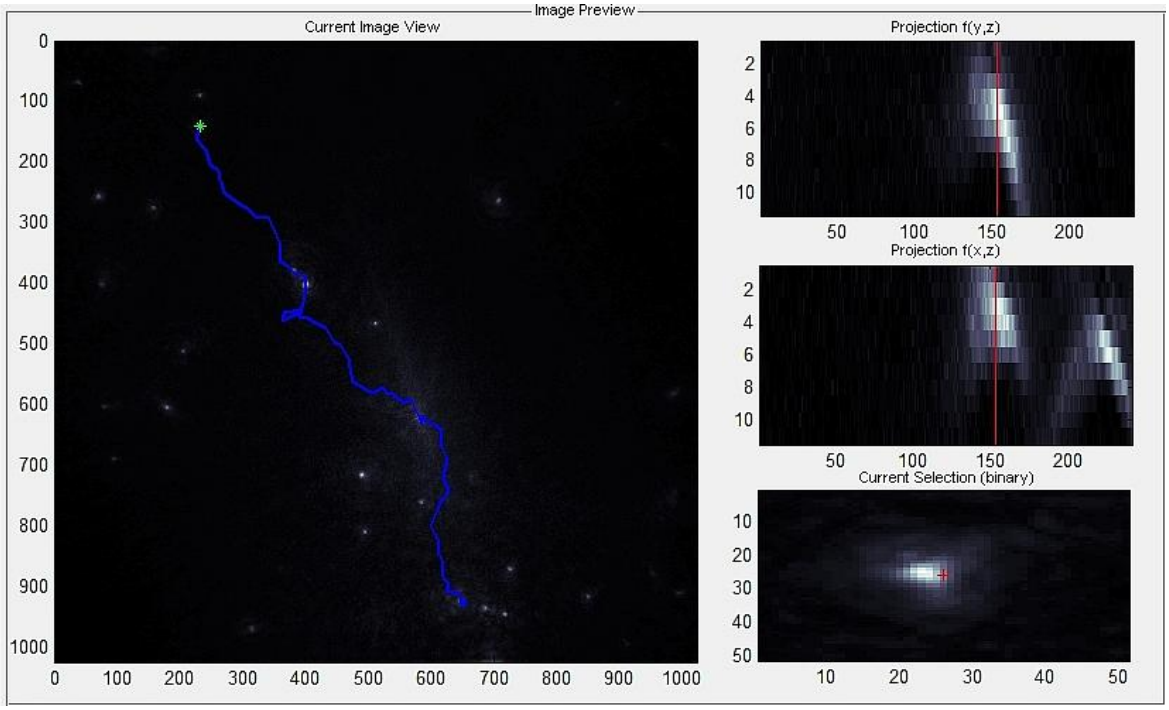

Figure B.7.: The image preview group of the GUI. In this part of the main dialog the magnified xy projection is shown together with the xz and yz projections. The contents of the current tracking window can be found in the lower right corner of the group.

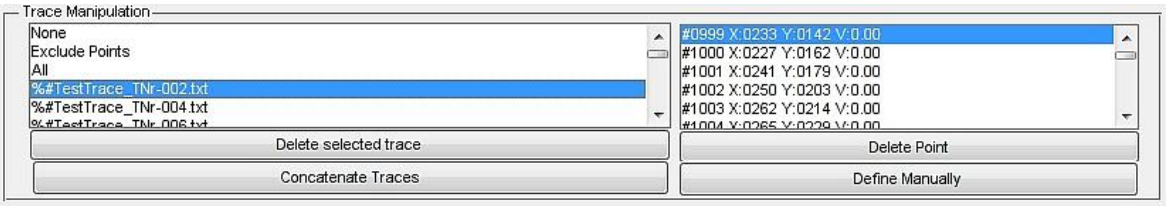

Figure B.8.: The trace manipulation group of the GUI. A trajectory selection control is positioned on the left of the dialog and on the right the coordinate points corresponding to the selected trajectory are shown.

list.

f) Special Features group

In this control the user has the possibility to control the automatic tracking. The Start Automatic and Stop Automatic buttons initiate and interrupt the automatic tracking algorithm for the next N images. If the Next N Images is

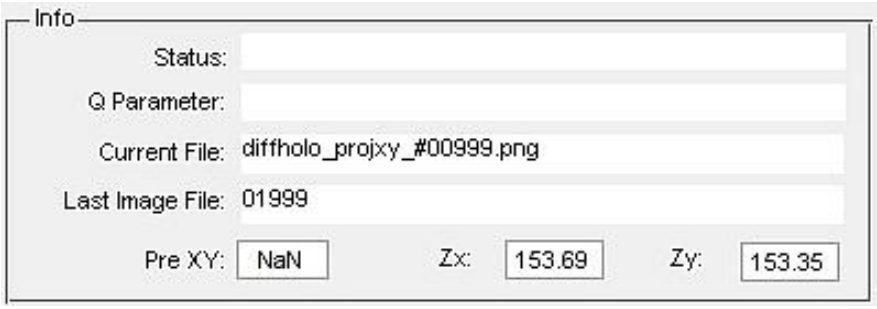

Figure B.9.: The info group of the GUI. This part of the dialog is an output, which is used by the software to provide information on the tracking success and to present error messages to the user. Most information contained here is used for debugging purposes or optimization.

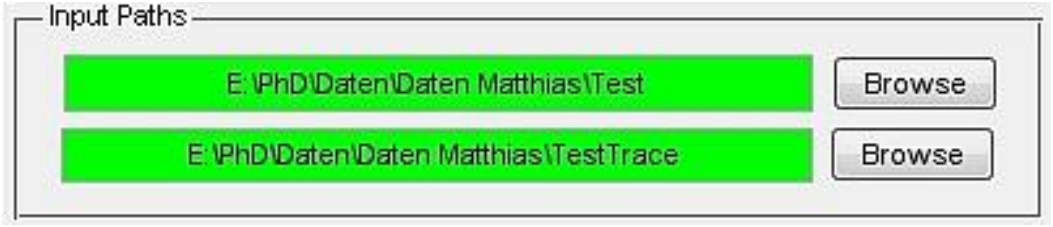

Figure B.10.: The input paths group of the GUI. These values define the paths which contain the image data, used for the tracking as well as the path containing the already tracked trajectories.

Figure B.11.: The point manipulation group of the GUI. These fields are used to input information on the current working mode of the software - whether points are being defined or excluded.

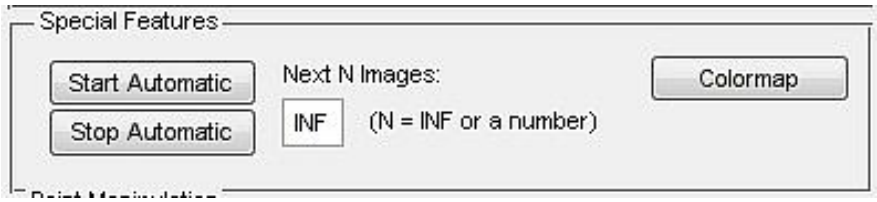

Figure B.12.: The special features group of the GUI. The controls contained in the group are used to start and stop the automatic tracking procedure.

set to INF the algorithm tracks until a termination criterion has been fulfilled: end of image sequence, particle goes out of the field of view or difficulties in the tracking (because of the quality or crossing of unresolved points). The Colormap feature allows the user to change the contrast between objects and background in order to overcome some limitations in images with low quality concerning the contrast.

g) Reconstruction Parameters group
This group is primarily used for information. It shows the loaded reconstruc-

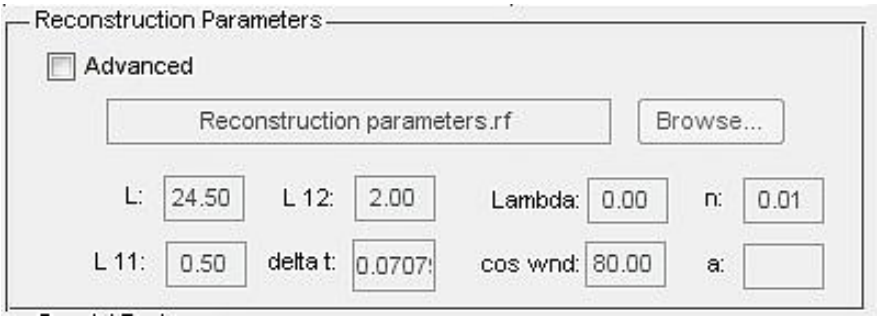

Figure B.13.: The reconstruction parameter group of the GUI. This group is used to output the values of the reconstruction parameters, located in the parameter file. If the check box is activated, the user can change single values of these parameters.

tion parameter file and the values needed for the calculation of different output parameters like speed, position of particle, etc. Checking the Advanced check box allows a manual edit of the values, which has to be done only by advanced users as it influences the whole output file values of the TraceMaster.

h) Advanced Settings group
These settings control the automatic tracking algorithm. If the Enable check

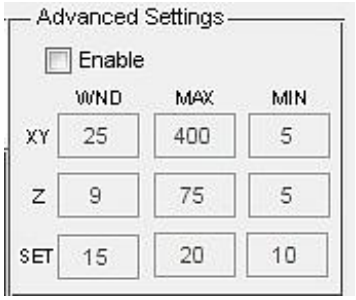

Figure B.14.: The advanced settings group of the GUI. The parameters controlling the tracking algorithm can be changed in this group.

box is not activated the software uses the default values which are coded in the

software. Activating the check box allows the manual adjustment of the values. The first row controls the values in XY WND window size for the search of the next microorganism (depends on the swimming speed of the tracked particle), MAX and MIN values for the size of the detected particle to be accepted in the list of valid candidates. In the second row are the same controls for the Z projections. The last row contains the special parameters for controlling the automatic algorithm. The first one is responsible for the maximal difference in the sizes of the objects found in the XZ and YZ projections. The other two parameters control the maximal distances to the previous Z resp. XY positions. This allows the limitation of the jumps in these two directions.

i) Image Navigation group
This group can be used to jump to a certain image. It also provides information

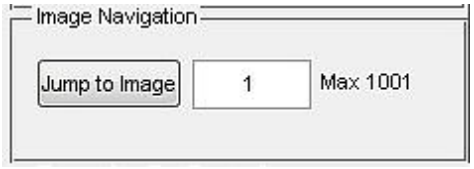

Figure B.15.: The image navigation group of the GUI. The control allows a faster scrolling and jumping through the images in the input path.

on how many images have been found in the input folder. The first number corresponds to the sequential number of the current manipulated image.

j) Position group
This group has informative meaning. The values communicate with the user the

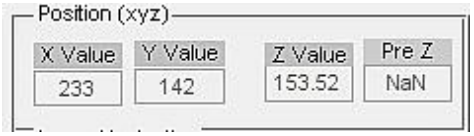

Figure B.16.: The position group of the GUI. This group outputs the current coordinates of the object being tracked in the field of view.

coordinates of the current object in X, Y, Z and the previous location in Z. This information can be used to manually verify that there has been no unexpected increase in the Z position, which would mean in most cases that there has been an error in the tracking algorithm.

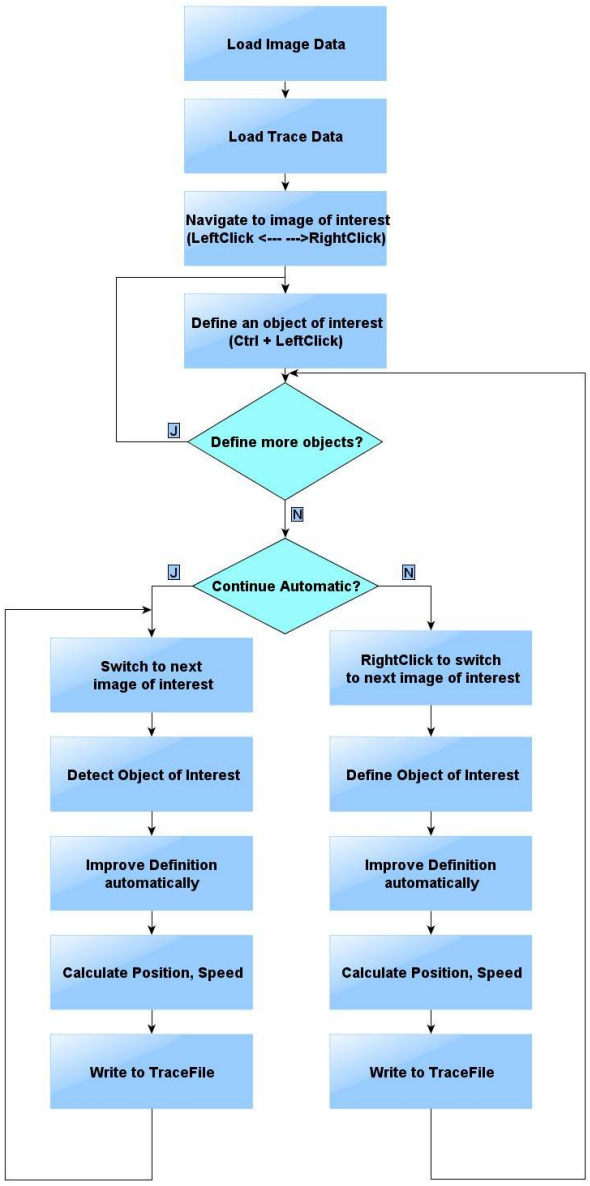

Figure B.17.: General overview of the tracking algorithm. The flowchart shows the main steps the tracking algorithm applies in order to follow the object of interest in the tracking window.

B.4. General tracking procedure

The central purpose of the program is the tracking of moving particles in reconstructed holographic images. The figure above shows the whole chain of functions in the software: The first step is to load the image data which needs to be in the same folder at this point of the development. This includes the XY and the XZ and YZ projection

files which have to meet the requirements of the naming convention mentioned before. If the input check has been successful and the image data has been loaded comes the next step. In the second step the trace files are loaded. If there are no trace files at least a destination folder needs to be input in which the produced trace files will be loaded. If on the other hand, there are trace files from previous tracings, they will be shown in the Trace Manipulation Control of the software. Usually at this point the user has to scroll through the images to find the ones where there is information of good quality and the tracking can start. The scrolling between the images can be done using a Left or a Right Click for incrementing or decrementing the number of the current image. For bigger jumps the Image Navigation group can be used. After a suitable image has been found the user has to define an object of interest by clicking on it on the XY-plane representation. After this click a zoomed version of the region of interest is shown in the lower right corner of the Current Image View group. The user is expected to refine his selection by clicking in the object again, this time in the zoomed view. As a result of the click the software automatically searches for a reasonable match of objects in both XZ and YZ projections and defines the clicked object as a valid particle candidate. If there was no trace selected in the Trace Manipulation group each click of the user defines a new trajectory and a new trace file is created. If on the other hand a trace has been selected, the current object coordinate points are added in the current trace file, thus appending / modifying points of the current trace. The user can define multiple objects of interest, after which a selection needs to be made how to continue with the tracking. If the user wants to track the following points MANUALLY then a manual switch to the next image should be executed (right mouse click). In the manual routine comes a loop in which the user defines a new object of interest in the manner described above. To ensure correct object detection the software cross checks the object in the XZ and YZ projections and also analyses the descriptor values for an unusual change of the persistency. All the parameters of interest, describing the object are calculated in the following step and after that the point with all the values are written in the trace file. If a new point needs to be added the loop starts again from the beginning. If an AUTOMATIC tracking is selected, the software automatically loops through all the images of interest and follows the current particle, monitoring the statistical parameters and saving the results in the trace file. The routine would abort if the end of the images has been reached, the particle leaves the field of view or there has been a problem with the algorithm (statistical descriptor inconsistency, etc.)

B.5. Operation Mode: MANUAL THREE CLICK Tracking

In the manual tracking it is often needed to define numerous numbers of points. Thats why the manual tracking has been developed to be achieved in three simple steps:

1. The user selects an object of interest in the main XY view (left click + holding the Ctrl key);
2. The user refines the selection by clicking in the current selection zoom window;
3. The user clicks the right mouse button to switch to the next image;

These three simple steps can be repeated until the end of the trace has been reached or all of the images have been used.

B.6. Operation Mode: SEMI-AUTOMATIC Tracking

In the semi-automatic mode the software continues until it is aborted by the user or internal abort criteria have been reached. The automatic tracking uses the three steps described in the previous chapter adding the monitoring of statistical parameter such as size and speed persistency, etc. It can be start from any point of a given trace. The user needs to select a point in the Trace Manipulation group and click on the Start Automatic button. If there has been selected All Traces in the trace list, the software iteratively starts an automatic tracking for all of the loaded trace files sequentially. After the automatic tracking of a single trace has been aborted, it jumps to the next trace file and continues the tracking from the last point in the list.

B.7. Examples

In this chapter the main use cases which can occur in real life situations are presented in a step-by-step manner.

B.7.1. Manual tracking

The manual tracking is the simplest feature of the software. In this tutorial the user can learn how to: define points, define new trace files, browse the images, jump to images and delete points from a given trace file. This tutorial continues after the first two steps of selecting the image path and selecting the trace files path.

1. Browse through the images to find some moving objects by using the left / right mouse button and then return to image number 1, by clicking the left / right mouse buttons again or by using the Jump to image button in the Image Navigation group.
2. Make sure that in the Trace Manipulation group the NONE is selected

3. Press and hold the Ctrl key (in the Point Manipulation Group the Mode is changed to: Define Points)

4. Click with the left mouse button on the XY-plane on the object of interest. In the Current Selection (binary) a zoomed version of the region of interest is presented.

5. Click on the Current Selection (binary) to refine your selection. After this the software automatically detects the objects in XZ and YZ projections marking them with red crosses. If the detection went ok, the originally clicked point in the XY plane is marked with a green cross.

6. Look in the Trace Manipulation group: the software automatically created a new trace file called

7. Using the same procedure (1.-6.) the user can create many different starting points. As long as the trace selection says NONE, each defined point will be saved in a new trace file, assuming that this is the start point of a new trace.

8. To continue with the manual tracking of a given trace go to the Trace Manipulation group and select the trace which you want to continue e.g.

9. You can see that the trace contains only one point which can be seen in the right list of trace points and also on the XY projection plane. If there are many points, the user should manually select in the list the point from which the trace should be continued (here the 1st point).

10. Click on the right mouse button to proceed to the next image.

11. Holding the Ctrl key click on the object which now has moved a little bit

12. Refine your selection by clicking on the zoomed presentation on the lower right corner. If the detection went well, the software would connect the trace points with a blue line indicating the trace.

13. Continue the procedure (10.-12.) as long as there are points of interest. The figure shows the result of tracking an object in the first 10 example pictures (Green star indicates the start of the trace)

B.7.2. Automatic

The automatic tracking mode allows to continue the execution of the points 10.-13. from the manual tracking tutorial in a loop manner. This tutorial continues from point 9. of the manual tracking.

1. Select the last point of the trace which was just tracked (%#TEST_TRACES_TNR-004.TXT, image 809)

2. Click on the Start Automatic Button. The software will start the automatic tracking procedure.

3. In the automatic procedure monitor the Status output in the Info group, where eventual errors are reported to the user. As long as the Start Automatic button is not active, the automatic routine is running. You can interrupt it anytime by pressing the Stop Automatic button. In our example the software would track all 21 example images and finish with the following trace:

B.7.3. Exclude points

In this tutorial it is shown how to define some static points as exclude points in order to prevent the software from considering them as candidate particles. For this purpose we select NONE in the Trace Manipulation group.

1. Browse through the images to find some static points

2. Independent on which image you are at the moment, hold the SHIFT key. The Point Manipulation Mode is switched to Exclude Points.

3. Click on the constant point in the XY plane with the left mouse button

4. The region of interest is presented in the lower right window. Click on to refine the selection of the point.

5. The software automatically marks the static point using a small quadrate and showing in the Exclude Point list of the Point Manipulation group the sign: Ready.

6. In the Exclude Points in the Trace Manipulation List the user can see which points are defined as exclude points and delete / redefine them.

7. In this example we will delete the currently defined point by clicking on it in the list on the right and selecting the button Delete Point.

8. The Exclude Points List sign changes to N/A again. Remark: All of the Exclude points are saved in the file called Exclude Points, which can be deleted or moved in order to use the defined points in different projects.

B.7.4. Point refinement

This tutorial shows how to change and refine a point from a trace file. This could be very helpful in case that the automatic tracking has made a mistake and after a manual control the user notices that there is a certain point which is wrong.

1. Select the Point of Interest, which you want to refine in the Trace Manipulation group.
2. Click on the button Define Manually to start the process
3. Click on the point in the XY plane
4. Click on the point in the lower right window, with the zoomed representation of the region of interest.
5. The software checks whether there are reasonable values in the XZ and YZ projections and if this check is positive, the user is asked to select what to be done with the following points: Delete All, Update Automatically or Leave Unchanged. All these options make sense in different use cases.

B.7.5. Trace concatenation

This feature allows the user to merge two trace files. The prerequisite for this merging is that the first and the second file have sequential numbers of images (meaning that the last image of the first file should be the first image of the second file 1).

1. Click on the first trace in the Trace Manipulation group and click on the button Concatenate Traces
2. Holding the Shift key, select the second trace from the list
3. Click on the button Select Traces to Concatenate
4. The software automatically creates a new trace file containing the new trace.

B.8. Future features

Due to the complexity of the algorithm and the software, the fact that it can be used with different particles and microorganism and the always growing need of new features, in this chapter the future features will be presented.

- Colormap
  Sometimes the quality of the reconstruction data is not very high, because of poor reconstruction parameters, environment influence and candidate objects

which produce a low contrast. This makes MANUAL tracking not very easy. The possibility to allow the user to change the colormap of the pictures, so that there is more contrast is planned to be added as a new feature;

- Local histogram stretching
  For poor quality reconstructions and reconstruction of holograms with objects with low contrast there might be problems with the AUTOMATIC tracking algorithm. In order to overcome this problem an automatic local histogram stretching algorithm will be available, which will enhance the contrast in the holograms and at the same time keep the signal-to-noise ratio in reasonable limits;

- Zooming
  Although the idea of the MANUAL THREE CLICK tracking is to click first on the big image, then in the second step a small region is represented zoomed on the right lower corner where you can refine your selection, there is still the need of the possibility to zoom regions of the big image. Especially by reconstruction images of not very high quality;

- Object optimized filters (Matched Filters)
  The tracking can be optimized if so called matched filters are used. These filters are specially defined to correspond to the form of the object which is going to be tracked. By using these filters a better detection of candidate particles can be achieved and some reconstruction artifacts can be attenuated;

- No reconstruction parameter file
  For some tracking tasks it is not important to get the absolute values of the positions of the object. It is more interesting to see the form and the relative positions. For this purpose the need of a reconstruction parameter file will be removed;

- 4D Representation (time!!)
  Some traces are more interesting to be resolved in the 4th dimension. This feature is also in the plan of future releases;

B.9. Troubleshooting

Q: Right, Left click navigation is not working properly
A: Some times the control responsible for the key pressed events looses the focus. To repair this, just click on the XY-plane and press the CTRL key. You should be able to see that the Mode changes from No Function to Define Points which means that the problem is fixed.

Q: Define Point, Exclude Point mode cannot be switched
A: Same problem as the one above. Left mouse click on the XY-plane and pressing of the CTRL key solved the problem so far.

Q: No Trace files are not shown
A: The format of the Trace Files is important for the program. If the internal version check fails the file is not loaded. If you are using old trace files, please adapt them by adding a Version number in the uppermost line.

Q: No parameter file is loaded
A: Due to backwards compatibility the software recognizes the parameter files on the extension. Please refer to the previous chapters on this matter. There is also an example parameter file delivered in the package, which can be used.

Q: No time stamp file is loaded
A: Same problems as with the parameter file. Make sure that the naming convention is fulfilled and that the format of the file corresponds to the format described earlier in this manual.

Q: No images are loaded
A: The software checks internally for the number of XY and XZ and YZ projections which should be the same and should be in the same folder. If this is not fulfilled the program would not load any images. Also very important is to keep in mind the naming convention.

Q: Format problems
A: All the formats of the critical files are included in this tutorial. Please refer to them and try to follow them strictly.

Q: Exclude point problems
A: The software sets the pixels around the exclude points to the mean value of the background pixels. This could be problematic in some situations. The user is advised to disclaim from using this feature if he is not familiar with its meaning.

List of Abbreviations

AA	alginic acid
AF	Antifouling
ASW	artificial seawater
AUDT	11-Amino-1-undecanethiol hydrochloride
B. amphitrite	Balanus amphitrite
BSR	Bulk swimming region
CA	Contact angle
CAD	Computer-aided design
cdf	cumulative distribution function
CVD	Chemical vapor deposition
DDT	1-Dodecanethiol
ECDF	empirical cumulative distribution function
EG	Ethylene glycol
FIT	Florida Institute of Technology
FOV	Field of view
FR	Fouling release
FSW	Fresh sea water
GUI	Graphical user interface
HA	Hyaluronic acid
HUDT	11-Mercapto-1-undecanol
IMO	International Maritime Organization

KIT	Karlsruhe Institute of Technology
LSR	Lower swimming region
MQ	MilliQ
OV	Occurrence value
pdf	probability density function
PEG	Polyethylene glycol
PNG	Portable network graphics image format
PS	Polystyrene
quantumCAT	quantitative analysis of two-dimensional undirected motion by computer assisted tracking
S. balanoides	Semibalanus balanoides
SA	Swimming area
SAM	Self-assembled monolayer
SD	Standard Deviation
SEM	Standard error of the mean
SIPC	Settlement inducing protein complex
TBT	Tributyltin
UV	Ultraviolet
USO	Unidentifed swimming object
USR	Upper swimming region
XPS	X-ray photoelecton spectroscopy

List of Figures

Publications

Publications with peer-review process

- **Maleschlijski S.**, Bauer S., Sendra G.H., Di Fino A., Clare A.S., Rosenhahn A. (2014): Barnacle cyprid motility and distribution in the water column as an indicator of the settlement inhibiting potential of nontoxic antifouling chemistries. *Biofouling* (**accepted**)

- Vater S., Weisse S., **Maleschlijski S.**, Lotz C., Koschintzki F., Schwartz T., Obst U., Rosenhahn A. (2014): Swimming behavior of *Pseudomonas aeruginosa* studied by holographic 3D tracking. *PLoS ONE* **9**(1)

- **Maleschlijski S.**, Sendra G.H., DiFino A., Leal-Taixé L., Thome I., Terfort A., Aldred N., Grunze M., Clare A.S., Rosenhahn B., Rosenhahn A. (2012): Three dimensional tracking of exploratory behavior of barnacle cyprids using stereoscopy. *Biointerphases* **7**(1-4), pp. 1-9

- Sendra G.H., Weisse S., **Maleschlijski S.**, Rosenhahn A. (2012): Hologram reconstruction corrected for measurements through layers with different refractive indices in digital in-line holographic microscopy. *Applied Optics* **51**(16), pp. 3416-3423.

- **Maleschlijski S.**, Bauer S., Aldred N., Clare A.S., Rosenhahn A. (2014): Classification of swimming behaviour of barnacle cyprids during surface exploration. *Journal of the Royal Society Interface* (**submitted**)

- Hanke M., Fuchs K., **Maleschlijski S.**, Sleeman J., Orian-Rousseau V., Rosenhahn A., CD44 mediates the Flow Induced Rolling of HepG2 Epithelial Cancer Cells on Hyaluronan, (**in preparation**).

Publications without peer-review process

- **Maleschlijski S.**, Leal-Taixé L., Weisse S., Di Fino A., Aldred N., Clare A.S., Sendra G.H., Rosenhahn B., Rosenhahn A. (2011): A stereoscopic approach for three dimensional tracking of marine biofouling microorganisms. *Proceedings Microscopic Image Analysis with Applications in Biology*, Heidelberg, Germany (2011).

Eidesstattliche Versicherung gemäß § 8 der Promotionsordnung der Naturwissenschaftlich-Mathematischen Gesamtfakultät der Universität Heidelberg

1. Bei der eingereichten Dissertation zu dem Thema

_____

_____

_____

handelt es sich um meine eigenständig erbrachte Leistung.

2. Ich habe nur die angegebenen Quellen und Hilfsmittel benutzt und mich keiner unzulässigen Hilfe Dritter bedient. Insbesondere habe ich wörtlich oder sinngemäß aus anderen Werken übernommene Inhalte als solche kenntlich gemacht.

3. Die Arbeit oder Teile davon habe ich wie folgt/bislang nicht[1)] an einer Hochschule des In- oder Auslands als Bestandteil einer Prüfungs- oder Qualifikationsleistung vorgelegt.

Titel der Arbeit:_____

_____

Hochschule und Jahr:_____

Art der Prüfungs- oder Qualifikationsleistung:_____

4. Die Richtigkeit der vorstehenden Erklärungen bestätige ich.

5. Die Bedeutung der eidesstattlichen Versicherung und die strafrechtlichen Folgen einer unrichtigen oder unvollständigen eidesstattlichen Versicherung sind mir bekannt.

Ich versichere an Eides statt, dass ich nach bestem Wissen die reine Wahrheit erklärt und nichts verschwiegen habe.

_____ _____

Ort und Datum Unterschrift

[1)] Nicht Zutreffendes streichen. Bei Bejahung sind anzugeben: der Titel der andernorts vorgelegten Arbeit, die Hochschule, das Jahr der Vorlage und die Art der Prüfungs- oder Qualifikationsleistung.